A study on the time evolution of Be stars

Adrián Castañón Esteban

A thesis submitted in partial fulfilment of the
requirements of Liverpool John Moores University
for the degree of Doctor of Philosophy

August 2024

Declaration

The work presented in this thesis was carried out at the Astrophysics Research Institute, Liverpool John Moores University. Unless otherwise stated, it is the original work of the author.

While registered as a candidate for the degree of Doctor of Philosophy, for which submission is now made, the author has not been registered as a candidate for any other award. This thesis has not been submitted in whole, or in part, for any other degree.

Adrián Castañón Esteban
Astrophysics Research Institute
Liverpool John Moores University
IC2, Liverpool Science Park
146 Brownlow Hill
Liverpool
L3 5RF
UK

November 2024

Abstract

The work presented in this thesis shows the results from an in-depth study of a sample of 58 Be stars observed between the years 1998 and 2022.

The spectroscopy of this sample has been studied, starting from the raw observations and converting them into data that could be analyzed. A classification based on the morphology of the Hα and Hβ emission was done, and this classification has been used for the rest of the study, showing repeated times the differences between objects with different classifications. A big part of the posterior study has focused on the difference between single and double peak emission stars. With this classification, a study of the separation between peaks has been done, showing that the emission of the Hβ line happens at a different part of the disk than the Hα line, and it hints at the fact that single peak lines might be formed from two very close emission peaks that have merged into one. The projected rotational velocities and the critical velocities of the central stars have been calculated, and it has been proven that the populations of the classification have different projected rotational velocities trends. Some objects also show variability between emission and no emission, with a rate of change between 0.73% and 0.78% of the sample changing every year on average.

Some basic polarimetry results have also been obtained from an observation taken with MOPTOP in the year 2022. After calculating the values of the Stokes parameters from the observations, and the polarization degree and angle from the Stokes parameters, the intrinsic and interstellar values of the polarization degree and angle have been separated using a big sample of nearby stars. After this, using the polarization degree, the angle dependency has been removed from the projected rotational velocity and finding that after this the single and double peak populations could be the same, meaning that the only difference between these two type of objects is the angle of inclination. After this, no direct relation has been found between the interstellar polarization degree and the distance or the reddening, meaning that other processes might be involved in increasing or decreasing the interstellar polarization degree.

Finally, a study of the variability of the sample has been done. The V/R variability has been studied, showing period of $\bar{T} = 0.86 \pm 0.32$ years for Hα and $\bar{T} = 1.07 \pm 0.39$ years for Hβ. These values are much shorter than the usual estimated value of $T \sim 7$ years that are considered for the V/R variability, and could indicate that the process is in the mid-term timescale instead of the long-term timescale. After that, a study of the emission variability and how it relates to other observables has been done, finding a higher value of the emission and the variability for stars around a stellar class of B1.5; however, no other relation was found with the polarization degree, the projected rotational velocity of the star, or the distance between peaks. Finally, the change in the values of the emission and the polarization of the sample were analyzed, finding no apparent correlation between them, which could mean that there is no relation between the radius and the density of the disk.

Publications

In the course of completing the work presented in this thesis, the partial contents of Chapters 2 and 3 have been submitted and accepted for publication in a refereed journal:

Castañón Esteban, A. & Steele, I. A. & Jermak, H. E., 2024, MNRAS, 529, 1555 - *A study of Be stars in the time domain - I. Spectral data and polarimetry*

To my mother, who always listens to me when I talk about science. . .

Acknowledgements

During this PhD, I have accumulated many debts of gratitude. The most direct one is to my supervisor, Iain Steele, and my co-supervisor, Helen Jermak, for always helping me to move forward with this project and thesis so I can successfully reach the finish line. I also want to thank Marie Martig, because without her help, this project would have never started and the PhD would have been unsuccessful.

The beginning of the COVID-19 pandemic in 2020 was very difficult, and I would have suffered more in complete isolation if not for the help of Kyle, who helped me feel that Liverpool was a less lonely place for a stranger like me at one of the most difficult times.

I also want to thank all of my friends for supporting me, but there are three people that I want to give some special thanks: Andrés, for always managing to have some time to spare when I struggled, Jimena, for regularly check on my status, and Almudena, for not letting me feel alone while I was working on the last part project.

Last, but not least, I want to thank my mother Mar, for always supporting and believing in me, even at the times when I was not able to do it myself.

Without all of you, I probably would have been crushed under the pressure and would have not finished this thesis. With all my heart, thank you.

Contents

List of Figures

List of Tables

Chapter 1

Introduction

The mystery of what are called *Be stars* is still not completely solved, 158 years after their initial discovery. Multiple mechanisms for creating and maintaining the structure that emits around the star are still not confirmed, and the variability of the emission and changes from emitting to no emitting stars and vice versa are not fully understood. This thesis aims to shed some light on these problems using a long term sample of spectroscopic observations of Be stars collected over ~ 20 years combined with recent polarimetric observations.

In this chapter, an introduction to the general topic of Be stars is provided. In Section 1.1, the current definition of a Be is examined in detail, with some discussion on each of its components. In Section 1.2 a general overview of γ Cas, the first discovered and maybe most studied Be star, is presented as an example of this group. In Section 1.3, the current understanding of the mechanisms behind the emission is discussed. In Section 1.4, other stellar objects with a similar emission to Be stars are briefly reviewed. Finally, in Section 1.5, an overview of the current discussion about the possible origin and creation of Be stars is given.

1.1 What are Be stars?

The accepted definition of Be stars is the one given by Jaschek et al. (1981) and Collins (1987): Be stars are, on a fundamental level, non-supergiant B stars that show, or have shown in the past, one or more Balmer hydrogen lines in emission. This is in clear contradiction with the usual spectrum of B stars, that only show them in absorption. Not only do they show emission lines, but this emission can change with time, for which reason they are also considered a type of variable star.

1.1.1 Non-supergiant stars

B-type and A-type supergiant stars, classified as spectral luminosity classes I and II, have been known to emit Hα radiation for long time (Kaufer et al., 1996). This emission of Hα has a P Cygni profile, that can also be double peaked like some Be stars, but with a much shorter periodicity (Kaufer et al., 2006), in the order of days, which clearly differentiates it from Be star variability, which is in the order of months or years.

The emission from supergiants is understood as originating from stellar winds, with the emission profile being related to the structure of the wind (Markova et al., 2008). The mass loss that produces this stellar wind is also enhanced by short-lived pulsation *p-modes*, *g-modes* and *strange-modes* (Kraus et al., 2015; Haucke et al., 2018). The current most comprehensive general review on massive winds is Puls et al. (2008), with one more focused on their effects in supergiant stars can be found in Martínez-Núñez et al. (2017).

All these differences show that the emission of Hα line from supergiant stars comes from a different physical origin than Be stars, and for that reason they are excluded from the main definition.

1.1.2 B stars

B stars are one of the fundamental classes of stars in the current classification. They were first classified as such in the Harvard Catalogue (Pickering, 1890, 1908), differentiated clearly from other types because of their helium absorption lines.

In the current MK system, the only acceptable and meaningful way to classify the stars is in comparison of the spectra with other previously classified standard stars (Morgan & Keenan, 1973), with a more precise classification for B standard stars available in (Jaschek & Gomez, 1998).

The typical accepted values for the masses of these objects are between 2.5 and 16.5 $M_\odot$ for main sequence stars, and 10 to 30 $M_\odot$ for supergiants (Underhill & Doazan, 1982). It is worth noting, however, that these values might be somewhat outdated, and more recent modelling for the masses of stars will be taken into account in this work. As was said before, strong He I lines can be seen, as well as C II, N II, O II, Mg II, Si II, Si III and Si IV lines. Other weaker lines of Fe II or other elements and ionization states may also be seen (Underhill & Doazan, 1982), depending if they are *early* B stars, which are closer to the O class, or *late* B stars, which are closer to the A class.

1.1.3 Balmer lines

When electrons in atomic energy levels decay to lower levels, they emit energy in the form of photons, which form what are known as emission lines. In 1885, Balmer proposed an explanation to some of these lines of the hydrogen atom (Balmer, 1885), proposing certain coefficients and relating them to the second level of the atom, and obtaining an equation that could quantify these values:

$$H = h\frac{m^2}{m^2-4} \tag{1.1}$$

with $h = 3645.6$ a constant, m the number of the initial level of the transition, and H the wavelength of the emitted photon.

These values would later be taken into account by Rydberg in 1890 (Rydberg, 1890) to develop the famous Rydberg formula for the hydrogen atom, which was initially:

$$n = n_0 + \frac{N_0}{m+\mu} \tag{1.2}$$

with $n = \frac{10^8}{\lambda}$ the wavenumber for the emitted line, m the initial level of the transition, n_0 the wavenumber the series approach as m tends to infinite, N_0 a constant for all series, and μ a constant particular for each series. After applying Balmer's formula for the particular case of the hydrogen atom it had the form:

$$n = n_0 - \frac{4n_0}{m^2} \tag{1.3}$$

This work ended later with Bohr obtaining a formula that explained the frequency of the emitted photon in the transition (Bohr, 1913):

$$\nu = \frac{2\pi^2 me^4}{h^3}\left(\frac{1}{\tau_2^2} - \frac{1}{\tau_1^2}\right) \tag{1.4}$$

with ν the frequency, m and e the mass and the charge of the electron respectively, h Planck's constant, and τ_2 and τ_1 the numbers corresponding to the final and initial levels respectively.

What is known as the Balmer lines series therefore corresponds to those where electrons in a Hydrogen atom suffer a transition down to level 2. That way, a transition from level 3 to level 2 is called Hα, a transition from level 4 to level 2 is called Hβ, etc. We can calculate the wavelength and energy emitted in these transitions using the equation for the transition, remembering that the energy is $E = h\nu$, with h being the Planck constant, and the wavelength is $\lambda = c/\nu$, with c being the speed of light:

Initial level	Final level	Name	Wavelength (Å)	Energy (eV)
3	2	Hα [1]	6562.79	1.89
4	2	Hβ [2]	4861.35	2.55
5	2	Hγ [3]	4340.47	2.86
6	2	Hδ [3]	4101.74	3.02
7	2	Hϵ [3]	3970.08	3.12

TABLE 1.1: Some of the wavelengths and energies emitted by the first 5 lines in the Balmer series. Values and sources found in the NIST Database (Ralchenko, 2005).

One of the most interesting aspects of this line series, compared with other hydrogen series like Lyman or Paschen, which correspond to the transition to the levels 1 and 3 respectively, is that the Balmer series is contained in the optical range and near ultraviolet, while the Lyman series corresponds to the extreme ultraviolet and Paschen lines or higher correspond to the near or mid-infrared range. For this reason, Balmer lines have always been very easily distinguishable even with even basic astronomical instrumentation, and are widely used in astronomy.

1.2 A historic overview of Be stars

The Be phenomenon has been known for more than 150 years. Despite a lot of observations and modelling, a lot of aspects about Be stars are still unclear. In this section, a short review presents some of the most important observations and challenges found on the first discovered and potentially one of the best studied Be stars, γ Cassiopeiae, with some conclusions on the difficulties in modelling it.

1.2.1 The first Be star observed: γ Cassiopeiae

In 1866, A. Secchi was observing the B star γ Cassiopeiae when he realised that the spectral line at $\lambda = 4861.34$Å, which corresponds to Hβ, also called Fraunhofer F line, was different from other stars like β Cas: In the particular case of γ Cas, instead of the usual absorption line characteristic from all stars, the line was in emission (Secchi, 1866). A few months later, Huggins (1867) identified some more lines in the spectrum of γ Cas, including this time not only a confirmation of Hβ emission, but also of Hα.

As the first Be star to be observed, it has also been one of the most studied, and there have been numerous reviews of the observations. It therefore serves as a useful example of the kind of behaviour we expect to observe in this thesis from other Be stars.

---

[1] Mitchell (1947); Kramida (2010)

[2] Dyson (1906)

[3] Wood (1922)

Curtiss (1916) compiled all the observations until that year, noticing several key features, like a double peak emission with a central absorption (a “shell” spectrum), emission Hα simultaneous with no emission Hβ, and small or no variation of the radial velocity of the star - even if the estimate of the value was clearly too low. Some years later, Edwards (1944) reviewed 100 years of observations of γ Cassiopeiae, including some before its classification as a star with emission lines. The result was that it showed some clear variability that seemed regular and periodic, but with some exceptions that broke that periodicity, like the unexpected extra brightness in 1934. After an episode of very high intensity that reached a new maximum in 1936 (McLaughlin, 1937), the shell emission lines started to fade, disappearing completely or almost completely between 1941 and 1948, and behaving like a normal B star (Merrill & Burwell, 1949; Cowley & Marlborough, 1968).

With a slow new start of emission in 1946, a new phase on the observations of this star began, finding some big differences with the previous behaviour, finding for example that the V/R variations (i.e. asymmetries in the line profile between the violet and red components) were not anymore an indicator of big changes on the spectrum (Doazan et al., 1983). It has been accepted that γ Cassiopeiae shows three distinctive phases: A clear Be phase, a Be-shell phase, and a normal B star phase, but the period of the variation has not been determined, and it might not be possible with our understanding (Underhill & Doazan, 1982). The cycles started to show a growing length of their periods (Miroshnichenko et al., 2002), but the lack of more data makes impossible a better determination of the length of the cycles. It was noted a continuous decrease of the line between 1993 and 2001, which anticipated a new B star phase. Finally, around 2018, a new emission cycle started (Baade et al., 2023).

Slettebak (1982) estimated a value for the velocity of $v \sin i = 230$ km/s, but that value might be too slow to be the real velocity of the star (Baade et al., 2023). Assuming an inclination of $i = 45°$, Harmanec (2002) found a velocity $v = 385$ km/s, which disagrees with the one previously estimated. A possible companion star might exist, but it has only been indirectly detected (Baade et al., 2023).

For more details about γ Cassiopeiae, the most recent review is Baade et al. (2023).

1.3 The Be phenomenon

Between their discovery in 1866 (Secchi, 1866) and 1922, Be stars were commonly referred as *B stars with bright lines*. It was in 1922, at the First General Assembly of the IAU that Fowler (1922) suggested the use of *e* to denote emission lines in the spectra of stars (Collins, 1987). Even if the previous denomination was still used for a few more years, it was clear from this point that these objects were to be studied separately from the rest of the B stars.

The origin of the Balmer emission lines in Be stars was quickly understood to not happen in the stellar atmosphere (Milne, 1928), but in an envelope around the star. Shaped like a ring, this model was suggested by Struve (1931) from observational similarities with Wolf-Rayet stars and novae to be caused by a nebula enveloping the B star, created by matter ejected by the rapid rotation of the central star, with a possible binary origin also suggested as the reason for this for this excess in the velocity of rotation for the first time. Earlier stars have a certain tendency to show these emission lines when compared with later stars, with the maximum being around B2 (Merrill & Burwell, 1933).

It was later, with the use of polarimetry measurements, that it was proposed for the geometry of the system to be an inclined thin cylindrical disk around the star (Capps et al., 1973; Poeckert & Marlborough, 1976, 1978b). The general idea of the model has been confirmed by the use of interferometry (Quirrenbach, 1994), and has been part of the understanding for the Be stars since then. The next section explores the physics of the disk and of the emission mechanisms.

1.3.1 A structure surrounding the star: The disk

While the view of a disk-like structure is generally accepted, the values of the parameters that compose the disk are still unclear. While the opening angle of the disk, i.e. the angle formed between the superior and the inferior layers of the disk, has generally been accepted as a small value (Owocki et al., 1994; Wood et al., 1997; Stee, 2003; Rivinius et al., 2013) of $\Delta\theta \sim 1 - 3^\circ$, some other studies establish a higher value of the superior limit for the opening angle at $\Delta\theta \sim 15 - 20^\circ$ (Bjorkman & Cassinelli, 1990; Hanuschik, 1996; Quirrenbach et al., 1997; Meilland et al., 2006), but even with these higher values, the disk is considered thin.

The current understanding of the structure of the disks of Be stars is generally reflected in two models that are used to try to explain the multiple variations on the emission: The *one-armed global oscillations model* and the *viscous decretion disk model.*

One-armed oscillations started to be studied from a perspective that the structure of the disk can be studied in a similar way to disk-like galaxies (Kato, 1983). It is apparent from the formulation in Kato (1983) that only a one-armed and low frequency wave can exist confined in the disks of Be stars, initially thought as a retrograde wave (Okazaki, 1991) but later demonstrated that it can also be manifested as a prograde wave (Papaloizou et al., 1992). Through small perturbations, this model can successfully recreate the called *V/R variations* (explained in more detail in Section 4.2) in the emission of Be stars: the disk precedes around the star, with a period depending on the radius, which gives it a shape like a spiral (Rivinius et al., 2013). The observations generally support this prograde wave (Telting et al., 1994; Mennickent et al., 1997; Vakili et al., 1998), however sometimes have failed to reproduce the variability of some lines (Carciofi et al., 2009) and the 3D structure of the disk might need to be taken into account. Finally, while this model has some acceptance, it is still not understood what mechanism excites the oscillations (Rivinius et al., 2013; Okazaki, 2016).

The other model, which is the most accepted explanation for the structure of the disk, is the viscous decretion disk model (Lee et al., 1991). The basic idea of this model is that it follows the same hydrodynamics as an accretion disk (Shakura & Sunyaev, 1973; Pringle, 1981), starting from the equation of conservation of mass, also known as equation of continuity, combined with the equation of conservation of angular momentum, but the mass gain of the first one is instead a negative mass flow (Lee et al., 1991), called *decretion* because instead of increasing the amount of mass in the star, it decreases it. These equations allow, under certain circumstances, for an analytical solution of the surface density Σ (Bjorkman & Carciofi, 2005; Rivinius et al., 2013), with a dependence on the distance to the central star r of $\Sigma(r) \propto r^{-2}$. The main idea of this model is that the star transfers its excess of angular momentum to the disk through viscous diffusion that leads to mass loss. The disk is assumed to be isothermal (Okazaki, 2007), with a value of around $T_{\rm disk} = 0.6 T_{\rm eff}$ (Carciofi & Bjorkman, 2006). As a final note, while this model is generally accepted, some important parts of it, like the mass transfer mechanism or the origin of the viscosity of the disk, are still unexplained (Okazaki, 2016).

More mathematical details about these models can be found in the reviews by Rivinius et al. (2013) and Okazaki (2016).

1.3.2 Emission mechanisms in Be stars

As is expected, most of the observed spectrum from Be stars comes from the central star: the continuum from black-body radiation and the absorption lines from the photosphere of the star (Burbidge & Burbidge, 1953). At the same time, there is no question that the emitted hydrogen lines that distinguish these objects from the rest of the B type stars have their origin in the recombination of electrons with ionized hydrogen atoms (Woolf et al., 1970; Capps et al., 1973) in the disk.

However, there is also an excess of infrared continuum emission (Allen, 1973). The main source of this infrared excess has been understood as free-free emission (Woolf et al., 1970; Carciofi & Bjorkman, 2006) - emission through the interaction between two charged particles in movement - originated from the same ionized material that forms the disk and creates the emission lines, with the possibility of it being dust ruled out on Be stars (Gehrz et al., 1974) because of the lack of the characteristic emission at wavelengths 10μm and 20μm. The lack of dust is, as can be seen in Section 1.4, one of the key differences between Be stars and other similar objects.

1.4 What are NOT Be stars?

Some objects of the stellar class B might also emit Balmer lines, in a similar way than Be stars. Despite these similarities, they are different from the objects that are studied here, which are also referred as *classical Be stars*, to differentiate them from these other emitting B stars. This section discusses some of these objects and their differences with classical Be stars.

1.4.1 B[e] stars

B[e] stars were initially classified as *peculiar* Be stars: They are B-type stars and show emission of the Balmer lines in their spectra. However, they were also found to emit not only hydrogen Balmer lines, but also *forbidden lines*[1] of multiple elements, including [O I], [S II], [Fe II], [Ni II], [Cr II], and others (Swings, 1973), which are not seen in classical Be stars. They also show a stronger infrared excess, thought to be originated from dust (Allen & Swings, 1976) that distinguish them from classical Be stars. For this reason, they were proposed as a completely separated group, which was denominated B[e] stars (Conti, 1997). However, the current classification, proposed by Lamers et al. (1998), refers to them as *B[e] phenomenon*, and groups them into five categories: Supergiant stars, pre-main sequence stars, compact planetary nebulae stars, symbiotic binary stars, and finally unclassified for the ones in an unclear evolutionary phase. The nebula part that surrounds the star is also expected to form a circumstellar disk. This final group, of unclassified stars, has been renamed as FS CMa (FS Canis Majoris) in Miroshnichenko (2007), due to them sharing similar properties with this object.

Despite having central stars at very different evolutionary stages, similar conditions in their gaseous and dusty envelopes can be found. Some are responsible for forming their own circumstellar dust, like supergiants and binaries, while the pre-main sequence and

---

[1] Lines that are not allowed by the atomic transition selection rules, and only have a small possibility of the transition happening compared with the allowed transitions.

compact planetary nebulae stars inherit it from previous generations of stars in the former and previous evolutionary stages in the latter (Miroshnichenko, 2007).

This summarizes most of the current understanding on the B[e] phenomenon. Detailed reviews of dusty environments around stars and the B[e] phenomenon are given by Cherchneff & Sarangi (2017) and Oudmaijer & Miroshnichenko (2017).

1.4.2 Herbig Ae/Be stars

These objects were classified for the first time by Herbig (1960). They are intermediate mass stars, with a mass between a lower value of 1.5-2 $M_\odot$ and an upper value of 8-10 $M_\odot$.

The most common definition for Herbig Ae/Be stars (also abbreviated as HAeBe stars) is that they are stellar type A or B stars and luminosity class III (giants) to V (main-sequence), with Hα emission, and that show infrared excess due to hot or cool (or both) interstellar dust (Davies et al., 1990; Hillenbrand et al., 1992). This infrared excess due to the dust distinguish them from classical Be stars, at the same time that their luminosity class excludes them from being supergiants, differentiating them from B[e] stars. However, both of these characteristics are not always easy enough to distinguish between the different types.

They show polarization, both intrinsic and variable, in part due to electron scattering, but mostly due to dust scattering. The degree of polarization is large, and the variation in polarization is often correlated with dense dust clouds obscuring the light from the star, which allow only scattered light by dust particles to escape (Grinin, 1994). They also show strong variations in polarization angle.

Spectra of the central stars show normal absorption spectral lines for A and B stars, with a rotational velocity estimated between 60 and 200 km/s, much slower than classical Be stars (Finkenzeller, 1985). At the same time, they show Balmer emission lines with single, double and P cygni profiles (Garrison & Anderson, 1977). The UV continuum is sometimes characterized by an excess of emission, which can be attributed to warm gas near the star, with temperatures exceeding its $T_{\rm eff}$ (Blondel & Djie, 1994). In the infrared, they show the presence of polycyclic aromatic hydrocarbons (PAHs), in up to 70% of the cases (Seok & Li, 2017).

While these objects are mostly thought to be a star surrounded by a Keplerian disk (Marsh et al., 1995), other mechanisms, like outflows (Mundt & Ray, 1994) or envelopes (Di Francesco et al., 1997), have been proposed.

For a more complete review on the topic, please check Waters & Waelkens (1998) and Brittain et al. (2023).

1.4.3 Algol binaries

Algol binaries consist in two stars in close proximity with a comparable size, but with different mass, making the less massive also less luminous. In consequence, the system is an eclipsing binary (Budding et al., 2004). The existence of emission Balmer lines (Wyse, 1934) has been explained as a disk of matter around the star (Joy, 1942) that is currently understood as an accretion disk, with the less massive star filling its Roche lobe and the other one not being degenerate (Batten, 1989).

Even if they have a disk around the main star, which can be a B-type star, and show emission Balmer lines, Algol binaries are not confused with Be stars: they show high variability between eclipses, the disks are non-Keplerian, and the broadening is thought to be caused by some other mechanism than rotational velocity (Kaitchuck & Park, 1988). However, as it will be discussed in Section 1.5.2, binarity is one of the mechanisms that have been proposed as the origin of Be stars, and they must not be confused with Algol binaries.

1.5 The possible origins of Be stars

One of key questions that is still debated regarding Be stars is the mechanism that creates the disk: It is understood that a rapid rotational velocity v plays an important role (Slettebak, 1979), although in general they do not rotate at the full break-up velocities (Porter, 1996). Magnetic fields may also play a role (Cassinelli et al., 2002; Brown et al., 2008), but so far no magnetic fields have been found on Be stars, in contrast with non-emitting B stars (Wade et al., 2014). The topic of magnetic fields in Be stars will be covered in more detail in Section 3.1.4. The question not only extends to the physical mechanisms involved in the process, but also if the origin is only one single star or if it is instead due to interaction with a binary companion. Both possibilities are discussed next.

1.5.1 Single star origin

It was proposed by Struve (1931) that B stars in extremely fast rotation could eject matter at the equator. It is indeed possible that a very fast rotator can cancel or even overcome the effects of the gravity on its higher layers with centrifugal force and lose matter. This is what is is called *critical velocity*, the theoretical equilibrium velocity at which the central B star would need to rotate over to eject the material on its equator purely by compensating gravity with rotation. The formula can be found for example in Townsend et al. (2004):

$$v_{\text{crit}} = \sqrt{\frac{2}{3}\frac{GM}{R_P}} \tag{1.5}$$

with M being the mass of the central star and R_P its polar radius.

The results obtained from the observations show, however, that while Be stars rotate very fast they are not at critical velocity (Slettebak, 1979; Cranmer, 2005; Balona, 2022). This creates the question if a B star in that situation could create a disk, and how. Three possibilities have been proposed: the rotational velocities have been underestimated because of *gravity darkening*, the star loses mass due to non-radial pulsation, or a magnetic field plays some role on ejecting the matter.

As is explained in more detail in 3.1.4, no magnetic fields have been found on Be stars, and even if they are below the detectable limit, it is questionable if they will be strong enough to make the star lose matter and create the disk at the same time that keeping the constraints from observations (Limber & Marlborough, 1968).

Due to not having a perfectly spherical shape, a star will suffer *gravity darkening*: the equatorial region is cooler (von Zeipel, 1924), and in turn, it is more faint, which can lead to underestimating the values of the rotational velocity (Slettebak, 1949; Townsend et al., 2004; Frémat et al., 2005; Zorec et al., 2016). Even when correcting for gravity darkening Be stars might still not be close to critical velocity (Zorec et al., 2016), and while lower values in the range of 70-80% of the critical velocity could still explain it, many Be stars are below this reduced value as well (Hastings et al., 2020).

The final possibility for a single star origin is non-radial pulsation: a star can suffer small perturbations to their pressure, gravity or rotational velocity, and a posterior return to equilibrium, in what are called *p-modes*, *g-modes* and *r-modes* respectively (Baade, 1988). These perturbations, well known to asteroseismology (Maeder, 2009; Aerts et al., 2010) can create outbursts of gas (Rivinius et al., 1998) that can repeat, and g-modes coupled with those outbursts have been found using some high-cadence long term monitoring (Baade et al., 2017; Zwintz et al., 2024). The velocity of these modes is theoretically very slow in comparison with the critical velocity necessary for the star to lose mass (Owocki, 2006), but it could be enough if added on top of the very fast rotating velocity of the star. But even in those conditions, non-radial pulsations seem insufficient for the creation of the Be star disk (Rivinius et al., 2013).

1.5.2 Binary origin

Another possibility is that the creation of the disk is due to interaction with a companion star: Kriz & Harmanec (1975) suggested this origin for all Be stars by assuming a scenario similar to Algol binaries, where the mass is transferred between the two stars. This could also be a possible explanation for the fast rotational velocity of the central B star in Be stars, as the mass-gaining star in the transfer transforms the orbital angular momentum into rotational angular momentum (Plavec, 1970).

While it is generally accepted that this mechanism *could* produce a Be star, the deep eclipses that can be seen in Algol binaries are not seen in Be stars (Plavec & Polidan, 1976), which already puts a limit on the size of these stars. At the same time, while some Be stars have close companions, in others the donor star seems to be too far to create a scenario like the mass transfer one in Algol binaries, and even if interaction between the two objects should not be discarded, they are too separated for it to be the main disk creation mechanism, considering them effectively the same as single Be stars (Kogure, 1981; Kogure & Suzuki, 1986). This is in agreement with the observations, as very few interacting binary Be stars have been observed, and it is understood that Be stars are not mass transferring binaries at the time of observation (Porter & Rivinius, 2003), but the system might be a post mass-exchange binary (Pols et al., 1991; Baade, 1992).

Depending on the mass of the companion, the system post mass-exchange could end as a rapidly rotating B star that can be interpreted as a Be star, or a slow rotating B star, with a minimum mass ratio between the central B star and the companion of $q_{\min} = M_{\mathrm{B}}/M_{\mathrm{companion}} = 0.4$ (Pols et al., 1991). It is estimated as well that this mechanism can only account for 40-60% of all Be stars, even in the most optimistic of cases. Suggested companions to the Be star that might be observed are helium stars, neutron stars and white dwarfs. However, as very massive stars are expected to produce black holes, this creates an upper bound on the possible initial mass of the companion (Portegies Zwart, 1995) and in consequence, a lower possibility for neutron star remnants.

One of the questions about this model is the amount of Be stars with this origin, and the values depend on the study: Only $\sim$30% of stars are found in binaries, the same amount as in non-emitting B stars (Oudmaijer & Parr, 2010), but 50-75% of Be stars should have a companion (McSwain & Gies, 2005; Miroshnichenko, 2016) and come from a mass transfer origin. More recently, some subdwarf O type companions of Be stars have been found directly through interferometry (Mourard et al., 2015; Klement et al., 2022). These objects might be remnants of the donor star, and are expected to evolve into white dwarfs or neutron stars, as predicted before.

While some companion stars are visible, none of Be stars studied were in visible binaries with main sequence stars. At the same time, a large fraction of the fast-rotating B stars were, supporting the idea that binarity mass-transfer may be the cause of the fast rotation and the companion is barely visible anymore after the mass transfer and suggesting that most Be stars were formed from the binary channel (Bodensteiner et al., 2020). At the same time, modelling by Hastings et al. (2021) estimated that only $\sim$ 30% of Be stars could have been spun up through binary interaction enough to become emission objects, but with some more extreme assumptions, all could have a binary interaction origin.

1.6 This work

In this work, a number of spectroscopic observations from a sample of Be stars collected for 23 years, in addition to a polarimetry observation for each object taken in 2022, are presented. The author presents next the results of an analysis of this sample of data.

The rest of this thesis is structured as follows: In Chapter 2 the sample is presented, and the objects presented there are classified and analyzed. In Chapter 3 some basic introduction to polarimetry is given, the values of the observations are compared with other authors, and the only value obtained is used to remove the angular dependence. Finally, in Chapter 4, the time and emission variability of the objects that show emission lines in the sample is studied.

Chapter 2

Spectroscopy

2.1 Spectroscopy in Be stars

Spectral observations have always been very important for the topic of Be stars. As was commented in Section 1.2.1, its discovery originated from the observation of emission Hβ lines instead of the expected absorption from stars.

The most frequent uses of spectroscopy for the topic of Be stars are to study the shape of the emission lines, the rotational velocity and the variability of the emission. Some other studies have focused as well on the study of other rare emission or absorption lines.

The variability and shape of the emission line has also been a matter of study: It can be a single or double peak (Hanuschik et al., 1988) with variable values of asymmetry between the peaks (Hanuschik et al., 1995) or have the shape of shell lines (Hanuschik, 1995). These profiles have been successfully modelled and theoretically reproduced (Silaj et al., 2010).

In this chapter, the emission line shapes and rotational velocities of a sample of observed Be stars are studied from an average perspective, leaving the topic of variability of the emission of those objects for Chapter 4.

2.2 Telescopes

The spectral observations used in this project were taken using two telescopes: The Isaac Newton Telescope (INT) and the Liverpool Telescope (LT).

Table 2.1: The resolution of the FRODOspec observations, depending on the settings.

	Blue Arm	Red Arm
Low resolution	0.97 Å	1.64 Å
High resolution	0.33 Å	0.61 Å

2.2.1 The Isaac Newton Telescope

The Isaac Newton Telescope (INT) is a 2.54 metre telescope[1] situated at the Roque de los Muchachos Observatory on La Palma in the Canary Islands, Spain. Part of the Isaac Newton Group of Telescopes (ING) with the William Herschel Telescope (WHT) and the Jacobus Kapteyn Telescope (JKT). The INT currently has, and had at the time of observation, two instruments of choice: the Wide Field Camera (WFC), which is a photometric optical detector, and the Intermediate Dispersion Spectrograph (IDS), which is a low resolution spectrograph. Multiple gratings are available for IDS, of which the R1200B, R1200Y and 1200R, centered around 4000, 6000 and 8000Å respectively, and with a dispersion of $\sim$ 0.5Å on the EEV12 CCD[2], were used.

2.2.2 The Liverpool Telescope

The Liverpool Telescope (LT) is a 2 metre telescope[3] (Steele et al., 2004) situated at the Roque de los Muchachos Observatory on La Palma in the Canary Islands, Spain. This telescope is fully robotic and is operated remotely from the Astrophysics Research Institute in Liverpool, United Kingdom.

Two instruments were used for the spectroscopic observations at the LT: FRODOspec and SPRAT.

The Fibre-fed RObotic Dual-beam Optical Spectrograph, more known as FRODOspec (Morales-Rueda et al., 2004; Barnsley et al., 2012) has capabilities to be used at low and high resolution, and separated blue and red arms. Depending on the settings and the arm, a different resolution is offered, as is shown in Table 2.1.

The SPectrograph for the Rapid Acquisition of Transients, more known as SPRAT (Piascik et al., 2014) is a very low resolution spectrograph, with a dispersion of 4.78Å. This precision was not enough for a detailed study, but it can confirm if the objects still show or not the Hα emission line.

---

[1] https://www.ing.iac.es/Astronomy/telescopes/int/

[2] https://www.ing.iac.es/Engineering/detectors/ultra_eev12.htm

[3] https://telescope.livjm.ac.uk/About/

2.3 Observations

2.3.1 Sample selection

The sample used on this work was originally introduced in Steele et al. (1999): The 58 stars in the sample were were initially classified as Be stars in the database presented in Jaschek & Egret (1982), and were selected to cover several objects for each spectral and luminosity class for Be stars, to make it as representative as possible. However, because Be stars are variable, some of the stars classified as Be stars in 1982 might not show Hα emission anymore. As the raw data used in their initial classification is generally unavailable and was compiled from a wide variety of sources, they may also have been misclassified. Several of the stars might also have changed to no emission at some point before or between the observations.

Previous work on the sample is described in a series of five papers published between 1999 and 2013. In paper I (Steele et al., 1999), the criteria for the selection of the sample was presented: the initial aim was to select a representative sample of all types of Be stars A basic study of the rotational velocities of the stars was done based on a single spectrum of each object, as well as a reclassification of their spectral type. Paper II (Clark & Steele, 2000) studied the same sample plus another 8 sources in the K band (2.05-2.22 μm). It determined that some objects do not show Brγ emission ($\lambda = 21660$ Å), which might indicate no hydrogen emission in general, putting in doubt their classification as a Be star. Different sets of the spectra showed H I, He I, Mg II, Fe II and Na I lines, with He I and Mg II features as a good diagnostic of early spectral type. At the same time, stars that did not show Brγ emission seemed to have a lower projected rotational velocity. Paper III (Steele & Clark, 2001) studied 57 of the stars from paper 1 in the H band (1.53-1.69 μm). H I Brackett lines were again examined, as well as Fe II. It showed that the analysis of the H band spectra alone only allows for the classification into "early" (B0e-B4e) and "late" (B5e-B9e) types. Paper IV (Howells et al., 2001) studied 52 of the stars from paper 1 with JHK infrared photometry, separating values for the interstellar reddening and the circumstellar excess, and finding a strong correlation between the derived interstellar reddening values and the equivalent width of the interstellar sodium lines, giving confidence in the measured reddening. Paper V (Barnsley & Steele, 2013) studied the equivalent width variability of the Hα line for the measurements taken for 55 stars between 1998 and 2010, finding that stars of earlier types, with higher values of the projected rotational velocity, show a higher degree of variability in the Hα emission.

The time of exposure for the observations using the INT were all in the range between 5 and 300 seconds, while the observations using the LT were in the range between 10 and 1000 seconds, depending on the brightness of the object.

2.3.2 Nights of observation

Multiple observations have been taken of each object in the sample, as is shown in Table A.1. However, due to their position in the sky, by the time of observation, some might have been very difficult to observe or even not visible at all. For that reason, or other observational constraints, only a few dates have resulted in observations for most of the objects in the sample, with the 58 objects being observed only in 1998, 1 in 2001, 9 in 2002, 1 in 2005, 1 in 2007, 54 in 2009, 54 in 2010, 39 in 2013, 4 in 2017, 54 in 2018, 50 in 2019, 42 in 2020, 7 in 2021 and 48 in 2022. The total number of observations for the blue arm is 628, while the total number of observations for the red arm, which include the 2022 SPRAT observations, is 708.

2.3.3 Extraction of data

The data obtained on the nights of observation are available for download on the ING and LT data archives, in the format of .fits files. This raw format, shown in Figure 2.1, needs some processing before it can be used for some calculations.

To extract the spectra from these .fits files the data reduction pipeline, ASPIRED (Lam et al., 2023) has been used. On simple terms, what the code does is to open the .fits file and trace a line along the maximum emission. It then takes two parallel lines at a set distance from the line, and calculates the number of counts contained in that range. In the case that the detector has only one channel, only one line will be represented, while in the case of multi-channel fibres like FRODOspec, a section of the maximum value of adjacent parallel fibres will be taken and they will be coadded. After this, it takes two parallel lines at a set distance over the previous top line and another two under the previous bottom line, on a section that should contain no emission from the object, to calculate the sky emission and subtract it. This distance depends on the object and the detector, and it is not necessarily the same frame to frame. The result from this process is that we obtain a number of counts from the source for each pixel of the detector, as is shown in Fig 2.2.

The next step is the calibration of the wavelength axis. While ASPIRED can do that automatically from a provided list of lines and the arc lamp file, it can have difficulties for a large number of lines or some arc lines that are very close, like the ones shown in Fig 2.3. For that reason, the arc lamp files have been extracted as normal observations, and they have been manually calibrated. A fourth degree polynomial, which provided the best accuracy, was used to fit the data to account for any possible flexure of the detector, with the biggest difference for the low resolution observations, as can be seen

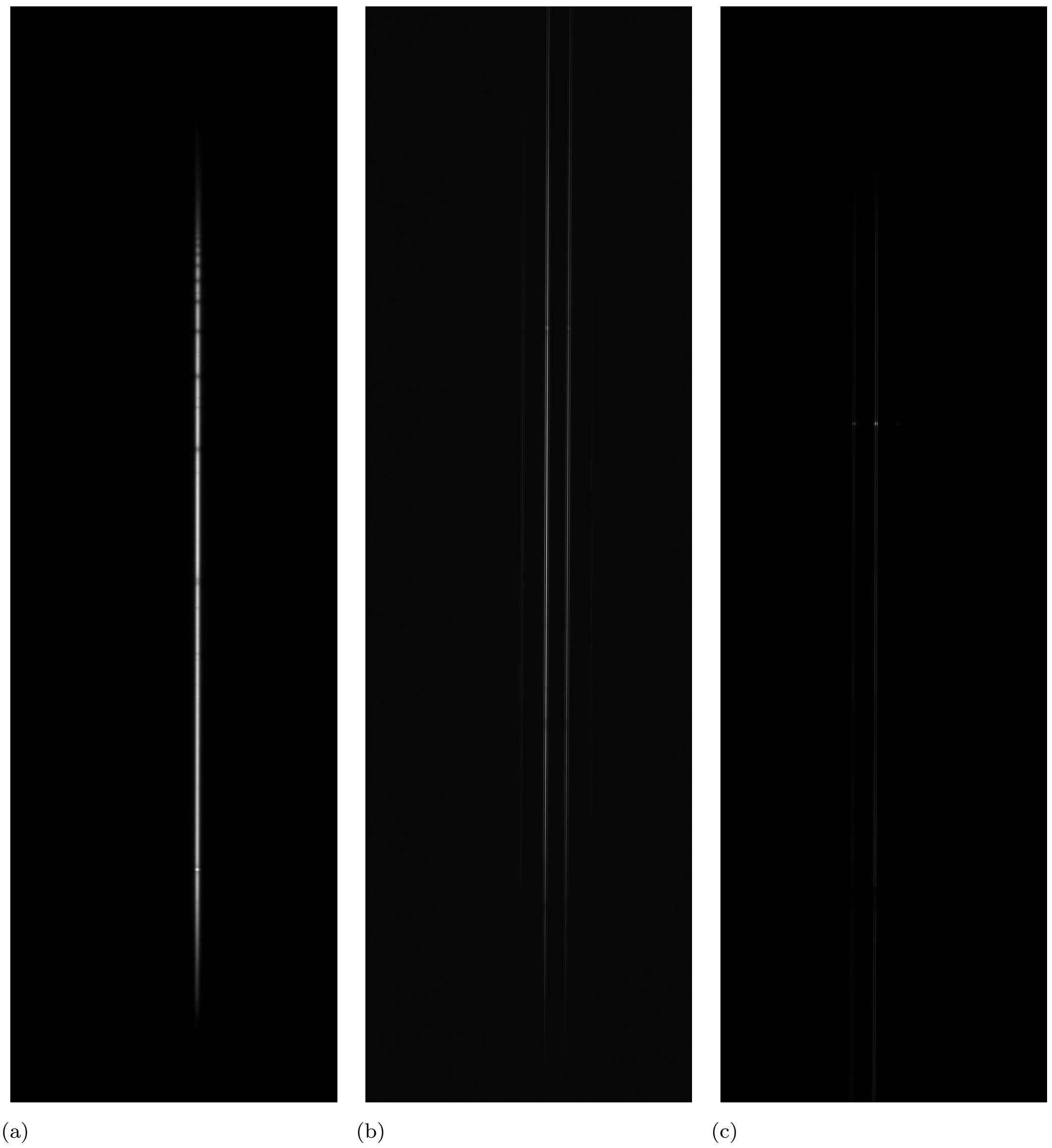
(a) (b) (c)

Figure 2.1: The raw fits files of one of the observations. In the form this is right now, it is not useful for the calculations. (a) is one of the INT observations of the star BD+47 183 in August 1998, in the blue band, while (b) and (c) are the blue and red arm FRODOspec observations in July 2019 of the same star.

in Fig 2.4. The wavelength error depends on the observations and the instrument used, and they can be seen in Table 2.2, however it is worth noting that the axes might behave on a non-linear way, and the error might be higher at the wavelength extremes. The lamp type is also specified in Table 2.2. Multiple arc lamp observations were taken for the IDS observations, as it is possible for it to suffer some changes from flexure while moving, but all of them had the same values within an error of 1 pixel. For the FRODOspec observations, which is more stable, an arc lamp observation was used for all the observations of the same band taken on the same date.

Once this step was completed, a series of values for the axis of each observation was

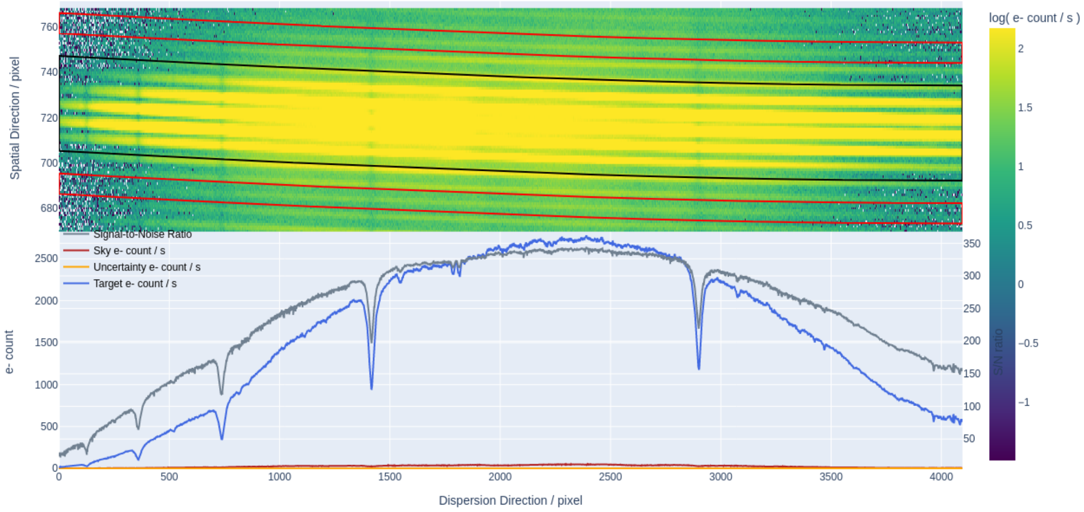

Figure 2.2: A picture showing an observation of one of the standard stars, HD 23850, being reduced using ASPIRED. On the image on top, the region contained between the black lines is the one for the object spectra, while the regions contained between the red lines are the ones for the sky. On the image at the bottom, it is possible to see the target counts, the sky counts, the uncertainty of the counts, and the signal to noise ratio.

Table 2.2: A table showing the dispersion of the wavelength axes, depending on the instrument used for the observation.

Instrument	Blue arm	Red arm	Lamp type
INT	∼0.47Å	∼0.47Å	CuAr+CuNe
FRODOSpec (low resolution)	∼1.5Å	∼1.7Å	Xe
FRODOSpec (high resolution)	∼0.35Å	∼0.6Å	Xe

obtained, completing the calibration of the wavelength. For the amount of observed light, the counts in our observation are not a physical value, and need to be calibrated. To do this, two possibilities exist: For the first one, some reference values are used, like standard stars, and the flux of the stars in the sample is calibrated with respect to them. However, no standard stars were measured on the same dates as the rest of the sample, and so the second option has been chosen, which is the normalization of the values with respect to the continuum.

To do this, the continuum was fitted to a fourth degree polynomial spline, carefully selecting areas that do not show any absorption or emission. The obtained result is what can be considered the continuum of emission from the star, with no emission or absorption lines. After this, the obtained value of counts from the observation is divided by the obtained value of counts from the fit. From this normalization, it is expected for the continuum parts of the spectrum to have a value of 1, with any value smaller than

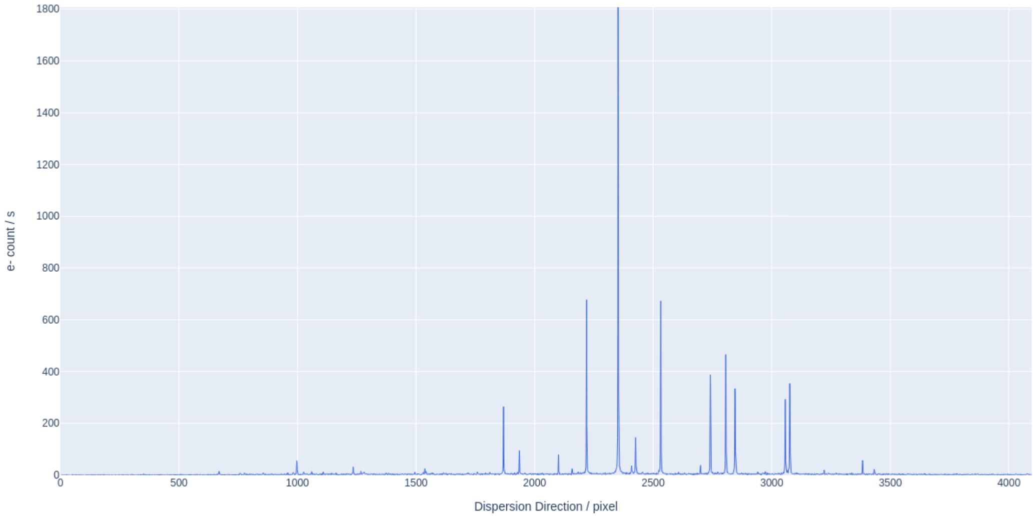

(a)

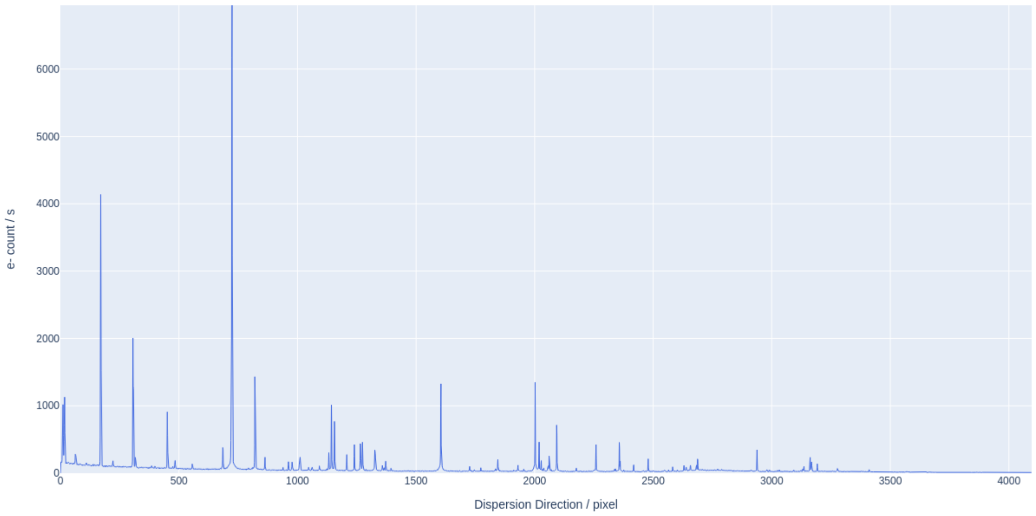

(b)

Figure 2.3: Two of the observation lamps, corresponding (a) for the blue arm and (b) for the red arm. The lines are easy to be identified and a wavelength value can be assigned to them from a reference image or table, allowing this way the conversion from pixels to wavelength. so we can assign a wavelength value to each pixel.

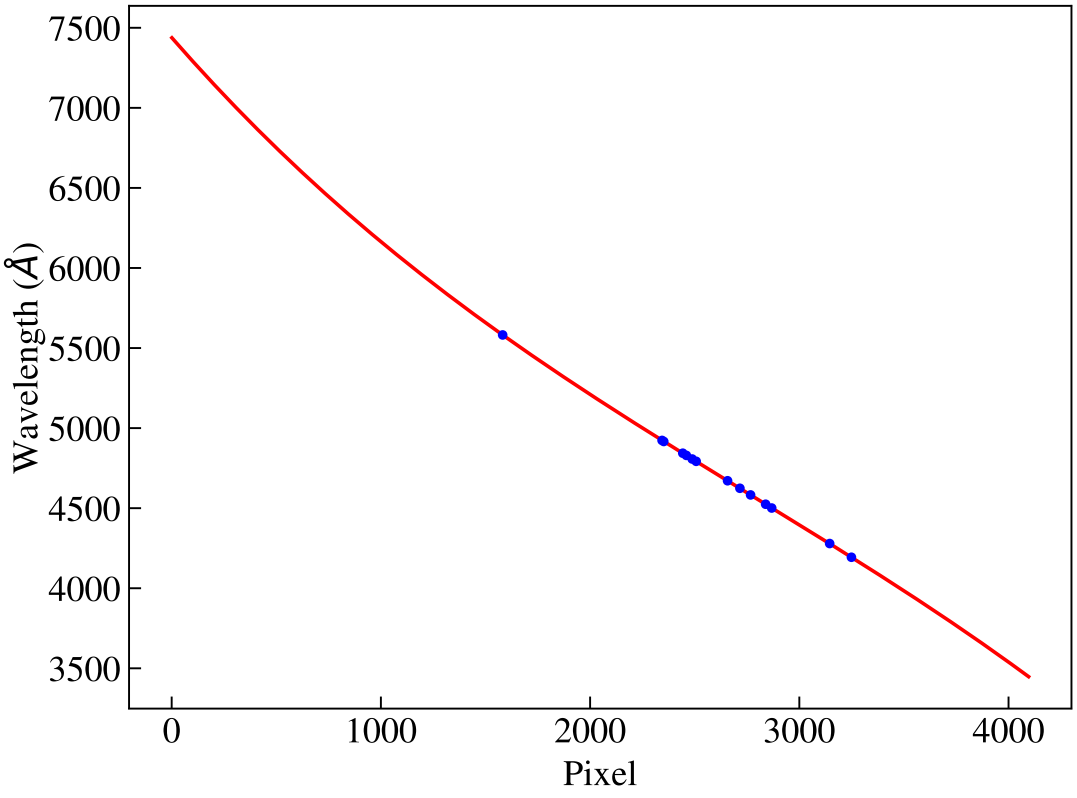

(a)

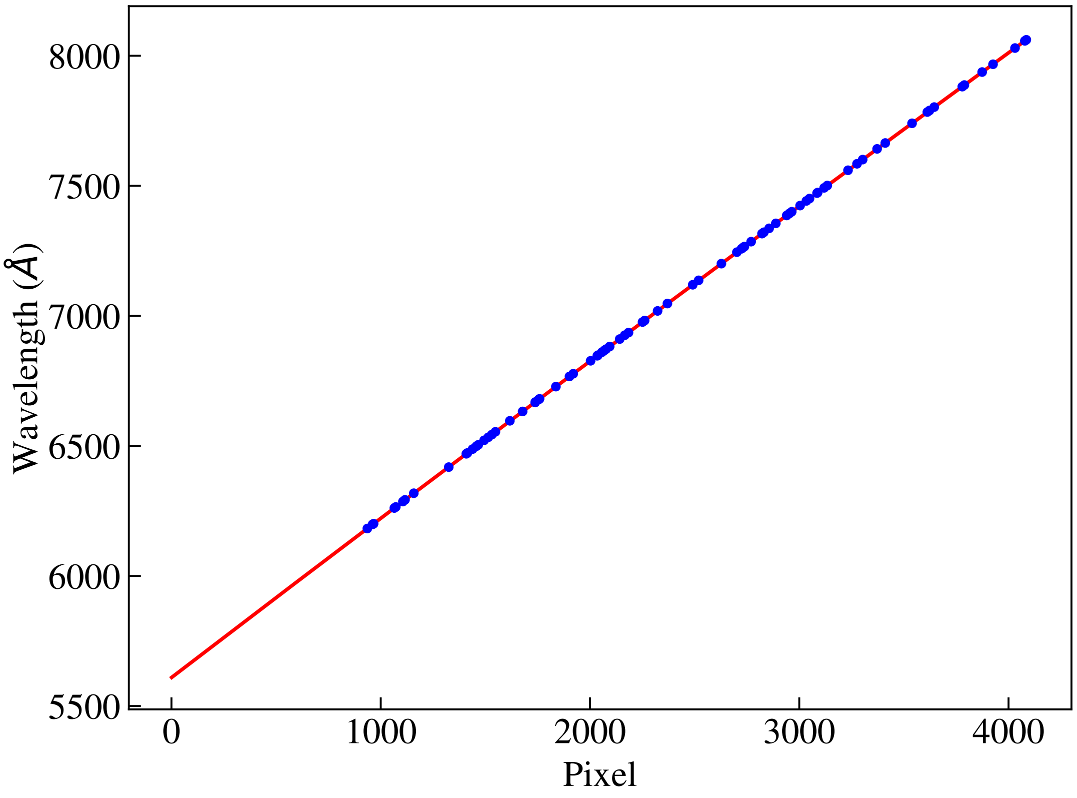

(b)

Figure 2.4: The fits of two of the lamps, corresponding (a) low resolution for the blue arm and (b) high resolution for the red arm. Some non-linearity can be clearly seen on (a) when approaching the edges of the detector.

1 being an absorption line and over 1 being an emission line. The fit to the continuum and the normalization can be seen in Figure 2.5.

Once this step is completed, the spectra are extracted and ready to be used. The main focus of analysis in the rest of this chapter is about the hydrogen emission line shape, the distance between peaks, and a determination of the rotational velocity from the helium lines, mostly assuming that these values are static for such a short timescale, while leaving the spectral variability of the sample for Chapter 4.

2.4 Peak type classification

2.4.1 Hα classification

The most basic classification that can be made for Be stars from their spectra is the one that takes into account the shape of the Hα line: some Be stars show a single peak emission, while others show a mostly symmetric double peak emission. An example of this can be found in Figure 2.6. At the same time, other stars classified as Be stars do not show any Hα emission anymore, and show an absorption line instead. With a long time study like the one presented here, it is also possible to see some changing their peak type with time. For classification purposes, unless stated otherwise, the objects are classified as they show for the most recent observation because it is the closest one to the time the polarization observations were taken.

From the sample of 58 stars, 11 never showed any Hα emission between 1998 and the last observation, another 16 show a single peak emission in all of the observations, and 19 show a double peak emission in all of them. The remaining 12 in the sample have changed with time, with 5 of them showing emission and 7 not showing emission in the last observation. In total, from the criteria of the last observation, 18 do not show hydrogen emission and 40 show hydrogen emission lines.

With a closer examination of the 12 objects that changed their Hα emission peak shape with time, it can be seen that 10 of them spent some time as no emission, with the other 2 always emitting and changing only between double peak and single peak. It is possible now to assume a change rate between emission and absorption of 10/47 in a period of 24 years, or 0.89% of the total sample changing between emission and absorption every year, counting only the objects that have been observed actively changing from the first observation. Similarly, if it is instead assumed that all the objects that did not show any absorption in 1998 are changed from their original observations, compiled in Jaschek &

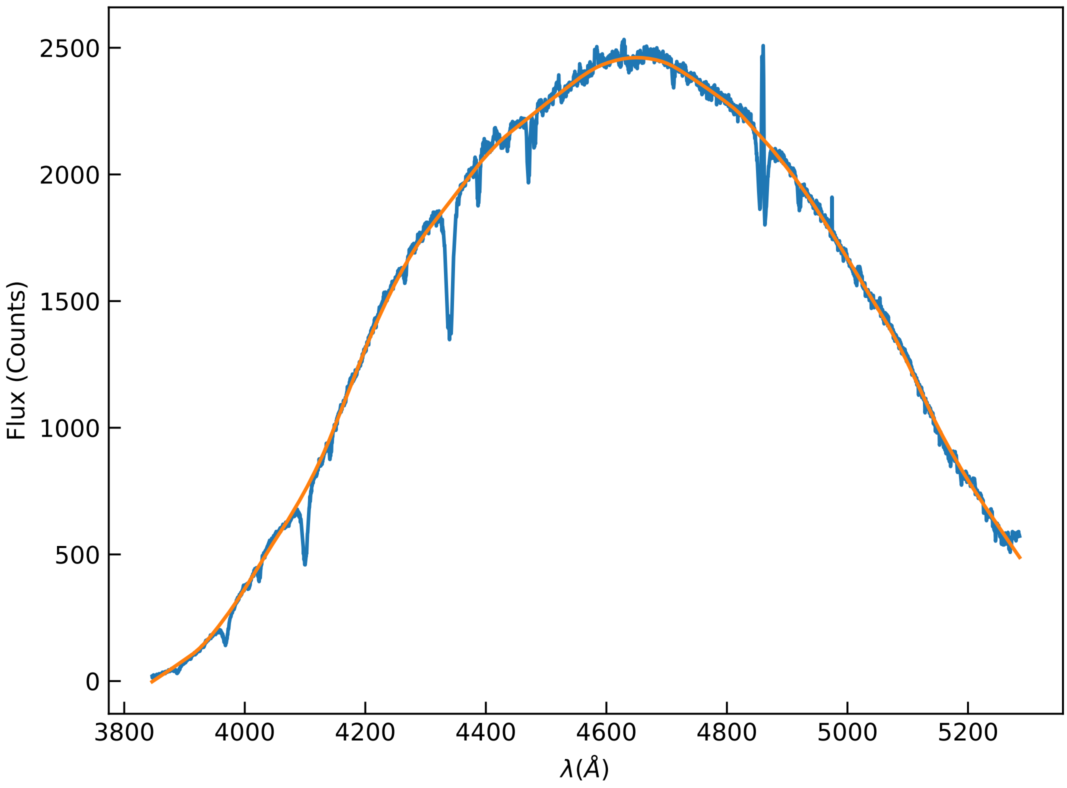

(a)

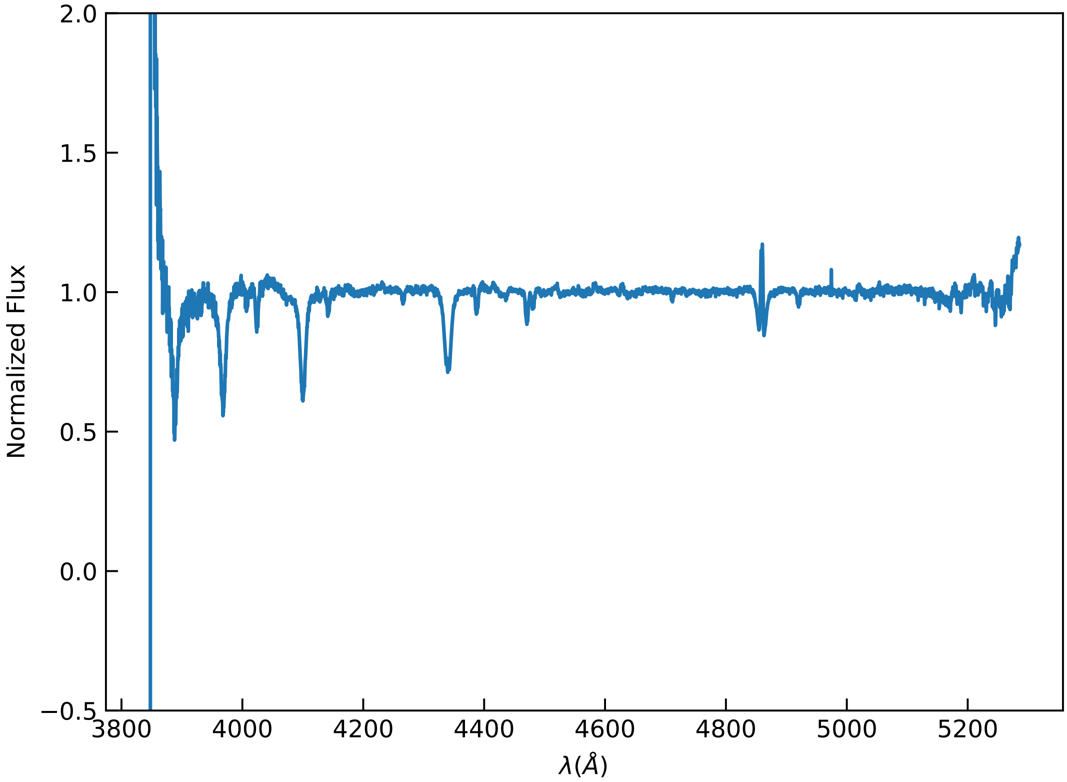

(b)

FIGURE 2.5: The same spectrum, in (a) not normalized and in (b) normalized.

Egret (1982) but originally from the 1960s and 1970s, we would have a fraction 21/58 over an estimated time of 45 years, or a total of 0.80% every year.

Previous determinations of this change rate (McSwain et al., 2008, 2009; Barnsley & Steele, 2013; Dimitrov et al., 2018) over shorter time periods (4–12 years) have ranged between 0.3 and 25 % every year. This wide range can be attributed to how the different samples used for the studies were constructed. Using the same sample as here but only between 1998 and 2010, Barnsley & Steele (2013) found 2 changing objects over 55 analyzed Be stars over a period of 12 years, or 0.30%/year. However McSwain et al. (2008) observed 16 Be stars in a sample of 191 B stars, with 11 of them changing between emission and no emission during a period of observation of 4 years. If these 11 are counted only from the 16 Be stars, then the change rate would be of 11/16 over 4 years, or 17%/year. Alternatively if we count them over the whole sample of B stars, then the change rate would be 11/191 over 4 years, or 1.4%/year. A similar study (McSwain et al., 2009) observed 45 Be stars in a sample of 296 B stars over 2 years, with 23 of them showing variability in emission. Same as the previous study, counting only 23/45 for 2 years would give a change rate of 25.5%/year, while 23/296 for 2 years would give instead a change rate of 3.89%/year. Finally Dimitrov et al. (2018) observed 60 Be stars over a period on 3 years, and 4 of them changed in emission, giving a change rate of 2.2%/year. Overall, comparing the values with at least similar methodologies, which includes the determination from this work, it appears that a change rate of no more than a few percent per year is something like the true value.

2.4.2 Hβ and Hγ classification

While there has been some other work on the other Balmer lines for Be stars, it is very rare to find studies on the simultaneous evolution of the three strongest hydrogen Balmer lines: Hα, Hβ and Hγ.

The next step taken here is to see how well these three lines correlate with each other in shape and emission.

First, a comparison on the shape between Hα and Hβ is done. The results are shown in Table 2.3. It is easy to see that Hβ depends on some way on the shape of Hα: It can be SP only if the Hα line is SP. The reverse is not true, and Hα emission does not guarantee Hβ emission, as can be seen in a few cases. It is also interesting that in the cases when Hα is not in emission, Hβ is always not in emission. This correlation also extends to the variable peaks, where the disappearance of Hβ precedes sometimes the one of Hα.

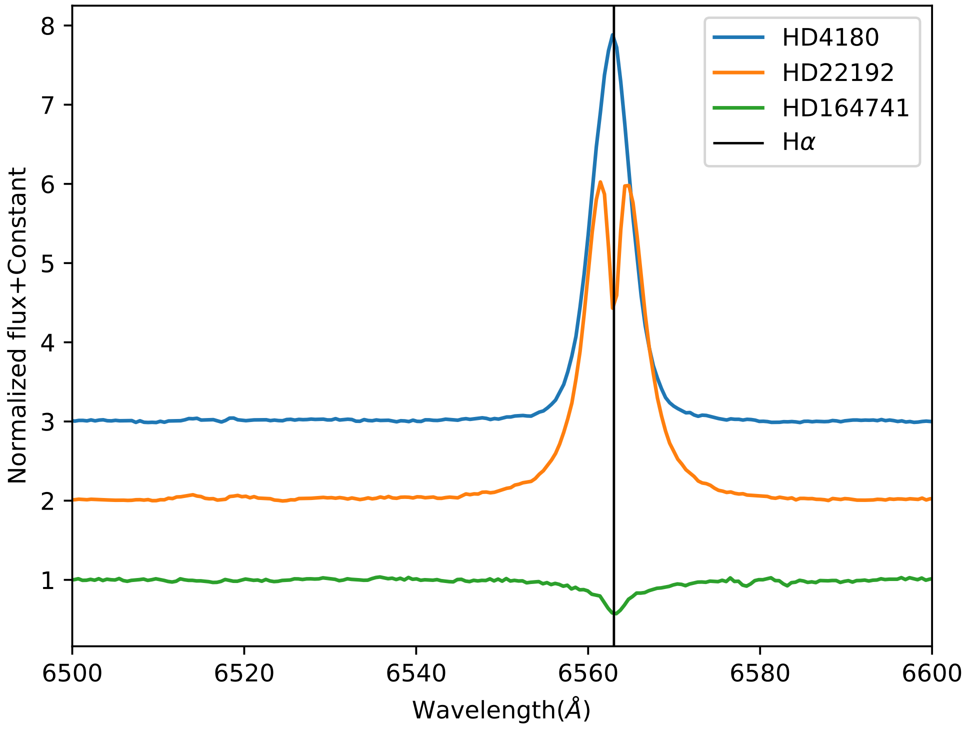

Figure 2.6: Representative plots of the three types of Hα peaks, extracted from the 1998 observations. BD+47 183 is an example of a single peak, BD+47 857 is an example of a double peak, and CD-25 12642 is instead an example of absorption in Hα. The rest wavelength of Hα is indicated by the vertical line.

Table 2.3: A table showing how the Hα peak type and Hβ peak type correlate. They are considered of one type if all the observations have shown the same type, or variable in the contrary.

	Hβ SP	Hβ DP	Hβ NP	Hβ Variable
Hα SP	5	6	1	4
Hα DP	0	12	5	2
Hα NP	0	0	11	0
Hα Variable	0	2	6	4
Total	5	20	23	10

It is possible to extend this study to Hγ. The results observed, shown in Table 2.4, are similar to the ones observed for the relation between Hα and Hβ: Hγ SP can only happen if there is a Hβ SP, and Hβ NP always imply a Hγ NP.

While only 11 of the 58 objects in the sample showed no Hα line emission in all observations, this was extended to 23 for the Hβ line and 38 for the Hγ line. The full list of all the objects and how the three Balmer lines look like on them is shown on Table 2.5. It is possible to assume that something similar would keep happening for the rest of the Balmer lines, which are not only more difficult to observe but also less intense.

Table 2.4: A table showing how the Hβ peak type and Hγ peak type correlate. They are considered of one type if all the observations have shown the same type, or variable in the contrary.

	Hγ SP	Hγ DP	Hγ NP	Hγ Variable
Hβ SP	4	1	0	0
Hβ DP	0	7	11	2
Hβ NP	0	0	23	0
Hβ Variable	0	1	4	5
Total	4	9	38	7

In the cases where the peak type remained the same, the results were expected. However, it is unclear why some that show SP look like a DP on the next line, or why some emit Hα but appear as not emitting on the next lines. The difference in emission type between SP and DP for the same object could be related to the strength of the line: The SP could be a strong DP where the two lines are close enough that they blend into a single one. If this is correct, weaker lines that show DP might be closer to the actual shape of the line because they are too weak to merge into a single peak.

2.4.3 Peak separation distance

One of the observables that can be measured in some cases is the distance of separation between the maximums of the double peaked emission lines. With that purpose, the objects that show both Hα DP and Hβ DP were chosen, including some from the variable ones. The peak distances for all of these objects were measured, and from all the measurements for each object the average was calculated. The average values for the peak distances for Hα and Hβ are shown in Table 2.6.

The next question is how the values of the distance of Hα and Hβ correlate. As can be seen in Figure 2.7, the results are linear. It is expected from pure Doppler effect that if the lines are emitted from the same region, the slope of this linear fit would be:

$$z = \frac{v}{c} = \frac{\Delta\lambda}{\lambda} \longrightarrow \frac{\Delta\lambda_{\mathrm{H}\alpha}}{\lambda_{\mathrm{H}\alpha}} = \frac{\Delta\lambda_{\mathrm{H}\beta}}{\lambda_{\mathrm{H}\beta}} \longrightarrow \Delta\lambda_{\mathrm{H}\alpha} = \Delta\lambda_{\mathrm{H}\beta}\frac{6562.79}{4861.35} = 1.35\Delta\lambda_{\mathrm{H}\beta} \tag{2.1}$$

so the expected slope of the linear fit $y = Ax$ is $A = 1.35$. However, the obtained slope from the fit is $A = 1.005$. This value of the slope is similar to the one obtained by Zamanov et al. (2023), which would be of $A = 0.990$, although the best fit in this case do not include an intercept. An interesting implication from this relation is that the values of the peak distance between Hα peaks can be deduced, and are very similar to the ones of Hβ. It can also be seen that this implies that the region with maximum Hβ emission has a higher velocity than the region with maximum Hα emission, which at the same time implies, from orbital mechanics, that they are at different distances. It is

TABLE 2.5: A list of observed objects, with their H type peak: SP for Single Peak, DP for Double Peak, NP for No Peak, and V for variable emission.

Object	Other Identifier	$H\alpha$ (6563Å)	$H\beta$ (4861Å)	$H\gamma$ (4340Å)
CD-28 14778	HD 171757	SP	SP	SP
CD-27 11872	HD 161103	SP	DP	DP
CD-27 16010	HD 214748	DP	NP	NP
CD-25 12642	HD 164741	NP	NP	NP
CD-22 13183	HD 172158	DP	DP	NP
BD-20 5381	HD 177015	DP	DP	NP
BD-19 5036	HD 170682	NP	NP	NP
BD-12 5132	HD 172252	SP	DP	NP
BD-02 5328	HD 196712	SP	DP	NP
BD-01 3834	HD 187350	SP	V	DP
BD-00 3543	HD 173371	DP	DP	NP
BD+02 3815	HD 179343	DP	NP	NP
BD+05 3704	HD 168797	V	NP	NP
BD+17 4087	HD 350559	V	NP	NP
BD+19 578	HD 23016	NP	NP	NP
BD+20 4449	HD 191531	NP	NP	NP
BD+21 4695	HD 210129	SP	DP	NP
BD+23 1148	HD 250289	NP	NP	NP
BD+25 4083	HD 339483	NP	NP	NP
BD+27 797	HD 244894	V	DP	DP
BD+27 850	HD 246878	NP	NP	NP
BD+27 3411	HD 183914	V	NP	NP
BD+28 3598	HD 333452	NP	NP	NP
BD+29 3842	HD 333226	NP	NP	NP
BD+29 4453	HD 205618	SP	DP	DP
BD+30 3227	HD 171406	V	NP	NP
BD+31 4018	HD 193009	SP	DP	DP
BD+36 3946	HD 228438	SP	V	V
BD+37 675	HD 18552	DP	DP	NP
BD+37 3856	HD 228650	NP	NP	NP
BD+40 1213	HD 33604	SP	SP	SP
BD+42 1376	HD 37657	V	V	NP
BD+42 4538	HD 216581	DP	DP	DP
BD+43 1048	HD 276738	DP	DP	NP
BD+45 933	HD 27846	NP	NP	NP
BD+45 3879	HD 211835	DP	DP	DP
BD+46 275	HD 6811	V	NP	NP
BD+47 183	HD 4180	SP	V	NP
BD+47 857	HD 22192	DP	DP	DP
BD+47 939	HD 25940	SP	SP	DP
BD+47 3985	HD 217050	DP	V	NP
BD+49 614	HD 13867	SP	SP	SP
BD+50 825	HD 23552	V	NP	NP
BD+50 3430	HD 207232	DP	DP	NP
BD+51 3091	HD 20551	SP	NP	NP
BD+53 2599	HD 203356	DP	NP	NP
BD+55 552	HD 13669	DP	V	V
BD+55 605	HD 14605	V	V	NP
BD+55 2411	HD 195554	DP	NP	NP
BD+56 473	V356 Per	DP	DP	V
BD+56 478	HD 13890	V	DP	V
BD+56 484	V502 Per	SP	V	V
BD+56 493	-	V	V	V
BD+56 511	-	DP	NP	NP
BD+56 573	-	SP	SP	SP
BD+57 681	HD 237056	V	V	V
BD+58 554	HD 237060	DP	DP	NP
BD+58 2320	HD 239758	DP	DP	NP

TABLE 2.6: A table that shows the values of the peak separation distance for the Hα and Hβ DP or V stars in the cases where the distance between the peaks was measured.

Identifier	Hα DP (Å)	σ(Hα DP) (Å)	Hβ DP (Å)	σ(Hβ DP) (Å)
CD-22 13183	2.93	0.09	3.12	0.69
BD-20 5381	2.40	0.02	2.54	0.22
BD+37 675	3.37	0.35	3.74	0.31
BD+42 4538	2.63	0.45	2.81	0.31
BD+43 1048	5.54	0.39	4.75	0.65
BD+45 3879	2.68	0.44	3.21	0.39
BD+47 857	3.12	0.21	2.93	0.22
BD+47 3985	6.41	1.00	6.85	1.18
BD+50 3430	4.44	0.29	4.52	0.36
BD+55 552	5.03	1.37	4.37	0.52
BD+56 473	3.49	1.10	3.48	0.51
BD+58 554	2.88	0.27	3.43	0.38
BD+58 2320	6.56	0.62	5.94	0.28

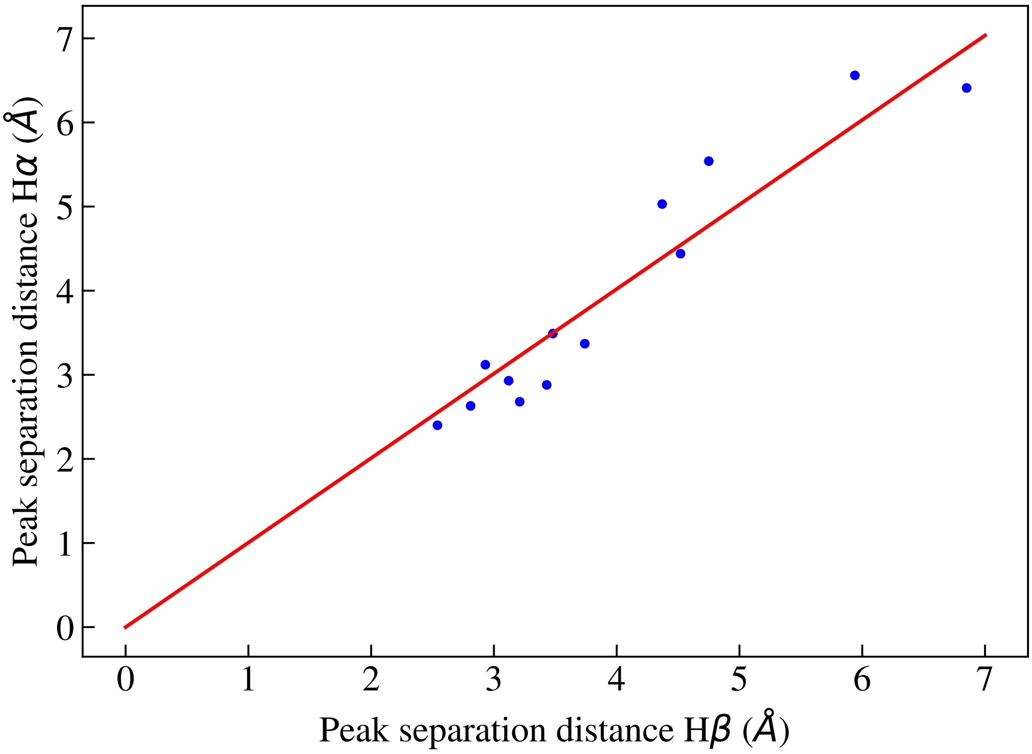

FIGURE 2.7: A plot that shows the peak separation distance between Hα DP against the peak separation distance between Hβ DP. The red line is a linear fit $y = Ax$, with $A = 1.005 \pm 0.030$ and an R^2 value of $R^2 = 0.904$.

Table 2.7: A table that shows the values of the peak separation distance for the Hα DP stars with no emission Hβ or where the peaks were very weak and the distance between them could not be measured. The estimated values of Hβ, in bold, are derived from the Hα values and the results from the previous fit.

Identifier	Hα DP (Å)	σ(Hα DP) (Å)	Hβ NP (Å)	σ(Hβ NP) (Å)
CD-27 16010	2.67	0.41	**2.66**	**0.42**
BD-00 3543	4.80	0.27	**4.78**	**0.30**
BD+02 3815	5.01	0.27	**4.99**	**0.31**
BD+53 2599	5.39	0.80	**5.36**	**0.81**
BD+55 2411	3.10	0.34	**3.08**	**0.35**
BD+56 511	4.51	0.68	**4.49**	**0.69**

Table 2.8: A table that shows the values of the peak separation distance for the Hα SP stars. The values of Hα, in bold, are derived from the Hβ values and the results from the previous fit.

Identifier	Hα SP (Å)	σ(Hα SP) (Å)	Hβ DP (Å)	σ(Hβ DP) (Å)
CD-27 11872	**1.61**	**0.24**	1.60	0.23
BD-12 5132	**2.81**	**0.58**	2.80	0.57
BD-02 5328	**2.28**	**0.48**	2.27	0.47
BD-01 3834	**1.52**	**0.18**	1.51	0.17
BD+21 4695	**1.65**	**0.24**	1.64	0.23
BD+27 797	**1.68**	**0.34**	1.67	0.33
BD+31 4018	**2.75**	**0.75**	2.74	0.74
BD+36 3946	**1.58**	**0.35**	1.57	0.35
BD+47 183	**1.60**	**0.32**	1.59	0.31
BD+56 484	**1.68**	**0.30**	1.67	0.29

possible to calculate the $v \sin i$ for these two regions, and then, if the mass of the central star is known, and assuming a circular orbit for simplicity:

$$R = \frac{GM}{v^2} \tag{2.2}$$

From the previous fit, it is also possible to estimate what the values for Hβ should be in the cases where Hα is DP but Hβ is NP. Those values are shown in Table 2.7.

The values of the mass for each central star can be found in Table A.2.

It is possible to try to extend this analysis as well to Hα that show a SP line: they might be two lines that are very close and blended. Several fits to two lines, being two gaussians, two lorentzians and two voigt profiles were tried, but the results were unsuccessful. However, from the 16 Hα SP, 10 of them have for the whole time series or part of it a Hβ DP line.

The values of the corresponding Hβ line, and an estimation of the values for the Hα line can be seen in Table 2.8.

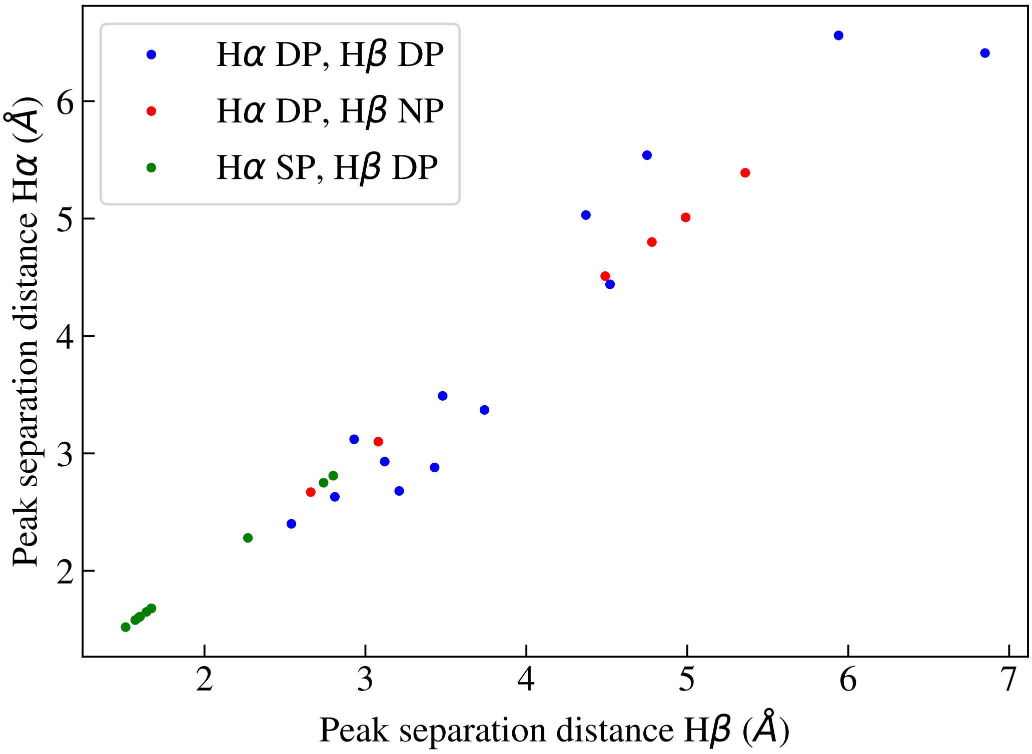

Figure 2.8: A plot that shows the actual or predicted peak separation distance of Hα against the peak separation distance of Hβ. The blue points are for the ones with Hα DP and Hβ DP, the red points are for the Hα DP and Hβ NP, and the green points are for the Hα SP and Hβ DP.

As is possible to see, the values in Table 2.8 are generally smaller than the ones in tables 2.6 and 2.7, and can be seen in Figure 2.8. This seems to be in agreement with the the hypothesis that Hα SP is probably just that the two very close Hα emission peaks blended together.

2.5 Results: rotation

2.5.1 Calculation of the rotational velocities

One of the most commonly studied values for Be stars is the projected rotational velocity of the central star, $v \sin i$. As was mentioned in Chapter 1, Be stars are fast rotating objects. However, it is still unclear how close they are to critical velocity or if this causes any difference on the creation or evolution of Be stars, mostly because of the difficulties to separate the velocity from the inclination angle of the disk, which is also unknown.

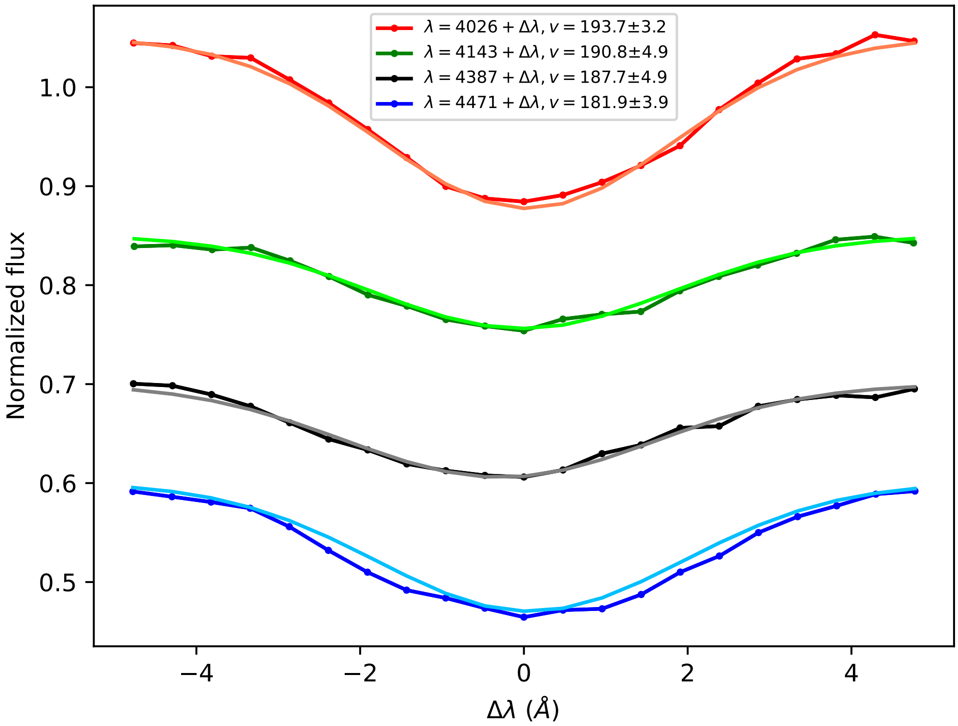

FIGURE 2.9: A plot, showing the fit to the helium I lines. In this case, it is the observation of star BD+47 183 taken in August 1998. We fit each line to a Gaussian profile and obtained the FWHM from them, and hence the velocity as described in Section 2.5.

The values of the projected rotational velocities of the stars in the study sample can be obtained through some of the most frequently observed absorption lines in the spectra, like the He-I absorption lines, more precisely the lines at wavelengths 4026 Å, 4143 Å, 4387 Å and 4471 Å. With a fit to a Gaussian profile to each of these lines, it is possible to obtain σ, the standard deviation of the Gaussian distribution, that then can be converted into the full width half maximum (FWHM) by using the equation:

$$\mathrm{FWHM} = 2\sqrt{2\ln 2}\sigma \tag{2.3}$$

The values of FWHM are not a measurement of the rotational velocity itself, since rotation is not the only line broadening mechanism. To convert them, a FWHM-$v \sin i$ relation derived from observational fits to rotationally broadened line profiles of model atmospheres of a wide sample of early type stars (Slettebak et al., 1975) can be used.

A linear fit was calculated for the values of FWHM and $v \sin i$ of the He I line ($\lambda = 4471$Å) shown in tables 1 and 2 of Slettebak et al. (1975), and shown in Figure 2.10, and this relation was then used to convert the values of the FWHM to rotational velocities, with

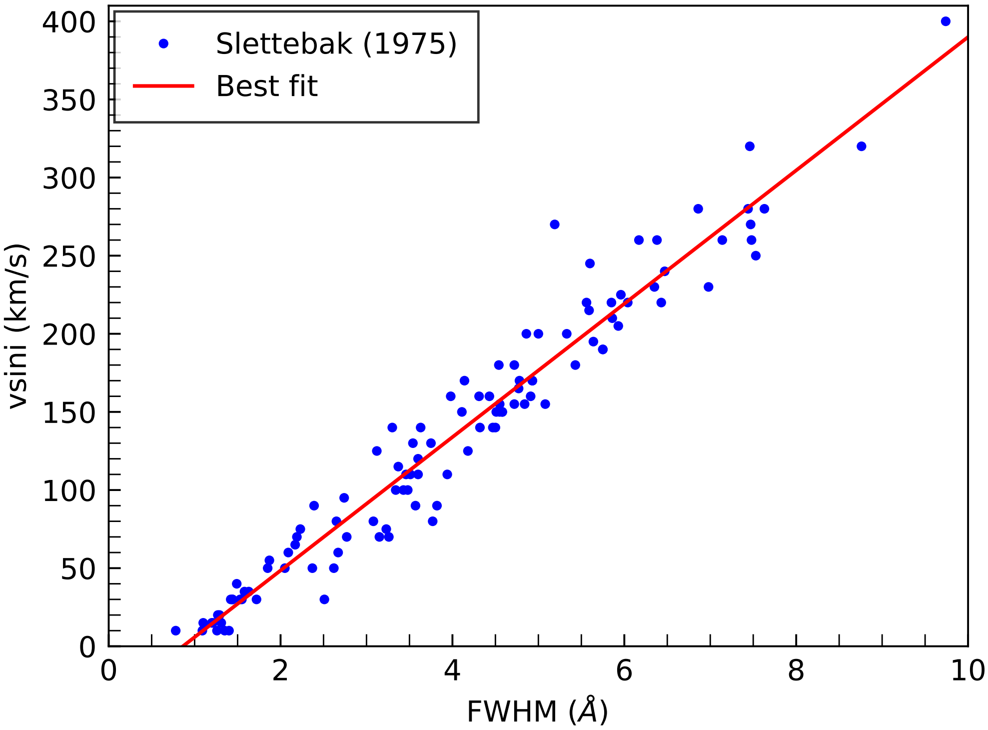

FIGURE 2.10: A plot of the rotational velocities of B stars against the FWHM of the He I 4471 Å line, extracted from tables 1 and 2 in Slettebak et al. (1975). The results of the linear fit $y = Ax + B$ are $A = 42.68 \pm 0.93$, $B = -36.84 \pm 4.17$, $R = 0.9746$.

a Doppler shift being applied to the FWHM dependent slope to change the values to the other three near He I lines ($\lambda = 4387$ Å, $\lambda = 4143$ Å, $\lambda = 4026$ Å). The intercept is not wavelength dependent and for that reason it was not Doppler shifted. The final equations obtained were:

$$\begin{aligned} v \sin i &= 42.68F(\lambda = 4471) - 36.84\text{kms}^{-1} \\ v \sin i &= 43.50F(\lambda = 4387) - 36.84\text{kms}^{-1} \\ v \sin i &= 46.06F(\lambda = 4143) - 36.84\text{kms}^{-1} \\ v \sin i &= 47.40F(\lambda = 4026) - 36.84\text{kms}^{-1} \end{aligned} \tag{2.4}$$

with $F(\lambda)$ being the measured FWHM of the Gaussian profile fit for the line at the corresponding wavelength.

For any particular object the results of the fits to these lines might show certain variation: a number of factors can cause this effect such as the noise in the spectrum or blending with another line. For that reason, we have chosen to calculate the weighted mean and standard deviation of the four lines and reject any values that are more than 4 σ away from the average value.

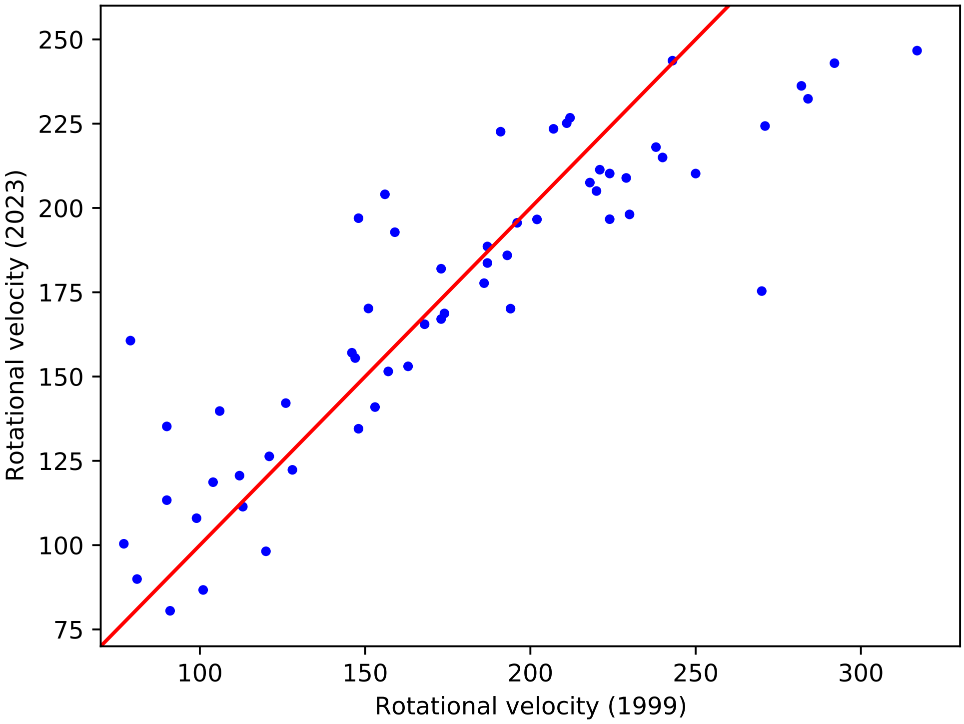

FIGURE 2.11: A plot comparing the values obtained for the rotational velocity in 2023 vs the values obtained for the rotational velocity in 1999. The red line is a 1:1 line for comparison.

After this, the rotational velocities have been measured for all observations of each star. While changes with time of the rotational velocities of Be stars have been reported previously, how relevant they are for the changes in the emission is still unclear. Even if they are possible, those changes are not expected to be big over the length of the few decades covered by this study, so a weighted mean of all the values for the velocity of each object was calculated. These results are shown in Table 2.9 and represented in Figure 2.11, where they are compared with the values previously obtained by Steele et al. (1999) for the same sample. While the rotational velocities obtained in this work are similar to the ones obtained in 1999 for the lower values, they are lower when compared with the higher values of 1999. The cause of this difference can perhaps be attributed to the amount of data used: Steele et al. (1999) used the only one available measurement for the results, while an average of all the measurements taken for up to 23 years was calculated here.

TABLE 2.9: A list of the observed objects, including the rotational velocities calculated in this work during the year 2023 and the rotational velocities obtained in Steele et al. (1999).

Object	Other Identifier	$v \sin i$ (km/s) (2023)	$v \sin i$ (km/s) (1999)
CD-28 14778	HD 171757	141 ± 23	153 ± 21
CD-27 11872	HD 161103	210 ± 17	224 ± 33
CD-27 16010	HD 214748	188.6 ± 7.2	187 ± 32
CD-25 12642	HD 164741	100 ± 24	77 ± 18
CD-22 13183	HD 172158	169 ± 79	174 ± 10
BD-20 5381	HD 177015	197 ± 72	202 ± 10
BD-19 5036	HD 170682	126 ± 17	121 ± 10
BD-12 5132	HD 172252	98 ± 11	120 ± 43
BD-02 5328	HD 196712	170.2 ± 8.4	151 ± 15
BD-01 3834	HD 187350	166 ± 12	168 ± 34
BD-00 3543	HD 173371	224 ± 15	271 ± 54
BD+02 3815	HD 179343	197 ± 10	224 ± 14
BD+05 3704	HD 168797	211 ± 59	221 ± 10
BD+17 4087	HD 350559	204 ± 79	156 ± 39
BD+19 578	HD 23016	215 ± 17	240 ± 70
BD+20 4449	HD 191531	90 ± 43	81 ± 11
BD+21 4695	HD 210129	157 ± 17	146 ± 10
BD+23 1148	HD 250289	87 ± 77	101 ± 10
BD+25 4083	HD 339483	161 ± 83	79 ± 11
BD+27 797	HD 244894	197 ± 18	148 ± 74
BD+27 850	HD 246878	121 ± 18	112 ± 25
BD+27 3411	HD 183914	170 ± 13	194 ± 10
BD+28 3598	HD 333452	113 ± 50	90 ± 12
BD+29 3842	HD 333226	81 ± 20	91 ± 16
BD+29 4453	HD 205618	247 ± 26	317 ± 20
BD+30 3227	HD 171406	207.5 ± 8.3	218 ± 21
BD+31 4018	HD 193009	225 ± 30	211 ± 11
BD+36 3946	HD 228438	178 ± 23	186 ± 21
BD+37 675	HD 18552	223 ± 21	207 ± 29
BD+37 3856	HD 228650	119 ± 18	104 ± 17
BD+40 1213	HD 33604	122.3 ± 7.4	128 ± 20
BD+42 1376	HD 37657	195.6 ± 9.6	196 ± 10
BD+42 4538	HD 216581	236 ± 30	282 ± 10
BD+43 1048	HD 276738	205 ± 46	220 ± 20
BD+45 933	HD 27846	135 ± 14	148 ± 16
BD+45 3879	HD 211835	186 ± 10	193 ± 10
BD+46 275	HD 6811	111 ± 20	113 ± 21
BD+47 183	HD 4180	167 ± 12	173 ± 12
BD+47 857	HD 22192	227 ± 12	212 ± 16
BD+47 939	HD 25940	153.0 ± 8.0	163 ± 12
BD+47 3985	HD 217050	232 ± 14	284 ± 20
BD+49 614	HD 13867	140 ± 110	90 ± 27
BD+50 825	HD 23552	184 ± 11	187 ± 10
BD+50 3430	HD 207232	198 ± 19	230 ± 15
BD+51 3091	HD 20551	139.8 ± 8.5	106 ± 10
BD+53 2599	HD 203356	223 ± 22	191 ± 23
BD+55 552	HD 13669	243 ± 29	292 ± 17
BD+55 605	HD 14605	142 ± 25	126 ± 35
BD+55 2411	HD 195554	192.8 ± 9.2	159 ± 90
BD+56 473	V356 Per	218 ± 23	238 ± 19
BD+56 478	HD 13890	152 ± 30	157 ± 12
BD+56 484	V502 Per	182 ± 39	173 ± 16
BD+56 493	-	175 ± 41	270 ± 10
BD+56 511	-	108 ± 54	99 ± 14
BD+56 573	-	210 ± 51	250 ± 58
BD+57 681	HD 237056	155 ± 20	147 ± 49
BD+58 554	HD 237060	209 ± 17	229 ± 10
BD+58 2320	HD 239758	244 ± 39	243 ± 20

2.5.2 Calculation of the critical velocity

As can be seen in Section 1.5.1, to calculate the values of the critical velocity for the sample from Equation 1.5, the values for the masses and the radii of the central B stars in the sample are required. To obtain these values, the classification of the spectral types from Steele et al. (1999), reproduced in Table A.2, were used to take stellar luminosities from de Jager & Nieuwenhuijzen (1987); Cox (2000). Masses and radii were then derived from those luminosity values using the equations shown in Tables 4 and 5 of Eker et al. (2018). First, the masses are calculated from the luminosities, with the following formulae:

$$\begin{aligned}
\log M &= (\log L - 0.010)/4.329; 1.05 < M/M_\odot \leq 2.40 \\
\log M &= (\log L - 0.093)/3.967; 2.4 < M/M_\odot \leq 7 \\
\log M &= (\log L - 1.105)/2.865; 7 < M/M_\odot
\end{aligned} \tag{2.5}$$

calculating the three values and choosing the appropriate one from the obtained values and ranges.

From the value of the mass, it is possible to calculate the effective temperature:

$$\log T_{\text{eff}} = -0.170(\log M)^2 + 0.888 \log M + 3.671 \tag{2.6}$$

and then it is possible to finally calculate the radius of the star using the Stefan-Boltzmann law:

$$R = \sqrt{\frac{L}{4\pi\sigma T_{\text{eff}}^4}} \tag{2.7}$$

After obtaining the values of the mass and radius of the star, the v_{crit} can be calculated. The critical fraction W, that shows how close the obtained equatorial rotational velocity is to the critical value, can also be calculated using the following equation:

$$W = \frac{v}{v_{\text{crit}}} \tag{2.8}$$

The values of the velocity available here are not the rotational velocity v, but the projected rotational velocity $v \sin i$, as the value of the inclination i is unknown. With this, instead, it is possible to calculate the value $W \sin i$, where in Equation 2.8 $v \sin i$ was used instead of v. All of these values are listed in Table A.2.

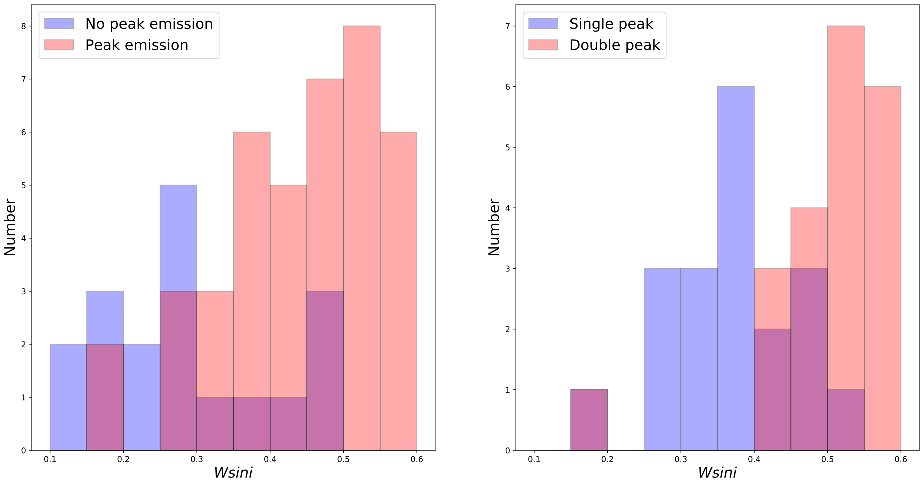

Figure 2.12: Two histograms showing the distribution of stars for different values and types of emission of the Hα line with respect to $Wsini$.

Table 2.10: Results from the KS tests. To say that the two groups are apparently drawn from the same parent population a minimum value of $p > 0.05$ would be required.

Values	NP vs P	SP vs DP
$v \sin i$	0.001	0.001
$W \sin i$	0.0003	0.00006

2.5.3 Analysis of the rotational velocity

One of the questions is if the rotational velocity is a key difference between the stars that emit and the stars that do not emit. For that, a series of Kolmogorov-Smirnov test have been performed to see if the populations, as a whole group, can be separated from the others from their rotational velocity and their critical fraction. The sample has been split into three groups: NP (No Peak or No Emission), SP (Single Peak) and DP (Double Peak), depending on the shape of the $H\alpha$ emission. In the case of the stars that have changed the shape of their emission line or have stopped emitting, they have been classified as the last available FRODOSpec observation indicates.

The results, shown in Table 2.10, reject the null hypothesis that both groups come from the same distribution in both cases, showing a clear difference between the emission and no emission groups, and the single and double peak emission groups. While the rotational velocity and critical fraction criteria was expected to work to separate the emission and no emission groups, it is currently unexplained from our data why single and double peak stars look different. This is further analysed in Section 3.5.3.

2.6 Summary

In this chapter, the spectral data available for this work has been introduced - a sample of 58 stars observed at different intervals for 24 years. A basic classification has been made using the data, grouping them depending on their $H\alpha$, $H\beta$ and $H\gamma$ line shape, which can be classified as NP (No Peak or No Emission), SP (Single Peak) and DP (Double Peak).

After that, the peak distances in the case for stars showing Hα DP, Hβ DP or both were studied, obtaining an empirical relationship between both of them, showing that the maximum of emission of Hβ and the maximum of emission of Hα happen at different distances from the star, and also that SP emission might be a DP where the two peaks were too close and blended together.

Next, the rotational velocity $v \sin i$ was calculated for each star from a relation with the FWHM (Full Width Half Maximum) of He I lines, and also the critical velocity from the spectral class of the central B stars and tabulated values on the mass and luminosity of them. With those values, some Kolmogorov-Smirnov tests were calculated to see if these rotational velocities, or the rotational velocities divided by the critical velocities, can separate between the different peak populations.

The final result from the tests is that the three populations are separated, although further analysis on the separation of SP and DP requires more data, and is left for the next chapter.

Chapter 3

Polarimetry

3.1 Brief introduction to polarimetry

Compared to the popularity of spectroscopy, that has been widely used since its discovery, polarization was mostly unused in astronomy until the second half of the XX century. In recent years, its use has become widespread across many fields.

In this chapter, the general physical concept of polarization is introduced, followed by some more concrete ideas of its use in astronomy. After that, the polarization data of the sample is presented, and the work of Chapter 2 is continued by adding and studying the polarization values, which is shown to allow insight into the system inclination angle.

3.1.1 Physics of polarimetry and Stokes parameters

In basic courses of Physical Optics, it is studied that the light can be described as electromagnetic waves from Maxwell's equations. The electric vector E can be described as changing between two components, x and y, while propagating along the z axis. From here, the two components of the E vector can be described as waves (Hecht, 2017):

$$\begin{aligned} E_x &= E_{0x}\cos(kz - \omega t) \\ E_y &= E_{0y}\cos(kz - \omega t + \varepsilon) \end{aligned} \tag{3.1}$$

with E_{0x} and E_{0y} the amplitude of the x and y components, and ε being the difference of phase between them.

If $\varepsilon = 0$ and $E_{0x} = E_{0y}$, the light would oscillate along a line in the XY plane while it travels in the Z direction. This is what it is known as *linear polarization.* If the difference of phase was instead $\varepsilon = \pm 90^\circ$ and $E_{0x} = E_{0y}$, the light would oscillate along a circle in the XY plane, in what it is known as *circular polarization*, with the negative value meaning that the light rotates clockwise and the positive meaning that the light rotates counterclockwise. The more general case, where ε, E_{0x} and E_{0y} can have any values, it is known as *elliptical polarization*.

Polarization can be represented in a more convenient and mathematical way using what are called the "Stokes parameters". The mathematical definition of these parameters is:

$$\begin{aligned} S_0 &= \langle E_{0x}^2 \rangle + \langle E_{0y}^2 \rangle \\ S_1 &= \langle E_{0x}^2 \rangle - \langle E_{0y}^2 \rangle \\ S_2 &= \langle 2E_{0x}E_{0y}\cos\varepsilon \rangle \\ S_3 &= \langle 2E_{0x}E_{0y}\sin\varepsilon \rangle \end{aligned} \tag{3.2}$$

Instead of using the names (S_0, S_1, S_2, S_3), the alternative names (I, Q, U, V) can be used (Stokes, 1851; Clarke, 1974). These four values represent the state of the polarization, with I being the irradiance, V representing the state of clockwise or counterclockwise rotation, and Q and U representing the shape of the polarization. A different representation can be used, where instead of using the absolute values of (I, Q, U, V), the normalized values with repect of the intensity are used, that is, the vector $(1, q, u, v)$, with $q = Q/I$, $u = U/I$ and $v = V/I$.

Finally, two more values can be obtained:

$$\begin{aligned} p &= \frac{\sqrt{Q^2 + U^2 + V^2}}{I} = \sqrt{q^2 + u^2 + v^2} \\ \theta &= \frac{1}{2}\arctan\left(\frac{U}{Q}\right) = \frac{1}{2}\arctan\left(\frac{u}{q}\right) \end{aligned} \tag{3.3}$$

with p being commonly referred as *polarization degree*, which says how much of the observed light is polarized, with the rest being unpolarized, and θ as *polarization angle*, which represents the angle that the major axis of the polarization is inclined. Due to instrumental limitations, the work presented in this chapter will only consider *linear* polarization, and we will assume in the above calculations that $V = 0$.

3.1.2 Mechanisms that create polarization in astronomy

There are many mechanisms that are responsible for the creation of polarization in astronomy. For a full list, Trippe (2014) gives a review. However, they can be mainly reduced to two types (Angel, 1974): Scattering and interaction with magnetic fields.

3.1.2.1 Scattering

When photons go through a gas, they can be absorbed and re-emitted at a different angle. This scattering of the light is known as Thompson scattering or Compton scattering if the interaction is between the photon and an electron, or Rayleigh scattering or Raman scattering if the interaction is between the photon and atoms or molecules (Angel, 1974). For an observer, the light will look linearly (Trippe, 2014) or elliptically (Born et al., 1999) polarized.

The other possibility of scattering is when the photons interact with dust. Dust is one of the main components of the interstellar matter, and while it is expected for it to interact with magnetic fields, dust can also scatter light in a geometrical way. If the grains are smaller than the wavelength of the light, the photons are scattered like in the case of the gas, but if the size of the grains is considerable, the problem of the scattering becomes more complex, as it involves the composition, the shape and the cross section of the grains. The solution of this problem is beyond the scope of this thesis, but for the details on the solution, that involves Mie theory, check Born et al. (1999) and Li (2008).

3.1.2.2 Interaction with magnetic fields

When charged particles move through a magnetic field, an interaction between them will happen. Depending on the type of particle, different effects will take place, and while a multitude of effects can happen (check e.g. Trippe (2014)), the three major effects are synchrotron radiation, Faraday rotation, and the Zeeman effect.

Synchrotron radiation affects mainly free charges, generally electrons, that move at relativistic speeds, and imposes a circular motion around the direction of the magnetic field. For example, if the magnetic field is in the z direction, the electron would move with a circular motion on the xy plane, however an observer would see it as an ellipse. As a consequence of this effect, the emission looks elliptically polarized for the observer.

If linearly polarized radiation goes through an ionized medium in the presence of a magnetic field, like a plasma, what is known as Faraday rotation will happen, an effect which will rotate the plane of propagation of the wave. The wave will still be linearly polarized, but it will be at a different angle.

Finally, when a level of an atom or molecule with a total angular momentum $\mathbf{J}$ different to zero, the emitted line, which usually shows as a single degenerate value, will split into a total of $n = 2J - 1$ lines, with an offset depending on the intensity of the magnetic field. The resulting lines can be split between the central line, which will be linearly polarized, and the rest, which will have circular polarization. This is known as the *Zeeman effect*, and while it is useful to easily see and measure very intense magnetic fields (Petit et al., 2013), very faint ones might be difficult to measure through this effect, as the line displacements would be too small to be easily observed with the current instrumentation.

A more in-depth description of these effects can be found in multiple basic books, for example, Spitzer (1978), Lequeux (2005) and Schneider (2006).

3.1.3 Intrinsic and interstellar polarization

Two possible origins of the polarization can be differentiated from their source: intrinsic and interstellar. The emitted light will be polarized at the source, due to circumstellar shells (Zellner & Serkowski, 1972), or inherent to the star, in what it is called *intrinsic polarization* (Gehrels, 1974).

The rest of the observed polarization will be caused while the light travels from the source to Earth, and for that reason it is called *interstellar polarization*. The main source for it is expected to be interstellar dust, which complicates the problem from simple scattering, as the size of the dust grains is not negligible (van de Hulst, 1950). It is also expected that if the light was at least partially polarized from the source, the resulting observed interstellar polarization will be circular (van de Hulst, 1957; Martin, 1972). The variation of the polarization has been shown to be wavelength dependent (Behr, 1959b; Gehrels, 1960; Serkowski, 1968; Serkowski et al., 1975), but even if there is also a correlation between wavelength and extinction (Clayton & Mathis, 1988; Cardelli et al., 1989), the correlation between interstellar polarization and extinction is more complicated, because while the reddening caused by extinction increases with the dust density, this might not be true for the polarization, as other effects, like magnetic fields, might reduce it (Angarita et al., 2023). The relation between interstellar polarization and extinction is explored in more detail in Section 3.5.4 for the Be star sample.

3.1.4 Polarization in Be stars

If Be stars are observed with polarimetry, an excess of the polarization degree when compared with other field stars can be found (Coyne, 1971). This excess of the intrinsic polarization was quickly understood as Thomson scattering (Coyne, 1976; Brown & McLean, 1977) from a circumstellar material (Zellner & Serkowski, 1972) which showed apparent axisymmetry (McLean & Brown, 1978) and was later understood as a disk from multiple observations. Despite multiple attempts and a big sample of observations, no large-scale magnetic fields have been found in Be stars (Grunhut et al., 2017), with an upper limit on them between 50 and 105 G (Wade et al., 2016), which reduces the possibility of strong magnetic fields as the mechanism to modify the polarization to only small-scale magnetic fields. However values under the current observational limit have been proposed to potentially exist in Be stars (Balona & Ozuyar, 2020) as magnetic fields of 10 G have been shown to have disruptive effects in the disk without destroying it (ud-Doula et al., 2018), while magnetic fields of up to 100 G would destroy it.

The value of the polarization shows some dependence with the spectral type, with the maximum mean value happening between B1 and B2 stars (Yudin, 2001). They also show some time variation in the polarization degree (Wisniewski et al., 2010) but the polarization angle seems to be generally constant (Wood et al., 1997), although short-time observations show some rapid and almost periodic variability in the polarization degree and angle (Carciofi et al., 2007). It has also been observed that the polarization degree varies with the wavelength of the observation (Bjorkman et al., 1991; Carciofi et al., 2006).

By using polarimetry observations, some properties of the Be star can be resolved without the need of modelling the properties of the disk (Marr et al., 2018).

3.2 MOPTOP

The Multicolour OPTimised Optical Polarimeter, more known as MOPTOP (Jermak et al., 2016a,b, 2018) is the polarimetry detector at the LT. It is composed of a rotating half-wave plate, which regulates the polarization angle, and a beamsplitter, that sends the p and s polarized states to each of the two cameras. A diagram that shows the optical scheme of MOPTOP can be seen in Figure 3.1.

The half-wave plate adds a π radians, or 180°, to the phase between the two observed components of the wave. By rotating the half-wave plate in angles of 22.5°, this can be modulated to phases of $\pi/4$ radians, or 45°, swapping the q and u values in the process. In the *fast mode*, which is the one that was used for the observations, a whole rotation through the 16 positions of 22.5° takes 8 seconds, while in the *slow mode* it takes 80 seconds.

MOPTOP also has available a series of filters, which include the B band (MOP-B, $\lambda = 3800 - 5200$ Å), the V band (MOP-V, $\lambda = 4900 - 5700$ Å), the R band (MOP-R: $\lambda = 5800 - 6950$ Å) and others like the optical broadband L (MOP-L) or near-infrared I band (MOP-I). For the observations in this work, only the optical B, V and R bands were observed.

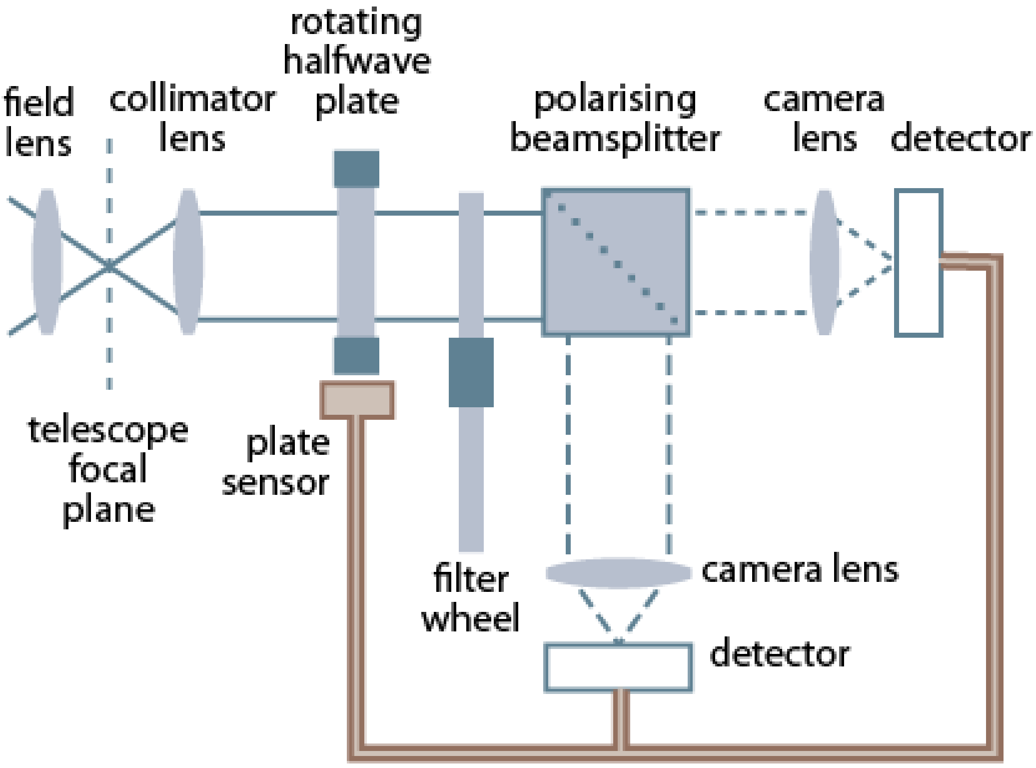

Figure 3.1: A diagram that shows how MOPTOP works. Available in the LT website, made by John Marchant.

3.3 Observations

3.3.1 Nights of observations

Two sets of polarimetric observations were taken with the MOPTOP polarimeter: The first one between the 22 and the 24 of August 2022, and the second one between the 3 and 17 of October 2022. The stars observed were the same introduced in Section 2.3.1, with all 58 observed in August and 57 (all except CD-2711872) observed in October.

Because the stars in the sample are very close, they are also very bright, with apparent magnitudes in the range of $V = 4.04$ and $V = 10.60$ (Steele et al., 1999). For this reason, if the brightest objects are observed directly, the observations are instantly saturated. To avoid this, the telescope was defocussed, with different values depending on how bright the stars are, spreading the light without saturating the detector. To avoid saturation as much as possible, the MOPTOP fast-rotation mode was selected. The values used for the defocussing are shown in Table 3.1.

Table 3.1: The values given for the defocus of the telescope when using MOPTOP for the different sources, depending on their apparent magnitude V.

V	Defocus (mm)
$m > 9.75$	0.0
$9.75 > m > 6.75$	1.0
$6.75 > m > 4.9$	2.0
$4.9 > m > 4.04$	2.5

Table 3.2: The values given for the radii of the observed sources depending on the defocus previously selected.

Defocus (mm)	Radius (pixels)
0.0	10
1.0	30
2.0	50
2.5	85

3.3.2 Data processing

The fast mode of MOPTOP was used to take all the observations. The obtained measurements include, as explained before, 16 photometric observations on different polarization angles with each of the two cameras.

The reduction of the MOPTOP data was carried out using aperture photometry routines from ASTROPY (Astropy Collaboration et al., 2022): the *CircularAperture* class of the *photutils* package was used to count the photons around the central position of the observed source. Depending on the defocus selected for that source, a bigger circle was selected. The values used for the radii of the different sources, depending on their defocus, are shown in Table 3.2.

After this, 4 sky positions without objects were selected around the source, and this process was repeated to obtain the value of the sky in those positions. After that, the average of those 4 values was calculated to obtain the average value of the sky around the observed star, and the value of this average sky was subtracted from the photometric counts in the object, leaving only the counts related to the object, without any extra sky background values. This process was repeated for all 16 observations with each camera, for all 3 group of observations in the filters B, V and R, for each object.

The extracted photometric counts were converted to Stokes q and u values following the procedure for the two camera observations outlined in Shrestha et al. (2020). Once these values were obtained, corrections for instrumental polarization were subtracted using the calibration values presented in Steele et al. (2023) and the formulae in Equation 3.4, depending on the parameter corrected and the photometric band. These values can be found in Table 3.3.

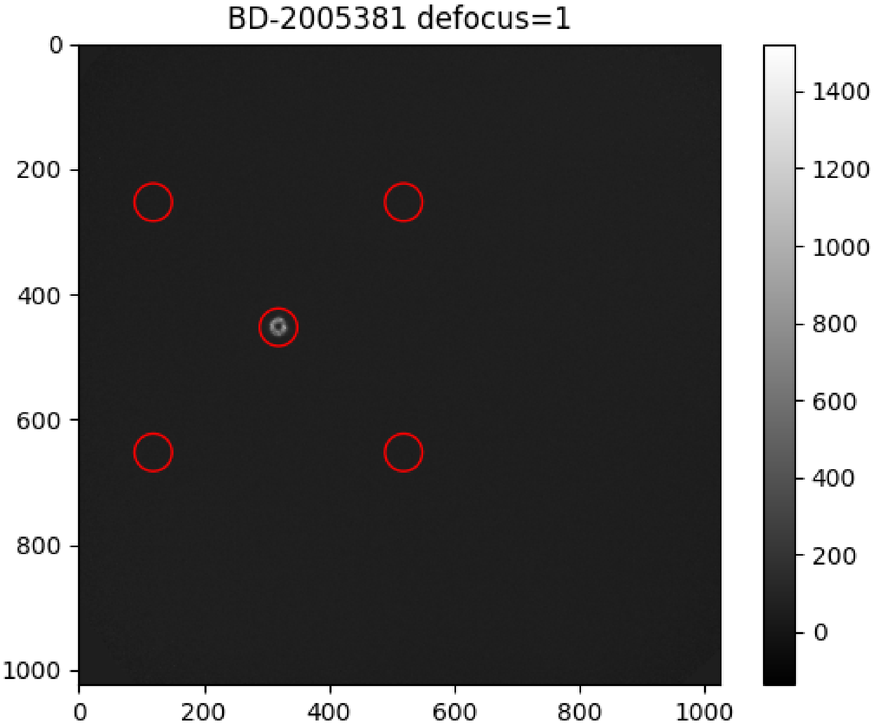

FIGURE 3.2: An image showing how the data reduction was calculated.

TABLE 3.3: The values of the correction values, for each of the parameters.

Parameter	B	V	R
q_0	0.001241	0.005554	0.010727
u_0	−0.011908	−0.023266	−0.030828
p_0	0.86	0.87	0.91
K_0	124.67	122.80	124.11

$$\begin{aligned} q_{\mathrm{f}} &= q - q_0 \\ u_{\mathrm{f}} &= u - u_0 \\ p_{\mathrm{f}} &= p/p_0 \\ \theta_{\mathrm{f}} &= \theta + K_0 + \mathrm{skyrot} \end{aligned} \tag{3.4}$$

After finishing this step, the polarization degrees and angles for the three bands for each of the observations have been obtained. From now on, the final polarization degree will be referred as P and the final polarization angle as θ. These results can be found in Tables 3.4 and 3.5 for the ones corresponding to August 2022 and Tables 3.6 and 3.7 for the ones corresponding to October 2022.

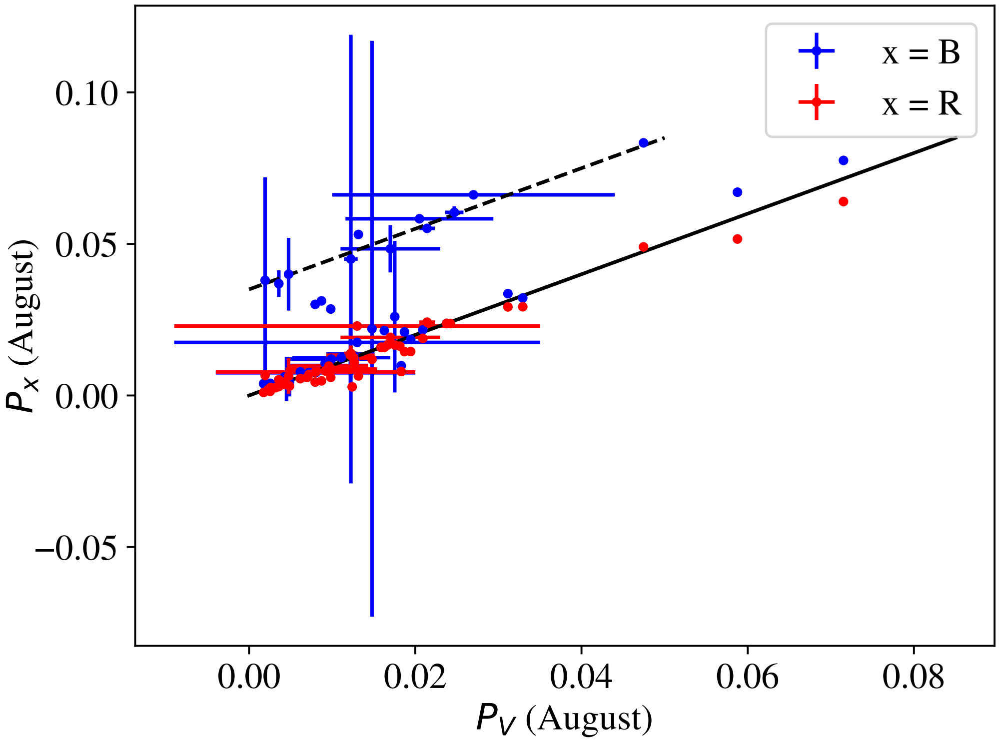

FIGURE 3.3: The polarization degree of V vs B and R for the August 2022 observations. It is possible to see that while the V and R bands show some agreement, part of the B band, represented by the dashed black line, shows a clear excess of 3.5% when compared with the 1:1 black line. The points with a $\sigma(P) > 0.1$ have not been represented in this plot.

3.4 Results: polarization

After finishing the extraction of the values of polarization degree and angle for all of the observations, the values were examined.

3.4.1 The August 2022 data

The values of the V and the R bands are very similar for the polarization degree and angle, as is shown in Figures 3.3 and 3.4. However, some of the observations showed an unexpected excess in the B band. The origin for this excess is still unknown, and it was not observed on the next observations. For that reason, all the August observations except 1 were discarded in our future analysis.

The values for CD-2711872 showed some good agreement between the bands, and they were accepted to be included between the final results.

Table 3.4: The list of objects, with the calculated polarization degrees for each BVR band, and the weighted polarization average of them, for the Aug 2022 observations. The errors quoted in this table have been calculated only from photon counting statistics and do not include the MOPTOP systematic errors of ~ 0.002. Because the error from the calculations is smaller than the systematic error, the final value of the error for the average polarization degree is $\sigma(\bar{P}) = 0.002$.

Object	P_{V}	$\sigma(P_{\mathrm{V}})$	P_{B}	$\sigma(P_{\mathrm{B}})$	P_{R}	$\sigma(P_{\mathrm{R}})$
CD-2814778	0.0163	0.0001	0.0214	0.0003	0.01590	$8 \cdot 10^{-5}$
CD-2716010	0.0017511	$9 \cdot 10^{-7}$	0.00391	$2 \cdot 10^{-5}$	0.0010046	$3 \cdot 10^{-7}$
CD-2711872	0.07152	$3 \cdot 10^{-5}$	0.07755	$6 \cdot 10^{-5}$	0.06398	$2 \cdot 10^{-5}$
CD-2512642	0.00810	$1 \cdot 10^{-5}$	0.00810	$1 \cdot 10^{-5}$	0.00810	$1 \cdot 10^{-5}$
CD-2213183	0.01266	$4 \cdot 10^{-5}$	0.0119	0.0001	0.01095	$1 \cdot 10^{-5}$
BD-2005381	0.01831	$4 \cdot 10^{-5}$	0.0098	0.0001	0.00792	$2 \cdot 10^{-5}$
BD-1905036	0.03114	$3 \cdot 10^{-5}$	0.034	0.001	0.02924	$2 \cdot 10^{-5}$
BD-1205132	0.0588	0.0001	0.0671	0.0003	0.05162	$5 \cdot 10^{-5}$
BD-0205328	0.00429	$9 \cdot 10^{-5}$	0.00618	$5 \cdot 10^{-5}$	0.00450	$2 \cdot 10^{-5}$
BD-0103834	0.010	0.006	0.0120	0.0004	0.0087	0.0006
BD-0003543	0.002255	$9 \cdot 10^{-6}$	0.0037	0.0005	0.001849	$4 \cdot 10^{-6}$
BD+0203815	0.00451	$1 \cdot 10^{-5}$	0.005	0.007	0.003594	$4 \cdot 10^{-6}$
BD+0503704	0.00916	$9 \cdot 10^{-5}$	0.011	0.002	0.00810	$1 \cdot 10^{-5}$
BD+1704087	0.01590	$8 \cdot 10^{-5}$	0.01590	$8 \cdot 10^{-5}$	0.01590	$8 \cdot 10^{-5}$
BD+1900578	0.018698	$4 \cdot 10^{-6}$	0.0210	0.0001	0.014497	$2 \cdot 10^{-6}$
BD+2004449	0.00697	$3 \cdot 10^{-5}$	0.0070	0.0001	0.00597	$1 \cdot 10^{-5}$
BD+2104695	0.003555	$2 \cdot 10^{-6}$	0.0051	0.0001	0.0029222	$5 \cdot 10^{-7}$
BD+2301148	0.0167	0.0002	0.0167	0.0002	0.0167	0.0002
BD+2504083	0.02090	$8 \cdot 10^{-5}$	0.0216	0.0002	0.01883	$4 \cdot 10^{-5}$
BD+2700797	0.005	0.005	0.04	0.30	0.01	0.12
BD+2700850	0.0175	0.0003	0.03	0.03	0.0167	0.0002
BD+2703411	0.012409	$2 \cdot 10^{-6}$	0.01315	$4 \cdot 10^{-5}$	0.002869	$1 \cdot 10^{-6}$
BD+2803598	0.0329	0.0003	0.0322	0.0005	0.0293	0.0004
BD+2903842	0.012	0.003	0.01	0.01	0.0133	0.0005
BD+2904453	0.01	0.01	0.0075	0.0006	0.0077	0.0001
BD+3003227	0.01	0.02	0.0175	0.0002	0.02292	$1 \cdot 10^{-5}$
BD+3104018	0.013	0.002	0.0131	0.0005	0.012	0.002
BD+3603946	0.01590	$8 \cdot 10^{-5}$	0.01590	$8 \cdot 10^{-5}$	0.01590	$8 \cdot 10^{-5}$
BD+3700675	0.00983	$1 \cdot 10^{-5}$	0.0285	0.0002	0.005979	$6 \cdot 10^{-6}$
BD+3703856	0.011	0.006	0.012	0.002	0.01	0.12
BD+4001213	0.0019	0.0001	0.04	0.03	0.00667	$1 \cdot 10^{-5}$
BD+4201376	0.0048	0.0006	0.04	0.01	0.006	0.006
BD+4204538	0.010	0.005	0.010	0.001	0.0097	0.0006
BD+4301048	0.0122	0.0008	0.04	0.07	0.014	0.003
BD+4500933	0.017	0.006	0.048	0.008	0.0192	0.0003
BD+4503879	0.00487	$6 \cdot 10^{-5}$	0.004	0.005	0.00312	$1 \cdot 10^{-5}$
BD+4600275	0.003170	$4 \cdot 10^{-6}$	0.03	0.15	0.002572	$1 \cdot 10^{-6}$
BD+4700183	0.00268	$4 \cdot 10^{-5}$	0.04	0.33	0.002524	$4 \cdot 10^{-6}$
BD+4700857	0.019444	$2 \cdot 10^{-6}$	0.0185	0.0008	0.0145115	$9 \cdot 10^{-7}$
BD+4700939	0.0087	0.0001	0.03121	$2 \cdot 10^{-5}$	0.004825	$5 \cdot 10^{-6}$
BD+4703985	0.004119	$1 \cdot 10^{-6}$	0.0053	0.0003	0.0036372	$4 \cdot 10^{-7}$
BD+4900614	0.0036	0.0001	0.037	0.004	0.00519	$2 \cdot 10^{-5}$
BD+5000825	0.00796	$1 \cdot 10^{-5}$	0.0301	0.0003	0.004423	$6 \cdot 10^{-6}$
BD+5003430	0.01479	$3 \cdot 10^{-5}$	0.022	0.095	0.01193	$2 \cdot 10^{-5}$
BD+5103091	0.007224	$7 \cdot 10^{-6}$	0.00761	$2 \cdot 10^{-5}$	0.006935	$3 \cdot 10^{-6}$
BD+5302599	0.00617	$4 \cdot 10^{-5}$	0.0078	0.0001	0.00556	$2 \cdot 10^{-5}$
BD+5500552	0.0132	$1 \cdot 10^{-4}$	0.0531	0.0008	0.00647	$4 \cdot 10^{-5}$
BD+5500605	0.020	0.009	0.058	0.002	0.03	0.12
BD+5502411	0.002548	$4 \cdot 10^{-6}$	0.0040	0.0002	0.001386	$1 \cdot 10^{-6}$
BD+5600473	0.002572	$1 \cdot 10^{-6}$	0.002572	$1 \cdot 10^{-6}$	0.002572	$1 \cdot 10^{-6}$
BD+5600478	0.0214	0.0009	0.0551	0.0003	0.0242	0.0006
BD+5600484	0.0242	0.0004	0.06	0.16	0.0238	0.0005
BD+5600493	0.03	0.02	0.066	0.001	0.0	1.3
BD+5600511	0.002573	$1 \cdot 10^{-6}$	0.002573	$1 \cdot 10^{-6}$	0.002573	$1 \cdot 10^{-6}$
BD+5600573	0.0238	0.0005	0.0238	0.0005	0.0238	0.0005
BD+5700681	0.0475	0.0002	0.0834	0.0003	0.0490	0.0005
BD+5800554	0.025	0.001	0.060	0.002	0.03	0.10
BD+5802320	0.0181	0.0002	0.01	0.12	0.0163	$1 \cdot 10^{-4}$

Table 3.5: The list of objects, with the calculated polarization angles for each BVR band, and the weighted polarization angle average of them, for the Aug 2022 observations. The angle values are between 0 and 180°. The errors quoted in this table have been calculated only from photon counting statistics and do not include the MOPTOP systematic errors of $\sim 1^\circ$. Because the error from the calculations is smaller than the systematic error, the final value of the error for the average polarization degree is $\sigma(\bar{\theta}) = 1^\circ$.

Object	θ_V (°)	$\sigma(\theta_\mathrm{V})$ (°)	θ_B (°)	$\sigma(\theta_\mathrm{B})$ (°)	θ_R (°)	$\sigma(\theta_\mathrm{R})$ (°)
CD-2814778	175	1	171	5	172.3	0.4
CD-2716010	193.70	0.03	180.5	0.3	183.08	0.03
CD-2711872	169.86	0.01	170.67	0.03	170.052	0.008
CD-2512642	230.54	0.04	230.54	0.04	230.54	0.04
CD-2213183	157.6	0.1	158.8	0.4	150.00	0.02
BD-2005381	166.2	0.3	156	1	167	1
BD-1905036	188.5	0.2	187	5	190.15	0.08
BD-1205132	151.09	0.05	150.7	0.1	146.65	0.02
BD-0205328	270	1	270	1	277.8	0.2
BD-0103834	261	22	264	2	260	3
BD-0003543	204.3	0.2	187	13	174.6	0.4
BD+0203815	182.1	0.2	177	15	172.48	0.05
BD+0503704	225.9	0.2	228.9	0.7	230.54	0.04
BD+1704087	172.3	0.4	172.3	0.4	172.3	0.4
BD+1900578	99.227	0.002	202.5	0.2	98.974	0.001
BD+2004449	180.5	0.1	180	2	173.87	0.03
BD+2104695	182.8946	0.006	199	3	189.776	0.002
BD+2301148	110.1	0.7	110.1	0.7	110.1	0.7
BD+2504083	155.2	0.5	156	2	151.7	0.1
BD+2700797	159	133	187	195	193	1027
BD+2700850	107.1	0.7	179	17	110.1	0.7
BD+2703411	180.826	0.003	178.18	0.08	133.44	0.04
BD+2803598	220.4	0.3	225.6	0.5	218.2	0.6
BD+2903842	270	4	267	8	269.1	0.9
BD+2904453	34	43	33	5	38.2	0.4
BD+3003227	179	76	173.4	0.2	67.361	0.003
BD+3104018	70	4	70	1	74	9
BD+3603946	172.3	0.4	172.3	0.4	172.3	0.4
BD+3700675	52.04	0.02	145.1	0.1	60.74	0.03
BD+3703856	313	46	262	86	314	2976
BD+4001213	150	2	165	17	150.66	0.01
BD+4201376	148	64	170	7	178	62
BD+4204538	77	19	75	1	81	3
BD+4301048	138	7	164	59	179	52
BD+4500933	125	9	144	2	127.4	0.3
BD+4503879	23	2	34	87	28	0.7
BD+4600275	189.00	0.08	89	64	47.04	0.03
BD+4700183	316.5	0.4	79	177	82.38	0.09
BD+4700857	44.870	0.001	136	1	48.186	0.001
BD+4700939	36.86	0.08	152.41	0.01	29.25	0.02
BD+4703985	68.544	0.005	86	8	74.943	0.001
BD+4900614	56	11	105	2	77.5	0.1
BD+5000825	42.75	0.03	135.4	0.2	51.35	0.06
BD+5003430	248.74	0.03	342	106	255.24	0.04
BD+5103091	26.11	0.05	21.6	0.3	20.81	0.02
BD+5302599	34	1	29	4	29.8	0.3
BD+5500552	14.09	0.09	107.9	0.3	19.9	0.3
BD+5500605	118	18	112.6	0.6	112	85
BD+5502411	49.6	0.3	179	9	50.42	0.03
BD+5600473	47.04	0.03	47.04	0.03	47.04	0.03
BD+5600478	115	2	111.7	0.1	112.1	0.6
BD+5600484	130	3	115	173	128	3
BD+5600493	119	51	114.1	0.4	113	1127
BD+5600511	47.04	0.03	47.04	0.03	47.04	0.03
BD+5600573	128	3	128	3	128	3
BD+5700681	123.0	0.1	121.23	0.09	122.9	0.4
BD+5800554	108.3	0.3	114.0	0.4	107	19
BD+5802320	45	1	49	324	48.7	0.4

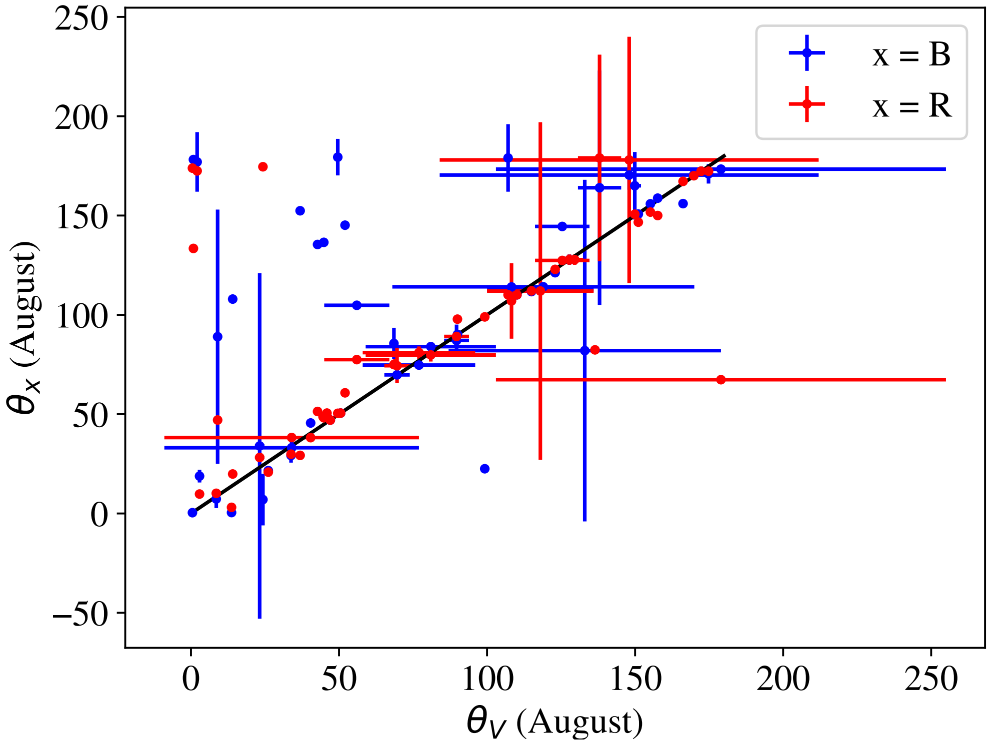

FIGURE 3.4: The polarization angle of V vs B and R for the August 2022 observations. Same as with the polarization degree in Figure 3.3, the V and R bands show a good agreement, while some of the B band observations show an excess in the angle when compared with the 1:1 black line. The points with a $\sigma(\theta) > 100°$ have not been represented in this plot.

3.4.2 The October 2022 data

From the sample of 58 objects, only 57 were available for observation in October: CD-2711872 was not possible to be observed at the time. For that reason, it was decided to add the August observations on this object on future tables, for completion of the sample. For the rest of the objects, the values of the polarization degree and angle in the B, V and R bands show some general good agreement; this time with no excess, as is shown in Figures 3.5 and 3.6. For that reason, these values are the ones that were decided to be used for the rest of our calculations, as the values for the V and R band show a small excess in the August data set when compared with the October data set, as is shown in Figure 3.7.

3.4.3 Calculation of the average polarization degree and angle

In the previous section the polarization degree (P) and angle (θ) values for the bands V, B and R were derived. However, as most of the values used to compare with our

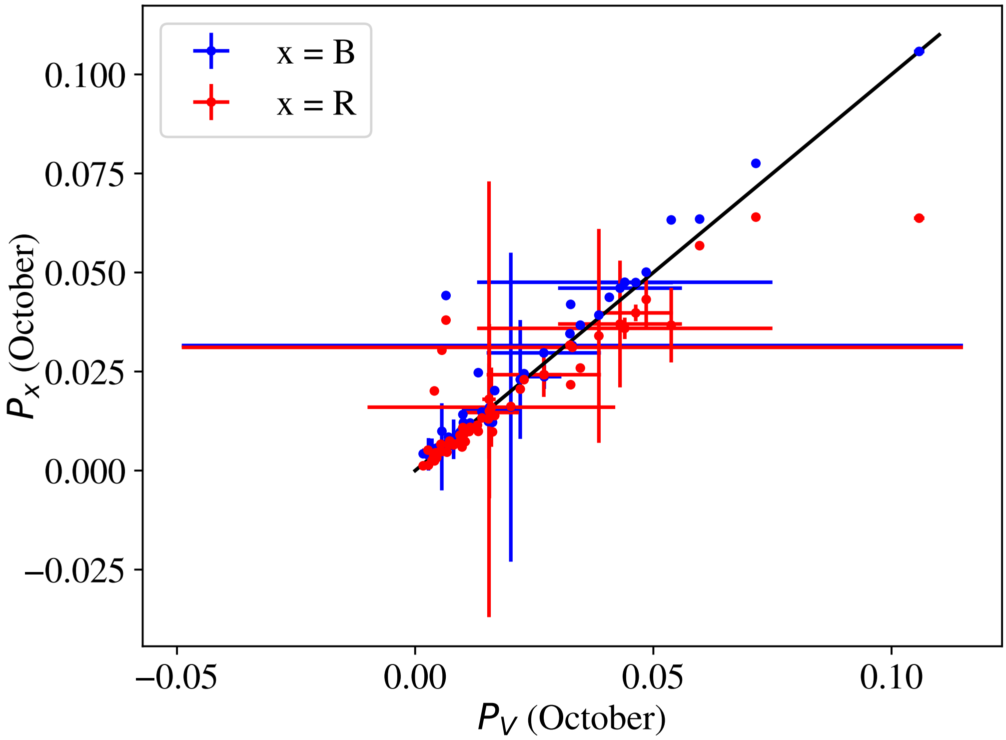

FIGURE 3.5: The polarization degree of V vs B and R for the October 2022 observations. The V band shows very similar values to the B and R bands, as is easy to see when compared with the 1:1 black line. The points with a $\sigma(P) > 0.1$ have not been represented in this plot.

polarization values (Section 3.5) are full-range/white-light instead of individual bands, the individual polarization degree and angle values for each band were converted to q and u values again, the averages $\bar{q}$ and $\bar{u}$ were obtained from those values, and from them the average polarization degree $\bar{p}$ and average polarization angle $\bar{\theta}$ were derived. It is worth mentioning that these values could not be calculated before finishing all the observational corrections, as some were required directly over the polarization degrees and angles.

It is also necessary to mention here that MOPTOP polarimetry suffers from systematic errors of ~ 0.002 in P and 1° in θ (Shrestha et al., 2020). These systematic errors are not included in the values presented in Tables 3.6 and 3.7 but are incorporated into the final interstellar corrected values calculated in Section 3.4.4.

3.4.4 Separation of the interstellar and intrinsic polarization

To separate the values of interstellar polarization from the total polarization, a selection of stars from the 9286 object catalogue (Heiles, 2000) that can be found within an angular

Table 3.6: The list of objects, with the calculated polarization degrees for each BVR band, and the weighted polarization average of them, for the Oct 2022 observations. The errors quoted in this table have been calculated only from photon counting statistics and do not include the MOPTOP systematic errors of ~ 0.002. Because the error from the calculations is smaller than the systematic error, the final value of the error for the average polarization degree is $\sigma(\bar{P}) = 0.002$. Final polarization measurements incorporating the systematic error and the effect of interstellar polarization are given in Table 3.8.

Object	P_{V}	$\sigma(P_{\mathrm{V}})$	P_{B}	$\sigma(P_{\mathrm{B}})$	P_{R}	$\sigma(P_{\mathrm{R}})$	$\bar{P}$
CD-28 14778	0.03467	$6 \cdot 10^{-5}$	0.0367	0.0001	0.02589	$3 \cdot 10^{-5}$	0.032
CD-27 11872	0.07152	$3 \cdot 10^{-5}$	0.07755	$6 \cdot 10^{-5}$	0.06398	$2 \cdot 10^{-5}$	0.071
CD-27 16010	0.0035203	$8 \cdot 10^{-7}$	0.005	0.003	0.0025063	$3 \cdot 10^{-7}$	0.004
CD-25 12642	0.03264	$5 \cdot 10^{-5}$	0.0420	0.0001	0.02167	$3 \cdot 10^{-5}$	0.032
CD-22 13183	0.010014	$9 \cdot 10^{-6}$	0.0142	0.0002	0.01086	$2 \cdot 10^{-5}$	0.012
BD-20 5381	0.0162	0.0001	0.0122	0.0004	0.00977	$3 \cdot 10^{-5}$	0.013
BD-19 5036	0.006470	$2 \cdot 10^{-6}$	0.0442	$4 \cdot 10^{-5}$	0.03798	$1 \cdot 10^{-5}$	0.029
BD-12 5132	0.106	0.001	0.106	0.001	0.064	0.001	0.091
BD-02 5328	0.003889	$3 \cdot 10^{-6}$	0.0046	0.0003	0.0036205	$9 \cdot 10^{-07}$	0.004
BD-01 3834	0.003	0.001	0.0040	0.0003	0.00516	$6 \cdot 10^{-5}$	0.004
BD-00 3543	0.008073	$6 \cdot 10^{-6}$	0.008	0.005	0.006470	$2 \cdot 10^{-6}$	0.007
BD+02 3815	0.010120	$8 \cdot 10^{-6}$	0.01210	$2 \cdot 10^{-5}$	0.007586	$3 \cdot 10^{-6}$	0.010
BD+05 3704	0.005612	$1 \cdot 10^{-6}$	0.009922	$8 \cdot 10^{-6}$	0.030378	$6 \cdot 10^{-6}$	0.014
BD+17 4087	0.0221	0.0003	0.02	0.02	0.0206	0.0002	0.022
BD+19 578	0.004838	$1 \cdot 10^{-6}$	0.0055	0.0001	0.0046032	$7 \cdot 10^{-7}$	0.005
BD+20 4449	0.01052	$2 \cdot 10^{-5}$	0.01025	$8 \cdot 10^{-5}$	0.007306	$9 \cdot 10^{-6}$	0.009
BD+21 4695	0.002800	$3 \cdot 10^{-6}$	0.004	0.004	0.001353	$1 \cdot 10^{-6}$	0.002
BD+23 1148	0.03	0.08	0.0316	0.0003	0.0311	0.0009	0.032
BD+25 4083	0.016	0.001	0.02	0.01	0.02	0.06	0.016
BD+27 797	0.02	0.03	-	-	0.02	0.01	0.017
BD+27 850	0.0099	0.0001	0.010	0.001	0.00595	$5 \cdot 10^{-5}$	0.009
BD+27 3411	0.0040326	$7 \cdot 10^{-7}$	0.005223	$2 \cdot 10^{-6}$	0.020104	$1 \cdot 10^{-6}$	0.010
BD+28 3598	0.0538	0.0002	0.0633	0.0003	0.037	0.009	0.051
BD+29 3842	0.0167	0.0001	0.0202	0.0004	0.01389	$5 \cdot 10^{-5}$	0.017
BD+29 4453	0.01030	$3 \cdot 10^{-5}$	0.0104	0.0002	0.00929	$1 \cdot 10^{-5}$	0.010
BD+30 3227	0.01325	$1 \cdot 10^{-5}$	0.0247	0.0004	0.009893	$7 \cdot 10^{-6}$	0.016
BD+31 4018	0.0140	0.0009	0.01481	$4 \cdot 10^{-5}$	0.01329	$2 \cdot 10^{-5}$	0.014
BD+36 3946	0.00725	$5 \cdot 10^{-5}$	0.0062	0.0002	0.00746	$1 \cdot 10^{-5}$	0.007
BD+37 675	0.00427	$2 \cdot 10^{-5}$	0.00553	$4 \cdot 10^{-5}$	0.004496	$6 \cdot 10^{-6}$	0.005
BD+37 3856	0.0154	0.0001	0.0124	0.0005	0.01304	$7 \cdot 10^{-5}$	0.014
BD+40 1213	0.016	0.006	0.015	0.002	0.0146	0.0002	0.015
BD+42 1376	0.0156	0.0002	0.02	0.01	0.02	0.02	0.015
BD+42 4538	0.00922	$3 \cdot 10^{-5}$	0.0093	0.0003	0.00704	$2 \cdot 10^{-5}$	0.008
BD+43 1048	0.027	0.004	0.024	0.003	0.024	0.002	0.025
BD+45 933	0.0229	0.0001	0.02446	$8 \cdot 10^{-5}$	0.0230	0.0002	0.023
BD+45 3879	0.00539	$3 \cdot 10^{-5}$	0.0064	0.0002	0.00665	$1 \cdot 10^{-5}$	0.006
BD+46 275	0.009412	$1 \cdot 10^{-6}$	0.00966	$3 \cdot 10^{-5}$	0.0089211	$6 \cdot 10^{-7}$	0.009
BD+47 183	0.011340	$1 \cdot 10^{-6}$	0.010746	$3 \cdot 10^{-6}$	0.0098539	$7 \cdot 10^{-7}$	0.011
BD+47 857	0.0045151	$4 \cdot 10^{-7}$	0.00568	$3 \cdot 10^{-5}$	0.0032336	$1 \cdot 10^{-7}$	0.002
BD+47 939	0.0115475	$3 \cdot 10^{-7}$	0.0120	0.0002	0.0109207	$1 \cdot 10^{-7}$	0.011
BD+47 3985	0.004066	$2 \cdot 10^{-6}$	0.004237	$5 \cdot 10^{-6}$	0.0024482	$8 \cdot 10^{-7}$	0.004
BD+49 614	0.01308	$5 \cdot 10^{-5}$	0.01	0.14	0.01148	$2 \cdot 10^{-5}$	0.012
BD+50 825	0.006995	$2 \cdot 10^{-6}$	0.00843	$4 \cdot 10^{-5}$	0.006553	$1 \cdot 10^{-6}$	0.007
BD+50 3430	0.00559	$1 \cdot 10^{-5}$	0.01	0.01	0.004803	$4 \cdot 10^{-6}$	0.005
BD+51 3091	0.007973	$6 \cdot 10^{-6}$	0.00772	$2 \cdot 10^{-5}$	0.006755	$3 \cdot 10^{-6}$	0.007
BD+53 2599	0.00668	$4 \cdot 10^{-5}$	0.007	0.002	0.00465	$2 \cdot 10^{-5}$	0.006
BD+55 552	0.03	0.01	0.0297	0.0004	0.02	0.01	0.027
BD+55 605	0.04	0.01	0.0460	0.0006	0.04	0.02	0.042
BD+55 2411	0.001685	$6 \cdot 10^{-6}$	0.00424	$4 \cdot 10^{-5}$	0.001212	$2 \cdot 10^{-6}$	0.002
BD+56 473	0.0485	0.0006	0.0501	0.0002	0.043	0.008	0.047
BD+56 478	0.0386	0.0007	0.0392	0.0002	0.03	0.03	0.037
BD+56 484	-	-	0.0417	0.0006	0.0327	0.0006	0.037
BD+56 493	0.046	0.008	0.0475	0.0005	0.040	0.002	0.044
BD+56 511	0.041	0.001	0.0437	0.0003	0.04	0.14	0.041
BD+56 573	0.04	0.03	0.0475	0.0006	0.036	0.003	0.042
BD+57 681	0.05971	$2 \cdot 10^{-5}$	0.06348	$6 \cdot 10^{-5}$	0.05678	$1 \cdot 10^{-5}$	0.060
BD+58 554	0.0325	0.0002	0.0346	0.0002	0.032	0.001	0.033
BD+58 2320	0.0201	0.0007	0.02	0.04	0.0162	0.0002	0.017

Table 3.7: The list of objects, with the calculated polarization angles for each BVR band, and the weighted polarization angle average of them, for the Oct 2022 observations. The angle values are between 0 and 180°. The errors quoted in this table have been calculated only from photon counting statistics and do not include the MOPTOP systematic errors of $\sim 1^\circ$. Because the error from the calculations is smaller than the systematic error, the final value of the error for the average polarization degree is $\sigma(\bar{\theta}) = 1^\circ$. Final polarization measurements incorporating the systematic error and the effect of interstellar polarization are given in Table 3.8.

Object	$\theta_{\rm V}$ (°)	$\sigma(\theta_{\rm V})$ (°)	$\theta_{\rm B}$ (°)	$\sigma(\theta_{\rm B})$ (°)	$\theta_{\rm R}$ (°)	$\sigma(\theta_{\rm R})$ (°)	$\bar{\theta}$ (°)
CD-28 14778	184.97	0.04	184.93	0.07	181.62	0.02	4
CD-27 11872	169.86	0.01	170.67	0.03	170.052	0.009	170
CD-27 16010	172.87	0.05	164	7	172.89	0.02	169
CD-25 12642	191.84	0.03	193.46	0.05	196.29	0.03	14
CD-22 13183	174.011	0.005	179.9	0.1	169.74	0.04	175
BD-20 5381	182.2	0.2	177.2	0.6	177.41	0.06	179
BD-19 5036	176.200	0.003	190.06	0.02	191.528	0.007	10
BD-12 5132	169.07	0.03	169.07	0.02	162.5	0.1	168
BD-02 5328	257.16	0.02	284	53	268.998	0.002	91
BD-01 3834	268	191	163	18	260.9	0.4	80
BD-00 3543	185.47	0.02	186	3	176.200	0.003	3
BD+02 3815	179.84	0.03	180.23	0.08	178.28	0.01	0
BD+05 3704	281.803	0.003	286.00	0.01	218.018	0.005	30
BD+17 4087	186	3	189	1231	188	5	8
BD+19 578	259.407	0.004	275	2	265.906	0.002	87
BD+20 4449	190.21	0.08	191.0	0.4	188.05	0.02	10
BD+21 4695	157.5	0.3	134	47	149.57	0.09	155
BD+23 1148	162	62	164.8	0.2	164.0	0.5	164
BD+25 4083	345	3	259	27	343	63	166
BD+27 797	187	25	-	-	189	17	8
BD+27 850	147.1	0.9	155	4	142.1	0.4	149
BD+27 3411	331.280	0.006	246.54	0.02	332.0686	0.0007	153
BD+28 3598	218.73	0.05	219.54	0.08	221	3	40
BD+29 3842	260.6	0.2	260.5	0.5	259.00	0.07	80
BD+29 4453	39.14	0.02	39.4	0.2	38.94	0.01	39
BD+30 3227	244.82	0.02	334.8	0.4	246.98	0.02	65
BD+31 4018	259.1	0.8	261.90	0.03	257.30	0.02	80
BD+36 3946	266	2	257	6	342.77	0.06	168
BD+37 675	144.2	0.3	149	2	148.33	0.05	147
BD+37 3856	307.5	0.2	306.0	0.8	307.6	0.1	127
BD+40 1213	162	5	166	2	166.9	0.4	165
BD+42 1376	172.6	0.4	176	19	176	51	175
BD+42 4538	81.7	0.2	92	1	83.0	0.1	86
BD+43 1048	356	1	90.7	0.4	178	2	88
BD+45 933	318.1	0.4	318.8	0.4	318	1	138
BD+45 3879	27.0	0.2	21.7	0.8	25.12	0.03	24
BD+46 275	85.205	0.002	91.30	0.02	90.0299	0.0009	89
BD+47 183	81.48	0.02	81.8	0.6	82.590	0.009	82
BD+47 857	38.778	0.001	54.9	0.3	47.7664	0.0004	64
BD+47 939	354.3414	0.0003	175.51	0.04	352.6755	0.0001	174
BD+47 3985	58.11	0.06	44.23	0.06	55.27	0.04	53
BD+49 614	102.87	0.03	106	25	103.123	0.007	104
BD+50 825	326.338	0.002	328.02	0.05	322.430	0.001	146
BD+50 3430	189.9	0.1	191	19	9.62	0.02	10
BD+51 3091	24.57	0.07	22.3	0.6	19.93	0.02	22
BD+53 2599	37.3	0.6	113	52	40.5	0.3	33
BD+55 552	110	9	114.3	0.4	110	3	112
BD+55 605	119	15	123.6	0.8	119	13	121
BD+55 2411	141.5	0.2	146.8	0.4	310.8	0.3	149
BD+56 473	108.0	0.1	110.50	0.05	109	1	109
BD+56 478	110.7	0.4	114.0	0.1	111	13	112
BD+56 484	-	-	126.8	0.9	123.6	0.7	124
BD+56 493	120	8	123.5	0.6	121	2	122
BD+56 511	111.8	0.4	115.8	0.1	113	36	114
BD+56 573	118	36	120.0	0.6	119	3	119
BD+57 681	307.438	0.002	309.860	0.005	307.1085	0.0005	128
BD+58 554	296.2	0.2	298.0	0.1	296.8	0.7	117
BD+58 2320	58	1	67	34	55.6	0.5	60

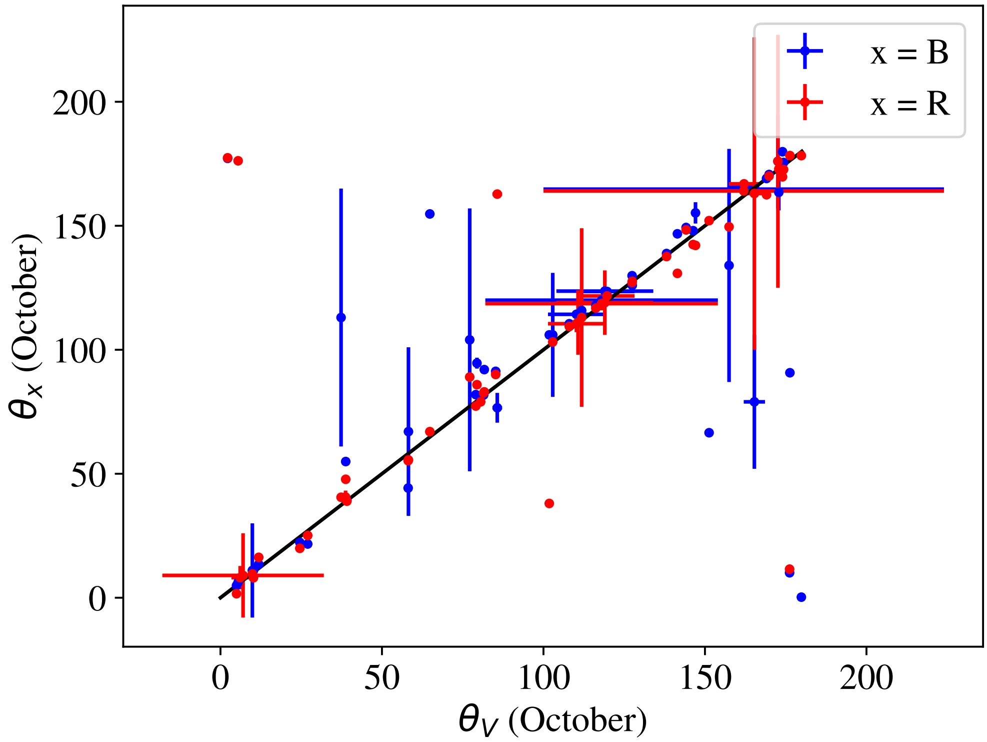

FIGURE 3.6: The polarization angle of V vs B and R for the October 2022 observations. The V bands shows very similar values to the B and R bands, with some marginal differences due to some values being very close but below 180°. The points with a $\sigma(\theta) > 100°$ have not been represented in this plot.

distance of 5° on the sky from each of our sample stars was chosen. The distances to these stars was found using the Gaia catalog. The Stokes parameters q and u were derived from the catalogue polarization degree and angle for these stars, then performed a linear fit to them to find the values of interstellar q and u with respect the distance. The q_{is} and u_{is} was estimated for our sample stars depending on their distance, using the previous linear fit, as shown in Figure 3.8. The errors for the interstellar polarization were derived from the values of the linear fit. The values of the interstellar q and u were subtracted for our sample stars from the total values of their Stokes parameters, obtaining the intrinsic values (q_{in} and u_{in}), and then calculated the values for both the interstellar and intrinsic polarization degree and angle as shown in Table 3.8.

TABLE 3.8: The calculated values for the interstellar and intrinsic polarization degrees and angles. The estimated systematic error from MOPTOP is $\sigma(\bar{P}) = 0.002$ and $\sigma(\bar{\theta}) = 1°$. The error of the interstellar polarization values has been obtained from the linear fit to nearby stars, while the error of the intrinsic polarization values has been obtained from the calculations of q_{in} and u_{in} and the following derivation of P_{in} and θ_{in}.

Object	$\bar{P}$	θ (°)	P_{is}	$\sigma(P_{\mathrm{is}})$	θ_{is} (°)	$\sigma(\theta_{\mathrm{is}})$ (°)	P_{in}	$\sigma(P_{\mathrm{in}})$	θ_{in} (°)	$\sigma(\theta_{\mathrm{in}})$ (°)
CD-28 14778	0.032	4	0.0063	0.0005	23.72	0.05	0.01	0.01	171	3
CD-27 11872	0.071	170	0.019	0.001	24.54	0.03	0.010	0.02	145.7	0.5
CD-27 16010	0.004	169	0.0195	0.0005	34.92	0.01	0.015	0.005	16.7	0.3
CD-25 12642	0.032	14	0.013	0.001	29.66	0.04	0.020	0.04	166	2
CD-22 13183	0.012	175	0.0277	0.0009	23.17	0.02	0.001	0.007	141.6	0.9
BD-20 5381	0.013	179	0.0079	0.0005	31.15	0.02	0.010	0.004	1	4
BD-19 5036	0.029	10	0.00072	0.00005	42.312	0.004	0.009	0.005	25.9	0.3
BD-12 5132	0.091	168	0.0044	0.0001	24.95	0.02	0.006	0.005	28.6	0.4
BD-02 5328	0.004	91	0.0069	0.0004	34.24	0.01	0.011	0.005	176	2
BD-01 3834	0.004	80	0.020	0.001	23.58	0.03	0.01	0.01	132.8	0.1
BD-00 3543	0.007	3	0.029	0.003	28.85	0.04	0.02	0.02	135.45	0.01
BD+02 3815	0.010	0	0.011	0.002	35.72	0.05	0.01	0.01	150.9	0.7
BD+05 3704	0.014	30	0.0065	0.0003	27.88	0.02	0.007	0.005	31.9	0.2
BD+17 4087	0.022	8	0.00094	0.00009	44.8314	0.0004	0.071	0.007	9.6	0.2
BD+19 578	0.005	87	0.00083	0.00007	44.7854	0.0004	0.032	0.006	13.3	0.3
BD+20 4449	0.009	10	0.002	0.002	20.6	0.7	0.014	0.006	25.6	0.2
BD+21 4695	0.002	155	0.001	0.002	27	1	0.001	0.005	34	1
BD+23 1148	0.032	164	0.032	0.002	35.26	0.01	0.029	0.005	41.04	0.02
BD+25 4083	0.016	166	0.0101	0.0005	19.86	0.04	0.004	0.004	78	1
BD+27 797	0.017	8	0.006	0.005	26.7	0.5	0.01	0.07	163	9
BD+27 850	0.009	149	0.004	0.001	5.1	0.8	0.01	0.01	178	23
BD+27 3411	0.010	153	0.007	0.001	7.9	0.4	0.00	0.09	107	32
BD+28 3598	0.051	40	0.030	0.002	12.86	0.06	0.01	0.02	114	1
BD+29 3842	0.017	80	0.0038	0.0002	3.9	0.2	0.00	0.01	26	5
BD+29 4453	0.010	39	0.001	0.002	30.4	0.8	0.004	0.006	8	4
BD+30 3227	0.016	65	0.0068	0.0005	21.78	0.05	0.00	0.01	125	1
BD+31 4018	0.014	80	0.039	0.006	20.5	0.1	0.003	0.008	86	10
BD+36 3946	0.007	168	0.052	0.004	20.11	0.06	0.021	0.006	81.8	0.5
BD+37 675	0.005	147	0.12	0.01	4.6	0.3	0.12	0.01	94.4	0.4
BD+37 3856	0.014	127	0.011	0.001	9.8	0.2	0.007	0.007	100	2
BD+40 1213	0.015	165	0.008	0.003	17.2	0.3	0.00	0.01	114	2
BD+42 1376	0.015	175	0.014	0.001	27.40	0.04	0.01	0.01	129.9	0.2
BD+42 4538	0.008	86	0.0043	0.0002	5.2	0.1	0.003	0.004	83	3
BD+43 1048	0.025	88	0.023	0.002	22.48	0.05	0.015	0.004	77.2	0.3
BD+45 933	0.023	138	0.042	0.002	20.75	0.03	0.015	0.005	71.4	0.3
BD+45 3879	0.006	24	0.0074	0.0006	3.6	0.3	0.007	0.004	68.7	0.4
BD+46 275	0.009	89	0.0021	0.0001	4.8	0.2	0.027	0.007	10.4	0.4
BD+47 183	0.011	82	0.0043	0.0003	36.82	0.01	0.01	0.04	158	5
BD+47 857	0.002	64	0.0050	0.0006	29.39	0.05	0.01	0.06	170	10
BD+47 939	0.011	174	0.007	0.001	29.36	0.07	0.004	0.004	54.0	0.2
BD+47 3985	0.004	53	0.0039	0.0008	5.1	0.6	0.007	0.008	10	2
BD+49 614	0.012	104	0.014	0.002	23.4	0.1	0.078	0.007	9.9	0.1
BD+50 825	0.007	146	0.041	0.003	20.41	0.05	0.012	0.006	68.3	0.3
BD+50 3430	0.005	10	0.005	0.001	13.5	0.2	0.004	0.004	79	1
BD+51 3091	0.007	22	0.0020	0.0003	20.91	0.09	0.003	0.004	49.9	0.2
BD+53 2599	0.006	33	0.023	0.002	17.83	0.07	0.010	0.006	11.7	0.9
BD+55 552	0.027	112	0.009	0.001	36.84	0.03	0.004	0.006	144.5	0.3
BD+55 605	0.042	121	0.0013	0.0002	28.49	0.06	0.031	0.006	3	1
BD+55 2411	0.002	149	0.0009	0.0001	20.29	0.07	0.001	0.006	29	2
BD+56 473	0.047	109	0.009	0.003	26.5	0.1	0.005	0.006	171	2
BD+56 478	0.037	112	0.0032	0.0002	10.90	0.06	0.005	0.005	46.85	0.04
BD+56 484	0.037	124	0.012	0.002	12.4	0.2	0.00	0.02	164	4
BD+56 493	0.044	122	0.0024	0.0004	15.0	0.1	0.003	0.005	45.66	0.02
BD+56 511	0.041	114	0.0026	0.0001	19.27	0.04	0.01	0.01	175	8
BD+56 573	0.042	119	0.047	0.003	20.12	0.05	0.009	0.005	90.0	0.9
BD+57 681	0.060	128	0.0106	0.0005	37.25	0.01	0.007	0.005	19.3	0.5
BD+58 554	0.033	117	0.0040	0.0004	28.60	0.04	0.009	0.005	176	3
BD+58 2320	0.017	60	0.016	0.001	25.66	0.03	0.038	0.004	45.843	0.002

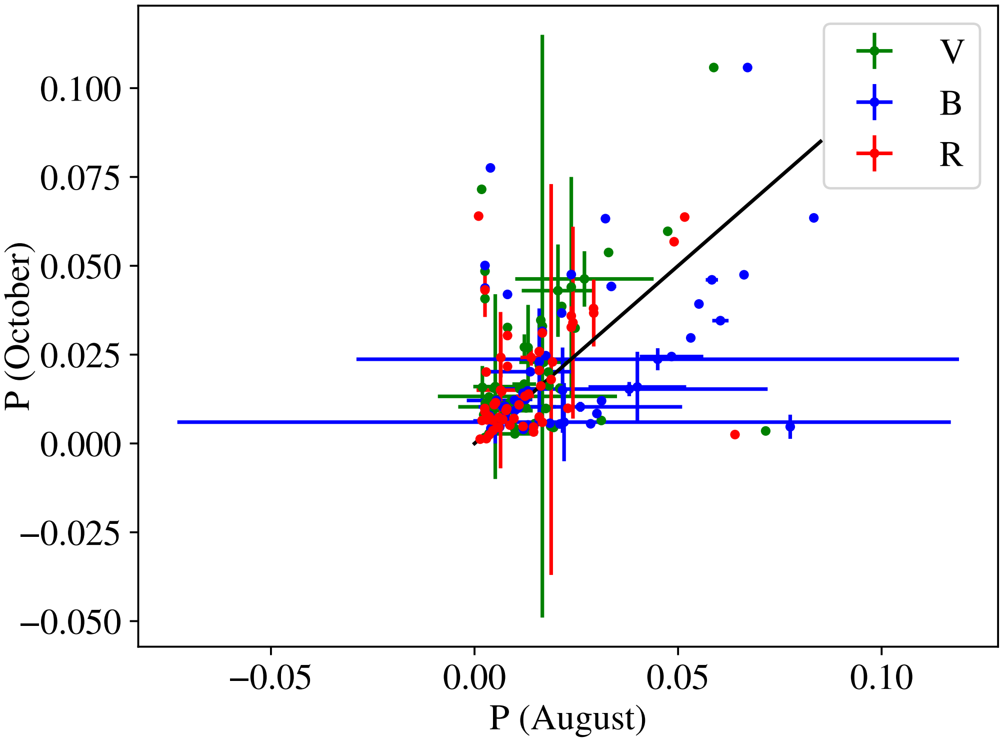

FIGURE 3.7: A comparison between the polarization degrees for the three bands between the August 2022 and October 2022 observations. The black 1:1 line is for comparison. It can be seen that the V and R bands show similar values between August and October, with a small excess for larger values, while there is a clear excess for the B band in the August observations. The points with a $\sigma(P) > 0.1$ have not been represented in this plot.

3.5 Analysis

3.5.1 Comparison of $\bar{P}$ and $\bar{\theta}$ with other authors

41 of the stars in the sample were measured for polarization previously by other authors, so it is possible to compare the 2022 values of $\bar{P}$ and $\bar{\theta}$ with those. The sources for these reference values are Hall (1958), Behr (1959a), Coyne & Gehrels (1967), Coyne & Kruszewski (1969), Serkowski (1968), Serkowski (1970), McLean & Clarke (1976), Coyne (1976), Poeckert & Marlborough (1976), McLean & Brown (1978) and Yudin (2001). These values have been reduced to 1950s, 1960s, 1970s and 2000s for simplicity, taking the average of all values where there is more than one.

In Table 3.9, the 2022 values are compared with the most studied Be stars from the sample, for a historical perspective, while in Table B.1 the entire sample is compared with the ones from Yudin (2001). It can be seen that the polarization degree changes with time, and while the polarization angle is mostly constant (Figure 3.9), there are a

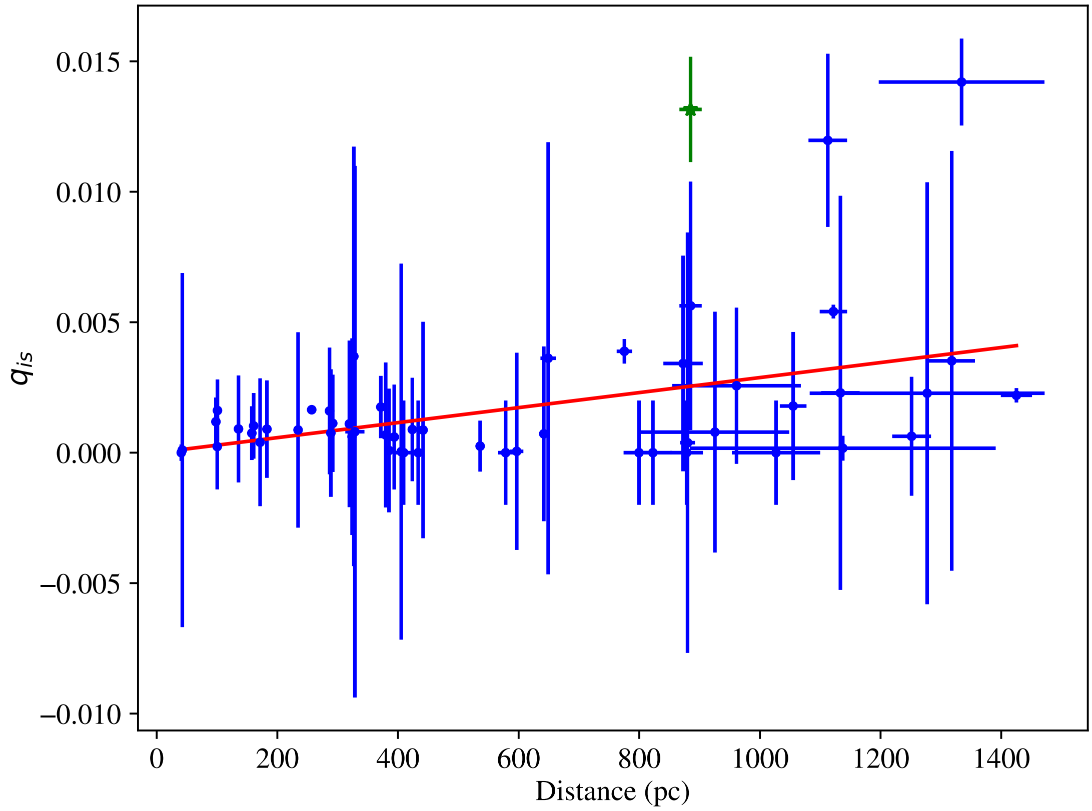

FIGURE 3.8: A plot showing the the polarization coefficient q of nearby stars, in blue, compared to the sample star BD+31 4018, in green. The red line is a linear fit to the data from the nearby stars, with the red line the estimated value of the interstellar polarization depending on the distance.

TABLE 3.9: The values $\bar{P}$ and $\bar{\theta}$ shown here are the weighted average of their years. For the 1950s, we have used the ones shown in Hall (1958) and Behr (1959a), for the 1960s we have used the ones shown in Coyne & Gehrels (1967), Coyne & Kruszewski (1969) and Serkowski (1968), for the 1970 we have used Serkowski (1970), McLean & Clarke (1976), Coyne (1976), Poeckert & Marlborough (1976) and McLean & Brown (1978), for 2001 we have used the ones shown in Yudin (2001), and for 2022 the values calculated in this work. In bold, the values for the polarization angles that have shown a difference bigger than 10° over the past 70 years.

Object	Other identifier	1950s		1960s		1970s		2001		2022		Peak
		$\bar{P}$ (%)	$\bar{\theta}$ (°)	$\bar{P}$ (%)	$\bar{\theta}$ (°)	$\bar{P}$ (%)	$\bar{\theta}$ (°)	$\bar{P}$(%)	$\bar{\theta}$ (°)	$\bar{P}$(%)	$\bar{\theta}$ (°)	
CD-27 11872	HD 161103	11.1	171	-	-	-	-	4.83	172	7.1	170	SP
CD-27 16010	HD 214748	-	-	-	-	1.75	163	0.09	155	0.4	169	DP
CD-25 12642	HD 164741	1.7	14	-	-	-	-	-	-	3.2	14	NP
CD-22 13183	HD 172252	1.7	178	-	-	-	-	4.65	148	1.2	175	SP
BD-20 5381	HD 177015	1.1	0	-	-	-	-	0.51	0	1.3	179	DP
BD-01 3834	HD 187350	1.7	82	-	-	-	-	0.78	82	0.4	80	SP
BD+05 3704	HD 168797	1.7	64	-	-	-	-	0.78	64	1.4	**30**	Change
BD+19 578	HD 23016	-	-	-	-	1.48	87	0.60	87	0.5	87	Change
BD+29 4453	HD 205618	2.7	26	-	-	-	-	1.24	26	1.0	**39**	SP
BD+30 3227	HD 171406	0.6	13	-	-	-	-	0.28	13	1.6	**65**	Change
BD+31 4018	HD 193009	1.4	75	-	-	-	-	0.65	75	1.4	80	SP
BD+40 1213	HD 33604	2.8	168	-	-	-	-	1.29	168	1.5	165	SP
BD+42 1376	HD 37657	3.6	174	-	-	-	-	1.66	174	1.5	175	Change
BD+46 275	HD 6811	2.08	90	-	-	8.75	94	7.4	90	0.9	89	Change
BD+47 183	HD 4180	1.975	84	1.05	84	0.815	82	0.70	85	1.1	82	SP
BD+47 857	HD 22192	1.55	42	-	-	1.07	42	0.80	45	0.2	**64**	DP
BD+47 939	HD 25940	2.28	173	1.09	158	1.025	172	0.25	145	1.1	174	SP
BD+47 3985	HD 217050	3.9	75	1.65	69	1.123	71	1.55	75	0.4	**53**	Change
BD+55 605	HD 14605	8.2	118	-	-	-	-	3.78	118	4.2	121	Change
BD+56 478	HD 13890	7.5	107	-	-	-	-	3.46	107	3.7	112	DP

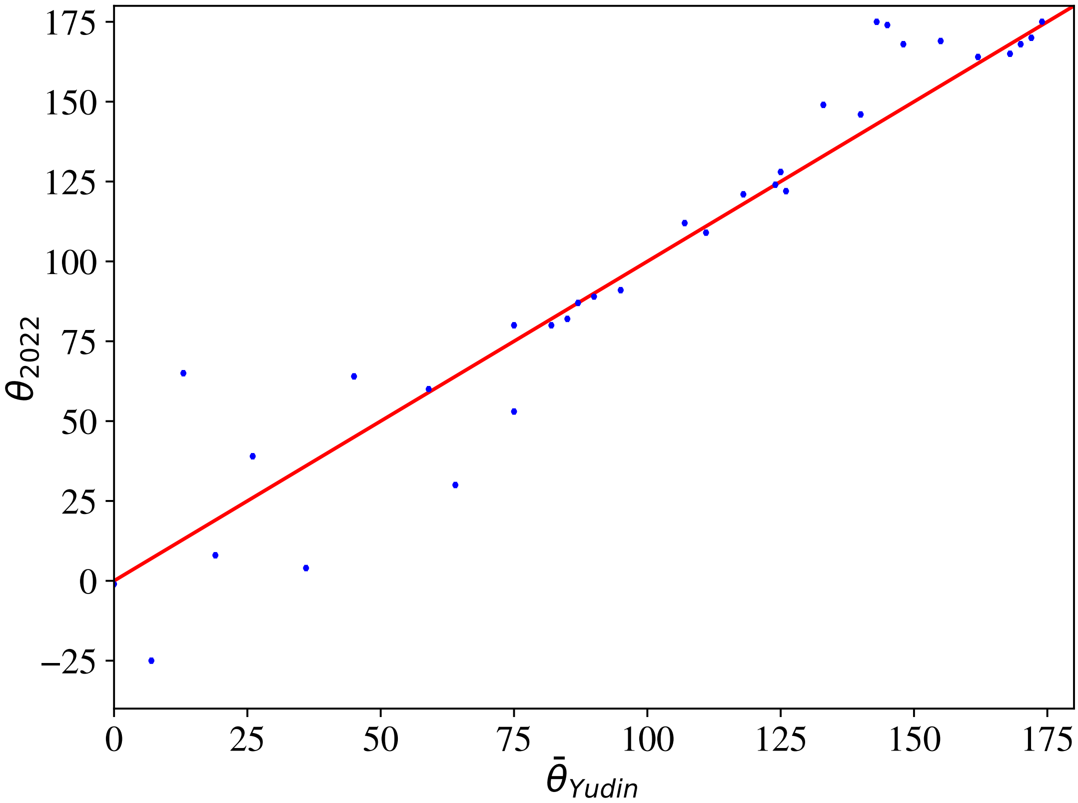

FIGURE 3.9: A plot of the polarization angles from the data collected for this work (2022) vs the polarization angles measured by Yudin (2001).

number of objects with significant (> 10°) changes over the 70 year time baseline. These objects have been highlighted in bold in Table 3.9. Large changes in polarization angle seem to be typically associated with large changes in the degree of polarization, either positive or negative, but it is worth noting that the objects that show such angle changes seem to be spread fairly evenly between those which do and do not show changes in their Hα peak morphology (see last line of table). Overall the changing polarization angle can be interpreted as either a varying ratio of interstellar and circumstellar polarization (which naturally have random polarization angles with respect to each other) as the disk strength varies, or as a change in the disk geometry as a function of time. Such behaviour has, for example, been seen in the interferometric and polarimetric measurements presented by Quirrenbach et al. (1997).

3.5.2 Removal of the inclination dependence

As radiation escapes the Be star and is scattered through the disk, it will get polarized. This polarization has been modeled by Brown & McLean (1977):

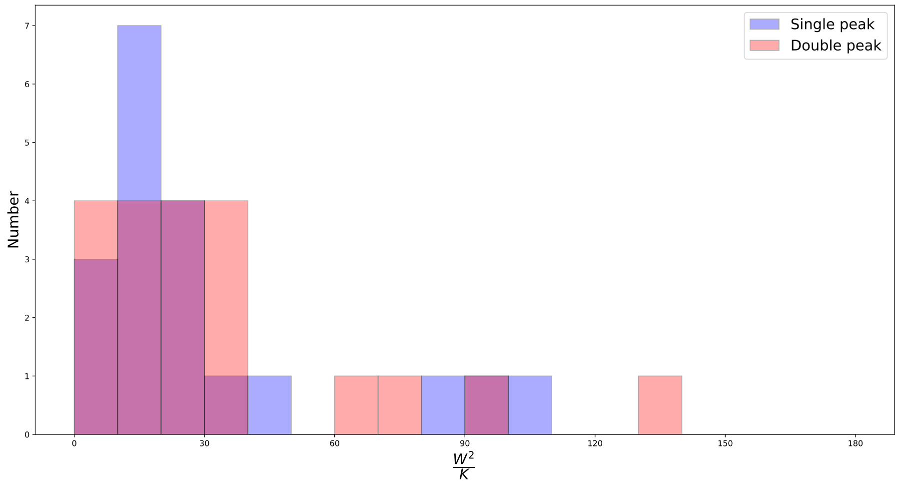

FIGURE 3.10: A histogram showing the distribution of stars for single and double peak Hα line with respect to $\frac{W^2}{K}$.

$$P \simeq \bar{\tau}(1 - 3\gamma)\sin^2 i \tag{3.5}$$

with P the polarization degree, $\bar{\tau}$ the average electron optical depth, γ a shape factor that describes the asymmetry of the disk, and i the inclination.

From the available data, it is not possible to separate these values without knowing the value of the inclination. However, as the rotational velocity $v \sin i$ was previously measured in Section 2.5.1, it is possible to obtain instead:

$$\frac{P}{(v \sin i)^2} = \frac{K}{v^2} \tag{3.6}$$

with $K = \bar{\tau}(1 - 3\gamma)$.

A value for v that is not dependent on the inclination of the star can be derived, in exchange of introducing some uncertainty related to the mean optical depth $\bar{\tau}$. Similarly, the values shown in Equation 3.6 can be multiplied by the critical velocity squared:

$$\frac{P}{(v \sin i)^2} v_{\text{crit}}^2 = \frac{K}{v^2} v_{\text{crit}}^2 = \frac{K}{W^2} \tag{3.7}$$

obtaining a measurement of the critical fraction W.

Table 3.10: Results from the KS tests. Distributions which are apparently drawn from the same parent population (i.e. $p > 0.05$) are highlighted in bold.

Values	SP vs DP
W^2/K	**0.64**
v^2/K	**0.98**

3.5.3 Testing the population differences

In order to test the validity of the above calculations, the distribution of the W^2/K and v^2/K quantities can be compared against the Hα emission shape classification made in Section 2.4.1. Kolmogorov-Smirnov tests have been calculated to compare these quantities, although only in the case of single peaked- (SP) and double peaked-emission (DP), as the no emission (NP) are expected to not show intrinsic polarization as well, and have been removed from the testing.

As was shown in Section 2.5.3, SP emission stars and DP emission stars seemingly were part of different distributions in terms of $v \sin i$ and $W \sin i$, with DP having higher values. However, when the angular dependence on the inclination is removed by using Equation 3.7, the null hypothesis can not be rejected, as can be seen in Figure 3.10 and in the results shown in Table 3.10. This can be interpreted as evidence for the idea that the cause of the difference between single and double peak Hα emission is the inclination of the disk, as predicted by emission line modelling (e.g. Poeckert & Marlborough (1976, 1978a), Sigut et al. (2020)). If that theory is taken as accepted, then this method of using polarization to eliminate the dependence on the inclination angle appears to work for the sample distribution.

3.5.4 Relation between interstellar polarization and extinction

As a final analysis, the values of the interstellar polarization can be compared to the extinction. The values of the extinction for the entire sample were taken from Barnsley & Steele (2013).

The values of the interstellar polarization degree are shown against the distance in Figure 3.11. The red line shows a linear fit, which shows a very small but negative trend, possibly influence by the distant points at a $d = 2500$ pc or more. However, the extremely small correlation coefficient and the almost constant value shows that there is not a direct linear relation between the distance and the interstellar polarization, which is in agreement with other studies of the local bubble (Berdyugin et al., 2014; Gontcharov & Mosenkov, 2019).

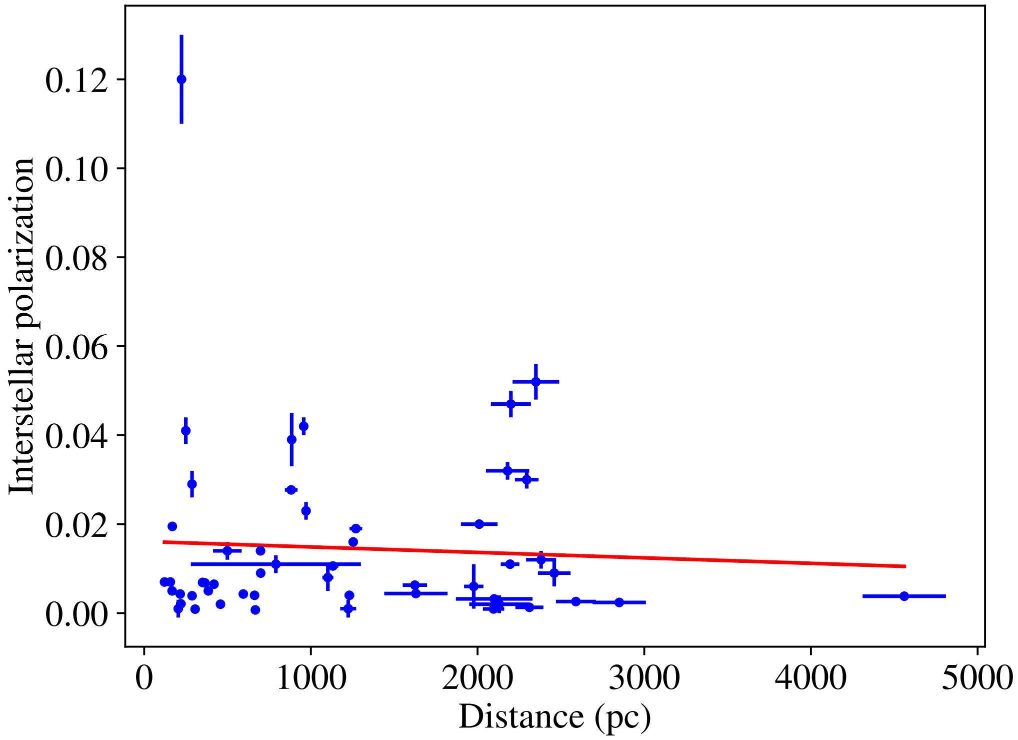

FIGURE 3.11: The values of the interstellar polarization degree plotted against the distance in parsecs. The red line is a linear fit $ax + b$ to the whole sample, with values $a = -1.1 \cdot 10^{-6}$, $b = 1.6 \cdot 10^{-2}$ and a correlation coefficient $R = -0.053$.

For the values between reddening and distance in Figure 3.12, it is possible to see a positive relation. Even if some of the near values show a negative value, there is a clear positive trend with distance.

Finally, comparing the values of the interstellar polarization degree and the reddening in Figure 3.13, it is not possible to see any direct correlation between the values. As was previously said in 3.1.3, the polarization degree might change in different ways than the reddening.

3.6 Summary

In this chapter, polarimetry observations for the entire sample introduced in Section 2.3.1 and their analysis have been presented. Even if two sets of observations were taken, only the October observations were selected for the analysis, as the August ones showed inconsistencies.

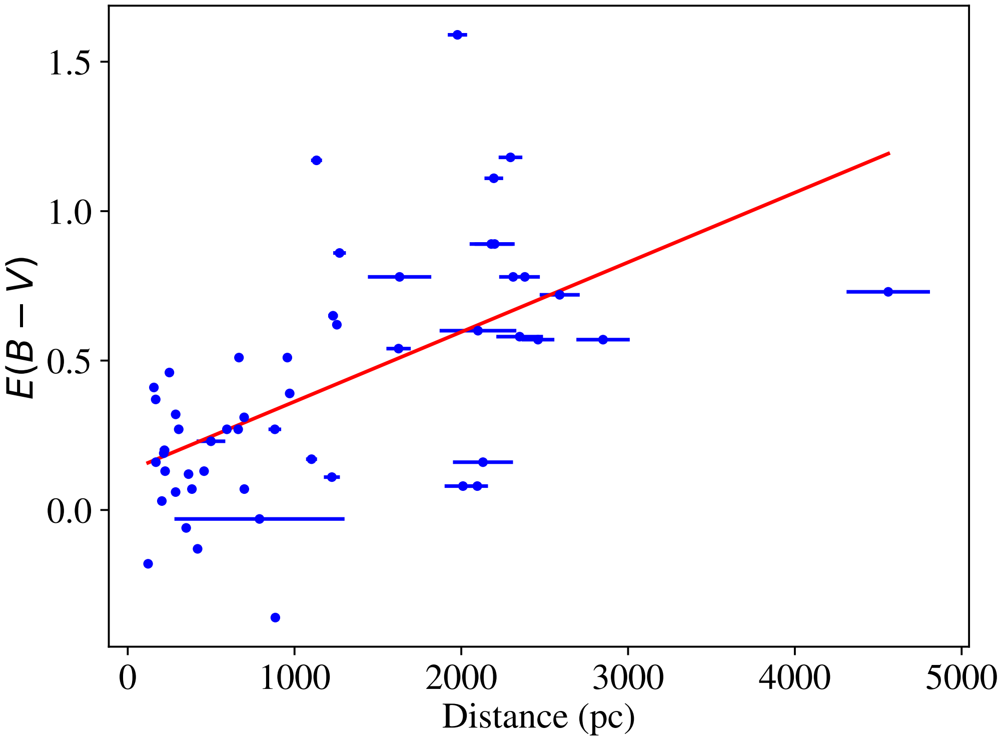

FIGURE 3.12: The values of the reddening against the distance in parsecs. The red line is a linear fit $ax + b$ to the whole sample, with values $a = 2.3 \cdot 10^{-4}$, $b = 9.4 \cdot 10^{-2}$ and a correlation coefficient $R = 0.554$.

After that, the interstellar and intrinsic values of the polarization degree and angle were separated, and the values of the intrinsic polarization were compared with previous work by other authors, which showed that the polarization angle is mostly constant, but some stars showed some big changes.

With the addition of the rotational velocity $v \sin i$ values obtained in Section 2.5.1 and the critical velocity values obtained in Section 2.5.2, the inclination dependence was removed from the polarization values. A Kolmogorov-Smirnov test was done to the single and double peak groups from the sample, and it was found that their distributions could not be separated after removing the dependence on the inclination. This implies that the key factor differentiating the two types of objects is the inclination angle.

Finally, it was explored how the interstellar polarization, the extinction, and the distance relate with each other. It was found that while there seems to be a certain relation between extinction and distance, there is no relation, or at least not a direct one, between the interstellar polarization degree and the extinction or the distance.

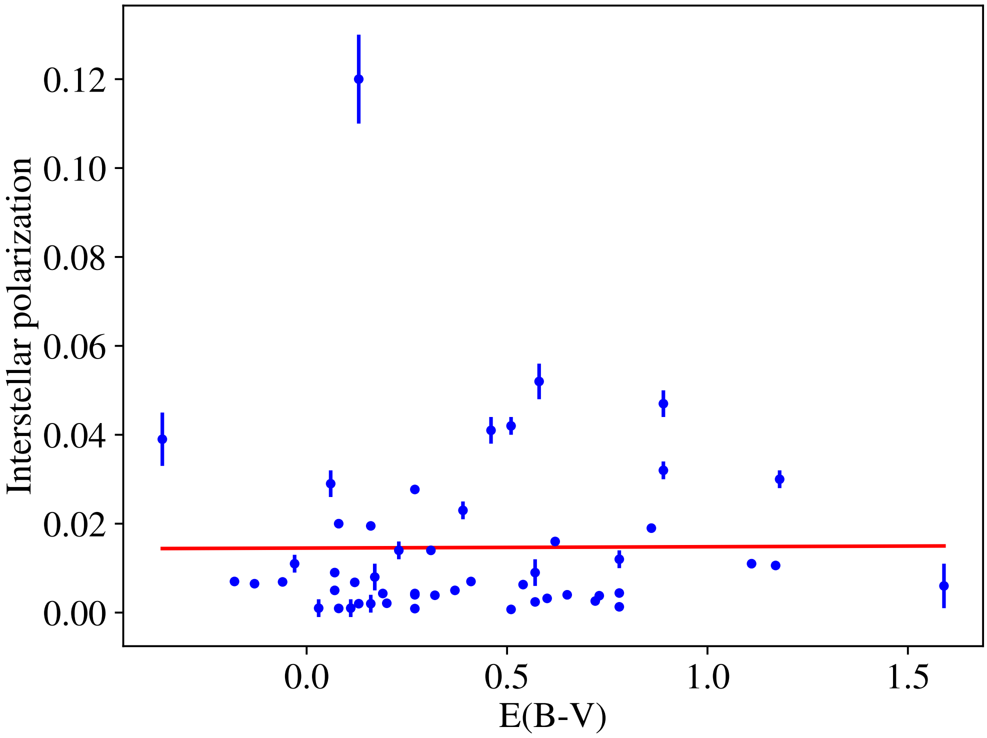

FIGURE 3.13: The values of the interstellar polarization degree plotted against the reddening. The red line is a linear fit $ax + b$ to the whole sample, with values $a = 1.3 \cdot 10^{-3}$, $b = 1.4 \cdot 10^{-2}$ and a correlation coefficient $R = 0.025$.

Chapter 4

Be stars variability

4.1 Timescale variability of Be stars

Be stars are, as was said in Section 1.1, variable stars. The multiple processes that affect the emission are usually classified in two or three groups, depending on the timescale of the process.

The *short-term* variability of Be stars can range from a few minutes to a few days (Porter & Rivinius, 2003). These variations are attributed to non-radial pulsations of the star, and can be found on photometric variations in the order of 0.01 magnitudes or lower (Percy et al., 1999) to find p and g modes, using the tools from asteroseismology, as was explained in Section 1.5.1. Both the type of data and the timescale do not correspond with our observations, and it will not be covered in more detail in this work.

At the same time, the *long-term* variability of Be stars ranges from a few years to decades to complete a cycle (Porter & Rivinius, 2003). These long-term variations are commonly related to the V/R variability, which is discussed in detail in Section 4.2, and emission line strength variability, which can take decades to complete a cycle, or which can lead to total dissipation of the line. The reason for this is still unexplained (Hubert, 2007).

Between the short-term variability and the long-term variability, mid-term variability can also be found, ranging from a few days to months or a few years. This variability is usually related to binarity (Rivinius et al., 2013), although processes that happen closer in the disk might also be in this range.

More details for the short-term variability and non-radial pulsations can be found in the reviews by Porter & Rivinius (2003), Hubert (2007) and Rivinius et al. (2013).

In this chapter, the variability of the emission for the objects in the sample is studied, with a focus on the V/R variability and the changes in total emission.

4.2 V/R variability

As was commented in Section 2.4, Balmer lines in Be stars might appear as a double peak emission: two separated peaks at a mostly symmetric distance from a central absorption line, with one shifted towards the violet (V) and the other shifted towards the red (R). The intensity ratio of V and R lines, also known as V/R ratio, has been studied for a long time. These values are known to slowly change in a way that follows $V > R \rightarrow V = R \rightarrow V < R \rightarrow V = R \rightarrow V > R$, in an apparent quasiperiodic cycle (Mennickent & Vogt, 1991), with much longer periods of $V > R$ and $V < R$ asymmetry than $V = R$ symmetry (Hanuschik et al., 1995). The observed properties of this V/R variation have been summarized by (Okazaki, 1991) and (Rivinius et al., 2013). Some important properties include a period of the variability that can range from years to decades, with ~ 7 years being the average, and with the period not being sensitive to the spectral type of the central star. The cycle lengths, however, are not constant. Phase lags of the variability when comparing different Balmer lines have also been found, attributed to variations in density which appear first on the inner part of the disk (Okazaki, 1991).

4.3 Equivalent Width

When a line suffers some type of dispersion in their wavelength, due for example either instrumental broadening or rotation related Doppler shifts, it might look less intense, as the maximum value is smaller. However, the total emission or absorption might still be the same for the line.

With that idea in mind, it is possible to calculate what is called *equivalent width* (EW) of the line, which is a measurement of the total strength of the line by comparing it to the section of normalized continuum that would have to be to be equal to the emission or absorption of the line. For that reason, the EW is measured in Angstroms, which would be the width of the continuum that is equivalent to the value of the line.

The calculation can only take place for spectra that have been normalized to the continuum, and it follows the equation:

$$\mathrm{EW} = \int \left(1 - \frac{F_{\mathrm{L}}}{F_{\mathrm{C}}}\right) d\lambda \tag{4.1}$$

with F_{L} the flux of the line and F_{C} the flux of the continuum.

From here, a few interesting values can be seen: If there is no line, the equivalent width will be 0. If the line is an absorption line, the value will be positive, as F_{L} will be smaller than F_{C}. However, if the line is an emission line, the value will be negative, as the flux of the line will be over the continuum.

The error can be calculated following the formula in Cayrel (1988):

$$\sigma(\mathrm{EW}) = 1.5\sqrt{\frac{\mathrm{FWHM} \cdot \delta x}{\mathrm{SNR}}} \tag{4.2}$$

with FWHM the value of the full width half maximum of the line, δx the distance between pixels, and SNR the average signal-to-noise ratio.

4.3.1 Measurement of the Equivalent Width

The first step for the calculation of the equivalent width is the determination of how wide is the line. For that, the FWHM of the line is calculated. In the case of the single peak emission and absorption lines this can be easily done by just interpolating the values that would have half of the intensity of the peak, however for the double peaks this estimation is more complicated, as the peak maxima can have different values. Instead, the left bound of the range is taken at half of the intensity of the left peak, and the right bound is taken at half of the intensity of the right peak.

Once the FWHM of the line has been obtained, the section to be used in the calculation is taken as 3 times this value from the centre. This is a big range, but it is expected that the part that is not part of the line is approximately equivalent to the continuum, and by taking a big range it can be avoided to miss any parts of the line.

Next, the Python module "equivalent_width" from the package Specutils is used for the calculation: When given a spectrum with wavelengths and normalized fluxes it can calculate the finite differences between the different wavelength measurements given and use them as $d\lambda$ in Equation 4.1. The finite sum of all the points is then calculated, which would be then equivalent to:

$$\mathrm{EW} = \sum \left(1 - \frac{F_{\mathrm{L}}}{F_{\mathrm{C}}}\right) \Delta\lambda \tag{4.3}$$

Table 4.1: The measured equivalent width of the Hα and Hβ absorption lines for the 20 B standard stars. The values of Hα obtained in Barnsley & Steele (2013) are shown for comparison. The stars have been ordered by luminosity class and spectral type.

Star	Spec. type	Lum. class	Hα EW (2024) (Å)	Hα EW (2013) (Å)	Hβ EW (2024) (Å)
HD 218376	B0.5	III	1.90 ± 0.08	3.0	2.27 ± 0.06
HD 23180	B1	III	2.64 ± 0.07	3.5	2.61 ± 0.06
HD 214993	B1.5	III	2.34 ± 0.06	4.0	2.90 ± 0.06
HD 29248	B2	III	2.57 ± 0.07	3.4	3.08 ± 0.06
HD 207330	B2.5	III	2.87 ± 0.07	3.9	3.37 ± 0.06
HD 184930	B5	III	4.88 ± 0.04	4.9	5.84 ± 0.03
HD 23850	B8	III	5.09 ± 0.04	5.8	5.56 ± 0.03
HD 176437	B9	III	6.28 ± 0.05	6.9	7.35 ± 0.03
HD 186882	B9.5	III	7.96 ± 0.04	7.6	8.77 ± 0.04
HD 886	B2	IV	2.61 ± 0.06	3.8	3.53 ± 0.07
HD 20365	B3	IV	4.52 ± 0.06	4.9	5.23 ± 0.06
HD 160762	B3	IV	3.08 ± 0.06	4.1	4.51 ± 0.12
HD 147394	B5	IV	4.69 ± 0.06	5.3	5.85 ± 0.05
HD 23288	B7	IV	6.30 ± 0.04	6.1	6.52 ± 0.03
HD 22951	B0.5	V	3.30 ± 0.08	4.2	3.17 ± 0.06
HD 219688	B5	V	4.38 ± 0.05	4.5	4.75 ± 0.04
HD 23338	B6	V	4.86 ± 0.05	5.7	5.66 ± 0.03
HD 214923	B8	V	6.69 ± 0.06	7.3	8.04 ± 0.03
HD 196867	B9	V	7.79 ± 0.05	7.6	8.58 ± 0.03
HD 222661	B9.5	V	10.16 ± 0.06	9.6	10.96 ± 0.05

4.3.2 Equivalent Width absorption correction

The central star is expected to be a normal B star, showing Hα and Hβ absorption lines in their spectra. These absorption lines, when combined with the disk, would show a reduced emission in the observations. For that reason, a correction to the values of the emission is necessary.

With that purpose, 20 known B standard stars that show absorption lines were measured in Barnsley & Steele (2013). The values for the Hα line have been remeasured here, as well obtaining as values for the Hβ line for the first time. These values have been added to Table 4.1 and can be seen in Figure 4.1, showing that the values measured in 2024 are generally lower than the ones obtained in 2013, presumably due to the use of different software tools. The 2024 measurements are preferred as these are made in the same way as the Be star measurements they are used to correct.

There are 3 groups of stars in the sample, depending on their luminosity class: They have been grouped depending if they are III, IV or V. With those groups, a fit of their Hα absorption EW vs the spectral type and a fit of their Hβ absorption EW vs the

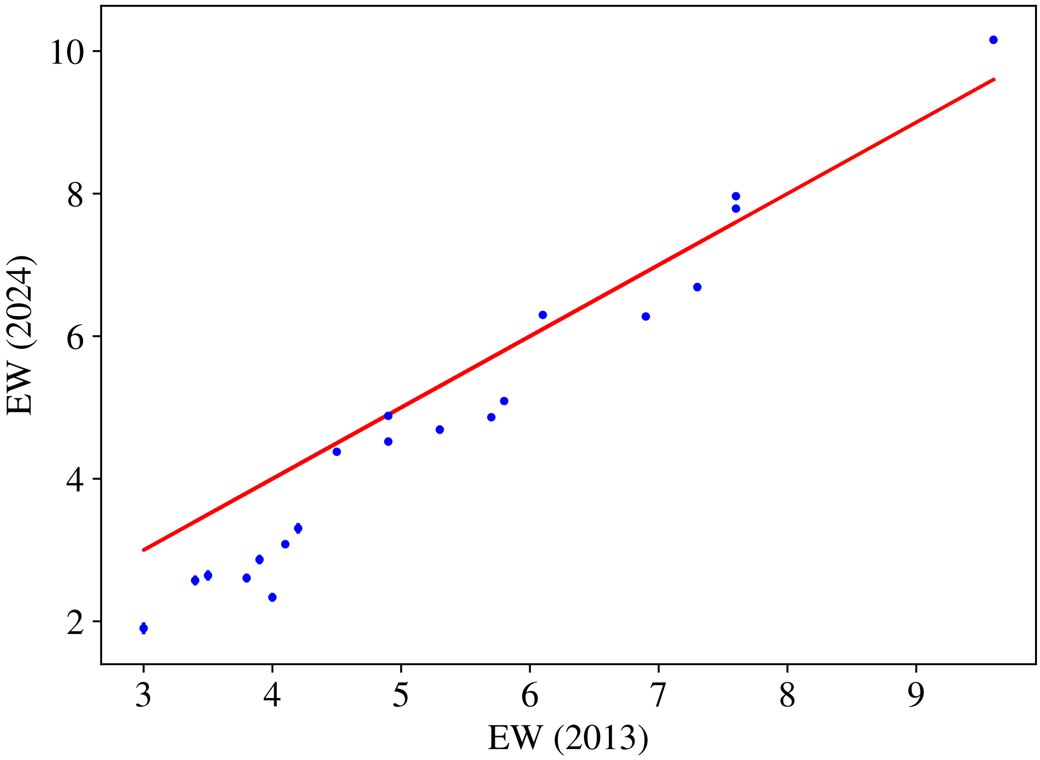

FIGURE 4.1: A plot comparing the values of the Hα EW obtained in 2024 vs the values of the Hα EW obtained in 2013. The red line is a 1:1 line for comparison.

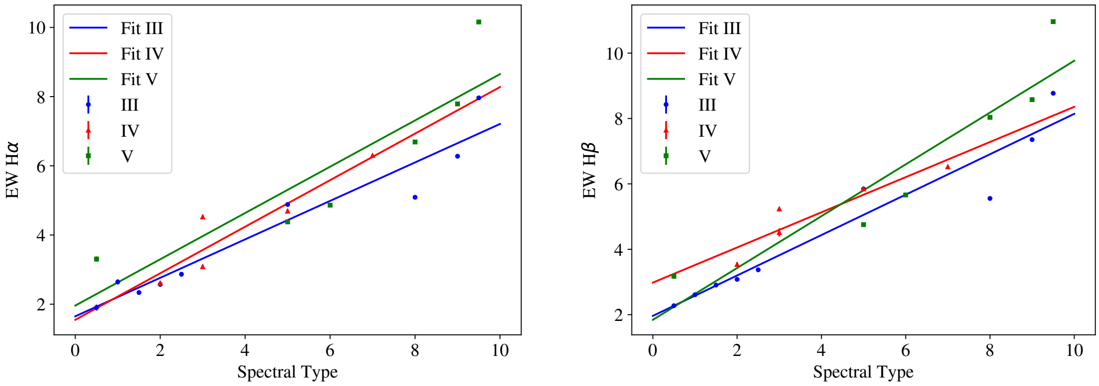

(a)

(b)

FIGURE 4.2: The equivalent width of Hα (a) and Hβ (b) vs the spectral type of the standard stars shown in Table 4.1. Individual fits to a $y = A + Bx$ line were obtained for each luminosity class, and the results are shown in Table 4.2.

spectral type were calculated. The results of the fits can be seen in Table 4.2 and in Figure 4.2.

The obtained values have been applied to each of the objects in the Be star sample to obtain an estimation of the calculated EW absorption for Hα and Hβ depending on the

Table 4.2: The results from the fit $y = A + Bx$ to the values in Table 4.1, with y the EW and x the spectral type.

Line	Lum. class	A (Å)	B (Å)	R
Hα	III	1.65 ±0.33	0.556 ±0.061	0.9607
Hα	IV	1.55 ±0.72	0.673 ± 0.16	0.9219
Hα	V	2.0 ± 1.2	0.67 ±0.18	0.8848
Hβ	III	1.96 ±0.38	0.618 ±0.068	0.9602
Hβ	IV	2.98 ±0.55	0.54 ± 0.13	0.9262
Hβ	V	1.8 ± 1.1	0.79 ± 0.16	0.9290

luminosity class and spectral type of the central star. Because of the limitations of the sample, two luminosity class II stars have been grouped with luminosity class III stars, and one case of an O9 star has been counted as B-1 for simplicity on these extreme cases. The obtained values can be seen in Table 4.3.

4.4 Analysis of the V/R variability

The values of V and R were obtained from the double peak stars at the same time that the peak separation distance in Section 2.4.3. This was done for the three possible cases: Hα double peak emission but no Hβ emission (6 cases), Hα single peak emission but Hβ double peak emission (10 cases), and Hα and Hβ double peak emission (13 cases).

4.4.1 Periodicity

A series of fits have been performed to the data taken in the year 2018, as many of the objects have multiple observations from that year. A minimum number of 4 observations is required for a fit, which will have the form $y = A\sin(\omega t + \alpha) + B$, with y the V/R values and t the Modified Julian Date (MJD) of the observations. The fits to the data match well the rest of the observations, and 4 examples of these fits can be seen in Figure 4.3.

On average, the period for Hα is $\bar{T} = 0.86 \pm 0.32$ years, and for Hβ is $\bar{T} = 1.07 \pm 0.39$ years. These values are clearly below the average obtained by Copeland & Heard (1963), of 6.8 years. The main difference in the results is the scale of the observations: While the ones in Copeland & Heard (1963) were studied only as long term variability, fitting points measurements separated for years or more, in this study the data points are closer in time, taken all in the same year, and therefore the fit is from an intermediate term variability point of view.

Table 4.3: The equivalent width of the H alpha absorption and H beta absorption for our sample stars.

Object	EW Hα (Å)	EW Hβ (Å)	Object	EW Hα (Å)	EW Hβ (Å)
CD-28 14778	2.77	3.2	BD+37 3856	2.295	2.235
CD-27 11872	2.1125	2.2525	BD+40 1213	3.225	4.33
CD-27 16010	6.91	7.3	BD+42 1376	3.3	3.42
CD-25 12642	2.042	2.394	BD+42 4538	3.635	3.815
CD-22 13183	6.65	7.37	BD+43 1048	5.01	5.68
BD-20 5381	5.31	5.79	BD+45 933	2.965	3.025
BD-19 5036	3.89	4.44	BD+45 3879	2.965	3.025
BD-12 5132	1.762	2.084	BD+46 275	4.45	5.06
BD-02 5328	6.65	7.37	BD+47 183	3.635	3.815
BD-01 3834	2.89	4.06	BD+47 857	4.435	5.07
BD-00 3543	6.65	7.37	BD+47 939	3.635	3.815
BD+02 3815	6.985	7.765	BD+47 3985	2.965	3.025
BD+05 3704	3.635	3.815	BD+49 614	4.45	5.06
BD+17 4087	5.495	6.13	BD+50 825	6.65	7.37
BD+19 578	7.32	8.16	BD+50 3430	7.32	8.16
BD+20 4449	1.65	1.96	BD+51 3091	5.57	6.3
BD+21 4695	5.495	6.13	BD+53 2599	7.32	8.16
BD+23 1148	2.77	3.2	BD+55 552	4.64	5
BD+25 4083	2.126	2.487	BD+55 605	2.63	2.63
BD+27 797	2.295	2.235	BD+55 2411	7.655	8.555
BD+27 850	2.555	3.79	BD+56 473	2.42	2.605
BD+27 3411	7.32	8.16	BD+56 478	2.965	3.025
BD+28 3598	1.09	1.34	BD+56 484	2.63	2.63
BD+29 3842	2.21	2.58	BD+56 493	2.425	3.075
BD+29 4453	2.965	3.025	BD+56 511	2.21	2.58
BD+30 3227	4.64	5	BD+56 573	2.965	3.025
BD+31 4018	2.965	3.025	BD+57 681	2.295	2.235
BD+36 3946	2.63	2.63	BD+58 554	6.65	7.37
BD+37 675	6.65	7.37	BD+58 2320	3.3	3.42

4.4.2 Period and phase differences between lines

One of the features from V/R variability can be clearly seen from the fits in Table 4.5: the phases and period of the V/R variability of Hα and Hβ are different, as can be seen in figures (a) and (d) of Figure 4.3. From the results in Table 4.5, it can be seen that, in 4 of the 9 cases where both lines have been observed, Hα has a significantly shorter period than Hβ, in 2 of the 9 cases Hα has a longer period than Hβ and in 3 cases the period is roughly the same for both.

Table 4.4: The values obtained from the fits to the V/R data. The value of the period was obtained from the equation $T = 2\pi/\omega$.

Object	Line	A	B	ω (yr^{-1})	α	T (yr)
CD-27 11872	Hβ	0.29 ±0.14	1.090 ±0.072	$0.008190 \pm 8.4 \cdot 10^{-5}$	-455.5 ±4.8	2.10
CD-27 16010	Hα	0.041 ±0.011	1.0241 ±0.0085	$0.019574 \pm 8.7 \cdot 10^{-5}$	-540.9 ±4.9	0.88
BD-02 5328	Hβ	-0.082 ±0.028	1.076 ±0.025	$0.018035 \pm 6.6 \cdot 10^{-5}$	-1031.6 ±3.8	0.95
BD-01 3834	Hβ	0.023 ±0.011	0.979 ±0.012	0.01721 ±0.00014	-981.8 ±8.3	1.00
BD-00 3543	Hα	0.061 ±0.032	1.005 ±0.020	0.05312 ±0.00013	-2952.7 ±7.1	0.32
BD+02 3815	Hα	0.0086 ±0.0032	1.0071 ±0.0024	0.04420 ±0.00012	-2569.7 ±7.0	0.39
BD+27 797	Hβ	-0.0365 ±0.0056	0.9930 ±0.0028	$0.028735 \pm 4.1 \cdot 10^{-5}$	-1652.0 ±2.3	0.60
BD+31 4018	Hβ	-0.184 ±0.065	1.013 ±0.040	$0.018799 \pm 7.1 \cdot 10^{-5}$	-1075.8 ±4.0	0.92
BD+36 3946	Hβ	0.117 ±0.055	1.100 ±0.037	$0.017371 \pm 5.1 \cdot 10^{-5}$	-995.7 ±2.9	0.99
BD+37 675	Hα	-0.0290 ±0.0040	0.9877 ±0.0032	$0.015498 \pm 5.1 \cdot 10^{-5}$	-887.6 ±2.9	1.11
BD+37 675	Hβ	0.0091 ±0.0047	0.9912 ±0.0037	0.02144 ±0.00025	-75.1 ±14.1	0.80
BD+42 4538	Hα	-0.052 ±0.015	0.943 ±0.014	0.02161 ±0.00020	-93.3 ±11.5	0.80
BD+42 4538	Hβ	0.128 ±0.031	0.958 ±0.021	$0.021156 \pm 5.2 \cdot 10^{-5}$	-67.8 ±3.0	0.81
BD+43 1048	Hα	0.081 ±0.031	1.030 ±0.039	$0.012675 \pm 8.2 \cdot 10^{-5}$	-722.2 ±4.6	1.36
BD+43 1048	Hβ	-0.047 ±0.032	0.971 ±0.023	$0.012885 \pm 6.2 \cdot 10^{-5}$	-735.6 ±3.5	1.34
BD+47 183	Hβ	0.014 ±0.010	0.9747 ±0.0076	0.01208 ±0.00061	-684.2 ±35.2	1.42
BD+47 857	Hα	0.018 ±0.012	0.9898 ±0.0093	0.01406 ±0.00032	-815.6 ±18.3	1.22
BD+47 857	Hβ	-0.0149 ±0.0071	1.0009 ±0.0050	0.01558 ±0.00015	-886.6 ±8.5	1.10
BD+47 3985	Hα	0.033 ±0.039	0.988 ±0.023	$0.016617 \pm 9.0 \cdot 10^{-5}$	-948.1 ±5.2	1.04
BD+47 3985	Hβ	0.0281 ±0.0024	0.9862 ±0.0023	$0.013748 \pm 8.2 \cdot 10^{-5}$	-781.4 ±4.8	1.25
BD+50 3430	Hα	0.11 ±0.12	0.995 ±0.080	0.02119 ±0.00026	-1235.2 ±15.0	0.81
BD+50 3430	Hβ	-0.0077 ±0.0091	1.0019 ±0.0059	0.02030 ±0.00026	-17.8 ±14.4	0.85
BD+53 2599	Hα	0.117 ±0.019	1.092 ±0.015	$0.018315 \pm 4.8 \cdot 10^{-5}$	-1050.6 ±2.7	0.94
BD+55 552	Hα	0.0296 ±0.0067	1.0419 ±0.0042	0.01800 ±0.00013	-1033.50 ±7.54	0.96
BD+55 552	Hβ	0.051 ±0.018	0.988 ±0.013	0.01282 ±0.00021	421.32 ±12.17	1.34
BD+55 2411	Hα	0.0133 ±0.0071	1.0014 ±0.0058	0.02411 ±0.00022	-1384.7 ±12.5	0.71
BD+56 511	Hα	-0.26 ±0.10	1.090 ±0.035	$0.025751 \pm 4.5 \cdot 10^{-5}$	27.6 ±2.6	0.67
BD+58 554	Hα	0.0186 ±0.0048	1.0204 ±0.0034	0.04354 ±0.00015	-2519.9 ±8.5	0.40
BD+58 554	Hβ	0.028 ±0.012	1.0081 ±0.0083	0.04258 ±0.00021	-2464.2 ±12.0	0.40
BD+58 2320	Hα	0.013 ±0.025	0.995 ±0.012	0.01408 ±0.00035	-799.2 ±20.0	1.22
BD+58 2320	Hβ	0.053 ±0.031	0.987 ±0.016	$0.014123 \pm 8.4 \cdot 10^{-5}$	-802.6 ±4.8	1.22

Table 4.5: The values obtained from the fits to the V/R data. The fit performed was to the equation $y = A\sin(\omega t + \alpha) + B$, with y the V/R values and t the Modified Julian Date (MJD) of the observations. The value of the period was obtained from the equation $T = 2\pi/\omega$.

Object	T_α (yr)	α_α	T_β (yr)	α_β
BD+37 675	1.11	-887.6	0.80	-75.1
BD+42 4538	0.80	-93.3	0.81	-67.8
BD+43 1048	1.36	-722.2	1.34	-735.6
BD+47 857	1.22	-815.6	1.10	-886.6
BD+47 3985	1.04	-948.1	1.25	-781.4
BD+50 3430	0.81	-1235.2	0.85	-17.8
BD+55 552	0.96	-1033.50	1.34	421.32
BD+58 554	0.40	-2519.9	0.40	-2464.2
BD+58 2320	1.22	-799.2	1.22	-802.6

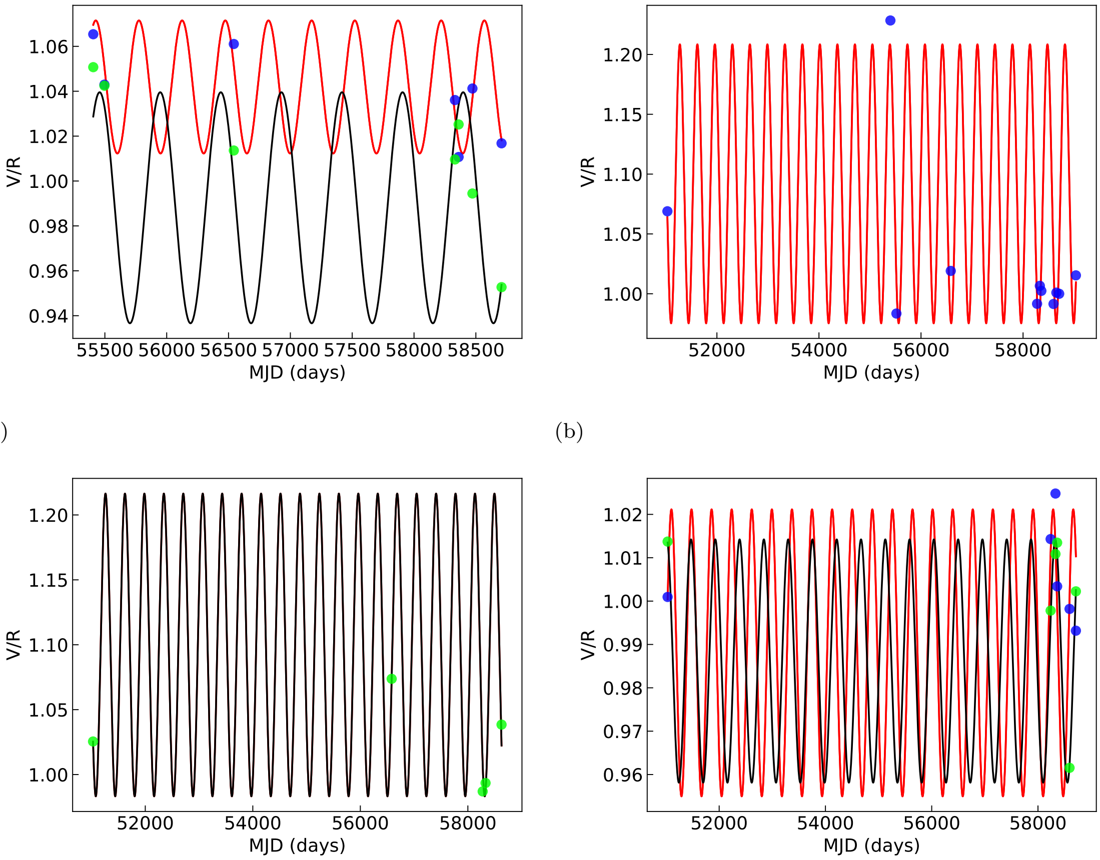

(a) (b) (c) (d)

Figure 4.3: The V/R data evolution with time, and the fits to the data. The blue points are Hα, the yellow points are Hβ, the red line is a fit to the Hα points, and the black line is a fit to the Hβ points. The objects are: (a) BD+55 552, (b) BD+53 2599, (c) BD+36 3946, (d) BD+47 3985. The results of the fits can be found in Table 4.4.

4.4.3 Analysis of the orbital parameters

From orbital mechanics (Roy, 2005) it is possible to obtain the value of the semi-major axis of the ellipse a from the period:

$$T = 2\pi \left(\frac{a^3}{\mu}\right)^{1/2} \tag{4.4}$$

with T the orbital period and $\mu = GM$.

It is possible to derive the maximum velocity (or velocity at periastron) V_P:

$$V_\mathrm{P} = \sqrt{\frac{\mu}{a}\left(\frac{1+e}{1-e}\right)} \tag{4.5}$$

Table 4.6: The values obtained from the fits to the V/R data. The fit performed was to the equation $y = A\sin(\omega t + \alpha) + B$, with y the V/R values and t the Modified Julian Date (MJD) of the observations. The value of the period was obtained from the equation $T = 2\pi/\omega$.

Object	Line	T (yr)	$M(M_\odot)$	a (10^7 km)	$v(e=0)$ (km s^{-1})	$v\sin i(\Delta\lambda)$ (km s^{-1})	$\frac{v\sin i(\Delta\lambda)}{v(e=0)}$
CD-27 11872	Hβ	2.1	12.604	5.71	54.13	49.33	0.91
CD-27 16010	Hα	0.88	3.678	2.12	47.98	60.98	1.27
BD-02 5328	Hβ	0.95	3.403	2.17	45.58	69.99	1.54
BD-01 3834	Hβ	1	9.008	3.11	61.98	46.56	0.75
BD-00 3543	Hα	0.32	3.403	1.05	65.51	109.63	1.67
BD+02 3815	Hα	0.39	3.195	1.18	60.05	114.43	1.91
BD+27 797	Hβ	0.6	12.604	2.48	82.19	51.49	0.63
BD+31 4018	Hβ	0.92	8.266	2.86	61.93	84.49	1.36
BD+36 3946	Hβ	0.99	10.228	3.23	64.88	48.41	0.75
BD+37 675	Hα	1.11	3.403	2.41	43.27	76.97	1.78
BD+37 675	Hβ	0.8	3.403	1.94	48.26	115.32	2.39
BD+42 4538	Hα	0.8	6.553	2.41	60.05	60.07	1
BD+42 4538	Hβ	0.81	6.553	2.43	59.8	86.64	1.45
BD+43 1048	Hα	1.36	5.662	3.27	47.92	126.54	2.64
BD+43 1048	Hβ	1.34	5.662	3.24	48.16	146.46	3.04
BD+47 183	Hβ	1.42	6.554	3.54	49.6	49.03	0.99
BD+47 857	Hα	1.22	5.208	2.96	48.32	71.26	1.47
BD+47 857	Hβ	1.1	5.208	2.76	50.02	90.34	1.81
BD+47 3985	Hα	1.04	8.266	3.11	59.45	146.41	2.46
BD+47 3985	Hβ	1.25	8.266	3.51	55.91	211.21	3.78
BD+50 3430	Hα	0.81	2.999	1.87	46.08	101.41	2.2
BD+50 3430	Hβ	0.85	2.999	1.94	45.35	139.37	3.07
BD+53 2599	Hα	0.94	2.999	2.07	43.85	123.11	2.81
BD+55 552	Hα	0.96	5.208	2.52	52.34	114.89	2.19
BD+55 552	Hβ	1.34	5.208	3.15	46.83	134.75	2.88
BD+55 2411	Hα	0.71	2.828	1.68	47.22	70.8	1.5
BD+56 511	Hα	0.67	15.409	2.85	84.71	103.01	1.22
BD+58 554	Hα	0.4	3.403	1.22	60.81	65.78	1.08
BD+58 554	Hβ	0.4	3.403	1.22	60.81	105.76	1.74
BD+58 2320	Hα	1.22	6.67	3.22	52.48	149.83	2.86
BD+58 2320	Hβ	1.22	6.67	3.22	52.48	183.16	3.49

with e the eccentricity. The value of the eccentricity is unknown, but an estimation for low eccentricity case $e = 0$ has been added to Table 4.6.

On the other hand, it was shown in Section 2.4.3 a number of peak distances. From calculating the Doppler effect that separates them from the central line, it is possible to obtain an estimation of the $v\sin i$ of the orbit.

These values have been added to Table 4.6:

As is possible to see, the values of the velocities calculated from the periods assuming low eccentricity do not match the values of $v\sin i$ obtained from the peak distance. This slower velocity, obtained from the V/R variations, could be the *group velocity* of the disk as it precesses around, instead of the velocity of the individual particles that form the disk.

4.4.4 Further analysis of the periodicity

To finish this section, a series of bootstrap errors were calculated for each of the objects in the sample to test the results of the fits. A random sample of values was calculated at the same times as the original sample, with values randomly generated with the same average and standard deviation as the original ones. The fit was recalculated to obtain a period from these values, and this process was repeated for a total of 10000 iterations for each object.

Histograms showing the bootstrap error results can be seen in Appendix C. The simulated results show very similar values to the ones previously obtained in Section 4.4.1 for the real data, implying that it is possible that the spacing of the points in the sample is driving the results. More observations of these objects in a short period of time are therefore clearly needed to give confidence to the results presented in this section.

4.5 Analysis of the total emission

The values for the equivalent width of all the object in the sample, including the ones only showing emission, has been done following the procedure explained in Section 4.3. While they show variability, it is possible to see that the emission, at least with the current observations, do not show a clear periodicity: The values increase or decrease with time, but not within a clear range like V/R. Even if there maybe exists some quasi-periodicity, it would be in the range of short term variability, and more data would be required to study it this way.

From these limitations, the rest of this study will analyze the values of the sample as a group instead of individually.

4.5.1 Average equivalent width

After the calculation of the equivalent width of all the stars, including the ones showing only absorption for Hα or Hβ, the average values have been calculated. To see how the values of Hα and Hβ relate to each other, they have been plotted together, and can be seen in Figure 4.4. A polynomial fit $y = Ax^2 + Bx + C$ has been calculated, with values $A = -0.84 \pm 0.19$, $B = -0.31 \pm 1.69$, $C = -9.54 \pm 3.50$, and a correlation value of $R^2 = 0.8310$.

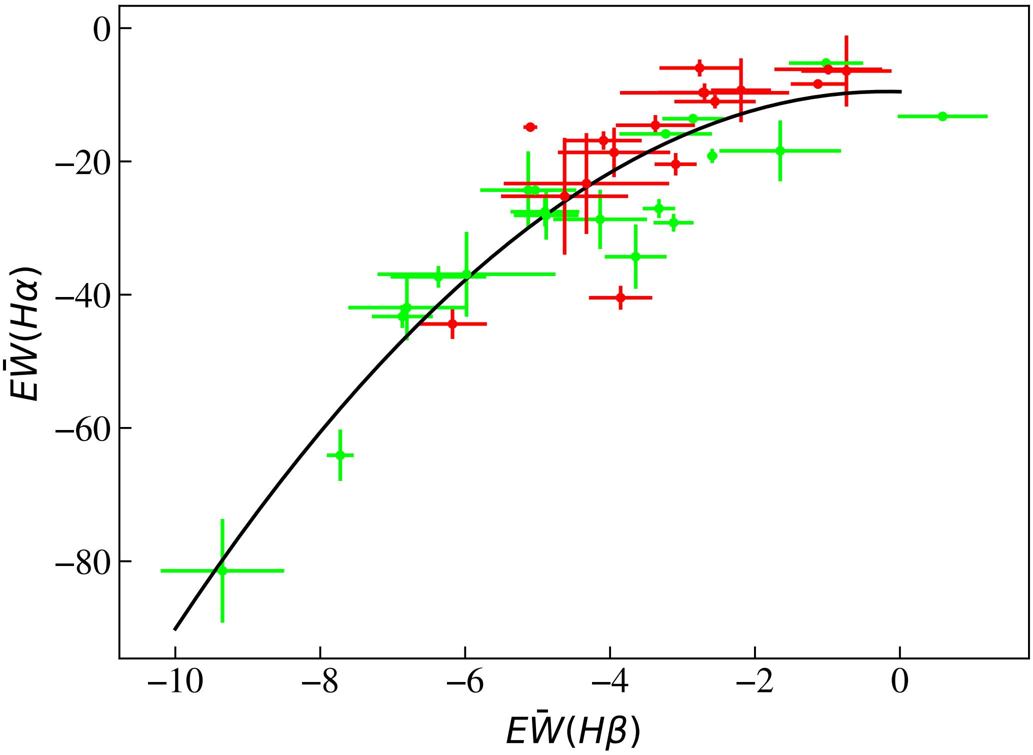

FIGURE 4.4: A plot showing the average values of the equivalent width for each object on our sample, depending on the peak type for the $H\alpha$ line. The green points are the objects that showed SP emission and the red points are the objects that showed DP emission. Variable and NP objects were removed, as their values might be dominated by absorption. The black line is a polynomial fit $y = Ax^2 + Bx + C$ to the data.

4.5.2 Dependence on the emission with respect to the peak distance separation

It is possible to compare the values of the equivalent width with the distance between the peaks when Hα, Hβ or both were DP. These values are shown in Figure 4.5.

While the trend appears to be linear, a linear fit and a quadratic fit have been calculated for Hα and Hβ. The results can be seen in Table 4.7. The R^2 values are low, which seems to indicate some weak correlation between the emission and the distance between peaks. As was explained in Section 2.4.3, there is a relation between the distance of separation between peaks and the distance of the emission maximum from the central star, so this result indicates that the total value of the emission is more complicated than a direct relation with the radial size of the disk.

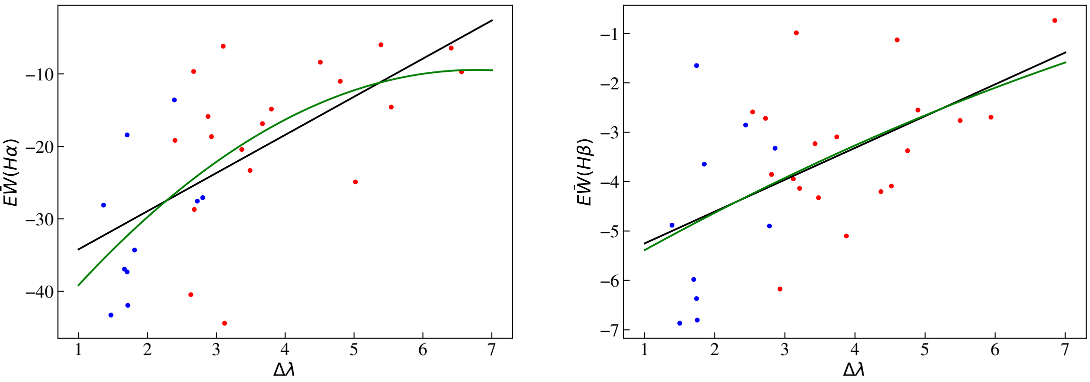

(a) (b)

Figure 4.5: The average value of the (a) $H\alpha$ EW and (b) $H\beta$ EW, plotted against the average value of the peak distance of the line. The red points indicate the values where both lines were DP, while the blue points indicate the values where only that line was observed as DP. The black line is a linear fit, and the green line is a quadratic fit, with the results available in Table 4.7.

Table 4.7: The values of the linear fits ($y = Ax + B$) and quadratic fits ($y = Ax^2 + Bx + C$) and the correlation coefficients R^2, calculated for the different values of the average Hα and Hβ equivalent width vs the average values of the peak distance.

Type of fit	Line	A	B	C	R^2
Linear fit	Hα	5.3 ± 1.2	-39.5 ± 4.3 Å	-	0.4082
Quadratic fit	Hα	-0.89 ± 0.81 Å^{-1}	12.1 ± 6.3	-50 ± 11 Å	0.4346
Linear fit	Hβ	0.64 ± 0.19	-5.89 ± 0.69 Å	-	0.2952
Quadratic fit	Hβ	-0.02 ± 0.12 Å^{-1}	0.83 ± 0.93	-6.2 ± 1.6 Å	0.2963

4.5.3 Dependence on the variability with respect to spectral type

In Figure 4.6, the values of the EW of Hα and Hβ are compared with the values of the spectral type and the mass of the stars.

As is possible to see, the highest values of emission for Hα and Hβ are at spectral type B1.5, or a mass of $\sim 8M_{\odot}$.

The variability of the emission has also been studied. The standard deviation of emission for each object, σ(EW), has been calculated as a measure of the variability, and the values are compared with the spectral type. Once again, the objects at spectral type B1.5 to B2 show the highest values of the variability, both for Hα and Hβ.

With this in mind, the relative value of the variability has been calculated as $r(\mathrm{EW}) = \sigma(\mathrm{EW})/\bar{\mathrm{EW}}$. This relative value indicates the fraction of the emission that is subject to variability. In contrast with Figure 4.7a and 4.7b, the values in 4.7c indicate that the change is mostly proportional to the total emission, with some higher values of the variability again at B1.5 and B7.

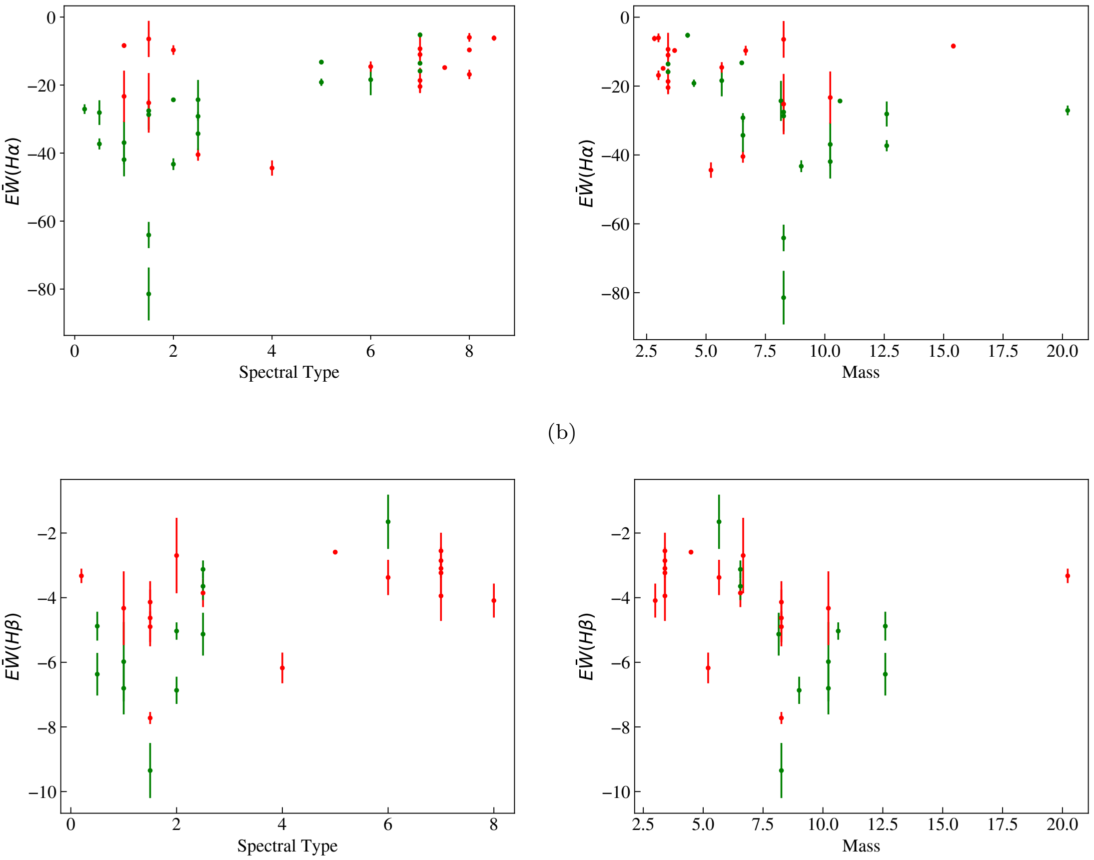

(a) (b)

(c) (d)

FIGURE 4.6: Average values of the EW vs spectral type and mass of the central star. The highest values are between spectral type 1-2, and mass of $\sim 8M_{\odot}$. The red points indicate that the line in emission is a DP, while the green points indicate that the line is a SP.

4.5.4 Rotational velocity of the central star dependence on the variability

The next question to be asked is if the total emission or its variability depend on the rotational velocity of the central star. In Figure 4.8, the values of the average EW of Hα and Hβ, as well as the variability of each emission, is compared with the rotational velocity. Similarly, in Figure 4.7d, the values of the relative value are represented against the rotational velocity.

To obtain a clear answer if these parameters are related to the rotational velocity of the star, a Spearman correlation tests has been calculated for each variable, and the results are shown in Table 4.8. The values are very small, ranging between -0.10 and 0.11, which indicates no correlation or a very weak correlation. This indicates then that the total emission and its variability is not related to the rotational velocity.

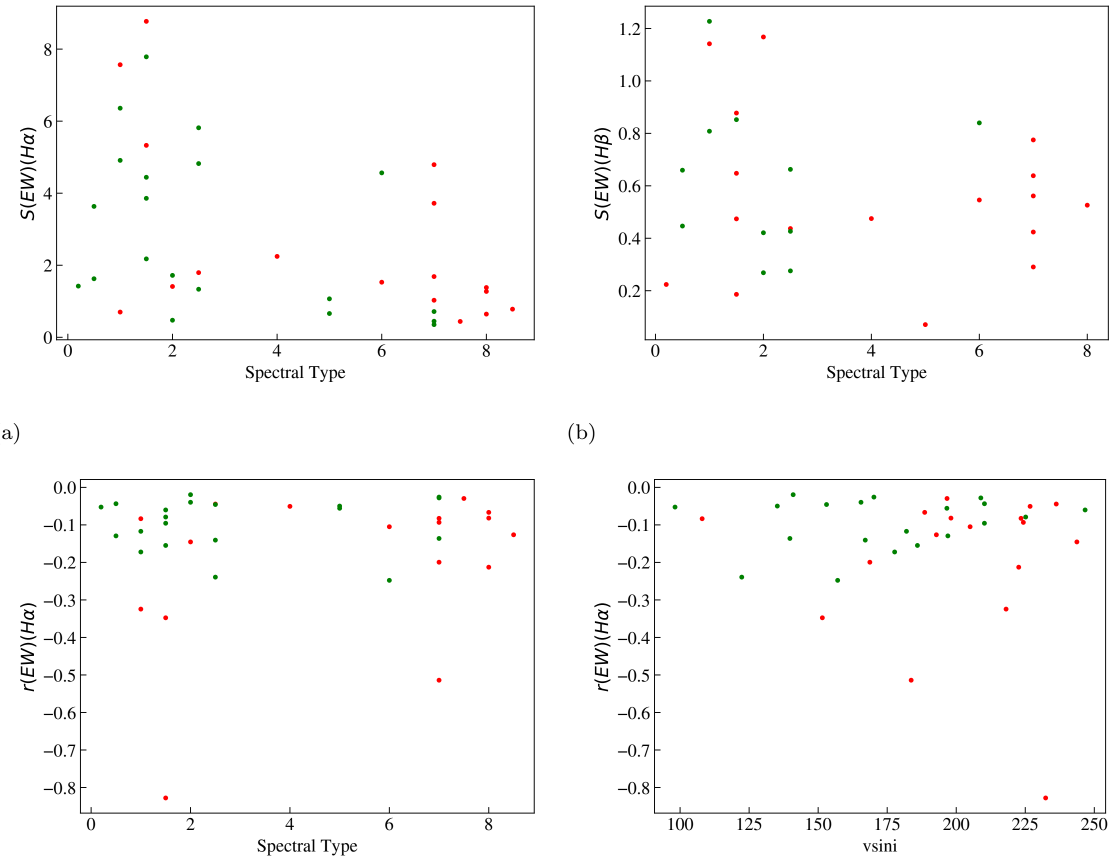

(a) (b)

(c) (d)

FIGURE 4.7: The variability of the emission. The standard deviation of Hα and Hβ vs the spectral type show that the maximum of variability happens at around 1-2, but also at around 7. The relative values of the variability, obtained from dividing the standard deviation by the average, show that there is no dependence with the spectral type or the rotational velocity, meaning that the changes in emission are mostly proportional to the amount of the emission. The red points indicate that the line in emission is a DP, while the green points indicate that the line is a SP.

TABLE 4.8: The Spearman correlation coefficients r and the probability value p calculated for the different values of the emission against the rotational velocity.

Variable	r	p
$\bar{EW}$(Hα) vs $v \sin i$	-0.0925	0.5862
$\bar{EW}$(Hβ) vs $v \sin i$	-0.0493	0.8034
σ(Hα) vs $v \sin i$	0.1081	0.5242
σ(Hβ) vs $v \sin i$	0.0717	0.7169
r(Hα) vs $v \sin i$	0.0107	0.9500

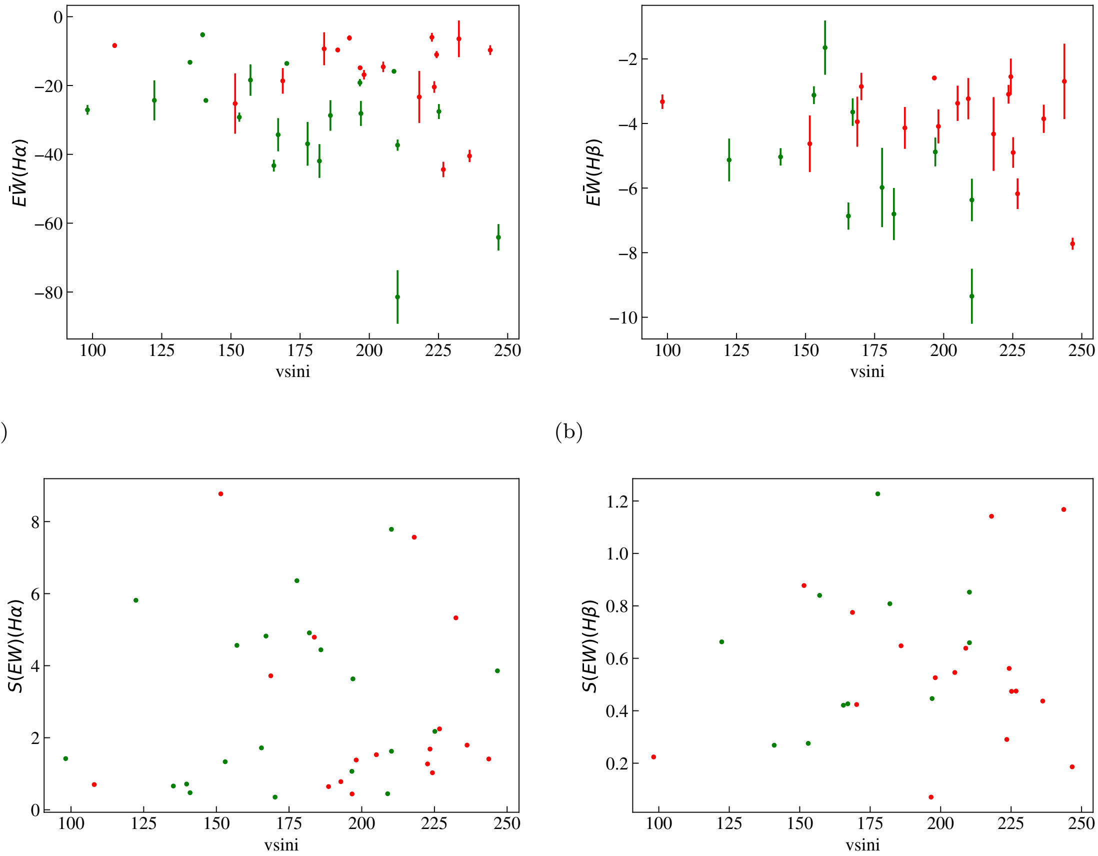

(a) (b)

(c) (d)

FIGURE 4.8: The average value and variability of the emission for Hα and Hβ against the value of the rotational velocity of the central star. A series of Spearman tests have been calculated, and they can be seen in Table 4.8, showing no apparent relation between these two observables. The red points indicate that the line in emission is a DP, while the green points indicate that the line is a SP.

4.5.5 Relation between emission and polarization

Finally, a comparison between the Hα and Hβ emission with the intrinsic polarization degree can be done.

It is possible to see in Figure 4.9 that the values of the intrinsic polarization and the emission of Hα and Hβ do not show a clear relation.

Further analysis can be done by looking at Figure 4.10, where the values of emission of Hα and Hβ are plotted against the values of $W/\sqrt{K}$. While no correlation can be seen between these values, the populations look indistinguishable.

Finally, an analysis of the variability with time of the polarization and the emission can be done. The 2001 values of the polarization degree and the equivalent width from Yudin (2001) were subtracted from the 2022 values of the polarization degree and the

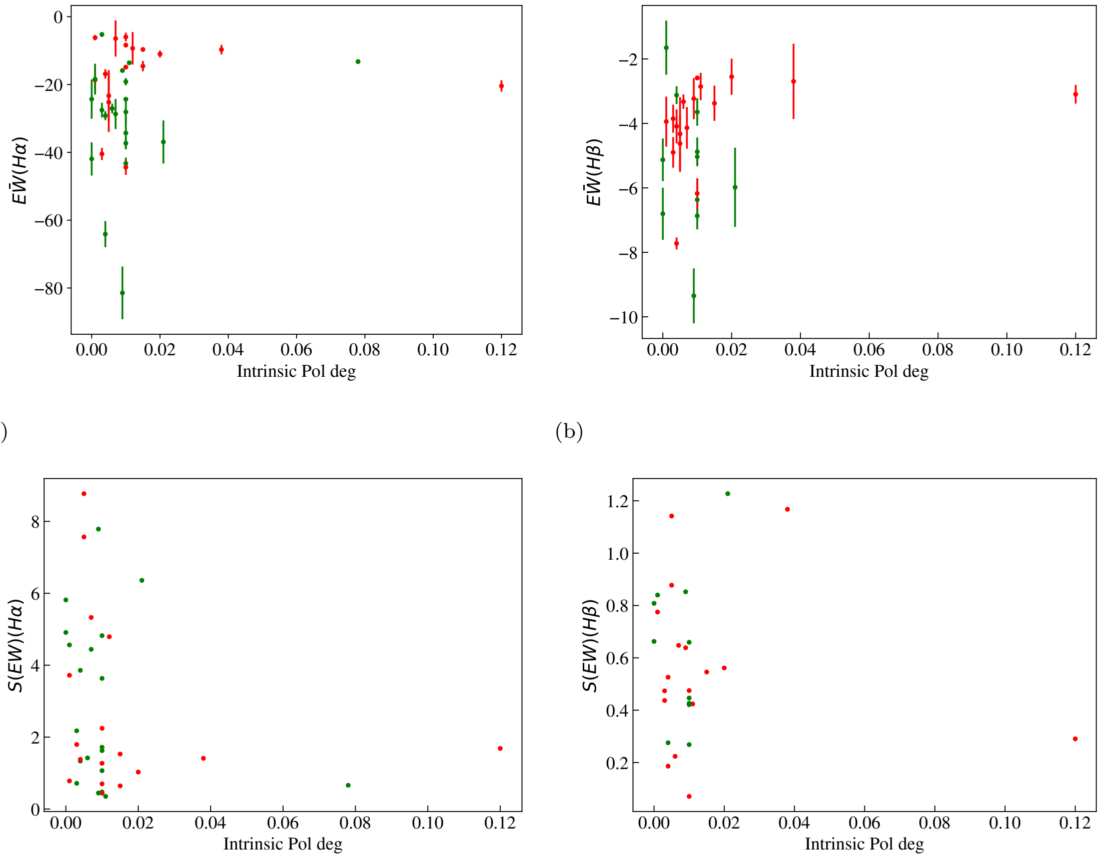

(a) (b)

(c) (d)

FIGURE 4.9: The average values and variability of the values of Hα and Hβ plotted against the polarization degree. No relation between these two values can be observed. The red points indicate that the line in emission is a DP, while the green points indicate that the line is a SP.

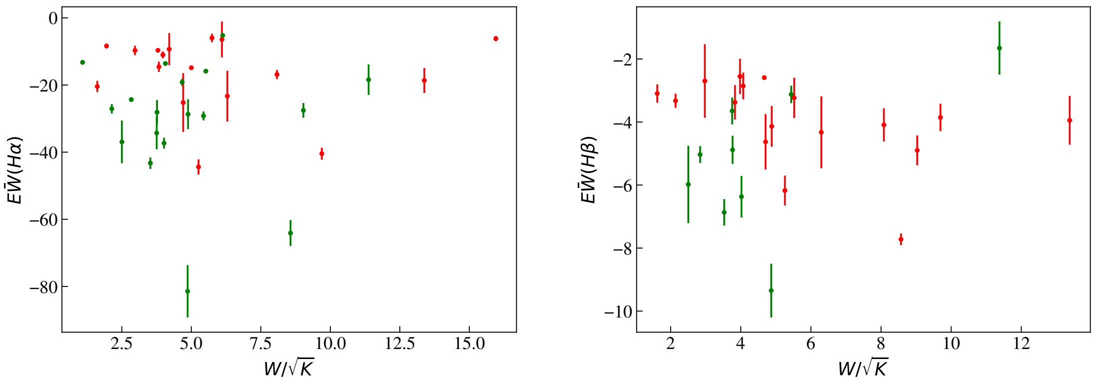

(a) (b)

FIGURE 4.10: The average values of (a) EW(Hα) and (b) EW(Hβ) plotted against the calculated values of $W/\sqrt{K}$, with the green points indicating the values where the line was SP and the red points indicating the values where the line was DP. No relation between these two values can be observed, but the removal of the inclination made both populations indistinguishable.

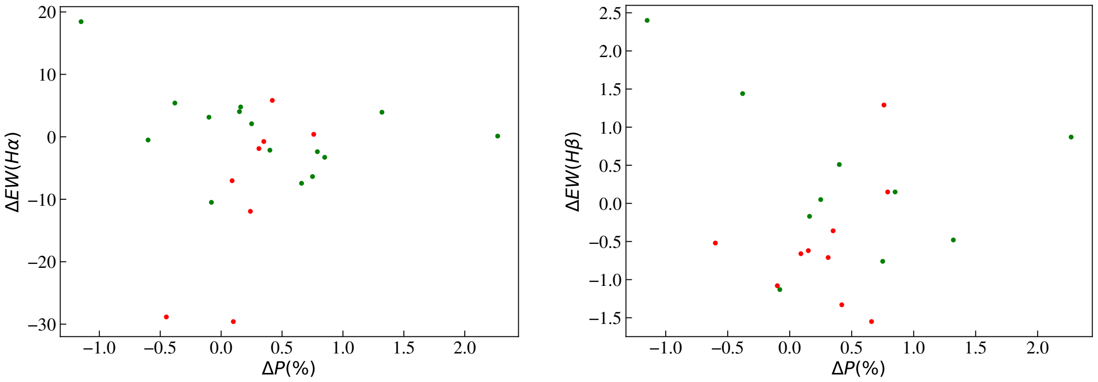

(a)

(b)

FIGURE 4.11: The difference between the 2001 values and the final values observed in the sample, of (a) EW(Hα) and (b) EW(Hβ) plotted against the polarization degree. The 2001 values were taken from Yudin (2001), the final values of the EW were taken from the the last spectral observation, and the final values for the polarization were taken from the 2022 observations. The red points indicate that the line in emission is a DP, while the green points indicate that the line is a SP.

last values of the equivalent width from the spectra. The values can be seen in Figure 4.11. These results are unexpected, as no correlation in the variations can be found, which could indicate that the variables depend on different things and are not related, with the polarization of the continuum being optically thin (Brown & McLean, 1977; Quirrenbach et al., 1997) and depending on the density and volume of the disk, while the emission of the Balmer lines is optically thick (Poeckert & Marlborough, 1978b) and depends on the surface area of the disk.

4.6 Summary

In this chapter, the variability of the sample introduced in Section 2.3.1 is studied, as a continuation of the results obtained in previous chapters.

The values of a correction to take into account the equivalent width absorption of the central stars have been calculated for Hα and Hβ, first by calculating the values of some standard B stars, and then deriving the values for the stars in the sample. After that, the values of the equivalent width for all the observations of the sample stars have been calculated, and they can be found in the appendix.

Next, the V/R variability of the objects showing double peak emission on the Hα line, the Hβ line or both has been studied. These objects show a clear periodicity, and a fit to a sin function has been calculated for each of them. The results obtained for the period of the variation are lower than expected, with values ranging between 0.32 and 2.10 years, while the expected average is of ∼7 years. This can be an indication that the V/R variation is in the timescale of mid-term variability, instead of long-term variability as is usually classified. However, a further analysis has been done and the periods obtained might be dependent only on the uneven and scarce sampling of the observations instead of the actual values of the V/R variations, which brings the reliability of the values obtained for the periods from the fits into question. Further measurements of the sample could help determine better the actual values of the periods.

Following, the values of the equivalent width of the lines have been studied by comparing them with other observables: A quadratic relation has been found between the average Hα EW and Hβ EW, which seems to indicate that higher values of emission in one line are related to higher values of emission on the other. There was no apparent relation to be found between the average peak distances and the average values of the EW for the objects showing double peak emission, which indicates that the dependence of the total emission is more complicated than just a bigger size of the disk.

The maximum value of the total emission and the variability of the emission was seen at B1.5, but no relation could be found between the total emission and variability with the rotational velocity of the star or the observed intrinsic polarization. The removal of the inclination angle by using $W/\sqrt{K}$ made the emission between SP and DP indistinguishable.

Finally, the difference between the 2001 observations from Yudin (2001) and the 2022 polarization observations shows that there is no apparent correlation between the polarization and line emission values. A possible explanation for this is that they are dependent on different variables.

Chapter 5

Conclusions and future work

5.1 Conclusions

In this thesis, an analysis of the spectral and polarimetry data from a sample of 58 Be stars, collected between 1998 and 2022, has been done.

In Chapter 2, the sample of 58 Be stars was presented. The procedure for the extraction of the data from the observation files was explained in Section 2.3.3. A basic classification of the objects in the sample, based on their peak morphology, was done in Section 2.4, separating them in 4 groups: Single Peak emission or SP, Double Peak emission or DP, No Peak emission or NP, and Variable for the ones that changed in shape between the observations. The change rate between emission and no emission and vice versa has been estimated between 0.80% and 0.89% every year, which is on the lower end of previous estimations, in the range between 0.3% and 25.5% every year, depending on the sample size and the objects examined.

An analysis of the peak separation distances for the DP emission in Hα, Hβ or both was done, finding that the relation between the peak distance of the Hα and Hβ lines is linear, with a slope of $A = 1.005 \pm 0.030$. The conclusion from this result is that the velocities of region with the maximum emission for Hα and Hβ are different, with the maximum of Hβ emission apparently closer to the central star than the maximum of Hα emission. Using this relation, a projection of the Hα peak distance has been calculated for the cases when Hα is SP but Hβ is DP, with the results being that this distance is smaller than in the cases where Hα is DP, showing that this emission can be explained as two lines that are very close and have blended together.

After this, in Section 2.5 the rotational velocities of the central B star were calculated from the FMWH of He I absorption lines present in the spectra. The average of the obtained rotational velocities for each object was calculated, followed by an estimation of the mass and radius of the central star from their stellar classification. With the values of the mass and the radius, the critical velocity of each object was obtained. Finally, a series of Kolmogorov-Smirnov tests were calculated, showing that the different morphology groups have a different distribution of the rotational velocity.

In Chapter 3, observations of polarimetric data, taken with MOPTOP in October 2022, were added. In Section 3.3, the process to take the observations and the data reduction was discussed. In Section 3.4 the average values of the polarization degree and angle were calculated, and they were separated between interstellar and intrinsic values.

After this, in Section 3.5, some of the values of the intrinsic polarization were compared with values previously published by other authors for the same objects, with some dating back to the 1950s. While the polarization degree showed large variations with time, the polarization angle was mostly constant, with a difference smaller than 10°, although some objects showed a larger variation of the polarization angle.

Next, in Section 3.5.2, using a dependency between the polarization degree and the inclination of the star, the inclination dependence was removed for the SP and DP objects. After this removal of the inclination, two KS tests were calculated, showing that the SP and DP populations became indistinguishable, proving that the difference in the morphology is due to the inclination of the disk, and that the polarization degree can be used to remove that dependence.

Finally, in Section 3.5.4, a brief study of the relation between distance and interstellar polarization was done, not finding a clear dependence of the interstellar polarization with the distance or the reddening. This can imply that the interstellar polarization changes in more ways that are not dependent of the distance or the reddening.

In Chapter 4, the variability of the sample was studied. In Section 4.3, the equivalent width of a group of reference standard B stars was calculated, and a correction to account for the absorption of the central B star was calculated for the objects in the sample. After that, the equivalent width of the Hα and Hβ lines for all the objects in the sample was calculated.

In Section 4.4, the V/R variability with time of the objects showing double peak emission in the sample was studied. A fit to a sin function was calculated for each of the objects, obtaining a short period which on average is $\bar{T} = 0.86 \pm 0.32$ years for Hα and $\bar{T} = 1.07 \pm 0.39$ years for Hβ, much shorter than the $T \sim 7$ years that is generally expected from previous studied. The difference in the values is probably caused by the sampling of the data: the multiple observations taken in 2018 allow for a mid-term variability study, compared with the usual study of this variability from observations separated in the order of years. With the values obtained in this study, one or more full oscillations could have been completed between observations in other studies. Some phase lags were also seen between the Hα and Hβ emission. A calculation from orbital mechanics to obtain the semi-major axis of the disk, assuming an elliptical shape, and the velocity from this orbit was calculated assuming low eccentricity, obtaining the group velocity of the disk, which is much lower than the rotational velocity of the disk itself. A series of bootstrap errors were calculated in Section 4.4.4, showing that the obtained values for the periods might be driven by the time spacing of the data points, bringing into question the reliability of the obtained values for the periods from the fits.

After this, in Section 4.5, an analysis of the total emission and the variability of emission of the objects in the sample was done. The equivalent width and its variability, represented using the average and the standard deviation of the values respectively, were compared with other values. The average equivalent width shows a quadratic relation between the Hα and Hβ lines. The highest values of the emission happened around a spectral class of B1.5. However, no correlation was found in the case of double peak emission between the total emission and the distance between peaks, meaning that the value of the emission is not directly related to the size of the disk. No correlation was found between the emission and the the rotational velocity of the central star, or between the emission and the polarization degree. Finally, the time change of the polarization degree and the time change of the line emission are apparently not related, which could indicate that they depend on different variables.

5.2 Applications of the results to the Be phenomenon model

The results from this thesis have explained certain features from Be stars.

Line profile shapes and the inclination: Since Struve (1931), the shape of the line profile has been expected to be related to the inclination. The difficulty of measuring the inclination angle of the disk has been a limiting factor in many works on the topic. In this study, this relation has been proven by removing the inclination dependence and seeing that the groups with different profiles in the sample became indistinguishable, in a way that does not depend on theoretical radiative transfer or kinematic models.

Using the polarization degree as a way to remove the inclination can be useful in future works where the inclination is still an unknown parameter.

Variability of the sample: All Be stars show variability. While this result was expected, the question of the dependence of the intensity and the variability with respect the spectral type remained. This study has shown that while stars around B1.5 show the maximum emission and variability, agreeing with Merrill & Burwell (1933), their relative proportion of change is independent with the spectral type, which can imply that it is more a factor of scale than a real difference, and that the variability might be proportional to the total emission.

At the same time, the emission and the variability of the sample shows no correlation with the rotational velocity of the central star, which is in agreement with previous studies. While the difference between objects with respect of their line profile is apparent from the rotational velocity distribution, the variability of the sample might be related to other mechanisms, like pulsation or binarity, as explained in Section 1.5.

Density vs radius: Finally, as the values of the polarization degree and the emission seem to change in different ways, the density and radius of the disk that they depend on respectively do not appear to be related. This result seems to be in apparent contradiction with previous studies on density models, that generally adopt a shape where the density ρ depends on the radius R (Hummel & Vrancken, 2000; Gies et al., 2007; Touhami et al., 2011), following the equation:

$$\rho(R) \propto \rho_0 R^{-n} \tag{5.1}$$

with the exponent n having an expected value between 1.5 and 4 (Silaj et al., 2010).

However, these previous models did not include polarization measurements. The inclusion of more polarimetry observations could help solve this difference.

5.3 Future work

There are several possibilities for the improvement of the results in this project. However, all of them require additional observations.

5.3.1 Additional spectroscopy observations

More spectroscopy observations can be added to the sample, completely or partially. Depending on the frequency of observations and the wavelength resolutions, different things can be studied.

Higher wavelength resolution observations: If observations with a higher wavelength resolution are available, in the order of 0.3Å or smaller for the Hα line, an additional observation of the objects in Table 2.8 could be taken. With that resolution, those objects could show a double peak shape instead a single peak one.

Whole sample observations: If observations for the whole sample are available, multiple objects could show reactivation or dissipation of the lines. A longer study of this process could help the understanding of the timescale of dissipation or reactivation of the emission lines from the disk. With the estimated value of 0.73%-0.78% of the sample every year on average, 1 object is expected to change every ~2.5 years, so multiple observations of the whole sample for the next decade could show a few objects changing between emission and no emission.

Multiple observations in one year: If multiple observations for the objects showing double peak emission can be taken in a short period of time, spaced only between a few days and a few months, the obtained values for the fits in Table 4.4 could be confirmed or disproved. This could prove that the V/R variability is not an long-term process, but a mid-term one, taking around 1 year in most cases, instead of a process that takes several years to complete. However, as there are four parameters in the fits, at least four observations are required in this short period of time.

At the same time, multiple observations in a short period of time could also allow to analyze in more detail the variability of the equivalent width of the lines. If any clear eclipses can be observed, it could potentially be a direct observation of binarity, but as the period of the binary orbit is generally very short, multiple observations would be required in a period of a month to be able to study it.

5.3.2 Additional polarimetry observations

Multiple polarimetry observations: More polarimetry observations can also be added to the sample. It is recommended to focus only on objects showing Hα emission, as objects with no emission are expected to show little or no polarization. These observations could help to confirm the measured values of the polarization, or to see if big changes of the polarization happen with time. No big changes to the polarization angle are expected, but big changes to the polarization degree have been seen, so a further analysis to the objects in Table 3.9 could give interesting results. A better study on the variability of the polarization from more polarimetry observations could also help constraining the formation and density models, and prove if they are related or not to the radius of the disk.

Combination of simultaneous polarimetry and spectroscopy observations: In combination, multiple spectroscopy and polarimetry observations taken at the same time can allow for a further and more precise analysis on the evolution of the disk density and radius evolution. This could be interesting at times where the line emission intensity increases or fades, as it would be a good opportunity to study disk formation and dissipation.

Appendix A

Chapter 2 tables

Table A.1: The list of observations taken for the respective objects.

Object	Alias	Observation years
CD-28 14778	HD 171757	1998, 2010, 2018, 2019
CD-27 11872	V3892 Sgr, HD 161103	1998, 2009, 2010, 2018, 2019, 2020
CD-27 16010	ϵ PsA, HR 8628, HD 214748	1998, 2009, 2010, 2013, 2018, 2019, 2020, 2022
CD-25 12642	HD 164741	1998, 2009, 2010, 2018, 2019, 2020
CD-22 13183	HD 172158	1998, 2009, 2010
BD-20 5381	HD 177015	1998, 2009, 2010, 2019
BD-19 5036	V3508 Sgr, HD 170682	1998, 2009, 2018, 2019
BD-12 5132	HD 172252	1998, 2018, 2019, 2020
BD-02 5328	HD 196712	1998, 2009, 2010, 2013, 2018, 2019, 2022
BD-01 3834	HD 187350	1998, 2009, 2010, 2018, 2019, 2020, 2022
BD-00 3543	HD 173371	1998, 2009, 2010, 2018, 2019, 2020
BD+02 3815	HD 179343	1998, 2009, 2010, 2018, 2019, 2020
BD+05 3704	HD 168797	1998, 2002, 2009, 2010, 2018, 2019, 2020
BD+17 4087	HD 350559	1998, 2018, 2019, 2020, 2022
BD+19 578	13 Tau, HR 1126, HD 23016	1998, 2009, 2010, 2013, 2017, 2018, 2019, 2020, 2022
BD+20 4449	HD 191531	1998, 2009, 2010, 2022
BD+21 4695	25 Peg, HD 210129	1998, 2009, 2010, 2013, 2018, 2020, 2022
BD+23 1148	HD 250289	1998, 2009, 2010, 2013, 2018, 2019, 2020, 2021, 2022
BD+25 4083	HD 339483	1998, 2009, 2010, 2018, 2019, 2020, 2022
BD+27 797	HD 244894	1998, 2009, 2010, 2013, 2018, 2019, 2022
BD+27 850	HD 246878	1998, 2009, 2010, 2013, 2018, 2020, 2021, 2022
BD+27 3411	β2 Cyg, HR 7418, HD 183914	1998, 2002, 2009, 2010, 2018, 2019, 2020, 2022
BD+28 3598	HD 333452	1998, 2009, 2010, 2018, 2019, 2020, 2022
BD+29 3842	HD 333226	1998, 2009, 2010, 2018, 2019, 2020, 2022
BD+29 4453	HD 205618	1998, 2009, 2010, 2013, 2018, 2019, 2020, 2022
BD+30 3227	HR 6971, HD 171406	1998, 2002, 2009, 2010, 2018, 2019, 2020, 2021, 2022
BD+31 4018	V2113 Cyg, HD 193009	1998, 2009, 2010, 2013, 2018, 2019, 2020, 2022
BD+36 3946	HD 228438	1998, 2002, 2009, 2010, 2013, 2018, 2019, 2020, 2022
BD+37 675	HR 894, HD 18552	1998, 2009, 2010, 2013, 2018, 2019, 2020, 2022
BD+37 3856	HD 228650	1998, 2009, 2010, 2013, 2018, 2019, 2020, 2022
BD+40 1213	HD 33604	1998, 2009, 2010, 2013, 2018, 2019, 2020, 2021, 2022
BD+42 1376	V434 Aur, HD 37657	1998, 2009, 2010, 2013, 2018, 2019, 2020, 2021, 2022
BD+42 4538	HD 216581	1998, 2002, 2009, 2010, 2013, 2018, 2019, 2020, 2022
BD+43 1048	HD 276738	1998, 2009, 2010, 2013, 2018, 2019, 2022
BD+45 933	HD 27846	1998, 2009, 2010, 2013, 2018, 2019, 2020, 2022
BD+45 3879	HD 211835	1998, 2002, 2009, 2010, 2013, 2018, 2019, 2020, 2022
BD+46 275	φ And, HR 335, HD 6811	1998, 2009, 2010, 2013, 2018, 2019, 2020, 2022
BD+47 183	22 Cas, HR 193, HD 4180	1998, 2009, 2010, 2013, 2018, 2019, 2020, 2022
BD+47 857	ψ Per, HR 1087, HD 22192	1998, 2009, 2010, 2013, 2017, 2018, 2019, 2020, 2022
BD+47 939	48 Per, HR 1273, HD 25940	1998, 2001, 2009, 2010, 2013, 2017, 2018, 2019, 2020, 2022
BD+47 3985	EW Lac, HR 8731, HD 217050	1998, 2002, 2005, 2017, 2018, 2019, 2020, 2022
BD+49 614	HD 13867	1998, 2009, 2010, 2013, 2018, 2022
BD+50 825	HR 1160, HD 23552	1998, 2007, 2009, 2010, 2013, 2018, 2019, 2020, 2021, 2022
BD+50 3430	HD 207232	1998, 2009, 2010, 2013, 2018, 2019, 2020, 2022
BD+51 3091	HR 8259, HD 20551	1998, 2009, 2010, 2013, 2018, 2019, 2022
BD+53 2599	HD 203356	1998, 2009, 2010, 2013, 2018, 2019, 2020, 2022
BD+55 552	HD 13669	1998, 2009, 2010, 2013, 2018, 2019, 2022
BD+55 605	V361 Per, HD 14605	1998, 2009, 2010, 2013, 2018, 2022
BD+55 2411	HD 195554	1998, 2002, 2009, 2010, 2013, 2018, 2019, 2020, 2022
BD+56 473	V356 Per	1998, 2009, 2010, 2013, 2018, 2022
BD+56 478	V358 Per, HD 13890	1998, 2002, 2009, 2010, 2013, 2018, 2019, 2020, 2022
BD+56 484	V502 Per	1998, 2009, 2010, 2013, 2018, 2020, 2022
BD+56 493	-	1998, 2009, 2010, 2013, 2018, 2019, 2022
BD+56 511	-	1998, 2009, 2010, 2013, 2018, 2019, 2021, 2022
BD+56 573	-	1998, 2009, 2010, 2013, 2018, 2019, 2022
BD+57 681	HD 237056	1998, 2009, 2010, 2013, 2018, 2019, 2020, 2022
BD+58 554	HD 237060	1998, 2009, 2010, 2013, 2018, 2019, 2020, 2022
BD+58 2320	HD 239758	1998, 2009, 2010, 2013, 2018, 2019, 2020, 2022

TABLE A.2: The list of objects, including the spectral and luminosity classes, distances, theoretical luminosities, masses and radius of the star, theoretical critical velocity and reddening. † indicates that the distances are from the Hipparcos catalog instead of Gaia. All the theoretical $\log(L/L_\odot)$ values come from de Jager & Nieuwenhuijzen (1987) and they only depend on the spectral type, while the $M/M_\odot$, $R/R_\odot$ and v_{crit} are derived from equations 1.5, 2.5, 2.6 and 2.7. The values of the reddening $E(\mathrm{B-V})$ come from Howells et al. (2001).

Object	Spectral Type	d (pc)	$\log(L/L_\odot)$	$M/M_\odot$	$R/R_\odot$	v_{crit} (km/s)	$E(\mathrm{B-V})$
CD-28 14778	B2III	1624 ± 73	4.047	10.638	5.490	496.1	0.54
CD-27 11872	B0.5V-III	1270 ± 38	4.258	12.604	5.855	522.9	0.86
CD-27 16010	B8IV	168.9 ± 8.4	2.337	3.678	2.844	405.3	0.16
CD-25 12642	B0.7III	1414 ± 39	5.034	23.517	7.983	611.7	-
CD-22 13183	B7V	882 ± 38	2.203	3.403	2.719	398.7	0.27
BD-20 5381	B5V	643 ± 16	2.681	4.491	3.220	420.9	-
BD-19 5036	B4III	667 ± 16	3.562	7.204	4.889	432.6	0.51
BD-12 5132	BN0.2III	1630 ± 190	4.846	20.219	7.328	592.0	0.78
BD-02 5328	B7V	350.4 ± 6.6	2.203	3.403	2.719	398.7	-0.06
BD-01 3834	B2IV	2010 ± 110	3.84	9.008	5.197	469.2	0.08
BD-00 3543	B7V	287.1 ± 3.0	2.203	3.403	2.719	398.7	0.06
BD+02 3815	B7-8sh	$790 \pm 510^{\dagger}$	2.094	3.195	2.624	393.2	-0.03
BD+05 3704	B2.5V	418.8 ± 7.7	3.332	6.554	4.206	444.9	-0.13
BD+17 4087	B6III-V	2096 ± 64	2.758	4.697	3.316	424.1	0.08
BD+19 578	B8V	159.3 ± 2.1	1.985	2.999	2.536	387.6	-
BD+20 4449	B0III	2130 ± 180	4.928	21.596	7.600	600.8	0.16
BD+21 4695	B6III-V	204.5 ± 3.7	3.08	5.662	3.774	436.5	0.03
BD+23 1148	B2III	2180 ± 130	4.047	10.638	5.490	496.1	0.89
BD+25 4083	B0.7-1III	1269 ± 22	4.573	16.236	6.549	561.1	-
BD+27 797	B0.5V	1977 ± 58	4.258	12.604	5.855	522.9	1.59
BD+27 850	B1.5IV	1231 ± 29	4.081	10.933	5.544	500.4	0.65
BD+27 3411	B8V	122.1 ± 1.2	1.985	2.999	2.536	387.6	-0.18
BD+28 3598	BO9II	2295 ± 71	5.516	34.643	10.253	655.1	1.18
BD+29 3842	B1II	4560 ± 250	4.93	21.631	7.607	601.0	0.73
BD+29 4453	B1.5V	1224 ± 48	3.733	8.266	5.067	455.2	0.11
BD+30 3227	B4V	364.5 ± 9.1	2.936	5.208	3.557	431.2	0.12
BD+31 4018	B1.5V	885 ± 18	3.733	8.266	5.067	455.2	-0.36
BD+36 3946	B1V	2350 ± 140	3.998	10.228	5.415	489.8	0.58
BD+37 675	B7V	224.1 ± 2.8	2.203	3.403	2.719	398.7	0.13
BD+37 3856	B0.5V	2195 ± 56	4.258	12.604	5.855	522.9	1.11
BD+40 1213	B2.5IV	1102 ± 33	3.716	8.153	5.048	452.9	0.17
BD+42 1376	B2V	698 ± 16	3.465	6.670	4.798	420.2	0.31
BD+42 4538	B2.5V	594.6 ± 9.9	3.332	6.553	4.206	444.9	0.27
BD+43 1048	B6IIIsh	971 ± 27	3.08	5.662	3.774	436.5	0.39
BD+45 933	B1.5V	957 ± 26	3.733	8.266	5.067	455.2	0.51
BD+45 3879	B1.5V	1876 ± 73	3.733	8.266	5.067	455.2	-
BD+46 275	B5III	$220 \pm 29^{\dagger}$	3.319	6.504	4.182	444.5	0.2
BD+47 183	B2.5V	$216 \pm 18^{\dagger}$	3.332	6.554	4.206	444.9	0.19
BD+47 857	B4V-III	167.7 ± 3.7	2.936	5.208	3.557	431.2	0.37
BD+47 939	B2.5V	156.8 ± 7.2	3.332	6.554	4.206	444.9	0.41
BD+47 3985	B1.5V	287.4 ± 5.8	3.733	8.266	5.067	455.2	0.32
BD+49 614	B5III	499 ± 86	3.319	6.504	4.182	444.5	0.23
BD+50 825	B7V	249.8 ± 2.1	2.203	3.403	2.719	398.7	0.46
BD+50 3430	B8V	384.8 ± 4.4	1.985	2.999	2.536	387.6	0.07
BD+51 3091	B7III	457.7 ± 6.3	2.576	4.226	3.096	416.3	0.13
BD+53 2599	B8V	637 ± 23	1.985	2.999	2.536	387.6	-
BD+55 552	B4V	699 ± 11	2.936	5.208	3.557	431.2	0.07
BD+55 605	B1V	2311 ± 84	3.998	10.227	5.415	489.8	0.78
BD+55 2411	B8.5V	305.7 ± 9.2	1.884	2.828	2.459	382.2	0.27
BD+56 473	B1V-III	2460 ± 98	3.998	10.228	5.415	489.8	0.57
BD+56 478	B1.5V	2100 ± 230	3.733	8.266	5.067	455.2	0.6
BD+56 484	B1V	2381 ± 90	3.998	10.228	5.415	489.8	0.78
BD+56 493	B1V	2850 ± 160	3.998	10.228	5.415	489.8	0.57
BD+56 511	B1III	2590 ± 120	4.508	15.409	6.389	553.5	0.72
BD+56 573	B1.5V	2200 ± 120	3.733	8.266	5.067	455.2	0.89
BD+57 681	B0.5V	1132 ± 33	4.258	12.604	5.855	522.9	1.17
BD+58 554	B7V	662.2 ± 6.9	2.203	3.403	2.719	398.7	0.27
BD+58 2320	B2V	1254 ± 24	3.465	6.670	4.798	420.2	0.62

Appendix B

Chapter 3 tables

Table B.1: Comparison of the 2022 with the ones from Yudin (2001).

Object	Object (2001)	$v \sin i$ (2001) (km/s)	P (%) (2001)	θ (2001) (°)	$v \sin i$ (2022) (km/s)	$\bar{P}$ (2022)	$\bar{\theta}$ (°)(2022) (°)
CD-28 14778	HD 171757	182 ± 18	0.43 ± 0.10	36	141 ± 23	3.2	4
CD-27 11872	HD 161103	260 ± 26	4.83 ± 0.12	172	210 ± 17	7.1	170
CD-27 16010	HD 214748	222 ± 26	0.09 ± 0.10	155	189 ± 7	0.4	169
CD-22 13183	HD 172158	232 ± 26	0.54 ± 0.10	143	169 ± 79	1.2	175
BD-20 5381	HD 177015	236 ± 24	0.51 ± 0.20	0	197 ± 72	1.3	179
BD-19 5036	HD 170682	121 ± 12	-	-	126 ± 17	2.9	10
BD-12 5132	HD 172252	146 ± 15	4.65 ± 0.20	148	98 ± 11	9.1	168
BD-02 5328	HD 196712	199 ± 19	0.35 ± 0.04	95	170 ± 8	0.4	91
BD-01 3834	HD 187350	199 ± 20	0.78 ± 0.20	82	166 ± 12	0.4	80
BD-00 3543	HD 173371	291 ± 4	-	-	224 ± 15	0.7	3
BD+02 3815	HD 179343	261 ± 36	-	-	197 ± 10	1.0	0
BD+05 3704	HD 168797	251 ± 6	0.78 ± 0.20	64	211 ± 59	1.4	30
BD+17 4087	HD 350559	186 ± 19	-	-	204 ± 79	2.2	8
BD+19 578	HD 23016	278 ± 14	0.60 ± 0.04	87	215 ± 17	0.5	87
BD+20 4449	HD 191531	80 ± 3	-	-	90 ± 43	0.9	10
BD+21 4695	HD 210129	201 ± 32	0.28 ± 0.04	7	157 ± 17	0.2	155
BD+23 1148	HD 250289	125 ± 13	2.95 ± 0.18	162	87 ± 77	3.2	164
BD+27 797	HD 244894	177 ± 18	1.61 ± 0.18	19	197 ± 18	1.7	8
BD+27 850	HD 246878	137 ± 14	0.55 ± 0.18	133	121 ± 18	0.9	149
BD+27 3411	HD 183914	220 ± 25	-	-	170 ± 13	1.0	153
BD+29 4453	HD 205618	299 ± 65	1.24 ± 0.20	26	247 ± 26	1.0	39
BD+30 3227	HD 171406	264 ± 10	0.28 ± 0.20	13	208 ± 8	1.6	65
BD+31 4018	HD 193009	220 ± 26	0.65 ± 0.20	75	225 ± 30	1.4	80
BD+36 3946	HD 228438	219 ± 22	1.15 ± 0.20	170	178 ± 23	0.7	168
BD+37 675	HD 18552	260 ± 12	-	-	223 ± 21	0.5	147
BD+40 1213	HD 33604	134 ± 20	1.29 ± 0.20	168	122 ± 7	1.5	165
BD+42 1376	HD 37657	216 ± 20	1.66 ± 0.20	174	196 ± 10	1.5	175
BD+42 4538	HD 216581	282 ± 28	-	-	236 ± 30	0.8	86
BD+43 1048	HD 276738	220 ± 22	-	-	205 ± 46	2.5	88
BD+45 933	HD 27846	134 ± 15	-	-	135 ± 14	2.3	138
BD+45 3879	HD 211835	207 ± 15	-	-	186 ± 10	0.6	24
BD+46 275	HD 6811	88 ± 13	0.74 ± 0.12	90	111 ± 20	0.9	89
BD+47 183	HD 4180	221 ± 9	0.70 ± 0.13	85	167 ± 12	1.1	82
BD+47 857	HD 22192	297 ± 41	0.80 ± 0.15	45	227 ± 12	0.2	64
BD+47 939	HD 25940	198 ± 31	0.25 ± 0.10	145	153 ± 8	1.1	174
BD+47 3985	HD 217050	301 ± 16	1.55 ± 0.20	75	232 ± 14	0.4	53
BD+49 614	HD 13867	93 ± 16	-	-	135 ± 114	1.2	104
BD+50 825	HD 23552	218 ± 3	0.55 ± 0.05	140	184 ± 11	0.7	146
BD+50 3430	HD 207232	281 ± 28	-	-	198 ± 19	0.5	10
BD+55 552	HD 13669	304 ± 22	-	-	243 ± 29	2.7	112
BD+55 605	HD 14605	150 ± 3	3.78 ± 0.20	118	142 ± 25	4.2	121
BD+55 2411	HD 195554	215 ± 21	-	-	193 ± 9	0.2	149
BD+56 473	V356 Per	258 ± 26	4.38 ± 0.18	111	218 ± 23	4.7	109
BD+56 478	HD 13890	179 ± 8	3.46 ± 0.18	107	152 ± 30	3.7	112
BD+56 484	V502 Per	228 ± 24	3.46 ± 0.18	124	182 ± 39	3.7	124
BD+56 493	BD+56 493	311 ± 31	3.64 ± 0.18	126	175 ± 41	4.4	122
BD+56 511	BD+56 511	111 ± 11	-	-	108 ± 54	4.1	114
BD+56 573	BD+56 573	335 ± 34	-	-	210 ± 51	4.2	119
BD+57 681	HD 237056	160 ± 17	5.90 ± 0.18	125	155 ± 20	6.0	128
BD+58 2320	HD 239758	281 ± 28	2.12 ± 0.18	59	244 ± 39	1.7	60

Appendix C

Chapter 4 plots

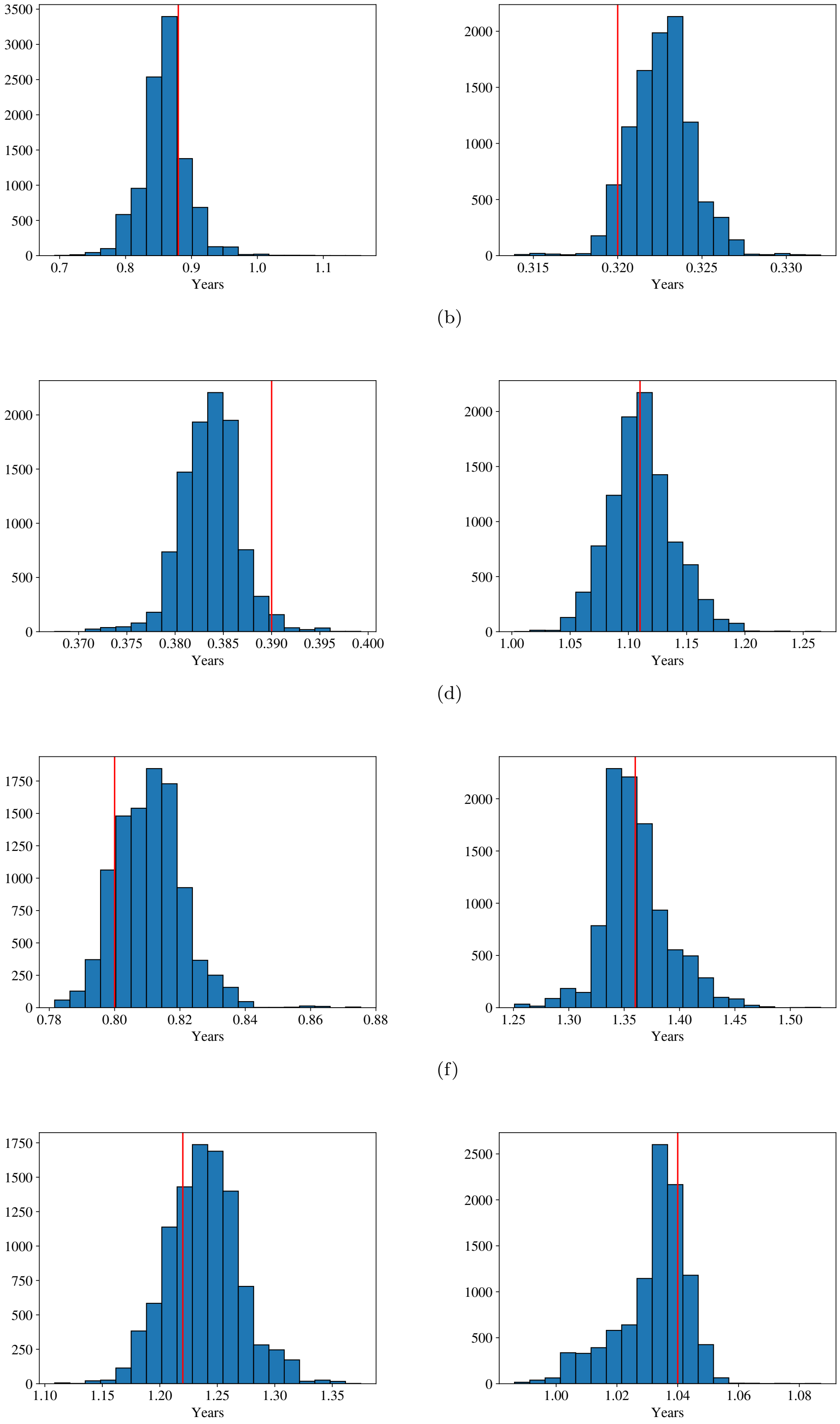

(a) (b)

(c) (d)

(e) (f)

(g) (h)

FIGURE C.1: A plot showing the results from 10000 simulations for the Hα fits for (a) CD-27 16010 (b) BD-00 3543 (c) BD+02 3815 (d) BD+37 675 (e) BD+42 4538 (f) BD+43 1048 (g) BD+47 857 (h) BD+47 3985 . The red line shows the result obtained from the fits shown in Table 4.4.

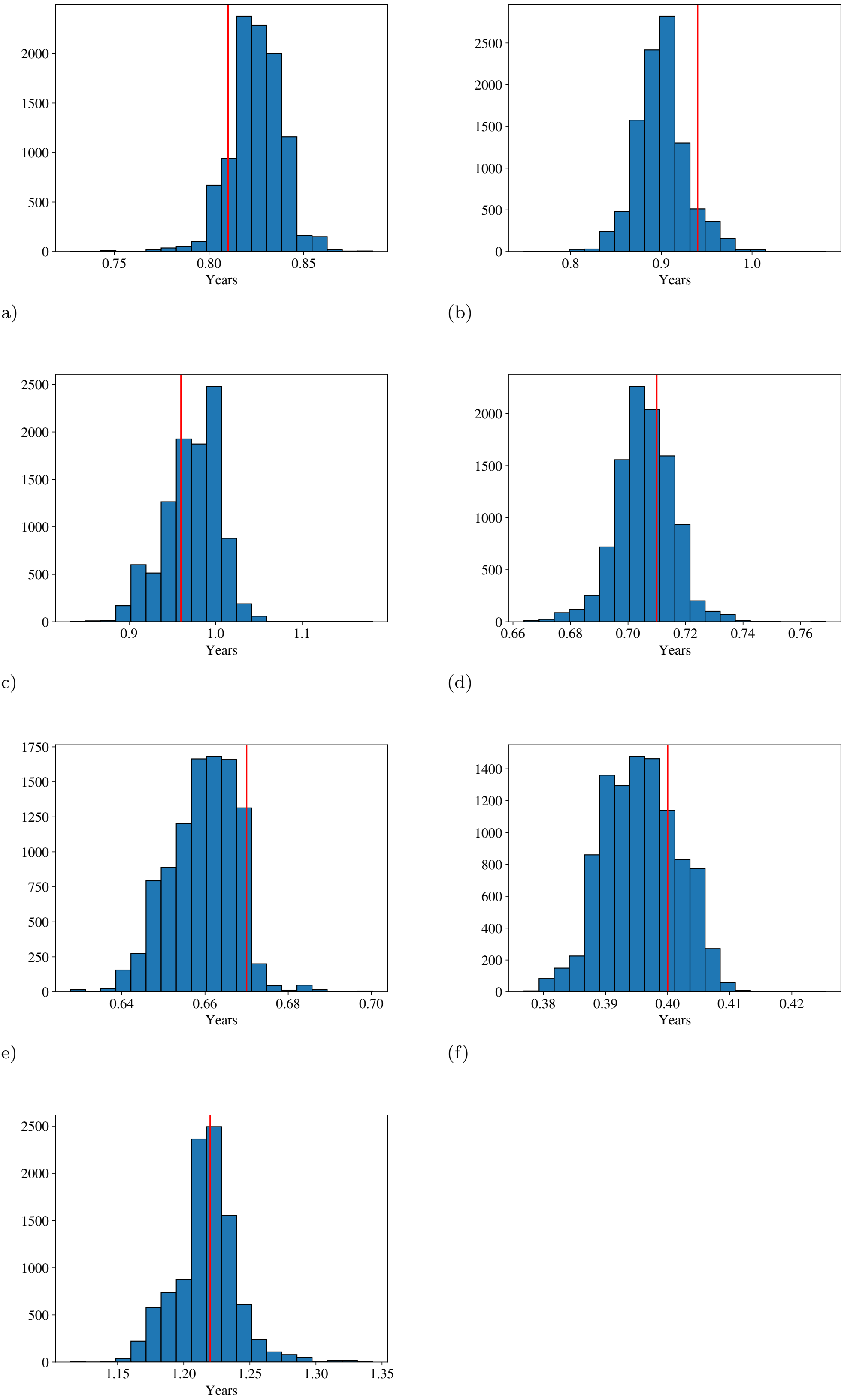

(a)

(b)

(c)

(d)

(e)

(f)

(g)

Figure C.2: A plot showing the results from 10000 simulations for the Hα fits for (a) BD+50 3430 (b) BD+53 2599 (c) BD+55 552 (d) BD+55 2411 (e) BD+56 511 (f) BD+58 554 (g) BD+58 2320. The red line shows the result obtained from the fits shown in Table 4.4.

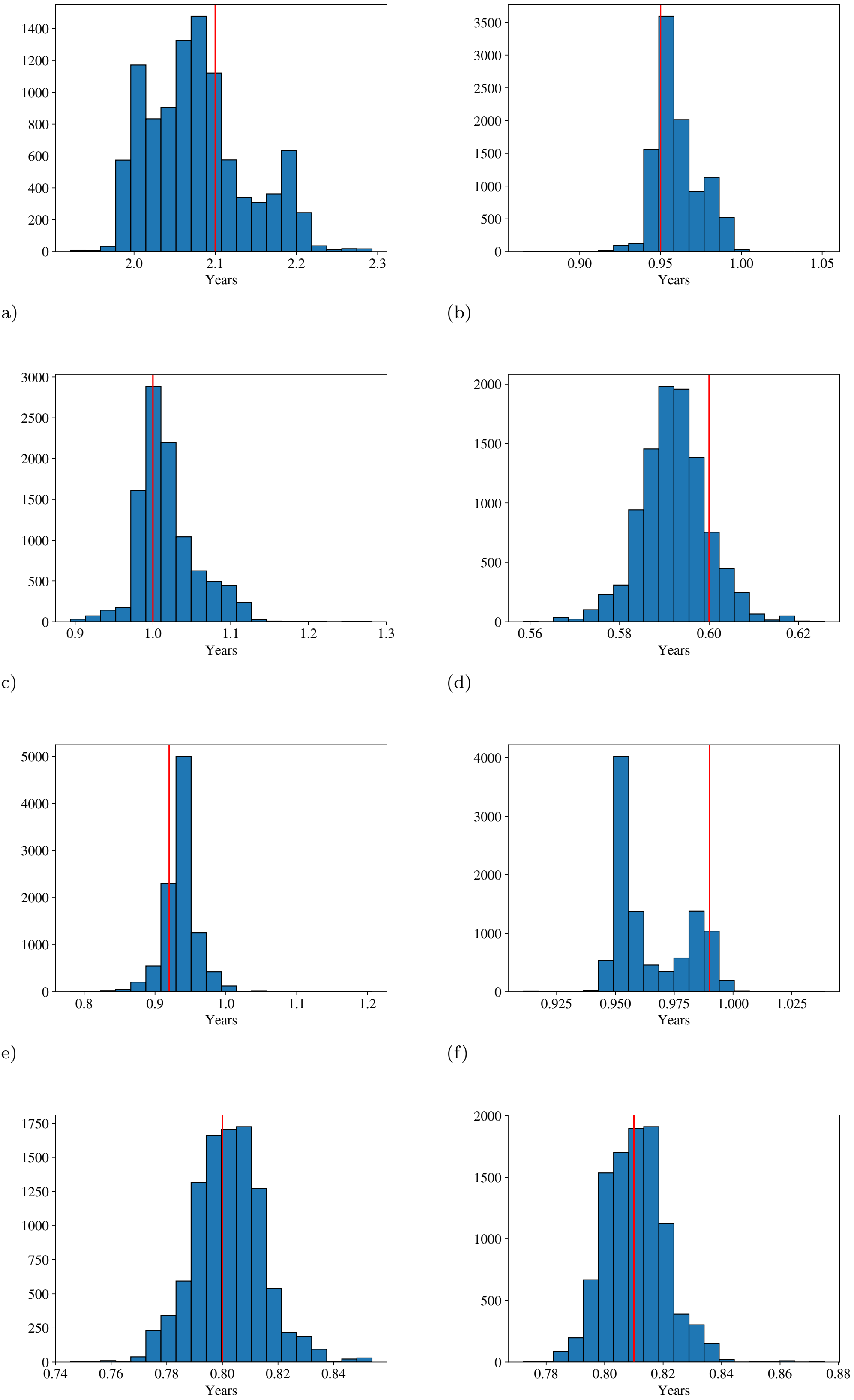

(a)

(b)

(c)

(d)

(e)

(f)

(g)

(h)

Figure C.3: A plot showing the results from 10000 simulations for the Hβ fits for (a) CD-27 11872 (b) BD-02 5328 (c) BD-01 3834 (d) BD+27 797 (e) BD+31 4018 (f) BD+36 3946 (g) BD+37 675 (h) BD+42 4538 . The red line shows the result obtained from the fits shown in Table 4.4.

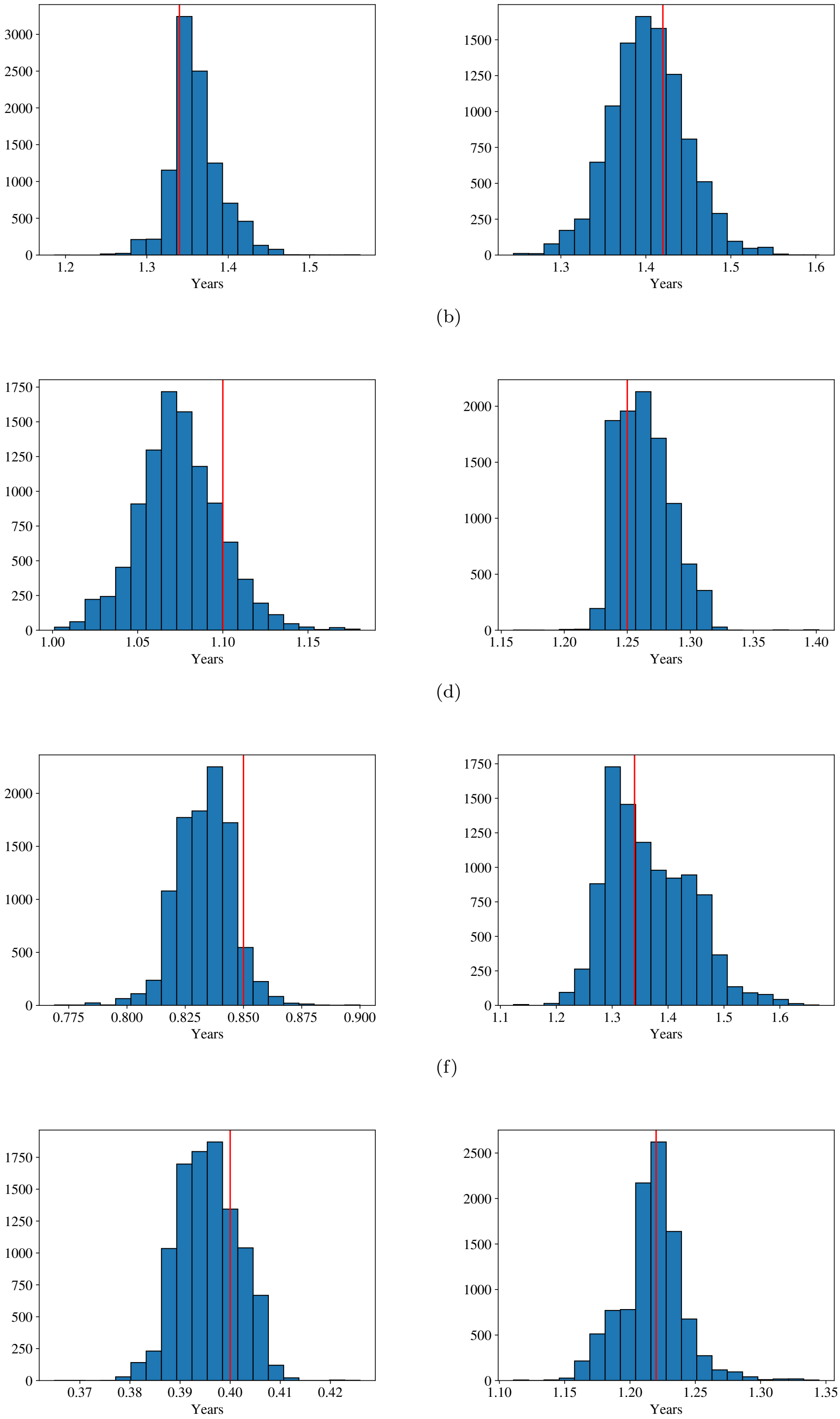

(a) (b) (c) (d) (e) (f) (g) (h)

FIGURE C.4: A plot showing the results from 10000 simulations for the Hβ fits for (a) BD+43 1048 (b) BD+47 183 (c) BD+47 857 (d) BD+47 3985 (e) BD+50 3430 (f) BD+55 552 (g) BD+58 554 (h) BD+58 2320. The red line shows the result obtained from the fits shown in Table 4.4.

Appendix D

Additional tables and plots

D.1 CD-28 14778, HD 171757

TABLE D.1: The equivalent widths (corrected for absorption) of the Hα and Hβ emission for the star CD-28 14778.

Date (MJD) (yr)	EW Hα (Å)	σ(EW Hα) (Å)	EW Hβ (Å)	σ(EW Hβ) (Å)	$v \sin i$ (km s^{-1})	σ($v \sin i$) (km s^{-1})
51029.64	-33.00	0.06	-	-	-	-
55405.12	-33.02	0.09	-	-	-	-
58276.62	-25.10	0.08	-5.09	0.04	143.82	12.01
58595.99	-24.23	0.08	-5.41	0.06	206.59	54.67
58628.43	-24.21	0.09	-4.66	0.03	135.31	10.96
58659.86	-23.80	0.08	-4.97	0.03	142.40	17.03

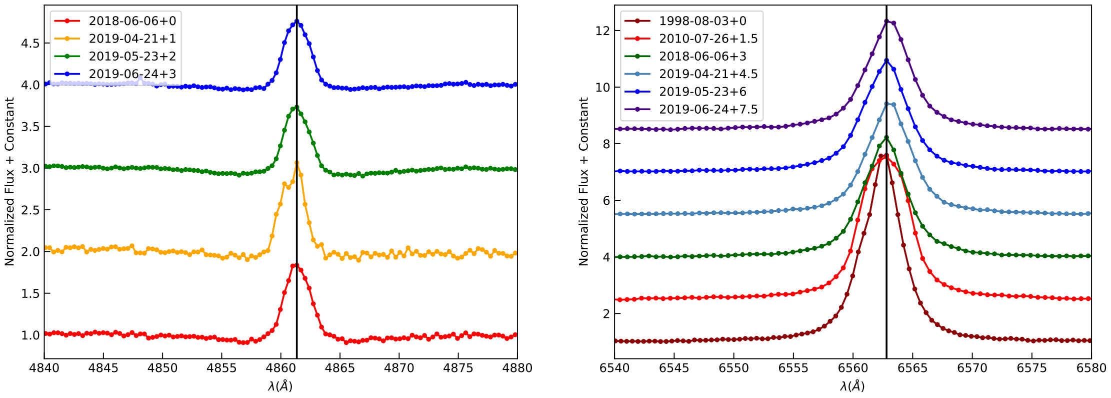

(a) (b)

FIGURE D.1: A plot showing the normalized Hβ (a) and Hα (b) lines for CD-28 14778.

D.2 CD-27 11872, HD161103

TABLE D.2: The equivalent widths (corrected for absorption) of the Hα and Hβ emission for the star CD-27 11872.

Date (MJD) (yr)	EW Hα (Å)	σ(EW Hα) (Å)	EW Hβ (Å)	σ(EW Hβ) (Å)	$v \sin i$ (km s^{-1})	$\sigma(v \sin i)$ (km s^{-1})
51029.64	-35.24	0.09	-6.26	0.48	212.27	6.22
55088.75	-36.32	0.24	-	-	-	-
55309.81	-37.34	0.52	-	-	-	-
55404.12	-39.28	0.13	-6.44	0.03	181.89	38.26
58300.62	-37.73	0.11	-6.07	0.03	207.93	15.87
58564.55	-37.15	0.15	-	-	-	-
58594.99	-37.60	0.12	-7.61	0.08	-	-
58657.86	-38.93	0.11	-6.44	0.03	205.94	18.6
59037.54	-35.12	0.11	-5.39	0.11	199.33	30.05

TABLE D.3: The Δλ distance between peaks and V and R peak values for the Hβ emission for the star CD-27 11872.

MJD (yr)	$\Delta\lambda_{\mathrm{H}\beta}$ (Å)	$\sigma(\Delta\lambda_{\mathrm{H}\beta})$ (Å)	V_β	R_β
51028.64	1.91	0.68	1.7394	1.5503
55404.12	1.74	0.49	1.6917	1.9329
58300.62	1.74	0.49	1.7351	1.6202
58594.99	1.40	0.49	1.7728	2.3273
58657.86	1.40	0.49	1.8800	1.7235
59037.54	1.39	0.49	1.8279	1.5515

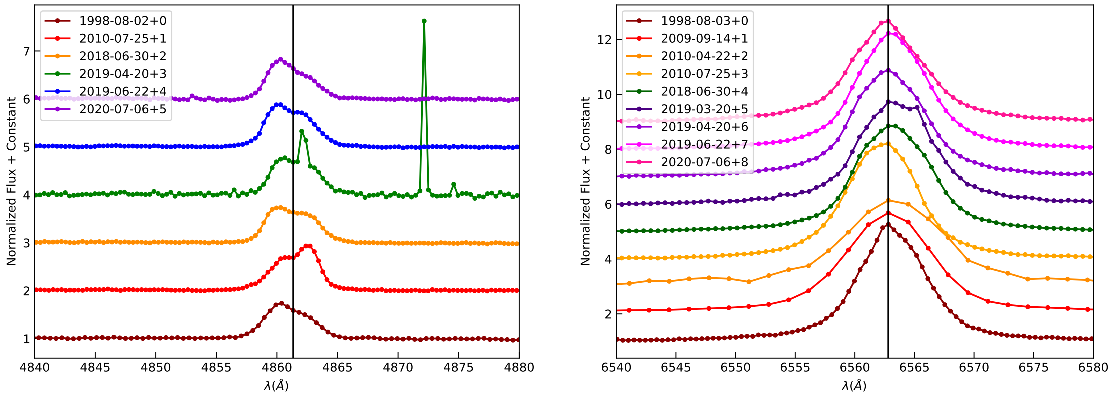

(a)

(b)

FIGURE D.2: A plot showing the normalized Hβ (a) and Hα (b) lines for CD-27 11872.

D.3 CD-27 16010, HD 214748

Table D.4: The equivalent widths (corrected for absorption) of the Hα and Hβ emission for the star CD-27 16010.

Date (MJD) (yr)	EW Hα (Å)	σ(EW Hα) (Å)	EW Hβ (Å)	σ(EW Hβ) (Å)	$v \sin i$ (km s^{-1})	$\sigma(v \sin i)$ (km s^{-1})
51029.64	-8.05	0.05	-1.57	0.65	169.20	12.03
55099.75	-10.06	0.14	-	-	-	-
55135.19	-	-	-3.17	0.14	186.59	11.91
55147.62	-10.00	0.14	-3.17	0.18	209.16	11.54
55410.12	-	-	-3.51	0.05	222.72	24.52
55438.55	-9.28	0.10	-4.08	0.05	198.98	30.2
55480.43	-9.28	0.10	-2.85	0.04	174.26	13.2
55517.86	-9.36	0.10	-3.42	0.04	183.92	14.21
56582.15	-9.54	0.09	-2.31	0.02	170.71	11.87
58280.62	-10.87	0.20	-2.32	0.11	190.79	67.17
58298.62	-9.89	0.07	-2.50	0.03	196.45	9.73
58353.49	-9.81	0.07	-2.64	0.03	188.93	9.93
58385.93	-9.86	0.07	-2.54	0.05	185.98	19.65
58662.86	-10.13	0.07	-2.95	0.04	197.52	40.27
58715.74	-9.93	0.08	-2.28	0.04	247.26	28.69
59068.98	-10.88	0.10	-	-	-	-

Table D.5: The $\Delta\lambda$ distance between peaks and V and R peak values for the Hα emission for the star CD-27 16010.

MJD (yr)	$\Delta\lambda_{\mathrm{H}\alpha}$ (Å)	$\sigma(\Delta\lambda_{\mathrm{H}\alpha})$ (Å)	V$_\alpha$	R$_\alpha$
51029.64	2.84	0.98	1.4349	1.4468
55438.55	3.0	1.1	1.5167	1.5506
55480.43	3.0	1.1	1.5472	1.5883
55517.86	3.0	1.1	1.5506	1.5844
56582.15	3.0	1.1	1.5839	1.4754
58298.62	3.0	1.1	1.6344	1.6210
58353.49	2.4	1.1	1.6056	1.6021
58385.93	2.4	1.1	1.5980	1.5780
58662.86	2.4	1.1	1.6422	1.6457
58715.74	2.4	1.1	1.6517	1.6550
59069.54	1.8	1.1	1.6571	1.6746

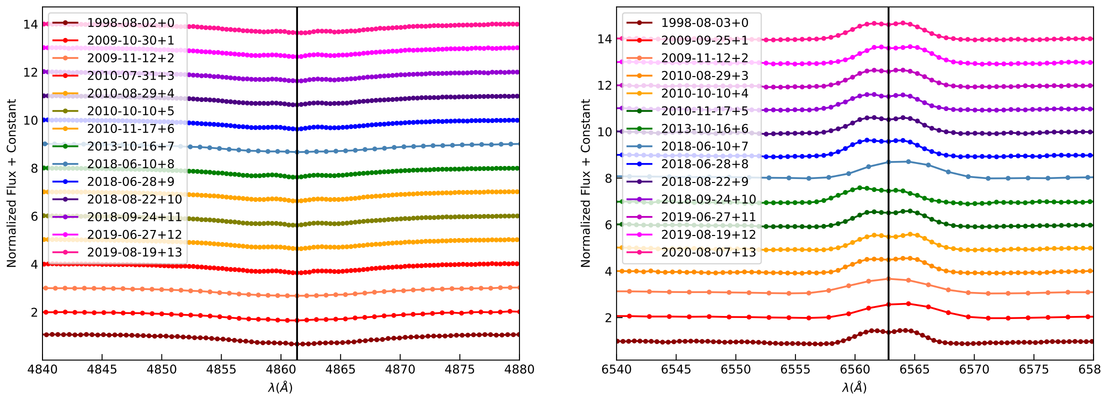

(a)

(b)

FIGURE D.3: A plot showing the normalized Hβ (a) and Hα (b) lines for CD-27 16010.

D.4 CD-25 12642, HD 164741

Table D.6: The equivalent widths (corrected for absorption) of the Hα and Hβ emission for the star CD-25 12642.

Date (MJD) (yr)	EW Hα (Å)	σ(EW Hα) (Å)	EW Hβ (Å)	σ(EW Hβ) (Å)	$v \sin i$ (km s^{-1})	$\sigma(v \sin i)$ (km s^{-1})
51029.64	0.36	0.06	0.07	0.52	101.14	1.75
55404.12	0.09	0.07	0.19	0.07	95.10	30.03
58276.62	0.17	0.07	0.35	0.07	71.56	17.75
58566.55	0.11	0.07	0.26	0.10	-	-
58599.99	0.09	0.07	0.26	0.07	80.32	47.05
58648.86	0.29	0.07	0.40	0.09	67.93	16.09
59037.54	0.38	0.07	0.44	0.06	69.98	50.53

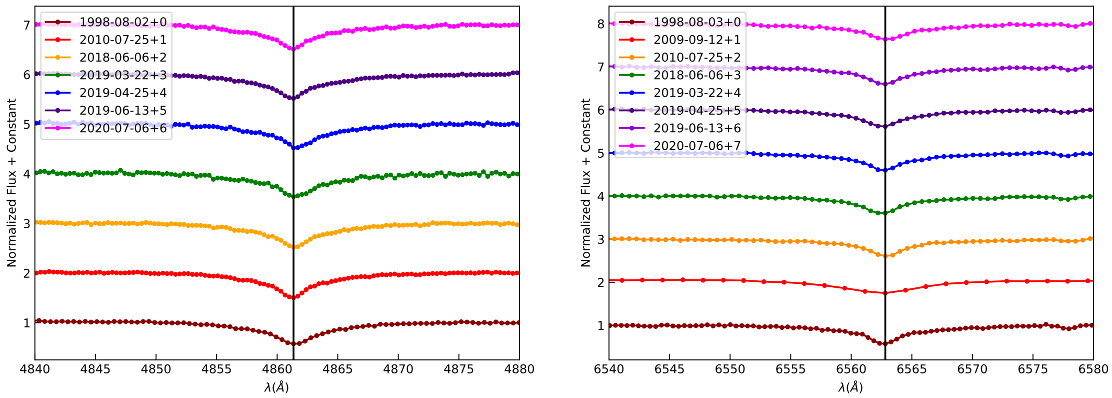

(a)

(b)

Figure D.4: A plot showing the normalized Hβ (a) and Hα (b) lines for CD-25 12642.

D.5 CD-22 13183, HD 172158

TABLE D.7: The equivalent widths (corrected for absorption) of the Hα and Hβ emission for the star CD-22 13183.

Date (MJD) (yr)	EW Hα (Å)	σ(EW Hα) (Å)	EW Hβ (Å)	σ(EW Hβ) (Å)	$v \sin i$ (km s^{-1})	$\sigma(v \sin i)$ (km s^{-1})
51029.64	-14.93	0.06	-3.17	0.77	167.20	7.97
55086.75	-21.65	0.16	-	-	-	-
55437.55	-22.37	0.12	-4.72	0.08	249.42	58.05

TABLE D.8: The $\Delta\lambda$ distance between peaks and V and R peak values for the Hα and Hβ emission for the star CD-22 13183.

MJD (yr)	$\Delta\lambda_{\mathrm{H}\alpha}$ (Å)	$\sigma(\Delta\lambda_{\mathrm{H}\alpha})$ (Å)	V$_\alpha$	R$_\alpha$	$\Delta\lambda_{\mathrm{H}\beta}$ (Å)	$\sigma(\Delta\lambda_{\mathrm{H}\beta})$ (Å)	V$_\beta$	R$_\beta$
51029.64	2.84	0.98	2.0700	2.0343	3.82	0.68	0.8885	0.8895
55437.55	3.0	1.1	2.7810	2.7617	2.43	0.49	1.0251	0.9617

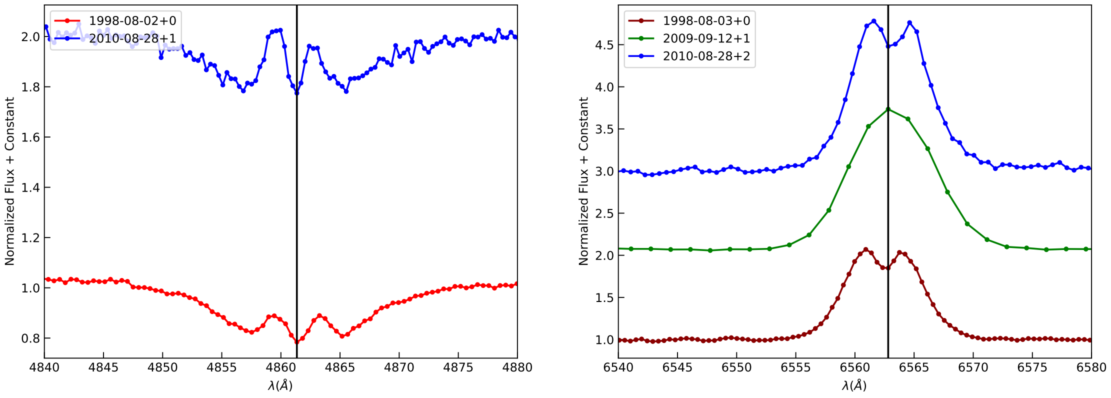

(a)

(b)

FIGURE D.5: A plot showing the normalized Hβ (a) and Hα (b) lines for CD-22 13183.

D.6 BD-20 5381, HD 177015

TABLE D.9: The equivalent widths (corrected for absorption) of the Hα and Hβ emission for the star BD-20 5381.

Date (MJD) (yr)	EW Hα (Å)	σ(EW Hα) (Å)	EW Hβ (Å)	σ(EW Hβ) (Å)	$v \sin i$ (km s^{-1})	$\sigma(v \sin i)$ (km s^{-1})
51029.64	-17.67	0.05	-2.69	0.48	196.27	1.12
55085.75	19.42	0.23	-	-	-	-
55437.55	-19.80	0.11	-2.54	0.12	299.97	16.83
58592.99	-20.27	0.07	-	-	-	-
58661.86	-20.05	0.07	-2.54	0.04	188.73	9.26

TABLE D.10: The $\Delta\lambda$ distance between peaks and V and R peak values for the Hα and Hβ emission for the star BD-20 5381.

MJD (yr)	$\Delta\lambda_{\mathrm{H}\alpha}$ (Å)	$\sigma(\Delta\lambda_{\mathrm{H}\alpha})$ (Å)	V$_\alpha$	R$_\alpha$	$\Delta\lambda_{\mathrm{H}\beta}$ (Å)	$\sigma(\Delta\lambda_{\mathrm{H}\beta})$ (Å)	V$_\beta$	R$_\beta$
51029.64	2.37	0.98	2.9821	2.5957	2.39	0.68	0.9657	0.9151
55437.55	2.4	1.1	3.0254	2.8852	2.43	0.49	0.9193	0.9510
58592.86	2.4	1.1	3.1522	2.7981	-	-	-	-
58661.86	2.4	1.1	3.0605	2.4864	2.79	0.49	0.9554	0.9019

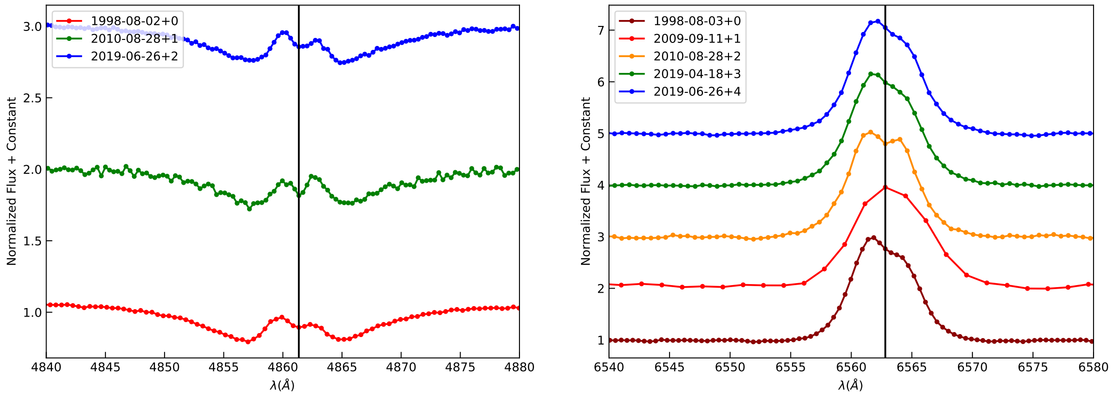

(a) (b)

FIGURE D.6: A plot showing the normalized Hβ (a) and Hα (b) lines for BD-20 5381.

D.7 BD-19 5036, HD 170682

TABLE D.11: The equivalent widths (corrected for absorption) of the Hα and Hβ emission for the star BD-19 5036.

Date (MJD) (yr)	EW Hα (Å)	σ(EW Hα) (Å)	EW Hβ (Å)	σ(EW Hβ) (Å)	$v \sin i$ (km s^{-1})	$\sigma(v \sin i)$ (km s^{-1})
51029.64	0.19	0.06	0.74	0.61	127.17	2.32
58300.62	0.31	0.04	0.84	0.04	114.13	9.19
58564.55	-0.09	0.05	0.53	0.07	139.39	323.36
58595.99	0.06	0.04	0.40	0.05	163.87	136.95
58627.43	0.27	0.06	0.94	0.07	136.56	18.81
58657.86	0.07	0.06	0.18	0.04	120.36	11.94

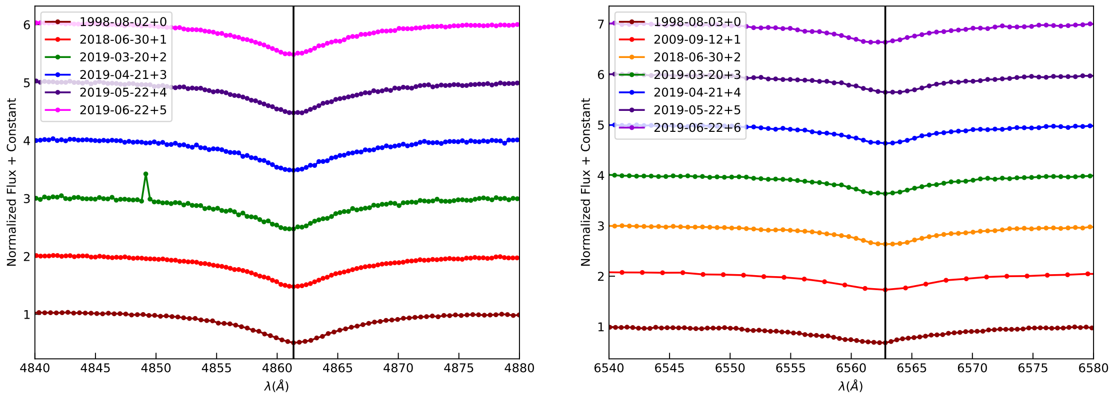

(a) (b)

FIGURE D.7: A plot showing the normalized Hβ (a) and Hα (b) lines for BD-19 5036.

D.8 BD-12 5132, HD 172252

Table D.12: The equivalent widths (corrected for absorption) of the Hα and Hβ emission for the star BD-12 5132.

Date (MJD) (yr)	EW Hα (Å)	σ(EW Hα) (Å)	EW Hβ (Å)	σ(EW Hβ) (Å)	$v \sin i$ (km s^{-1})	$\sigma(v \sin i)$ (km s^{-1})
51029.64	-25.22	0.10	-3.59	0.53	97.06	12.42
58292.62	-27.86	0.12	-3.37	0.05	91.13	45.42
58592.99	-29.29	0.13	-	-	-	-
58623.43	-26.29	0.12	-2.97	0.06	113.92	77.05
59037.54	-28.92	0.11	-3.37	0.06	112.01	41.67

Table D.13: The $\Delta\lambda$ distance between peaks and V and R peak values for the Hβ emission for the star BD-12 5132.

MJD (yr)	$\Delta\lambda_{\mathrm{H}\beta}$ (Å)	$\sigma(\Delta\lambda_{\mathrm{H}\beta})$ (Å)	V$_\beta$	R$_\beta$
51028.64	2.86	0.68	1.1722	1.1400
58292.62	3.48	0.49	1.2152	1.1923
58623.43	2.78	0.49	1.1696	1.1736
59037.54	2.09	0.49	1.2069	1.2143

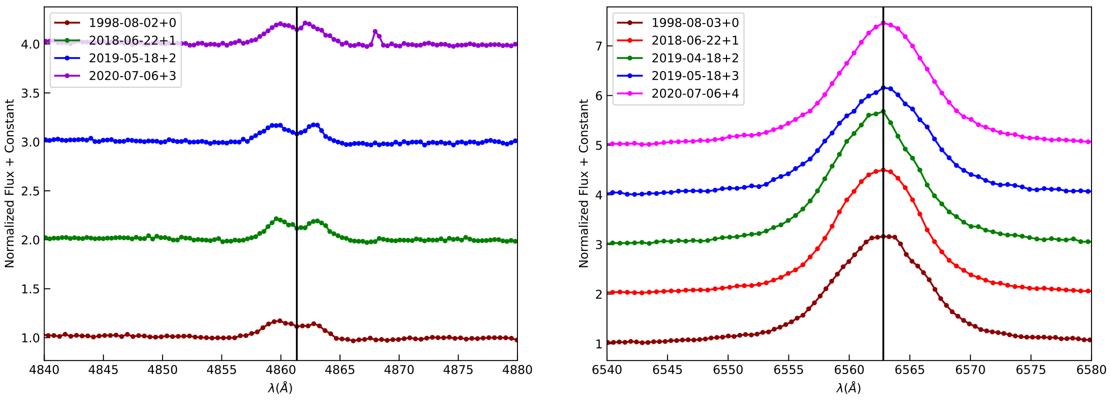

(a)

(b)

Figure D.8: A plot showing the normalized Hβ (a) and Hα (b) lines for BD-12 5132.

D.9 BD-02 5328, HD 196712

Table D.14: The equivalent widths (corrected for absorption) of the Hα and Hβ emission for the star BD-02 5328.

Date (MJD) (yr)	EW Hα (Å)	σ(EW Hα) (Å)	EW Hβ (Å)	σ(EW Hβ) (Å)	$v \sin i$ (km s^{-1})	$\sigma(v \sin i)$ (km s^{-1})
51029.64	-13.67	0.04	-1.76	0.64	159.29	5.11
55134.19	-	-	-3.26	0.11	-	-
55518.86	-14.00	0.07	-2.96	0.05	159.94	11.95
55519.86	-14.08	0.07	-2.51	0.05	156.51	15.08
55521.86	-14.13	0.08	-3.22	0.06	196.97	56.93
56584.15	-13.81	0.09	-2.91	0.03	177.59	17.66
58276.62	-13.27	0.08	-3.10	0.04	165.96	10.91
58332.06	-13.24	0.07	-2.62	0.03	170.20	23.9
58362.93	-13.23	0.10	-3.14	0.04	186.60	6.04
58616.43	-13.57	0.07	-2.85	0.05	198.10	45.85
58658.86	-13.22	0.05	-2.93	0.03	177.86	17.2
58713.74	-13.25	0.07	-3.41	0.04	192.29	18.55

Table D.15: The $\Delta\lambda$ distance between peaks and V and R peak values for the Hβ emission for the star BD-02 5328.

MJD (yr)	$\Delta\lambda_{H\beta}$ (Å)	$\sigma(\Delta\lambda_{H\beta})$ (Å)	V_β	R_β
51028.64	0.96	0.68	0.8345	0.8443
55518.86	2.44	0.49	0.7923	0.7956
55519.86	2.44	0.49	0.7854	0.7884
55521.86	2.78	0.49	0.7944	0.7890
56584.15	2.44	0.49	0.7796	0.7789
58276.62	2.44	0.49	0.7593	0.7538
58332.06	2.44	0.49	0.7435	0.7440
58362.93	2.09	0.49	0.7612	0.7546
58616.43	2.43	0.49	0.7535	0.7101
58658.86	2.09	0.49	0.7701	0.7643
58713.74	2.43	0.49	0.7698	0.7641

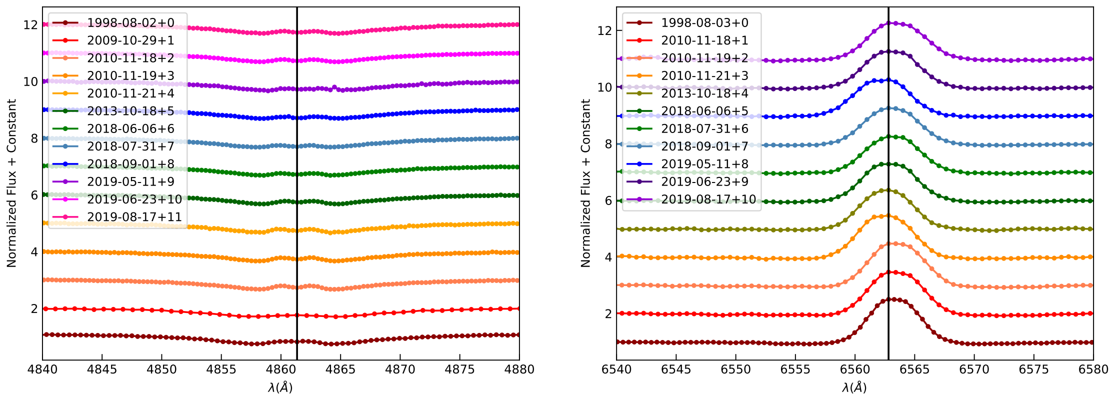

(a)

(b)

FIGURE D.9: A plot showing the normalized Hβ (a) and Hα (b) lines for BD-02 5328.

D.10 BD-01 3834, HD 187350

TABLE D.16: The equivalent widths (corrected for absorption) of the Hα and Hβ emission for the star BD-01 3834.

Date (MJD) (yr)	EW Hα (Å)	σ(EW Hα) (Å)	EW Hβ (Å)	σ(EW Hβ) (Å)	$v \sin i$ (km s^{-1})	$\sigma(v \sin i)$ (km s^{-1})
51028.64	-	-	6.79	0.44	165.33	4.49
55082.75	-49.85	0.21	-	-	-	-
55406.12	-47.70	0.09	-7.64	0.03	154.50	42.45
58276.62	-43.24	0.09	-7.15	0.03	153.80	10.15
58325.06	-42.68	0.08	-6.31	0.03	173.36	4.09
58357.49	-43.00	0.09	-6.81	0.07	199.81	114.75
58594.99	-42.48	0.09	-6.70	0.53	225.47	215.73
58627.43	-41.08	0.09	-6.83	0.03	162.79	6.0
58657.86	-43.66	0.08	-6.94	0.03	158.58	6.89
58712.74	-43.33	0.09	-7.22	0.03	148.20	8.84
59034.54	-42.29	0.09	-6.20	0.03	183.46	13.51

TABLE D.17: The $\Delta\lambda$ distance between peaks and V and R peak values for the Hβ emission for the star BD-01 3834.

MJD (yr)	$\Delta\lambda_{\mathrm{H}\beta}$ (Å)	$\sigma(\Delta\lambda_{\mathrm{H}\beta})$ (Å)	V$_\beta$	R$_\beta$
55406.12	1.39	0.49	1.7466	1.7742
58276.62	1.40	0.49	1.6482	1.6524
58325.06	1.39	0.49	1.5546	1.5905
58357.49	1.74	0.49	1.5806	1.6457
58594.99	1.39	0.49	1.6224	1.6223
58627.43	1.39	0.49	1.6045	1.5994
58657.86	1.74	0.49	1.6199	1.6284
58712.74	1.40	0.49	1.6531	1.6681
59034.54	1.74	0.49	1.5479	1.5654

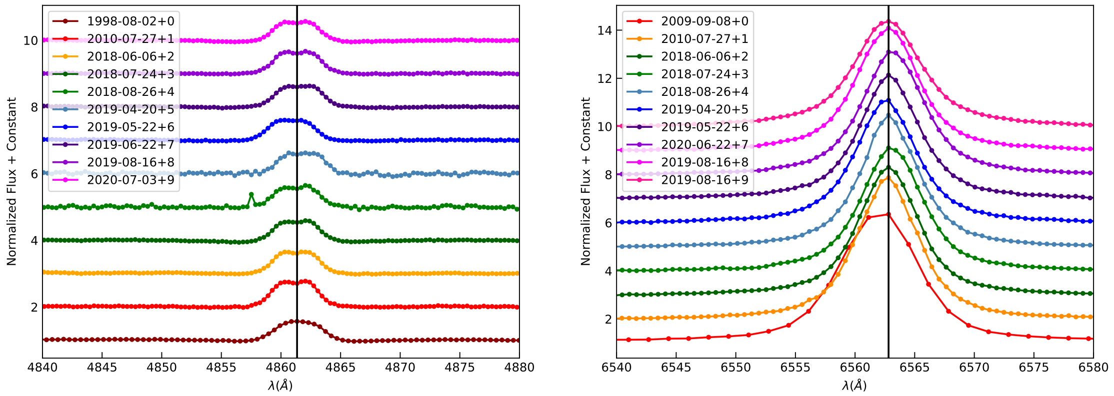

(a)

(b)

FIGURE D.10: A plot showing the normalized Hβ (a) and Hα (b) lines for BD-01 3834.

D.11 BD-00 3543, HD 173371

TABLE D.18: The equivalent widths (corrected for absorption) of the Hα and Hβ emission for the star BD-00 3543.

Date (MJD) (yr)	EW Hα (Å)	σ(EW Hα) (Å)	EW Hβ (Å)	σ(EW Hβ) (Å)	$v \sin i$ (km s^{-1})	$\sigma(v \sin i)$ (km s^{-1})
51029.64	-8.83	0.06	-1.37	0.66	219.40	10.81
55082.75	-13.42	0.16	-	-	-	-
55405.12	-13.82	0.10	-	-	-	-
58300.62	-11.66	0.09	-2.82	0.03	230.30	26.37
58534.12	-11.99	0.12	-2.98	0.07	250.98	244.79
58599.99	-11.40	0.07	-3.04	0.04	176.10	64.29
58654.86	-11.25	0.08	-2.53	0.03	223.92	27.57
59037.54	-10.99	0.12	-2.57	0.04	232.65	13.59

TABLE D.19: The $\Delta\lambda$ distance between peaks and V and R peak values for the Hα and Hβ emission for the star BD-00 3543.

MJD (yr)	$\Delta\lambda_{\mathrm{H}\alpha}$ (Å)	$\sigma(\Delta\lambda_{\mathrm{H}\alpha})$ (Å)	V$_\alpha$	R$_\alpha$
51029.64	5.21	0.98	1.4245	1.4223
55404.12	4.8	1.1	1.8707	1.8483
58300.62	4.8	1.1	1.7007	1.7067
58534.12	4.8	1.1	1.7077	1.7303
58566.99	4.8	1.1	1.8030	1.6061
58599.99	4.2	1.1	1.6749	1.6842
58654.86	4.8	1.1	1.6775	1.6711
59037.54	4.8	1.1	1.5703	1.5614

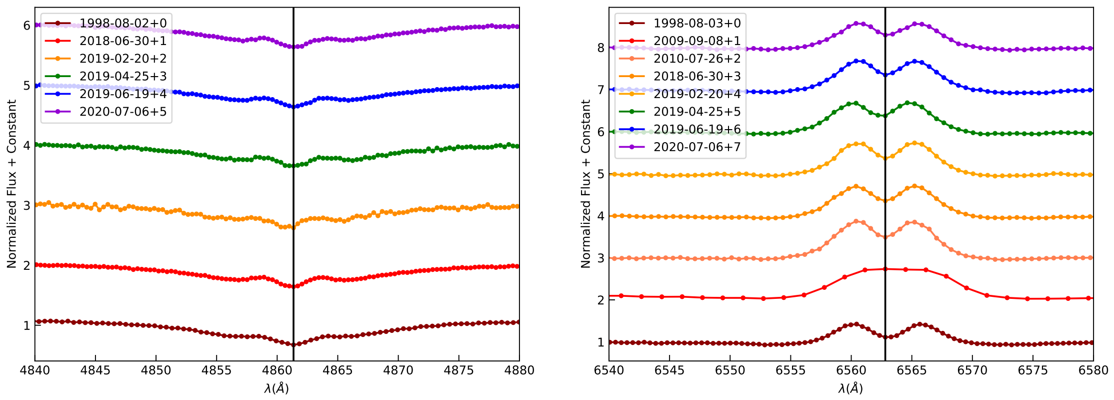

(a)

(b)

FIGURE D.11: A plot showing the normalized Hβ (a) and Hα (b) lines for BD-00 3543.

D.12 BD+02 3815, HD 179343

TABLE D.20: The equivalent widths (corrected for absorption) of the Hα and Hβ emission for the star BD+02 3815.

Date (MJD) (yr)	EW Hα (Å)	σ(EW Hα) (Å)	EW Hβ (Å)	σ(EW Hβ) (Å)	$v \sin i$ (km s^{-1})	$\sigma(v \sin i)$ (km s^{-1})
51029.64	-13.01	0.05	-	-	-	-
55400.12	-14.95	0.10	-	-	-	-
58275.62	-15.04	0.13	-5.17	0.03	208.15	29.74
58329.06	-14.83	0.10	-5.17	0.03	202.01	27.28
58564.55	-15.53	0.10	-4.96	0.05	238.41	131.76
58594.99	-15.29	0.10	-5.12	0.03	187.84	98.43
58627.43	-14.65	0.08	-4.95	0.04	199.36	40.26
58657.86	-14.13	0.10	-5.20	0.03	175.54	32.64
59034.54	-14.53	0.11	-5.13	0.03	180.35	68.36

TABLE D.21: The $\Delta\lambda$ distance between peaks and V and R peak values for the Hα emission for the star BD+02 3815.

MJD (yr)	$\Delta\lambda_{\mathrm{H}\alpha}$ (Å)	$\sigma(\Delta\lambda_{\mathrm{H}\alpha})$ (Å)	V_α	R_α
51029.64	5.21	0.98	1.9151	1.9033
55400.12	5.4	1.1	2.0449	2.0566
58275.62	4.8	1.1	2.0172	2.0208
58329.06	4.8	1.1	2.0073	1.9870
58564.55	4.8	1.1	2.0067	1.9806
58594.99	4.8	1.1	2.0155	1.9742
58627.43	4.8	1.1	2.0050	1.9762
58657.86	5.4	1.1	1.9520	1.9425
59034.54	4.8	1.1	1.8452	1.8266

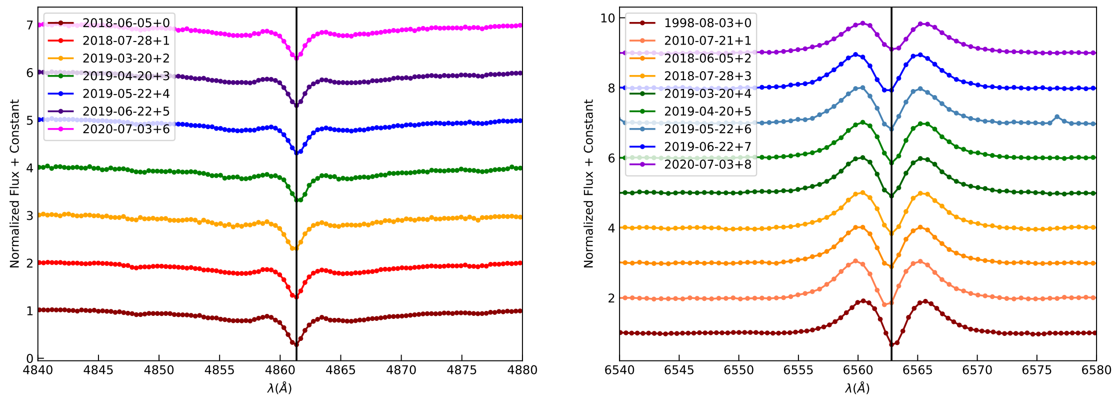

(a) (b)

FIGURE D.12: A plot showing the normalized Hβ (a) and Hα (b) lines for BD+02 3815.

D.13 BD+05 3704, HD 168797

Table D.22: The equivalent widths (corrected for absorption) of the Hα and Hβ emission for the star BD+05 3704.

Date (MJD) (yr)	EW Hα (Å)	σ(EW Hα) (Å)	EW Hβ (Å)	σ(EW Hβ) (Å)	$v \sin i$ (km s^{-1})	σ($v \sin i$) (km s^{-1})
51029.64	-4.02	0.06	-0.99	0.57	189.42	7.83
52576.49	-	-	-4.90	0.07	97.85	94.07
55085.75	-2.28	0.75	-	-	-	-
55401.12	-0.23	0.07	-	-	-	-
58275.62	-0.20	0.06	-0.23	0.06	202.76	12.59
58534.12	-0.71	0.05	-0.05	0.10	292.24	24.48
58567.55	-1.20	0.15	-0.79	0.19	304.42	115.57
58598.99	0.16	0.07	-0.12	0.06	209.08	9.16
58650.86	-0.23	0.06	-0.02	0.06	211.81	1.23
59034.54	-0.32	0.07	0.32	0.06	211.51	6.8

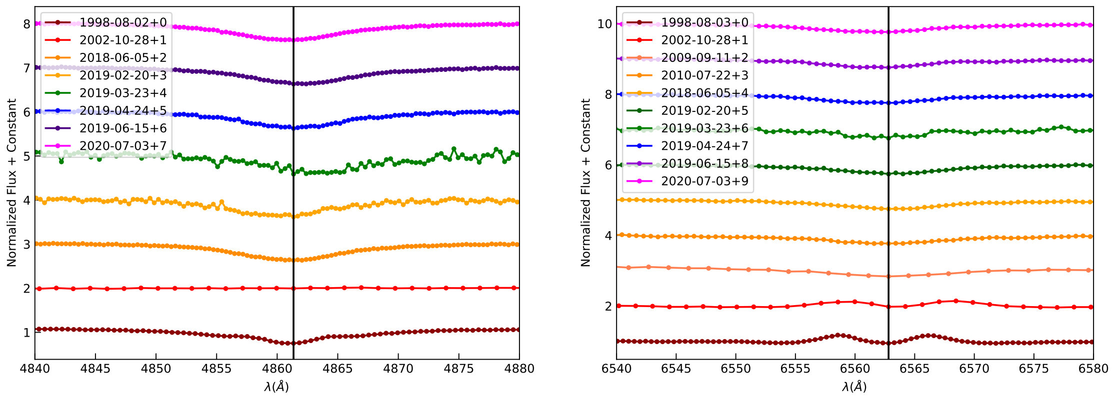

(a) (b)

Figure D.13: A plot showing the normalized Hβ (a) and Hα (b) lines for BD+05 3704.

D.14 BD+17 4087, HD 350559

TABLE D.23: The equivalent widths (corrected for absorption) of the Hα and Hβ emission for the star BD+17 4087.

Date (MJD) (yr)	EW Hα (Å)	σ(EW Hα) (Å)	EW Hβ (Å)	σ(EW Hβ) (Å)	$v \sin i$ (km s^{-1})	$\sigma(v \sin i)$ (km s^{-1})
51029.64	-1.58	0.08	-1.09	0.59	197.46	4.98
58275.62	-8.23	0.13	-3.13	0.03	227.75	71.49
58326.06	-7.29	0.12	-2.98	0.03	213.18	10.01
58358.49	-7.50	0.13	-2.79	0.03	208.9	11.71
58619.43	-5.81	0.11	-3.06	0.07	217.06	11.83
58651.86	-5.36	0.11	-	-	-	-
58687.30	-5.34	0.1	-2.36	0.05	226.5	51.66
59035.54	-4.88	0.08	-1.90	0.28	497.81	93.99

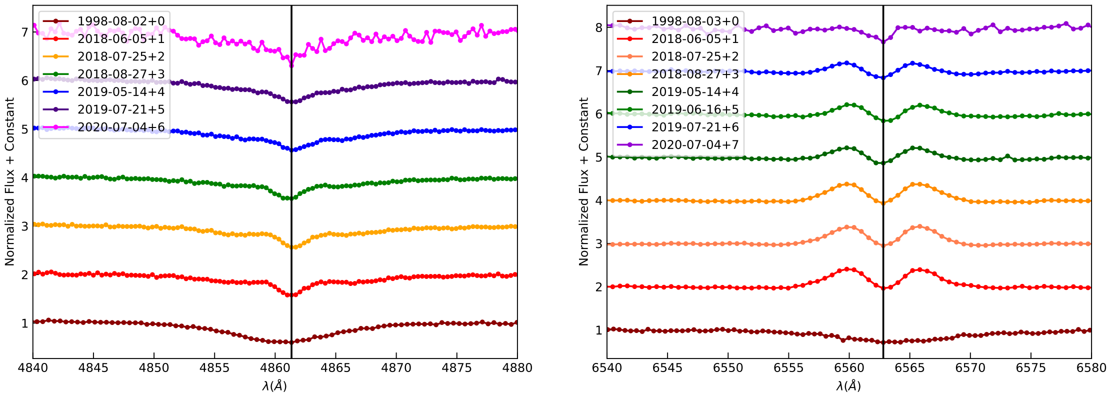

(a) (b)

FIGURE D.14: A plot showing the normalized Hβ (a) and Hα (b) lines for BD+17 4087.

D.15 BD+19 578, HD 23016

Table D.24: The equivalent widths (corrected for absorption) of the Hα and Hβ emission for the star BD+19 578.

Date (MJD) (yr)	EW Hα (Å)	σ(EW Hα) (Å)	EW Hβ (Å)	σ(EW Hβ) (Å)	$v \sin i$ (km s^{-1})	$\sigma(v \sin i)$ (km s^{-1})
51029.64	-3.37	0.06	-0.59	0.52	227.04	15.44
55091.75	-5.41	0.57	-	-	-	-
55143.62	-	-	-1.33	0.08	215.19	41.32
55423.55	-3.13	0.08	-2.25	0.05	231.65	6.79
55486.43	-2.63	0.05	-2.14	0.04	213.24	2.24
56543.72	-2.68	0.09	-1.54	0.03	283.88	6.15
57763.19	-6.82	0.56	-0.45	0.11	201.9	2.54
58355.49	-2.73	0.06	-1.90	0.03	183.9	17.23
58384.93	-2.27	0.05	-2.05	0.04	224.18	18.21
58469.24	-2.58	0.06	-1.48	0.04	253.18	28.1
58715.74	-2.47	0.05	-0.78	0.04	237.58	11.56
59212.73	-0.23	0.20	-1.67	0.04	215.49	28.43

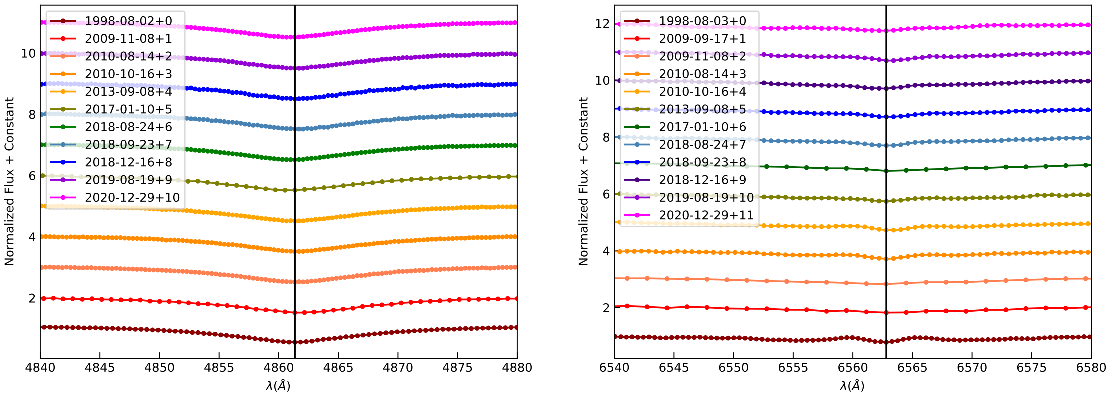

(a)

(b)

Figure D.15: A plot showing the normalized Hβ (a) and Hα (b) lines for BD+19 578.

D.16 BD+20 4449, HD 191531

Table D.25: The equivalent widths (corrected for absorption) of the Hα and Hβ emission for the star BD+20 4449.

Date (MJD) (yr)	EW Hα (Å)	σ(EW Hα) (Å)	EW Hβ (Å)	σ(EW Hβ) (Å)	$v \sin i$ (km s^{-1})	$\sigma(v \sin i)$ (km s^{-1})
51029.64	0.60	0.07	0.51	0.47	76.17	11.3
55138.62	-4.83	1.15	-0.10	0.09	174.86	20.77
55523.86	0.66	0.08	0.72	0.06	60.33	18.24

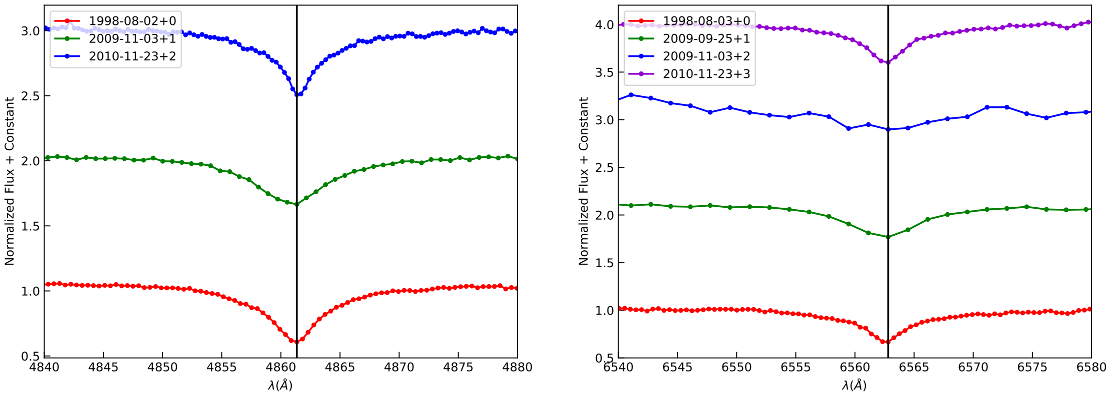

(a)

(b)

Figure D.16: A plot showing the normalized Hβ (a) and Hα (b) lines for BD+20 4449.

D.17 BD+21 4695, HD 210129

Table D.26: The equivalent widths (corrected for absorption) of the Hα and Hβ emission for the star BD+21 4695.

Date (MJD) (yr)	EW Hα (Å)	σ(EW Hα) (Å)	EW Hβ (Å)	σ(EW Hβ) (Å)	$v \sin i$ (km s^{-1})	$\sigma(v \sin i)$ (km s^{-1})
51029.64	-7.56	0.04	-0.28	0.55	136.93	8.8
55138.62	-20.97	0.15	-1.81	0.07	154.61	27.82
55396.12	-21.39	0.08	-3.09	0.04	160.06	3.42
55499.43	-21.29	0.07	-2.38	0.03	151.2	38.21
56582.15	-20.15	0.08	-1.54	0.03	156.15	28.41
58238.75	-19.52	0.21	-1.05	0.08	201.0	38.3
59034.54	-18.05	0.07	-1.41	0.03	147.33	23.16
59068.98	-18.60	0.70	-	-	-	-

Table D.27: The $\Delta\lambda$ distance between peaks and V and R peak values for the Hβ emission for the star BD+21 4695.

MJD (yr)	$\Delta\lambda_{\mathrm{H}\beta}$ (Å)	$\sigma(\Delta\lambda_{\mathrm{H}\beta})$ (Å)	V$_\beta$	R$_\beta$
51028.64	1.91	0.68	0.7580	0.7588
55396.12	1.74	0.49	1.0047	1.0065
55499.43	1.74	0.49	1.0285	1.0257
56582.15	1.40	0.49	1.0285	1.0257
59034.54	1.39	0.49	0.9457	0.9509

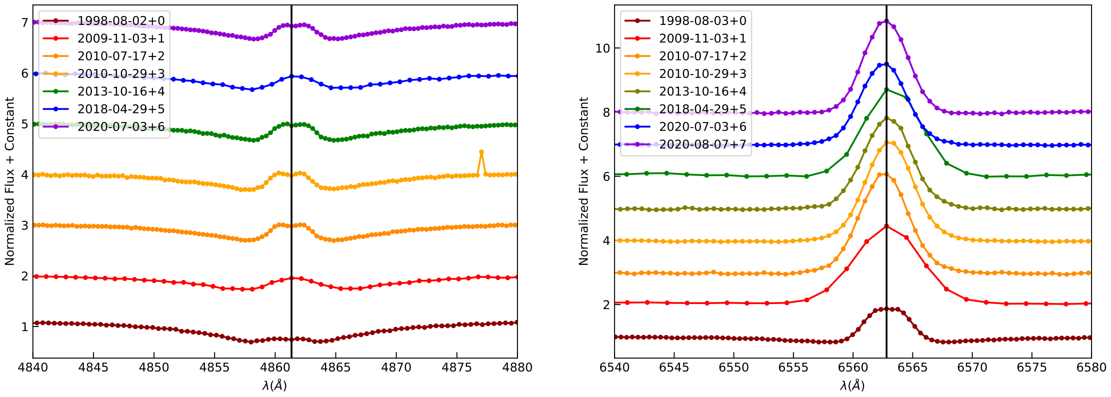

(a) (b)

Figure D.17: A plot showing the normalized Hβ (a) and Hα (b) lines for BD+21 4695.

D.18 BD+23 1148, HD 250289

Table D.28: The equivalent widths (corrected for absorption) of the Hα and Hβ emission for the star BD+23 1148.

Date (MJD) (yr)	EW Hα (Å)	σ(EW Hα) (Å)	EW Hβ (Å)	σ(EW Hβ) (Å)	$v \sin i$ (km s^{-1})	$\sigma(v \sin i)$ (km s^{-1})
51029.64	-2.31	0.06	-1.72	0.44	97.12	1.18
55100.75	-4.83	0.33	-	-	-	-
55137.62	-5.96	0.49	-2.33	0.07	128.83	29.89
55433.55	-2.41	0.09	-1.80	0.05	80.63	54.66
55486.43	-2.16	0.13	-1.72	0.05	38.26	2.96
56556.72	-2.87	0.06	-1.81	0.05	46.23	10.71
58361.49	-2.54	0.06	-1.80	0.04	42.11	9.22
58454.24	-2.58	0.07	-1.80	0.05	52.94	14.38
58484.68	-2.61	0.05	-	-	344.64	100.96
59187.73	-2.86	0.08	-1.93	0.05	44.68	9.8
59245.16	-0.22	0.25	-1.67	0.06	46.59	8.66

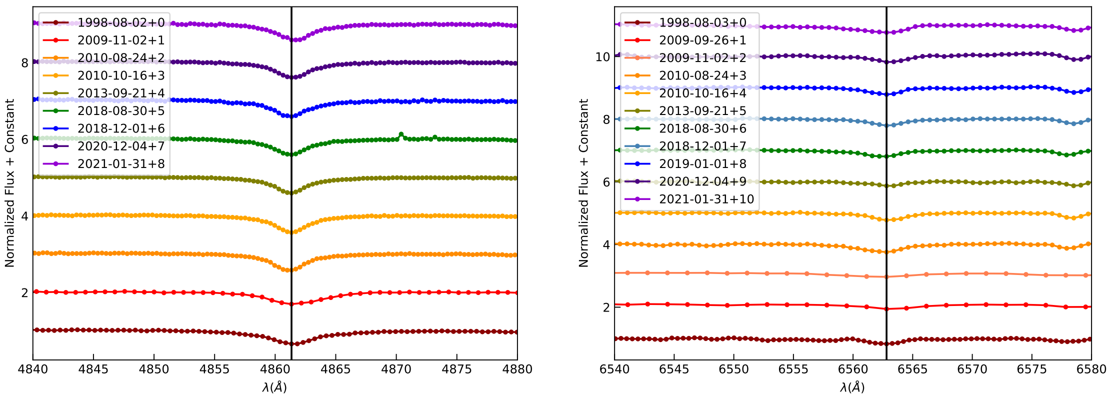

(a)

(b)

Figure D.18: A plot showing the normalized Hβ (a) and Hα (b) lines for BD+23 1148.

D.19 BD+25 4083, HD 339483

Table D.29: The equivalent widths (corrected for absorption) of the Hα and Hβ emission for the star BD+25 4083.

Date (MJD) (yr)	EW Hα (Å)	σ(EW Hα) (Å)	EW Hβ (Å)	σ(EW Hβ) (Å)	$v \sin i$ (km s^{-1})	$\sigma(v \sin i)$ (km s^{-1})
51028.64	-	-	-	-	69.49	12.21
55156.62	-1.73	0.37	-0.06	0.13	174.29	2.31
55523.86	-0.28	0.07	-0.14	0.06	57.37	18.07
58293.62	0.00	0.12	-0.17	0.06	60.11	16.31
58329.06	0.21	0.08	0.02	0.06	76.67	17.56
58363.93	-0.12	0.08	-0.16	0.06	72.46	15.59
58612.43	-0.21	0.08	0.07	0.06	56.23	296.3
58653.86	-0.18	0.08	0.15	0.06	67.9	18.23
58713.74	-0.14	0.08	0.10	0.06	70.83	27.38
59036.54	-0.09	0.07	0.07	0.06	65.79	21.15

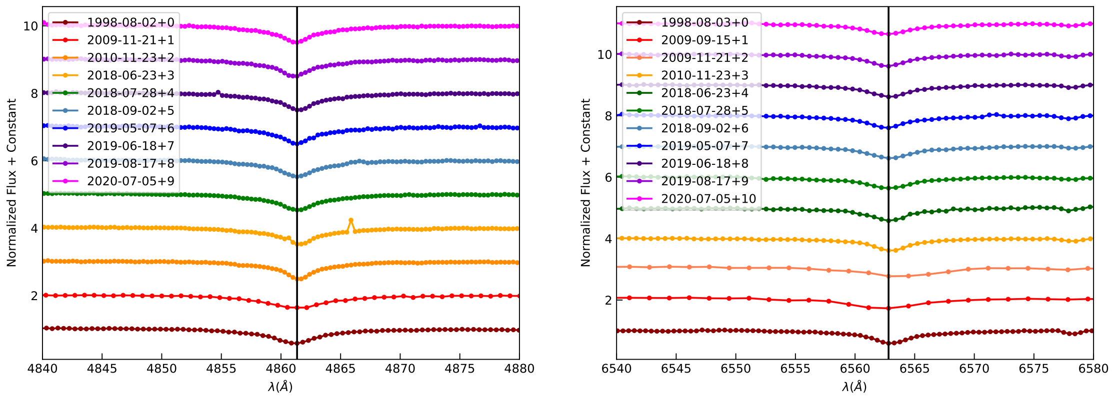

(a)

(b)

Figure D.19: A plot showing the normalized Hβ (a) and Hα (b) lines for BD+25 4083.

D.20 BD+27 797, HD 244894

TABLE D.30: The equivalent widths (corrected for absorption) of the Hα and Hβ emission for the star BD+27 797.

Date (MJD) (yr)	EW Hα (Å)	σ(EW Hα) (Å)	EW Hβ (Å)	σ(EW Hβ) (Å)	$v \sin i$ (km s^{-1})	$\sigma(v \sin i)$ (km s^{-1})
51029.64	-21.24	0.12	-4.13	0.52	138.68	14.12
55100.75	-21.74	0.26	-	-	-	-
55137.62	-23.60	0.54	-5.80	0.05	168.63	11.28
55432.55	-30.85	0.13	-6.16	0.05	159.65	104.38
55486.43	-25.23	0.37	-4.63	0.04	179.02	35.7
56557.72	-24.52	0.11	-4.75	0.02	194.95	10.7
58358.49	-27.78	0.1	-4.57	1.04	175.62	29.35
58362.93	-29.58	0.2	-4.80	0.03	192.86	24.14
58365.93	-27.91	0.1	-4.94	0.03	174.45	20.0
58370.93	-27.93	0.1	-4.65	0.06	241.44	52.16
58384.93	-27.93	0.1	-4.91	0.06	223.41	23603.07
58454.24	-26.78	1.18	-4.90	0.07	252.58	24.55
58469.24	-28.69	0.11	-4.65	0.05	237.15	25.94
58478.24	-29.10	0.1	-4.76	0.04	242.33	11.49
58481.24	-38.96	1.01	-4.82	0.08	239.99	56.88
58484.68	-29.64	0.11	-4.97	0.03	320.16	154.31
58498.68	-29.75	0.1	-4.75	0.03	203.94	40.88
58506.68	-28.27	1.41	-4.79	0.06	257.26	24.12

TABLE D.31: The $\Delta\lambda$ distance between peaks and V and R peak values for the Hβ emission for the star BD+27 797.

MJD (yr)	$\Delta\lambda_{\mathrm{H}\beta}$ (Å)	$\sigma(\Delta\lambda_{\mathrm{H}\beta})$ (Å)	V$_\beta$	R$_\beta$
51028.64	1.91	0.68	1.3678	1.3902
55432.55	1.39	0.49	1.8241	1.8049
55486.43	1.74	0.49	1.6122	1.5753
56557.72	1.75	0.49	1.5500	1.4787
58358.49	1.74	0.49	1.4744	1.4918
58362.93	1.74	0.49	1.4591	1.4828
58365.93	1.74	0.49	1.5007	1.5150
58370.93	1.74	0.49	1.4702	1.4883
58384.93	1.74	0.49	1.4889	1.5146
58454.24	2.44	0.49	1.5010	1.5465
58469.24	1.05	0.49	1.5187	1.5254
58478.24	1.75	0.49	1.4992	1.5195
58481.24	1.74	0.49	1.5064	1.5005
58484.68	1.74	0.49	1.5481	1.5225
58498.68	1.39	0.49	1.5508	1.5255
58506.68	1.05	0.49	1.5367	1.5210

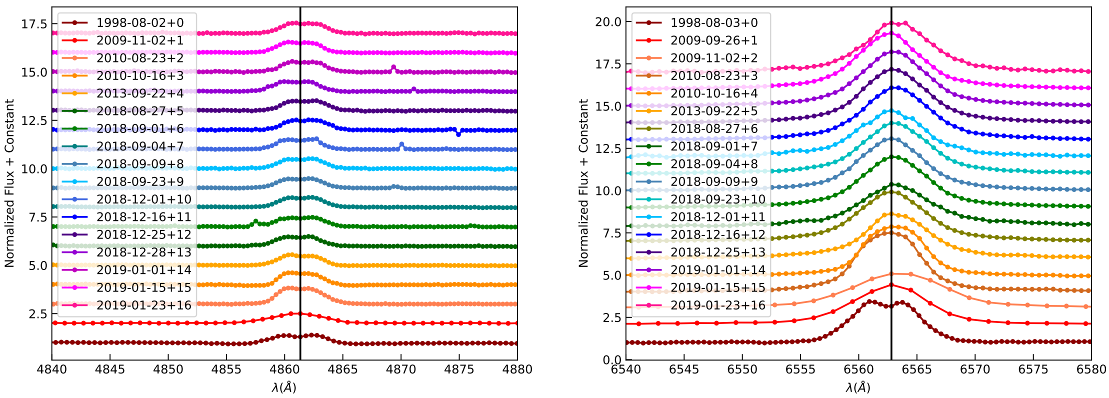

(a) (b)

FIGURE D.20: A plot showing the normalized Hβ (a) and Hα (b) lines for BD+27 797.

D.21 BD+27 850, HD 246878

TABLE D.32: The equivalent widths (corrected for absorption) of the Hα and Hβ emission for the star BD+27 850.

Date (MJD) (yr)	EW Hα (Å)	σ(EW Hα) (Å)	EW Hβ (Å)	σ(EW Hβ) (Å)	$v \sin i$ (km s^{-1})	$\sigma(v \sin i)$ (km s^{-1})
51029.64	0.69	0.06	0.22	0.62	105.99	3.28
55100.75	-2.44	0.31	-	-	-	-
55134.19	-	-	0.26	0.11	170.63	9.33
55137.62	-4.40	0.51	-0.25	0.10	158.1	8.72
55432.55	-0.02	0.08	-0.28	0.08	119.57	28.4
55486.43	0.09	0.06	-0.05	0.07	86.23	12.65
56557.72	0.38	0.08	-0.05	0.09	82.48	41.3
58358.49	-0.17	0.06	0.03	0.07	86.76	17.89
58448.80	-0.21	0.07	0.24	0.49	125.57	154.02
58481.24	-0.19	0.06	0.08	0.08	130.91	3.82
59187.73	0.15	0.22	-0.03	0.08	99.4	284.54
59215.16	-0.06	0.10	-0.14	0.07	92.43	19.97

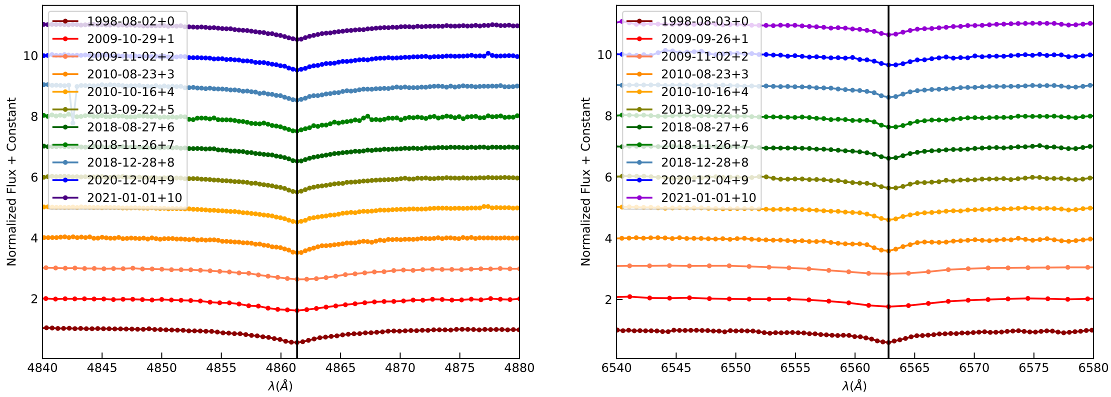

(a)

(b)

FIGURE D.21: A plot showing the normalized Hβ (a) and Hα (b) lines for BD+27 850.

D.22 BD+27 3411, HD 183914

TABLE D.33: The equivalent widths (corrected for absorption) of the Hα and Hβ emission for the star BD+27 3411.

Date (MJD) (yr)	EW Hα (Å)	σ(EW Hα) (Å)	EW Hβ (Å)	σ(EW Hβ) (Å)	$v \sin i$ (km s^{-1})	σ($v \sin i$) (km s^{-1})
51028.64	-	-	-	-	121.15	49.75
52575.49	-	-	-	-	159.33	341.18
55396.12	0.30	7.32	-6.59	0.39	203.86	108.4
58236.75	-2.99	7.32	-0.49	0.14	218.16	142.02
58293.62	0.45	7.32	-6.03	0.26	204.25	67.64
58384.93	0.56	7.32	-6.31	0.27	154.81	50.66
58623.43	0.42	7.32	-5.91	0.29	197.25	30.46
58653.86	-	-	-	-	170.6	45.03
58715.74	0.55	7.32	-5.73	0.24	148.66	59.36
59034.54	0.73	7.32	-5.90	0.26	150.64	43.74

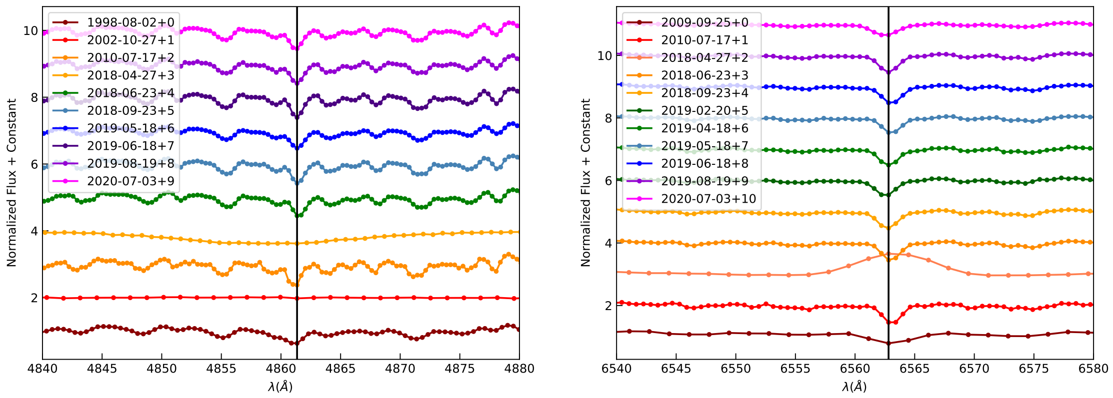

(a)

(b)

FIGURE D.22: A plot showing the normalized Hβ (a) and Hα (b) lines for BD+27 3411.

D.23 BD+28 3598, HD 333452

Table D.34: The equivalent widths (corrected for absorption) of the Hα and Hβ emission for the star BD+28 3598.

Date (MJD) (yr)	EW Hα (Å)	σ(EW Hα) (Å)	EW Hβ (Å)	σ(EW Hβ) (Å)	$v \sin i$ (km s^{-1})	$\sigma(v \sin i)$ (km s^{-1})
51029.64	0.19	0.07	0.17	0.53	107.96	4.76
55099.75	-1.36	0.16	-	-	-	-
55519.86	-0.05	0.08	0.41	0.05	136.78	86.47
58331.06	-0.33	0.08	0.62	0.07	201.1	20.96
58370.93	-0.45	0.07	0.35	0.05	193.56	40.73
58661.86	-0.57	0.09	0.42	0.07	104.52	20.09
59037.54	-0.03	0.07	0.11	0.05	142.19	59.95

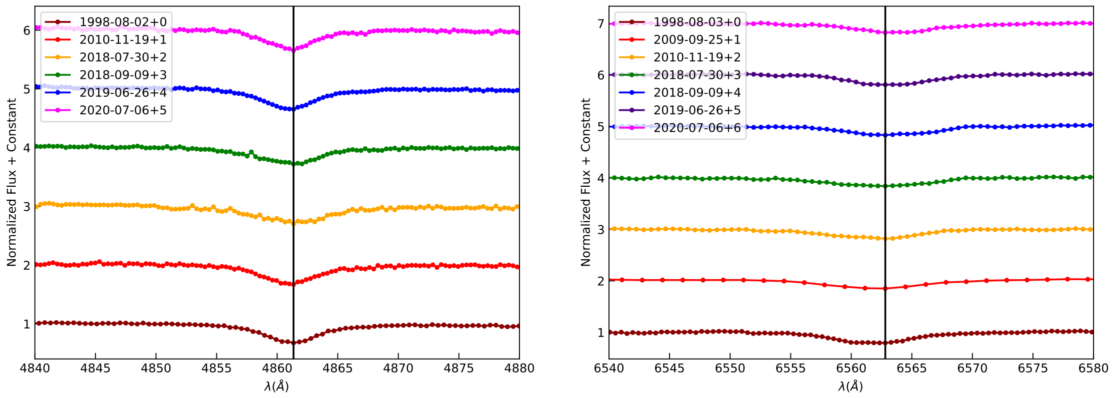

(a)

(b)

Figure D.23: A plot showing the normalized Hβ (a) and Hα (b) lines for BD+28 3598.

D.24 BD+29 3842, HD 333226

Table D.35: The equivalent widths (corrected for absorption) of the Hα and Hβ emission for the star BD+29 3842.

Date (MJD) (yr)	EW Hα (Å)	σ(EW Hα) (Å)	EW Hβ (Å)	σ(EW Hβ) (Å)	$v \sin i$ (km s^{-1})	$\sigma(v \sin i)$ (km s^{-1})
51029.64	-0.70	0.07	-0.88	0.43	86.2	4.13
55099.75	-2.23	0.30	-	-	-	-
55522.86	-1.06	0.08	-0.60	0.05	99.27	168.01
58299.62	-1.24	0.07	-0.72	0.04	80.11	29.96
58356.49	-1.14	0.07	-0.73	0.05	88.94	5.08
58566.55	-1.16	0.07	-0.83	0.06	110.73	77.78
58652.86	-0.97	0.07	-1.00	0.05	80.0	0.88
59035.54	-0.72	0.07	-0.93	0.05	116.54	100.85

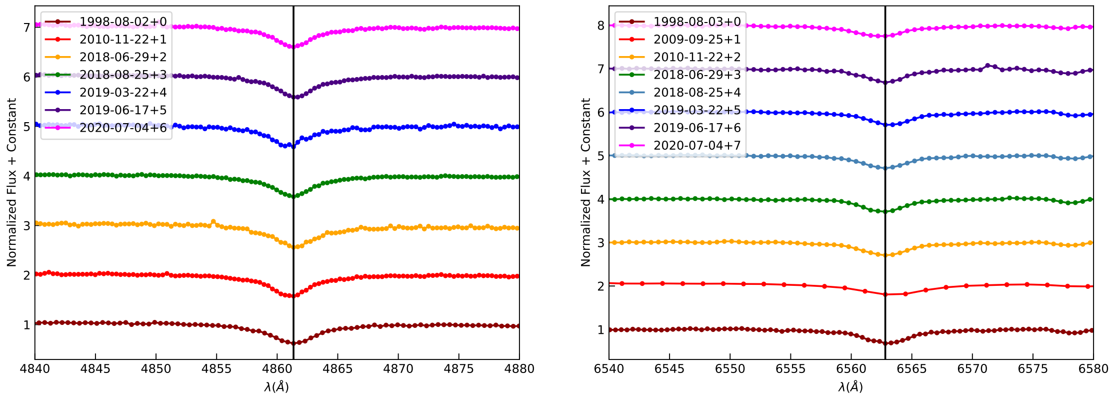

(a)

(b)

Figure D.24: A plot showing the normalized Hβ (a) and Hα (b) lines for BD+29 3842.

D.25 BD+29 4453, HD 205618

TABLE D.36: The equivalent widths (corrected for absorption) of the Hα and Hβ emission for the star BD+29 4453.

Date (MJD) (yr)	EW Hα (Å)	σ(EW Hα) (Å)	EW Hβ (Å)	σ(EW Hβ) (Å)	$v \sin i$ (km s^{-1})	$\sigma(v \sin i)$ (km s^{-1})
51029.64	-53.22	0.06	-7.86	0.48	264.78	4.13
55099.75	-64.93	0.22	-	-	-	-
55148.62	-64.12	0.23	-8.12	0.04	263.21	8.63
55518.86	-66.75	0.12	-7.76	0.03	278.69	4.83
56583.15	-67.01	0.15	-7.80	0.03	250.87	4.44
58296.62	-65.78	0.11	-7.67	0.02	288.09	2.17
58331.06	-66.30	0.13	-7.75	0.04	248.45	22.48
58360.49	-66.62	0.11	-7.69	0.03	281.24	14.72
58654.86	-64.20	0.13	-7.41	0.02	293.37	10.96
58712.74	-63.18	0.11	-7.48	0.02	244.83	0.38
59036.54	-63.83	0.12	-7.69	0.02	262.01	5.54

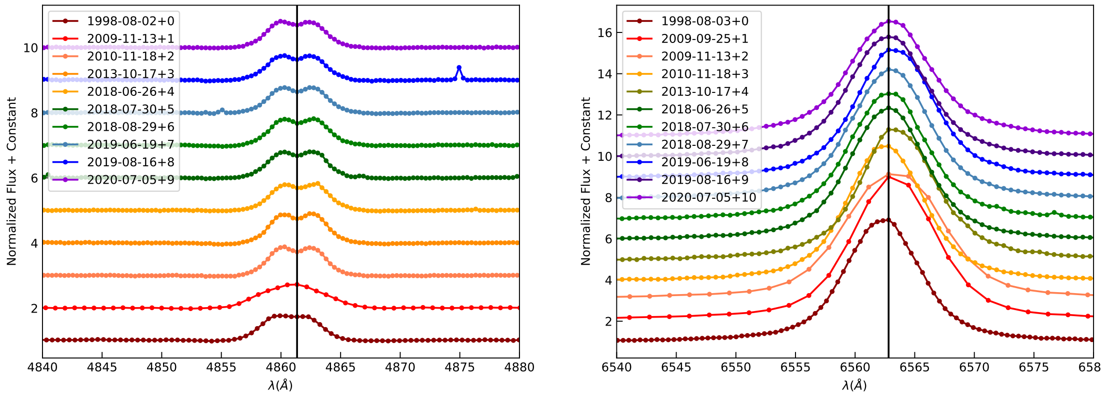

(a) (b)

FIGURE D.25: A plot showing the normalized Hβ (a) and Hα (b) lines for BD+29 4453.

D.26 BD+30 3227, HD 171406

Table D.37: The equivalent widths (corrected for absorption) of the Hα and Hβ emission for the star BD+30 3227.

Date (MJD) (yr)	EW Hα (Å)	σ(EW Hα) (Å)	EW Hβ (Å)	σ(EW Hβ) (Å)	$v \sin i$ (km s^{-1})	$\sigma(v \sin i)$ (km s^{-1})
51029.64	-3.69	0.04	1.52	0.84	201.87	3.97
55084.75	-1.44	0.68	-	-	-	-
55208.50	-5.38	0.85	0.76	0.10	235.58	30.62
58275.62	-5.20	0.14	-0.26	0.05	218.05	4.14
58497.68	-2.59	0.05	-0.19	0.06	210.15	40.46
58534.12	-2.37	0.07	0.12	0.06	221.73	68.9
58590.99	-2.25	0.09	0.11	0.07	216.97	44.96
58622.43	-	-	0.57	0.05	220.34	17.26
58652.86	-1.31	0.06	0.04	0.04	190.75	6.85
59034.54	0.64	0.04	0.83	0.04	210.91	7.75
59243.16	0.25	0.19	1.04	0.05	197.17	16.98

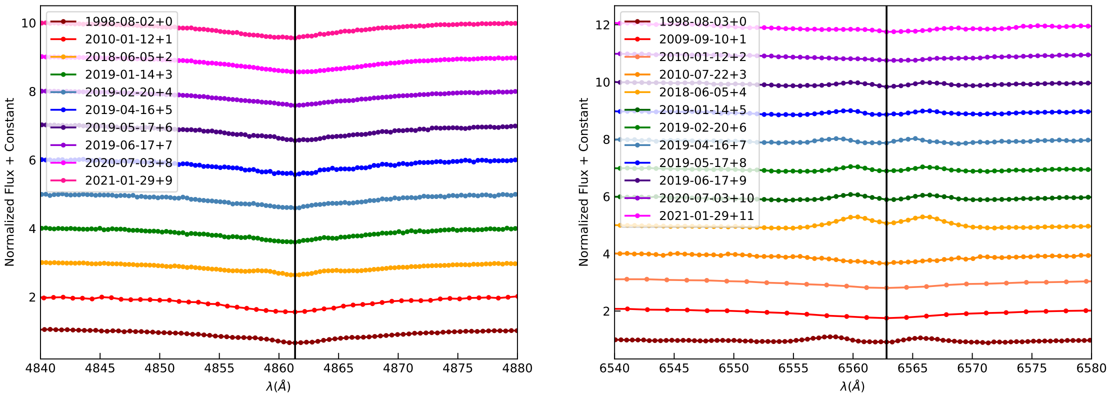

(a) (b)

Figure D.26: A plot showing the normalized Hβ (a) and Hα (b) lines for BD+30 3227.

D.27 BD+31 4018, HD 193009

Table D.38: The equivalent widths (corrected for absorption) of the Hα and Hβ emission for the star BD+31 4018.

Date (MJD) (yr)	EW Hα (Å)	σ(EW Hα) (Å)	EW Hβ (Å)	σ(EW Hβ) (Å)	$v \sin i$ (km s^{-1})	$\sigma(v \sin i)$ (km s^{-1})
51028.64	-	-	-4.76	0.52	184.09	2.7
55089.75	-25.26	0.26	-	-	-	-
55400.12	-23.85	0.11	-	-	-	-
55522.86	-24.42	0.11	-4.29	0.03	237.46	1.36
56583.15	-28.92	0.13	-4.84	0.03	181.52	22.39
58275.62	-24.46	0.14	-4.51	0.03	199.66	14.1
58331.06	-28.17	0.10	-4.51	0.03	170.81	13.24
58363.93	-29.81	0.11	-4.86	0.03	186.36	19.39
58564.55	-27.06	0.09	-4.52	0.05	178.44	34.72
58614.43	-29.69	0.08	-4.94	0.04	205.51	10.98
58651.86	-26.88	0.10	-5.70	0.05	177.3	19.91
58707.74	-25.32	0.29	-5.77	0.06	203.82	17.07
59036.54	-30.78	0.46	-5.05	0.12	222.35	177.63

Table D.39: The $\Delta\lambda$ distance between peaks and V and R peak values for the Hβ emission for the star BD+31 4018.

MJD (yr)	$\Delta\lambda_{\mathrm{H}\beta}$ (Å)	$\sigma(\Delta\lambda_{\mathrm{H}\beta})$ (Å)	V$_\beta$	R$_\beta$
51028.64	0.96	0.68	1.2444	1.2424
55522.86	2.78	0.49	1.4148	1.1665
56583.15	2.79	0.49	1.2611	1.4197
58275.62	3.48	0.49	1.2700	1.3086
58331.06	3.48	0.49	1.2382	1.4207
58363.93	3.48	0.49	1.2937	1.4475
58564.55	2.09	0.49	1.2558	1.4550
58651.86	2.78	0.49	1.2344	1.5062
58707.74	2.78	0.49	1.2542	1.4585
58614.43	3.13	0.49	1.2154	1.4244
59036.54	2.43	0.49	1.3399	1.4066

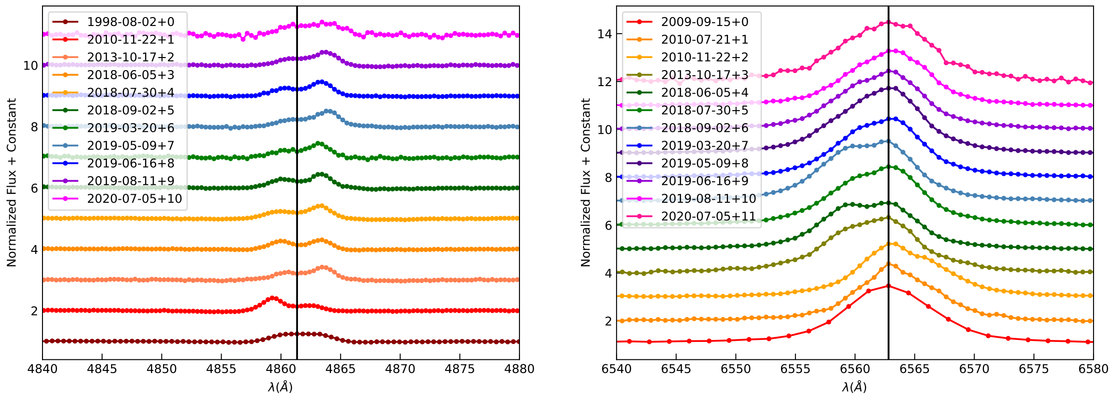

(a)

(b)

FIGURE D.27: A plot showing the normalized Hβ (a) and Hα (b) lines for BD+31 4018.

D.28 BD+36 3946, HD 228438

TABLE D.40: The equivalent widths (corrected for absorption) of the Hα and Hβ emission for the star BD+36 3946.

Date (MJD) (yr)	EW Hα (Å)	σ(EW Hα) (Å)	EW Hβ (Å)	σ(EW Hβ) (Å)	$v \sin i$ (km s^{-1})	$\sigma(v \sin i)$ (km s^{-1})
51029.64	-25.18	0.08	-4.58	0.47	175.05	1.01
55091.75	-34.95	0.22	-	-	-	-
55522.86	-38.35	0.12	-	-	-	-
55523.86	-38.31	0.11	-5.94	0.03	199.09	12.22
56583.15	-37.17	0.11	-5.41	0.02	191.7	9.32
58275.62	-	-	-5.31	0.02	187.22	11.45
58329.06	-34.76	0.10	-5.49	0.02	216.42	6.04
58362.93	-35.38	0.10	-5.40	0.02	182.95	6.88
58595.99	-35.33	0.09	-5.73	0.03	224.42	156.62
58626.43	-35.52	0.10	-5.57	0.02	173.4	19.07
58657.86	-37.22	0.09	-6.01	0.02	189.44	11.21
58668.30	-36.00	0.16	-6.02	0.04	208.84	9.28
58707.74	-37.42	0.09	-5.99	0.03	210.8	61.24
59035.54	-54.02	0.12	-9.65	0.03	208.03	7.13

TABLE D.41: The $\Delta\lambda$ distance between peaks and V and R peak values for the Hβ emission for the star BD+36 3946.

MJD (yr)	$\Delta\lambda_{\mathrm{H}\beta}$ (Å)	$\sigma(\Delta\lambda_{\mathrm{H}\beta})$ (Å)	V_β	R_β
51028.64	1.91	0.68	1.3448	1.3114
56583.15	1.39	0.49	1.6656	1.5512
58275.62	1.74	0.49	1.5423	1.5626
58329.06	1.05	0.49	1.5724	1.5827
58626.43	1.74	0.49	1.6253	1.5651

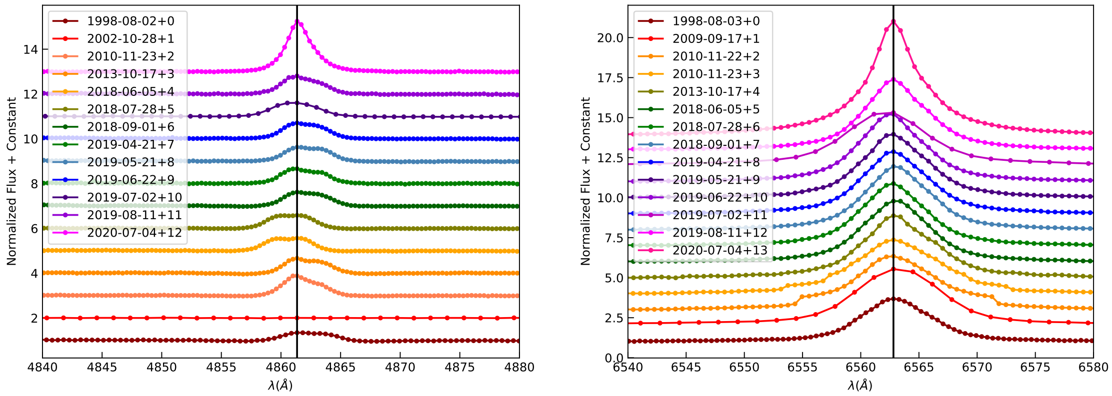

(a)

(b)

FIGURE D.28: A plot showing the normalized Hβ (a) and Hα (b) lines for BD+36 3946.

D.29 BD+37 675, HD 18552

TABLE D.42: The equivalent widths (corrected for absorption) of the Hα and Hβ emission for the star BD+37 675.

Date (MJD) (yr)	EW Hα (Å)	σ(EW Hα) (Å)	EW Hβ (Å)	σ(EW Hβ) (Å)	$v \sin i$ (km s^{-1})	$\sigma(v \sin i)$ (km s^{-1})
51028.64	-18.78	0.04	-	-	210.24	7.52
55143.62	-18.84	0.13	-3.36	0.08	157.28	102.13
55406.12	-18.98	0.09	-3.19	0.04	239.07	40.44
55497.43	-17.99	0.10	-2.70	0.04	254.67	19.38
56542.72	-19.33	0.13	-3.01	0.03	223.76	17.39
58355.49	-22.44	0.07	-3.06	0.03	243.49	12.89
58385.93	-21.95	0.08	-3.16	0.03	223.44	38.67
58474.24	-21.98	0.10	-3.60	0.04	287.9	10958.98
58697.30	-21.91	0.08	-2.68	0.03	238.61	23.99

TABLE D.43: The $\Delta\lambda$ distance between peaks and V and R peak values for the Hα and Hβ emission for the star BD+37 675.

MJD (yr)	$\Delta\lambda_{\mathrm{H}\alpha}$ (Å)	$\sigma(\Delta\lambda_{\mathrm{H}\alpha})$ (Å)	V$_\alpha$	R$_\alpha$	$\Delta\lambda_{\mathrm{H}\beta}$ (Å)	$\sigma(\Delta\lambda_{\mathrm{H}\beta})$ (Å)	V$_\beta$	R$_\beta$
51029.64	2.84	0.98	2.6325	2.6291	3.82	0.68	0.9267	0.9267
55406.12	3.6	1.1	2.3883	2.4398	3.48	0.49	0.8666	0.8698
55497.43	3.6	1.1	2.4041	2.3788	4.17	0.49	0.8583	0.8595
56542.72	3.6	1.1	2.2900	2.3863	4.18	0.49	0.9198	0.9227
58355.49	3.0	1.1	2.8314	2.7856	3.49	0.49	0.9102	0.9173
58385.93	3.0	1.1	2.7700	2.7114	3.480.49	0.9299	0.9320	
58474.24	3.6	1.1	2.7862	2.8164	3.49	0.49	0.9337	0.9518
58696.74	3.6	1.1	2.7582	2.8087	3.84	0.49	0.9132	0.9088

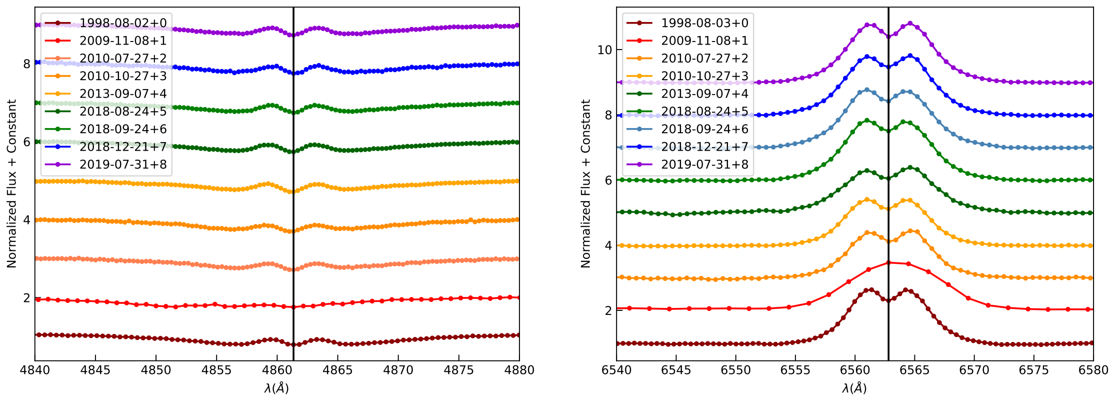

(a) (b)

FIGURE D.29: A plot showing the normalized Hβ (a) and Hα (b) lines for BD+37 675.

D.30 BD+37 3856, HD228650

Table D.44: The equivalent widths (corrected for absorption) of the Hα and Hβ emission for the star BD+37 3856.

Date (MJD)	EW Hα	σ(EW Hα)	EW Hβ	σ(EW Hβ)	$v \sin i$	$\sigma(v \sin i)$
(yr)	(Å)	(Å)	(Å)	(Å)	(km s^{-1})	(km s^{-1})
51029.64	0.55	0.06	0.63	0.48	107.26	11.32
55401.12	0.61	0.12	1.18	0.14	-	-
55521.86	0.41	0.07	0.80	0.06	149.13	82.05
56585.15	0.03	0.06	0.49	0.07	123.25	3.91
58277.62	0.46	0.07	0.86	0.06	114.47	49.02
58325.06	0.27	0.06	0.72	0.07	89.85	23.79
58355.49	0.13	0.07	0.44	0.09	107.78	20.95
58384.93	0.17	0.07	0.64	0.09	113.76	57.98
58596.99	0.11	0.06	0.9	0.07	167.58	217.23
58650.86	0.13	0.07	0.63	0.07	102.01	12.57
58711.74	-	-	-	-	103.43	28.57
59034.54	0.32	0.06	0.93	0.06	101.99	35.67

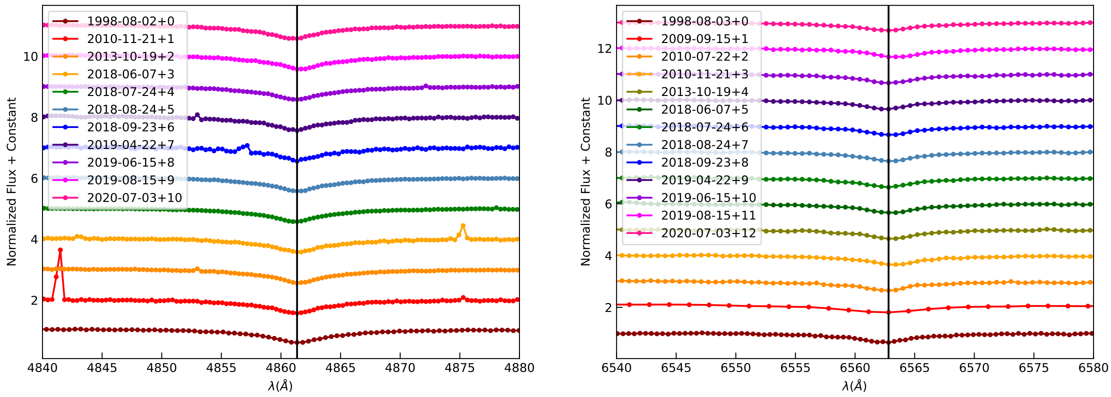

(a)

(b)

Figure D.30: A plot showing the normalized Hβ (a) and Hα (b) lines for BD+37 3856.

D.31 BD+40 1213, HD 33604

TABLE D.45: The equivalent widths (corrected for absorption) of the Hα and Hβ emission for the star BD+40 1213.

Date (MJD) (yr)	EW Hα (Å)	σ(EW Hα) (Å)	EW Hβ (Å)	σ(EW Hβ) (Å)	$v \sin i$ (km s^{-1})	σ($v \sin i$) (km s^{-1})
51029.64	-15.81	0.04	-4.11	0.24	109.91	4.74
55100.75	-19.18	0.15	-	-	-	-
55143.62	-19.00	0.20	-4.42	0.04	167.64	11.77
55432.55	-20.53	0.08	-4.56	0.03	148.26	9.71
55488.43	-16.88	0.08	-4.66	0.03	126.59	3.35
56556.72	-19.05	0.07	-4.27	0.02	127.44	4.43
58355.49	-33.91	0.70	-5.89	0.03	113.39	6.42
58385.93	-30.14	0.07	-5.66	0.03	111.14	22.16
58454.24	-30.62	0.08	-5.71	0.04	122.31	17.03
58484.68	-25.22	0.08	-5.42	0.03	118.86	3.73
58799.05	-23.11	0.06	-5.07	0.03	126.5	24.58
59187.73	-29.46	0.12	-5.93	0.03	109.95	18.82
59245.16	-27.99	0.12	-5.85	0.03	113.48	7.18

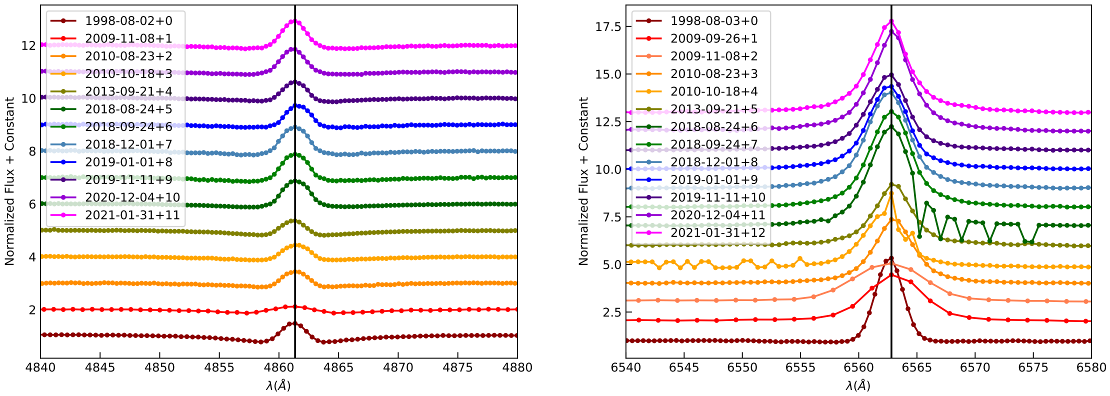

(a)

(b)

FIGURE D.31: A plot showing the normalized Hβ (a) and Hα (b) lines for BD+40 1213.

D.32 BD+42 1376, HD 37657

Table D.46: The equivalent widths (corrected for absorption) of the Hα and Hβ emission for the star BD+42 1376.

Date (MJD) (yr)	EW Hα (Å)	σ(EW Hα) (Å)	EW Hβ (Å)	σ(EW Hβ) (Å)	$v \sin i$ (km s^{-1})	σ($v \sin i$) (km s^{-1})
51029.64	-11.18	0.07	-2.60	0.51	165.57	1.51
55138.62	-19.38	0.16	-4.01	0.11	175.53	6.21
55432.55	-16.68	0.10	-2.27	0.04	198.54	1.98
55486.43	-17.57	0.10	-2.61	0.04	198.63	0.55
56557.72	-7.82	0.10	-1.07	0.06	181.96	10.21
58356.49	-2.42	0.05	-0.80	0.06	179.44	7.29
58448.80	-1.57	0.06	-0.03	0.04	198.07	25.0
58481.24	-2.27	0.06	-0.40	0.05	205.79	3.03
58564.55	-1.22	0.09	-0.16	0.06	188.45	11.92
58799.05	-1.46	0.11	-0.09	0.08	200.83	1.45
59186.73	0.17	0.12	-0.11	0.07	196.53	11.34
59244.16	0.98	0.18	0.87	0.13	192.05	4.1

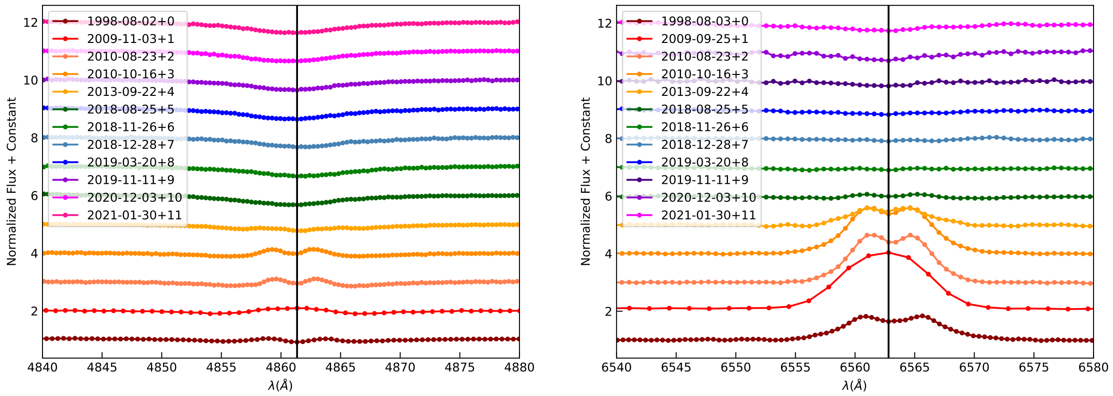

(a)

(b)

Figure D.32: A plot showing the normalized Hβ (a) and Hα (b) lines for BD+42 1376.

D.33 BD+42 4538, HD 216581

TABLE D.47: The equivalent widths (corrected for absorption) of the Hα and Hβ emission for the star BD+42 4538.

Date (MJD) (yr)	EW Hα (Å)	σ(EW Hα) (Å)	EW Hβ (Å)	σ(EW Hβ) (Å)	$v \sin i$ (km s^{-1})	$\sigma(v \sin i)$ (km s^{-1})
51029.64	-40.25	0.07	-4.25	0.40	209.59	3.64
55091.75	-41.74	0.24	-	-	-	-
55146.62	-43.78	0.23	-4.74	0.05	246.5	61.99
55517.86	-42.38	0.15	-4.02	0.03	268.31	10.87
56552.72	-41.62	0.11	-4.00	0.11	251.54	3.0
58326.06	-40.84	0.13	-3.92	0.06	294.38	71.16
58355.49	-38.57	0.08	-3.54	0.03	215.12	11.26
58385.93	-38.02	0.09	-3.49	0.04	267.0	18.24
58706.74	-39.94	0.08	-3.45	0.03	253.83	8.13
59035.54	-38.74	0.09	-3.28	0.03	208.95	19.28

TABLE D.48: The $\Delta\lambda$ distance between peaks and V and R peak values for the Hα and Hβ emission for the star BD+42 4538.

MJD (yr)	$\Delta\lambda_{\mathrm{H}\alpha}$ (Å)	$\sigma(\Delta\lambda_{\mathrm{H}\alpha})$ (Å)	V$_\alpha$	R$_\alpha$	$\Delta\lambda_{\mathrm{H}\beta}$ (Å)	$\sigma(\Delta\lambda_{\mathrm{H}\beta})$ (Å)	V$_\beta$	R$_\beta$
51029.64	2.37	0.98	5.0314	5.0629	3.34	0.68	1.3628	1.3711
55517.86	2.4	1.1	5.2465	5.8387	2.44	0.49	1.4267	1.3738
56552.72	3.0	1.1	4.8429	4.9996	3.14	0.49	1.3098	1.4894
58326.06	3.0	1.1	5.0047	4.9743	2.78	0.49	1.3080	1.5003
58355.49	3.0	1.1	4.8987	4.9483	2.79	0.49	1.2313	1.4599
58385.93	3.0	1.1	4.7386	4.9562	2.79	0.49	1.2234	1.4495
58706.74	1.8	1.1	4.7589	5.4092	2.44	0.49	1.1840	1.4486
59035.54	2.4	1.1	4.3929	4.7814	2.78	0.49	1.2944	1.3017

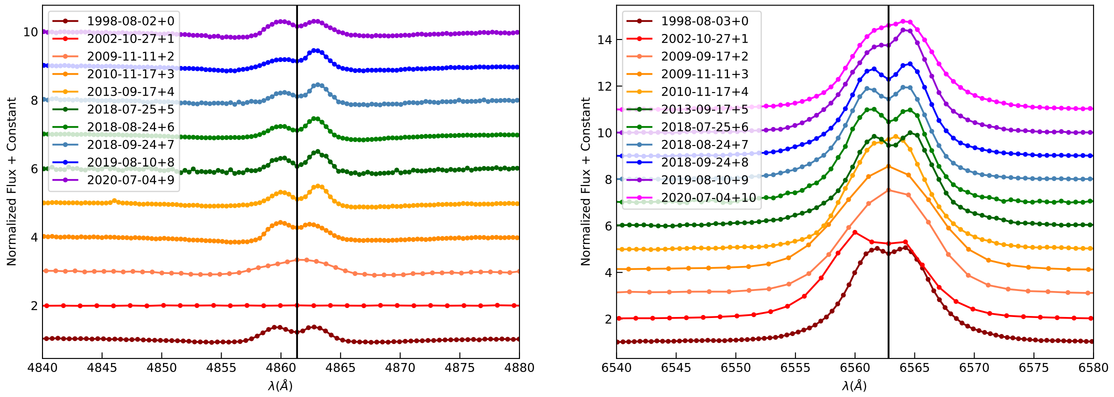

(a)

(b)

FIGURE D.33: A plot showing the normalized Hβ (a) and Hα (b) lines for BD+42 4538.

D.34 BD+43 1048, HD 276738

Table D.49: The equivalent widths (corrected for absorption) of the Hα and Hβ emission for the star BD+43 1048.

Date (MJD) (yr)	EW Hα (Å)	σ(EW Hα) (Å)	EW Hβ (Å)	σ(EW Hβ) (Å)	$v \sin i$ (km s^{-1})	$\sigma(v \sin i)$ (km s^{-1})
51029.64	-11.13	0.08	-2.91	0.35	203.44	1.01
55100.75	-14.27	0.21	-	-	-	-
55141.62	-13.62	0.19	-2.66	0.06	249.51	55.17
55428.55	-16.62	0.14	-3.70	0.03	201.62	17.38
55486.43	-15.26	0.11	-3.32	0.02	209.05	16.98
56556.72	-16.29	0.11	-4.05	0.02	182.1	38.61
58356.49	-13.90	0.11	-2.58	0.04	236.41	53.68
58447.80	-14.97	0.10	-4.19	0.04	311.43	17.09
58479.24	-14.57	0.11	-3.67	0.08	252.11	6.19
58831.48	-14.83	0.12	-3.29	0.03	169.51	26.28

Table D.50: The $\Delta\lambda$ distance between peaks and V and R peak values for the Hα and Hβ emission for the star BD+43 1048.

MJD (yr)	$\Delta\lambda_{\mathrm{H}\alpha}$ (Å)	$\sigma(\Delta\lambda_{\mathrm{H}\alpha})$ (Å)	V_α	R_α	$\Delta\lambda_{\mathrm{H}\beta}$ (Å)	$\sigma(\Delta\lambda_{\mathrm{H}\beta})$ (Å)	V_β	R_β
51029.64	5.68	0.98	1.6944	1.6402	5.26	0.68	0.8859	0.8861
55428.55	5.4	1.1	1.9416	1.8867	5.22	0.49	0.9245	0.9422
55486.43	5.4	1.1	1.8257	1.8708	5.23	0.49	0.9175	0.9154
56556.72	5.4	1.1	1.9952	1.8036	4.18	0.49	0.9132	0.9210
58831.48	6.0	1.1	1.6963	1.8173	5.22	0.49	0.9128	0.9083
58479.24	5.4	1.1	1.8785	1.8738	3.48	0.49	0.9712	0.9369
58447.80	4.8	1.1	1.8816	1.7756	4.53	0.49	0.9146	0.9085
58356.49	6.0	1.1	1.7482	1.8517	4.87	0.49	0.9079	0.9084

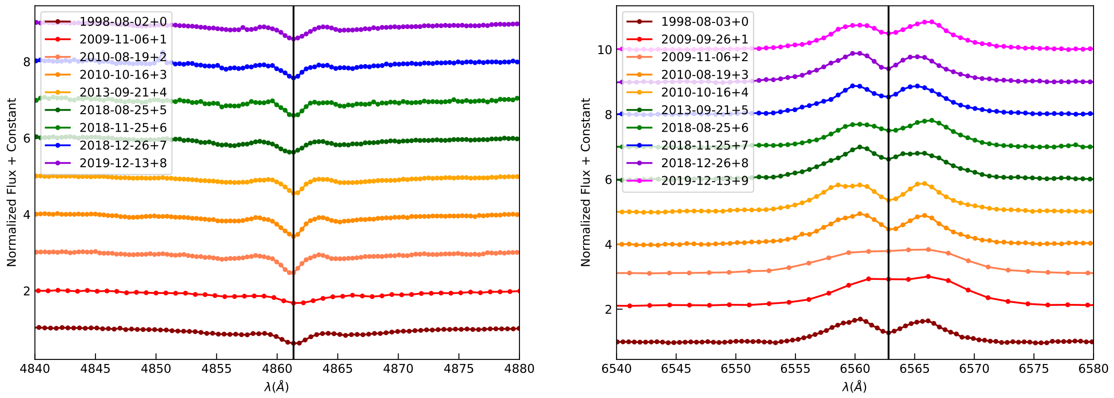

(a)

(b)

Figure D.34: A plot showing the normalized Hβ (a) and Hα (b) lines for BD+43 1048.

D.35 BD+45 933, HD 27846

Table D.51: The equivalent widths (corrected for absorption) of the Hα and Hβ emission for the star BD+45 933.

Date (MJD) (yr)	EW Hα (Å)	σ(EW Hα) (Å)	EW Hβ (Å)	σ(EW Hβ) (Å)	$v \sin i$ (km s^{-1})	σ($v \sin i$) (km s^{-1})
51029.64	0.29	0.06	0.11	0.54	127.12	6.25
55099.75	-5.64	0.32	-	-	-	-
55141.62	-3.33	0.38	-	-	-	-
55432.55	-0.53	0.07	-0.10	0.06	147.03	5.51
55488.43	-0.11	0.07	-	-	-	-
55492.43	-0.37	0.06	0.22	0.06	137.14	7.02
56555.72	-0.33	0.09	0.30	0.06	134.39	0.35
58355.49	-0.26	0.07	-0.34	0.06	129.71	8.15
58384.93	0.03	0.06	0.19	0.09	161.54	17.77
58455.24	-0.61	0.07	-0.24	0.07	147.27	6.12
58496.68	-1.50	0.08	0.05	0.08	152.21	12.1
58831.48	-0.08	0.06	0.46	0.06	148.41	6.62

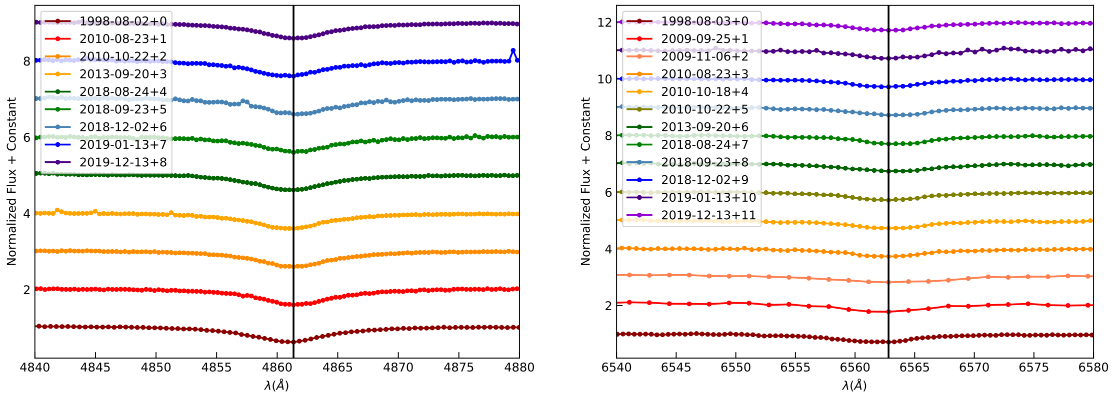

(a)

(b)

Figure D.35: A plot showing the normalized Hβ (a) and Hα (b) lines for BD+45 933.

D.36 BD+45 3879, HD 211835

TABLE D.52: The equivalent widths (corrected for absorption) of the Hα and Hβ emission for the star BD+45 3879.

Date (MJD) (yr)	EW Hα (Å)	σ(EW Hα) (Å)	EW Hβ (Å)	σ(EW Hβ) (Å)	$v \sin i$ (km s^{-1})	$\sigma(v \sin i)$ (km s^{-1})
51029.64	-32.30	0.06	-5.87	0.48	179.02	1.33
55089.75	-27.58	0.20	-	-	-	-
55149.62	-25.08	0.34	-4.55	0.06	186.12	3.05
55517.86	-27.66	0.10	-3.75	0.04	222.62	3.25
56557.72	-17.33	0.10	-3.54	0.03	200.89	3.24
58296.62	-30.62	0.10	-3.65	0.05	197.51	11.67
58328.06	-30.59	0.09	-3.77	0.03	202.36	12.32
58358.49	-30.64	0.09	-4.14	0.04	184.32	1.18
58656.86	-29.36	0.09	-4.28	0.04	187.37	3.46
58706.74	-29.31	0.09	-3.81	0.04	172.71	19.81
59034.54	-34.09	0.21	-4.01	0.04	172.37	12.98

TABLE D.53: The $\Delta\lambda$ distance between peaks and V and R peak values for the Hα, Hβ and H gamma emission for the star BD+45 3879.

MJD (yr)	$\Delta\lambda_{\mathrm{H}\alpha}$ (Å)	$\sigma(\Delta\lambda_{\mathrm{H}\alpha})$ (Å)	V$_\alpha$	R$_\alpha$	$\Delta\lambda_{\mathrm{H}\beta}$ (Å)	$\sigma(\Delta\lambda_{\mathrm{H}\beta})$ (Å)	V$_\beta$	R$_\beta$
51029.64	2.37	0.98	4.4760	4.0281	2.39	0.68	1.6042	1.4545
55517.86	2.4	1.1	3.5403	3.4115	3.14	0.49	1.3175	1.2700
56557.72	3.0	1.1	2.2133	2.2132	3.83	0.49	1.1566	1.1228
58296.62	2.4	1.1	3.8539	3.4259	3.49	0.49	1.3715	1.2356
58328.06	3.0	1.1	3.9368	3.4708	3.14	0.49	1.3803	1.2369
58358.49	3.0	1.1	3.7622	3.4826	3.14	0.49	1.3689	1.2675
58656.86	3.0	1.1	3.5116	3.4679	3.14	0.49	1.3184	1.3398
58706.74	3.0	1.1	3.4576	3.5240	3.48	0.49	1.2598	1.3321
59034.54	1.8	1.1	3.9312	3.7435	3.14	0.49	1.2711	1.3353

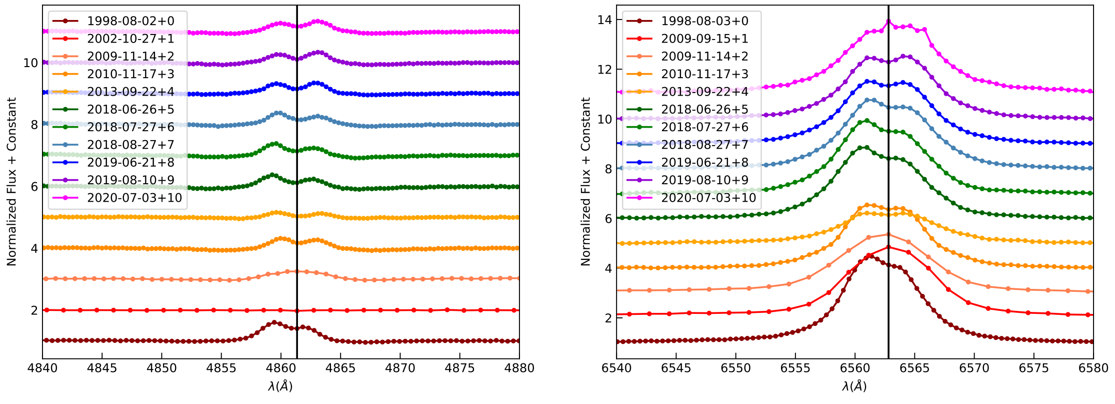

(a)

(b)

FIGURE D.36: A plot showing the normalized Hβ (a) and Hα (b) lines for BD+45 3879.

D.37 BD+46 275, HD 6811

TABLE D.54: The equivalent widths (corrected for absorption) of the Hα and Hβ emission for the star BD+46 275.

Date (MJD) (yr)	EW Hα (Å)	σ(EW Hα) (Å)	EW Hβ (Å)	σ(EW Hβ) (Å)	$v \sin i$ (km s^{-1})	$\sigma(v \sin i)$ (km s^{-1})
51029.64	-5.84	0.03	0.29	0.60	104.89	4.53
55091.75	-6.00	0.19	-	-	-	-
55138.62	-5.78	0.14	0.27	0.10	163.63	41.25
55396.12	-4.53	0.06	-0.32	0.04	149.97	37.67
55498.43	-4.59	0.06	0.35	0.04	103.03	19.14
56537.72	-	-	0.54	0.03	106.98	19.82
58139.44	-1.40	0.38	1.98	0.17	190.46	32.37
58326.06	-0.25	0.07	0.60	0.03	123.83	27.55
58355.49	-0.05	0.06	0.37	0.03	121.98	27.85
58385.93	-0.28	0.05	0.42	0.03	106.14	17.71
58484.24	-0.41	0.07	0.11	0.04	138.0	67.77
58687.30	-0.77	0.05	0.17	0.04	127.17	14.8
58830.48	-0.57	0.05	0.39	0.03	107.1	13.94
59036.54	-1.06	0.03	0.12	0.04	128.0	10.52

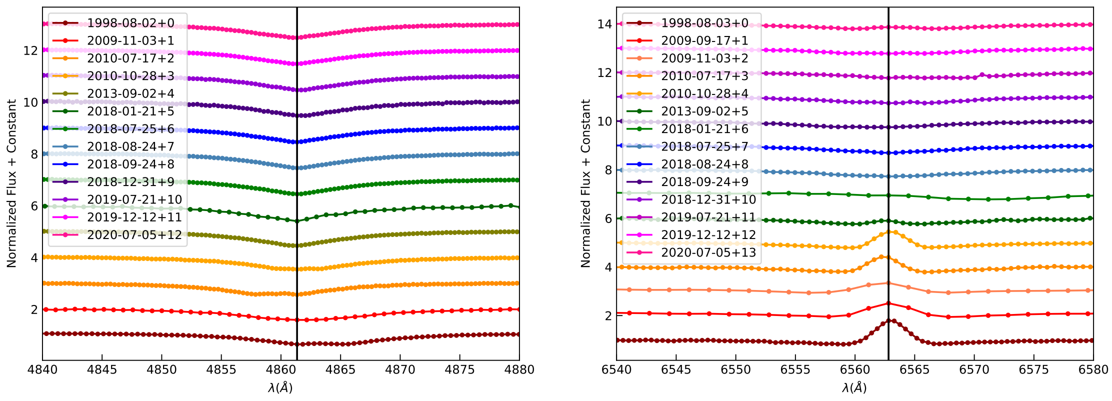

(a) (b)

FIGURE D.37: A plot showing the normalized Hβ (a) and Hα (b) lines for BD+46 275.

D.38 BD+47 183, HD 4180

Table D.55: The equivalent widths (corrected for absorption) of the Hα and Hβ emission for the star BD+47 183.

Date (MJD) (yr)	EW Hα (Å)	σ(EW Hα) (Å)	EW Hβ (Å)	σ(EW Hβ) (Å)	$v \sin i$ (km s^{-1})	$\sigma(v \sin i)$ (km s^{-1})
51029.64	-33.16	0.05	-3.99	0.38	158.99	1.57
55091.75	-39.64	0.16	-	-	-	-
55138.62	-40.32	0.26	-4.39	0.06	163.32	4.01
55396.12	-40.90	0.10	-4.11	0.02	184.65	8.91
55497.43	-40.22	0.09	-3.95	0.03	178.28	28.65
56552.72	-38.7	0.09	-3.83	0.02	154.41	3.19
58268.18	-28.48	0.19	-3.50	0.04	166.8	10.71
58312.06	-27.86	0.07	-2.87	0.01	178.31	2.27
58353.49	-28.26	0.06	-3.41	0.02	185.44	10.2
58384.93	-28.29	0.07	-2.98	0.03	217.35	23.25
58683.30	-35.38	0.06	-3.72	0.02	177.43	6.73
58713.74	-35.39	0.07	-3.53	0.02	178.95	2.68
59035.54	-35.30	0.09	-3.48	0.03	180.05	18.04

Table D.56: The $\Delta\lambda$ distance between peaks and V and R peak values for the Hβ emission for the star BD+47 183.

MJD (yr)	$\Delta\lambda_{\mathrm{H}\beta}$ (Å)	$\sigma(\Delta\lambda_{\mathrm{H}\beta})$ (Å)	V$_\beta$	R$_\beta$
51028.64	0.96	0.68	1.3950	1.3940
55396.12	1.74	0.49	1.4068	1.4508
55497.43	2.09	0.49	1.4154	1.4455
56552.72	1.39	0.49	1.3305	1.4355
58312.06	1.39	0.49	1.1559	1.1487
58353.49	1.74	0.49	1.1498	1.1722
58384.93	1.74	0.49	1.1668	1.2203
58683.30	1.40	0.49	1.2966	1.3246
58713.74	1.74	0.49	1.2865	1.3291
59035.54	1.75	0.49	1.3081	1.3312

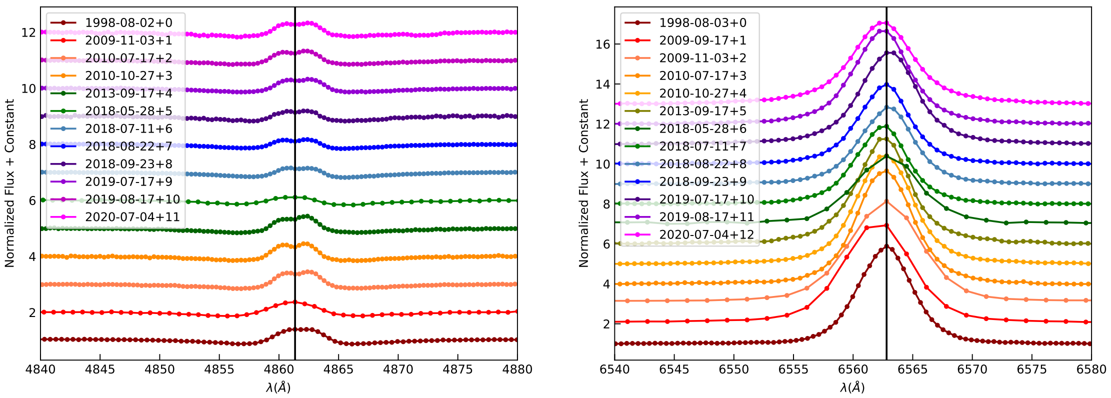

(a)

(b)

FIGURE D.38: A plot showing the normalized Hβ (a) and Hα (b) lines for BD+47 183.

D.39 BD+47 857, HD 22192

TABLE D.57: The equivalent widths (corrected for absorption) of the Hα and Hβ emission for the star BD+47 857.

Date (MJD) (yr)	EW Hα (Å)	σ(EW Hα) (Å)	EW Hβ (Å)	σ(EW Hβ) (Å)	$v \sin i$ (km s^{-1})	$\sigma(v \sin i)$ (km s^{-1})
51029.64	-39.73	0.06	-5.94	0.43	198.68	8.57
55143.62	-43.41	0.21	-6.02	0.05	213.06	3.74
55423.55	-46.33	0.12	-5.68	0.03	225.35	1.54
55496.43	-44.82	0.11	-6.66	0.01	227.06	0.39
56544.72	-45.37	0.12	-5.56	0.02	228.95	2.61
57756.19	-45.62	0.19	-6.99	0.03	242.97	17.51
58331.06	-44.94	0.10	-5.61	0.02	216.79	6.17
58360.49	-45.33	0.10	-6.66	0.01	212.94	23.99
58469.24	-45.68	0.09	-6.52	0.01	215.2	13.55
58701.74	-46.90	0.08	-5.82	0.03	224.16	5.07
59211.73	-40.24	0.17	-6.46	0.02	232.84	30.58

TABLE D.58: The $\Delta\lambda$ distance between peaks and V and R peak values for the Hα and Hβ emission for the star BD+47 857.

MJD (yr)	$\Delta\lambda_{\mathrm{H}\alpha}$ (Å)	$\sigma(\Delta\lambda_{\mathrm{H}\alpha})$ (Å)	V_α	R_α	$\Delta\lambda_{\mathrm{H}\beta}$ (Å)	$\sigma(\Delta\lambda_{\mathrm{H}\beta})$ (Å)	V_β	R_β
51029.64	3.31	0.98	5.0244	4.9791	3.34	0.68	1.4336	1.4540
55423.55	3.0	1.1	5.2382	5.1361	3.14	0.49	1.4976	1.5096
55496.43	3.0	1.1	5.2580	5.2755	2.78	0.49	1.5174	1.4947
56544.72	3.0	1.1	4.9415	5.2332	2.79	0.49	1.5004	1.5021
58331.06	3.0	1.1	4.9323	4.9431	2.79	0.49	1.4636	1.4680
58360.49	3.0	1.1	5.3430	5.3533	2.79	0.49	1.4840	1.4578
58469.24	3.0	1.1	5.3455	5.4912	2.79	0.49	1.4808	1.4745
58701.74	3.6	1.1	5.4380	5.5439	2.79	0.49	1.5119	1.5439
59211.73	3.0	1.1	4.7624	4.9537	3.13	0.49	1.4196	1.3971

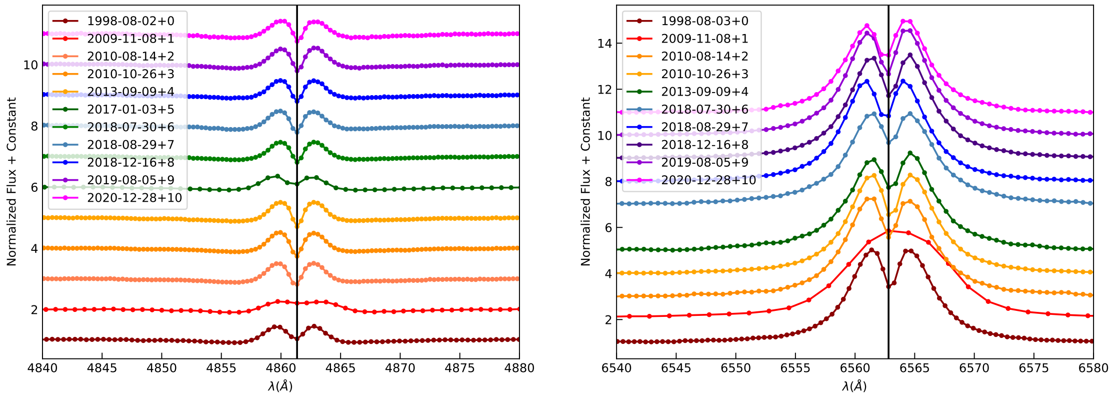

(a) (b)

FIGURE D.39: A plot showing the normalized Hβ (a) and Hα (b) lines for BD+47 857.

D.40 BD+47 939, HD 25940

Table D.59: The equivalent widths (corrected for absorption) of the Hα and Hβ emission for the star BD+47 939.

Date (MJD) (yr)	EW Hα (Å)	σ(EW Hα) (Å)	EW Hβ (Å)	σ(EW Hβ) (Å)	$v \sin i$ (km s^{-1})	σ($v \sin i$) (km s^{-1})
51029.64	-25.26	0.04	-3.18	0.22	150.89	0.74
55141.62	-	-	-3.59	0.03	164.67	6.23
55425.55	-29.24	0.10	-2.91	0.02	156.74	18.22
55486.43	-29.18	0.07	-2.83	0.02	159.26	3.19
56555.72	-	-	-2.94	0.02	153.6	3.19
57756.19	-29.88	0.14	-3.58	0.03	158.71	11.24
58329.06	-30.07	0.07	-2.96	0.02	167.45	5.93
58358.49	-29.57	0.06	-2.90	0.02	154.0	2.7
58430.80	-29.50	0.07	-3.71	0.02	183.01	6.86
58469.24	-30.40	0.06	-3.06	0.02	165.31	12.51
58715.74	-29.98	0.07	-2.93	0.02	164.04	10.95
58804.05	-29.54	0.06	-3.27	0.02	151.63	2.34
59211.73	-28.54	0.14	-3.03	0.02	159.25	1.86

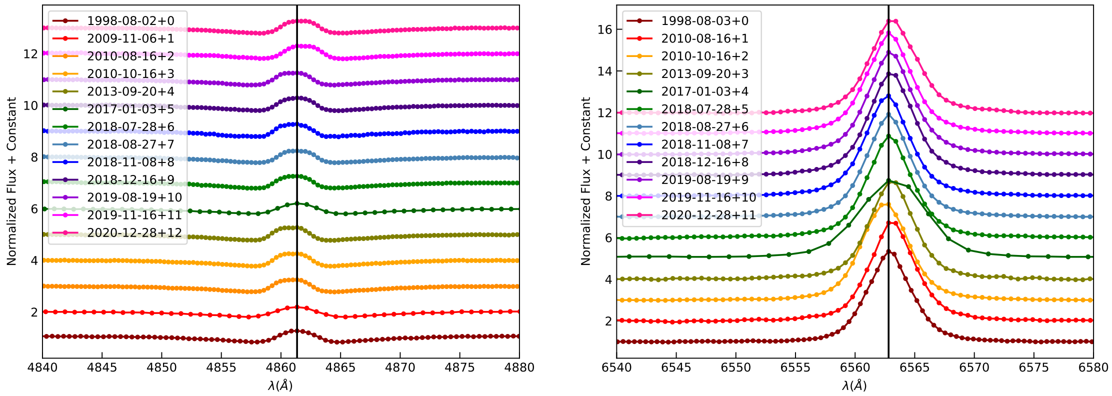

(a)

(b)

Figure D.40: A plot showing the normalized Hβ (a) and Hα (b) lines for BD+47 939.

D.41 BD+47 3985, HD 217050

Table D.60: The equivalent widths (corrected for absorption) of the Hα and Hβ emission for the star BD+47 3985.

Date (MJD) (yr)	EW Hα (Å)	σ(EW Hα) (Å)	EW Hβ (Å)	σ(EW Hβ) (Å)	$v \sin i$ (km s^{-1})	$\sigma(v \sin i)$ (km s^{-1})
51029.64	-20.22	0.08	-1.96	0.42	215.78	11.81
52539.05	-11.43	0.14	-	-	-	-
52541.05	-11.40	0.15	-	-	-	-
58237.75	-5.82	0.26	-0.84	0.08	217.17	17.58
58329.06	-5.32	0.14	-0.87	0.03	190.03	27.02
58360.49	-4.63	0.03	-0.47	0.03	210.93	20.3
58593.99	-4.46	0.04	-0.66	0.05	266.73	67.24
58626.43	-4.37	0.04	-0.53	0.03	229.14	15.67
58713.74	-4.89	0.04	-1.01	0.03	219.06	5.49
59032.54	-1.78	0.02	0.44	0.04	254.9	5.57
59068.98	-1.56	0.03	-	-	-	-

Table D.61: The $\Delta\lambda$ distance between peaks and V and R peak values for the Hα and Hβ emission for the star BD+47 3985.

MJD (yr)	$\Delta\lambda_{\mathrm{H}\alpha}$ (Å)	$\sigma(\Delta\lambda_{\mathrm{H}\alpha})$ (Å)	V_α	R_α	$\Delta\lambda_{\mathrm{H}\beta}$ (Å)	$\sigma(\Delta\lambda_{\mathrm{H}\beta})$ (Å)	V_β	R_β
51029.64	5.69	0.98	2.8280	2.8253	4.78	0.68	1.1593	1.1436
52539.05	5.0	1.1	2.5693	2.5581	-	-	-	-
52541.05	5.2	1.1	2.5600	2.5731	-	-	-	-
58237.75	7.4	1.1	1.4178	1.3978	8.14	0.49	0.9094	0.9114
58329.06	6.6	1.1	1.3591	1.3262	6.61	0.49	0.9026	0.8929
58360.49	6.0	1.1	1.2680	1.2637	6.62	0.49	0.8721	0.8605
58593.99	6.6	1.1	1.2728	1.2751	7.31	0.49	0.8952	0.9310
58626.43	7.8	1.1	1.2624	1.2063	-	-	-	-
58713.74	7.2	1.1	1.3530	1.3623	7.66	0.49	0.9357	0.9336

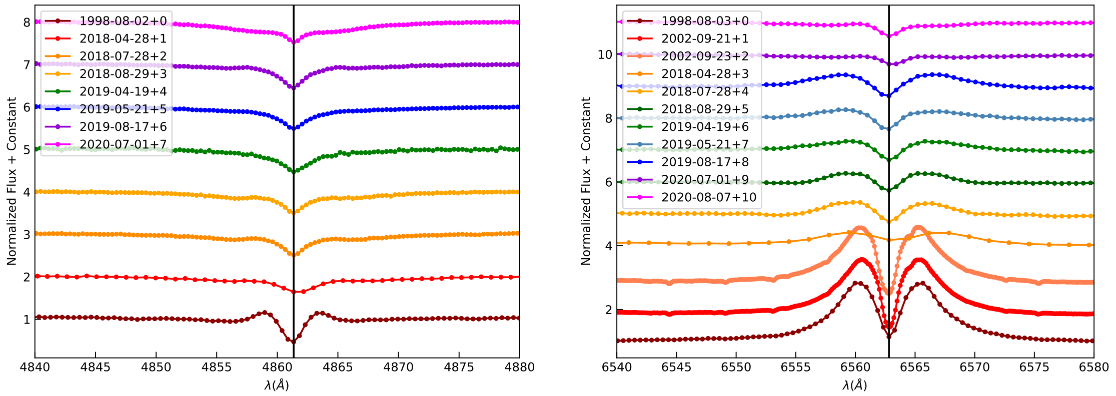

(a)

(b)

Figure D.41: A plot showing the normalized Hβ (a) and Hα (b) lines for BD+47 3985.

D.42 BD+49 614, HD 13867

Table D.62: The equivalent widths (corrected for absorption) of the Hα and Hβ emission for the star BD+49 614.

Date (MJD) (yr)	EW Hα (Å)	σ(EW Hα) (Å)	EW Hβ (Å)	σ(EW Hβ) (Å)	$v \sin i$ (km s^{-1})	σ($v \sin i$) (km s^{-1})
51029.64	-11.97	0.04	1.87	0.66	118.26	9.39
55091.75	-14.04	0.11	-	-	-	-
55146.62	-13.55	0.19	-0.27	0.12	398.57	33.65
55497.43	-14.26	0.06	0.23	0.08	90.59	76.06
56555.72	-13.62	0.06	0.64	0.03	39.79	115.51
58332.49	-13.38	0.04	0.47	0.05	61.11	97.01
58362.49	-12.97	0.04	0.89	0.03	51.35	73.38
58473.24	-12.99	0.05	0.30	0.04	60.06	194.81

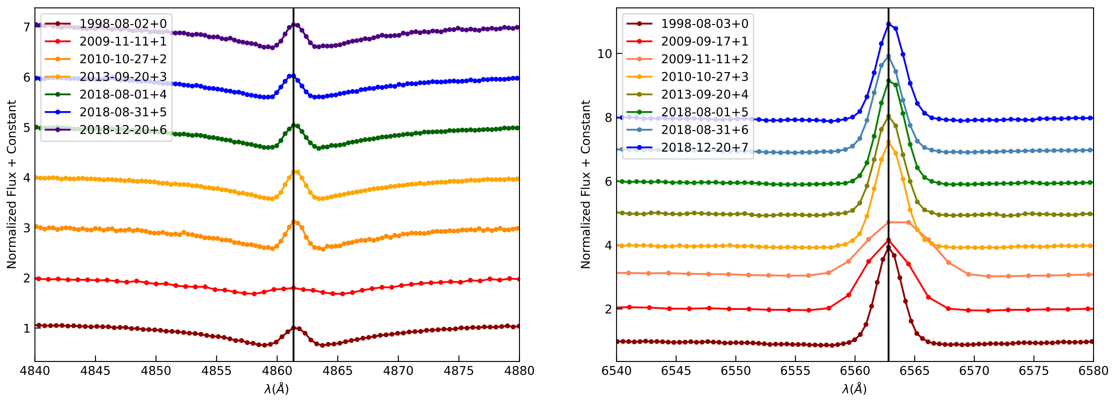

(a)

(b)

Figure D.42: A plot showing the normalized Hβ (a) and Hα (b) lines for BD+49 614.

D.43 BD+50 825, HD 23552

TABLE D.63: The equivalent widths (corrected for absorption) of the Hα and Hβ emission for the star BD+50 825.

Date (MJD) (yr)	EW Hα (Å)	σ(EW Hα) (Å)	EW Hβ (Å)	σ(EW Hβ) (Å)	$v \sin i$ (km s^{-1})	σ($v \sin i$) (km s^{-1})
51029.64	-9.28	0.05	-1.33	0.61	166.17	5.77
55141.62	-10.87	0.15	-2.76	0.13	205.28	19.02
55486.43	-9.84	0.10	-2.70	0.06	168.68	7.86
56547.72	-9.38	0.10	-2.23	0.03	192.89	10.21
56555.72	-9.34	0.11	-2.23	0.03	182.7	7.01
58337.49	-6.58	0.08	-2.23	0.05	205.04	29.99
58367.93	-6.67	0.06	-1.75	0.03	186.33	5.51
58456.24	-	-	-2.04	0.05	214.46	41.68
58496.68	-6.3	0.06	-2.66	0.05	213.26	39.85
58799.05	-5.71	0.10	-2.33	0.05	184.91	22.68
58830.48	-23.34	0.90	-1.95	0.04	205.92	7.36
59174.29	-	-	-1.53	0.06	207.01	27.48
59211.73	-5.24	0.15	-1.95	0.06	203.08	36.82

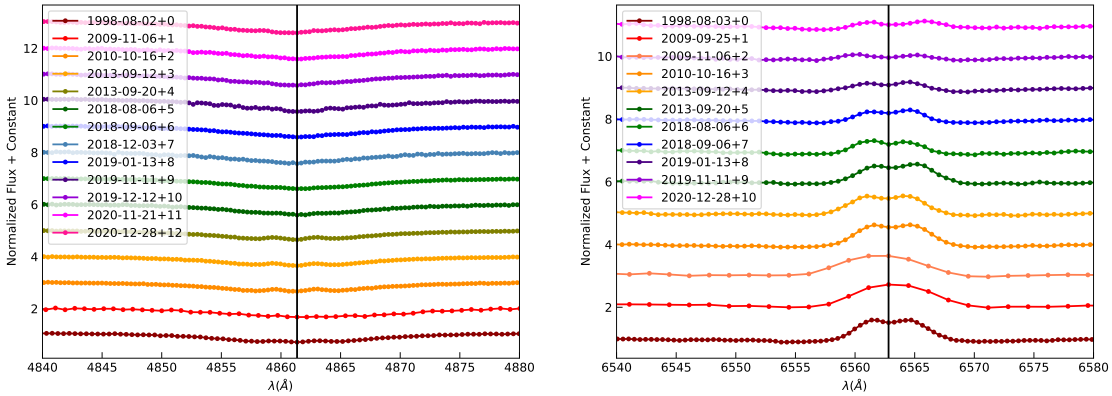

(a)

(b)

FIGURE D.43: A plot showing the normalized Hβ (a) and Hα (b) lines for BD+50 825.

D.44 BD+50 3430, HD 207232

TABLE D.64: The equivalent widths (corrected for absorption) of the Hα and Hβ emission for the star BD+50 3430.

Date (MJD) (yr)	EW Hα (Å)	σ(EW Hα) (Å)	EW Hβ (Å)	σ(EW Hβ) (Å)	$v \sin i$ (km s^{-1})	$\sigma(v \sin i)$ (km s^{-1})
51029.64	-13.66	0.05	-3.87	0.41	183.92	2.58
55091.75	-17.37	0.16	-	-	-	-
55149.62	-18.52	0.15	-5.49	0.10	182.57	46.52
55401.12	-19.51	0.13	-	-	-	-
55517.86	-19.04	0.10	-4.28	0.04	214.45	35.41
56579.15	-17.20	0.11	-3.65	0.03	230.31	18.4
58298.62	-16.04	0.09	-3.64	0.03	226.7	21.02
58329.06	-16.20	0.09	-4.04	0.03	198.18	12.91
58360.49	-16.02	0.08	-3.82	0.03	222.78	10.54
58592.99	-16.89	0.09	-4.05	0.15	266.38	62.06
58657.86	-16.82	0.08	-4.14	0.03	220.1	3.63
58712.74	-17.22	0.09	-4.51	0.03	197.01	23.14
59036.54	-17.95	0.11	-3.50	0.06	211.45	15.7

TABLE D.65: The $\Delta\lambda$ distance between peaks and V and R peak values for the Hα and Hβ emission for the star BD+50 3430.

MJD (yr)	$\Delta\lambda_{\mathrm{H}\alpha}$ (Å)	$\sigma(\Delta\lambda_{\mathrm{H}\alpha})$ (Å)	V_α	R_α	$\Delta\lambda_{\mathrm{H}\beta}$ (Å)	$\sigma(\Delta\lambda_{\mathrm{H}\beta})$ (Å)	V_β	R_β
51029.64	4.74	0.98	1.8764	1.8351	4.78	0.68	0.9082	0.9054
55398.12	4.2	1.1	2.1870	2.1994	-	-	-	-
55517.86	4.2	1.1	2.2428	2.3190	3.83	0.49	0.9091	0.9049
56579.15	4.8	1.1	2.0806	1.3925	4.52	0.49	0.8826	0.8777
58298.62	4.2	1.1	1.9411	1.9789	4.87	0.49	0.8515	0.8517
58329.06	4.2	1.1	1.9499	1.9465	4.53	0.49	0.8717	0.8608
58360.49	4.8	1.1	1.8937	1.9659	4.87	0.49	0.8662	0.8579
58592.99	4.2	1.1	1.9753	2.0366	4.89	0.49	0.8766	0.8828
58657.86	4.8	1.1	1.9520	2.0292	4.53	0.49	0.8791	0.8714
58712.74	4.2	1.1	2.0336	1.9826	4.18	0.49	0.8796	0.8891
59036.54	4.2	1.1	1.9673	2.0340	4.18	0.49	0.8942	0.8757

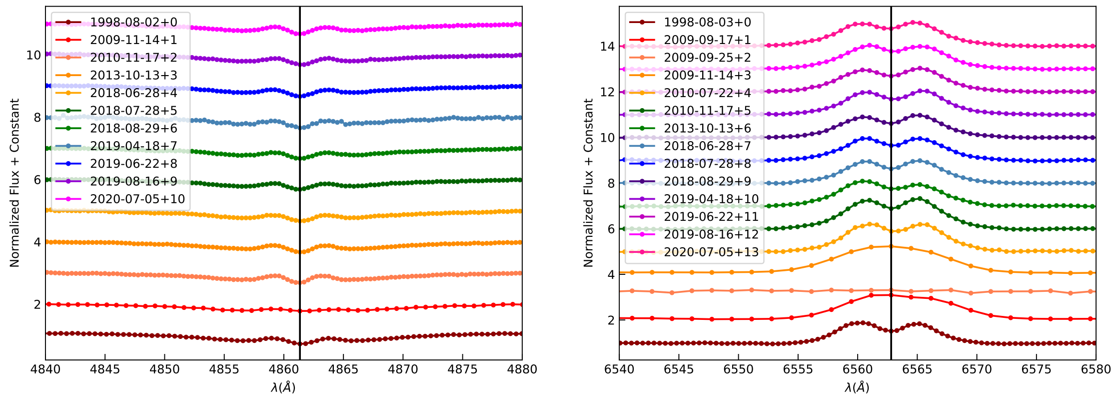

(a) (b)

FIGURE D.44: A plot showing the normalized Hβ (a) and Hα (b) lines for BD+50 3430.

D.45 BD+51 3091, HD20551

Table D.66: The equivalent widths (corrected for absorption) of the Hα and Hβ emission for the star BD+51 3091.

Date (MJD) (yr)	EW Hα (Å)	σ(EW Hα) (Å)	EW Hβ (Å)	σ(EW Hβ) (Å)	$v \sin i$ (km s^{-1})	σ($v \sin i$) (km s^{-1})
51029.64	-5.11	0.03	-0.81	0.53	124.04	44.44
55089.75	-6.84	0.12	-	-	-	-
55172.06	-6.88	0.13	-1.51	0.07	190.93	48.26
55401.12	-6.10	0.07	-	-	-	-
55517.86	-6.16	0.06	-2.24	0.04	137.15	52.83
56582.15	-5.70	0.08	-0.53	0.03	134.3	39.28
58298.62	-4.80	0.25	-1.12	0.03	124.07	38.07
58332.06	-4.80	0.04	-0.53	0.03	138.1	39.64
58361.49	-4.79	0.06	-0.72	0.03	124.87	37.44
58592.99	-4.66	0.05	-0.95	0.05	184.18	70.5
58635.43	-4.79	0.05	-0.55	0.03	148.96	43.55
58713.74	-4.78	0.05	-1.23	0.03	130.1	113.16

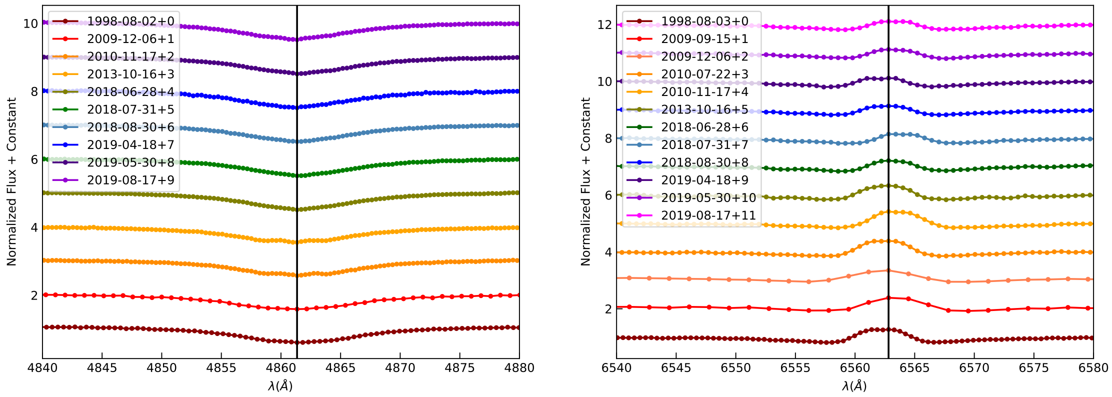

(a) (b)

Figure D.45: A plot showing the normalized Hβ (a) and Hα (b) lines for BD+51 3091.

D.46 BD+53 2599, HD 203356

Table D.67: The equivalent widths (corrected for absorption) of the Hα and Hβ emission for the star BD+53 2599.

Date (MJD) (yr)	EW Hα (Å)	σ(EW Hα) (Å)	EW Hβ (Å)	σ(EW Hβ) (Å)	$v \sin i$ (km s^{-1})	$\sigma(v \sin i)$ (km s^{-1})
51029.64	-8.68	0.05	-1.89	0.62	186.43	25.48
55091.75	-6.28	0.21	-	-	-	-
55155.62	-8.04	0.15	-3.52	0.06	-	-
55400.12	-8.12	0.05	-	-	-	-
55517.86	-6.42	0.10	-3.37	0.06	229.65	17.22
56583.15	-4.87	0.10	-2.33	0.03	215.47	23.92
58274.62	-4.00	0.36	-2.59	0.06	183.1	55.57
58329.06	-5.51	0.09	-2.67	0.03	209.97	40.84
58358.49	-5.29	0.05	-2.40	0.04	202.75	33.54
58596.99	-5.68	0.46	-2.69	0.05	374.54	59.36
58652.86	-5.77	0.07	-3.55	0.04	205.91	40.32
58707.74	-5.65	0.07	-3.28	0.04	245.93	20.72
59035.54	-5.91	0.10	-2.11	0.04	212.36	47.79

Table D.68: The $\Delta\lambda$ distance between peaks and V and R peak values for the Hα emission for the star BD+53 2599.

MJD (yr)	$\Delta\lambda_{\mathrm{H}\alpha}$ (Å)	$\sigma(\Delta\lambda_{\mathrm{H}\alpha})$ (Å)	V_α	R_α
51029.64	3.79	0.98	1.4744	1.3793
55400.12	4.2	1.1	1.1187	0.9107
55517.86	4.8	1.1	1.1127	1.1314
56583.15	6.0	1.1	1.0351	1.0157
58274.62	6.0	1.1	1.0412	1.0500
58329.06	5.4	1.1	1.0322	1.0254
58358.49	5.4	1.1	1.0342	1.0317
58596.99	6.0	1.1	1.1053	1.1148
58652.86	6.0	1.1	1.0660	1.0650
58707.74	5.4	1.1	1.0546	1.0546
59035.54	6.0	1.1	1.0629	1.0468

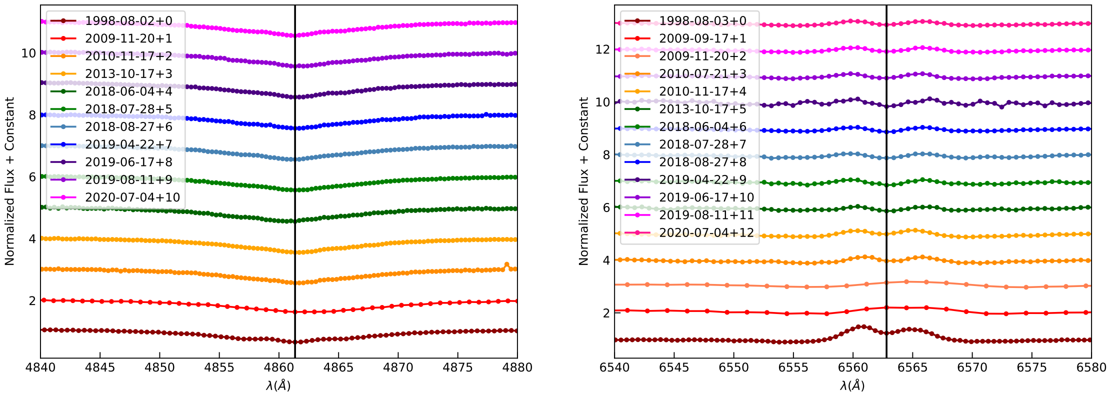

(a) (b)

FIGURE D.46: A plot showing the normalized Hβ (a) and Hα (b) lines for BD+53 2599.

D.47 BD+55 552, HD 13669

TABLE D.69: The equivalent widths (corrected for absorption) of the Hα and Hβ emission for the star BD+55 552.

Date (MJD) (yr)	EW Hα (Å)	σ(EW Hα) (Å)	EW Hβ (Å)	σ(EW Hβ) (Å)	$v \sin i$ (km s^{-1})	$\sigma(v \sin i)$ (km s^{-1})
51029.64	-6.15	0.08	-1.95	0.42	222.66	7.1
55091.75	-15.17	0.28	-	-	-	-
55147.62	-15.11	0.25	-4.74	0.11	280.66	16.37
55148.62	-15.88	0.20	-3.56	0.10	263.13	12.35
55406.12	-15.91	0.12	-3.49	0.03	251.29	39.55
55496.43	-16.61	0.11	-3.41	0.05	305.79	29.69
56542.72	-21.76	0.14	-3.55	0.04	244.19	13.05
58331.06	-38.28	0.13	-5.31	0.04	239.63	45.63
58360.49	-39.71	0.13	-5.52	0.04	262.26	33.98
58472.24	-40.10	0.14	-5.21	0.07	360.69	87.75
58707.74	-39.53	0.14	-5.29	0.05	302.43	62.33

TABLE D.70: The $\Delta\lambda$ distance between peaks and V and R peak values for the Hα and Hβ emission for the star BD+55 552.

MJD (yr)	$\Delta\lambda_{\mathrm{H}\alpha}$ (Å)	$\sigma(\Delta\lambda_{\mathrm{H}\alpha})$ (Å)	V$_\alpha$	R$_\alpha$	$\Delta\lambda_{\mathrm{H}\beta}$ (Å)	$\sigma(\Delta\lambda_{\mathrm{H}\beta})$ (Å)	V$_\beta$	R$_\beta$
51029.64	7.58	0.98	1.3161	1.3033	-	-	-	-
55406.12	6.0	1.1	2.0266	1.9022	4.86	0.49	0.9921	0.9442
55496.43	6.0	1.1	2.0380	1.9541	4.87	0.49	0.9943	0.9538
56542.72	4.2	1.1	2.3445	2.2096	4.52	0.49	1.0506	1.0365
58331.06	4.2	1.1	3.6298	3.5034	4.52	0.49	1.3344	1.3217
58360.49	4.2	1.1	3.8048	3.7645	3.48	0.49	1.3662	1.3326
58472.24	3.6	1.1	3.8873	3.7334	3.83	0.49	1.3432	1.3507
58707.74	4.2	1.1	3.7692	3.7069	4.53	0.49	1.3339	1.4001

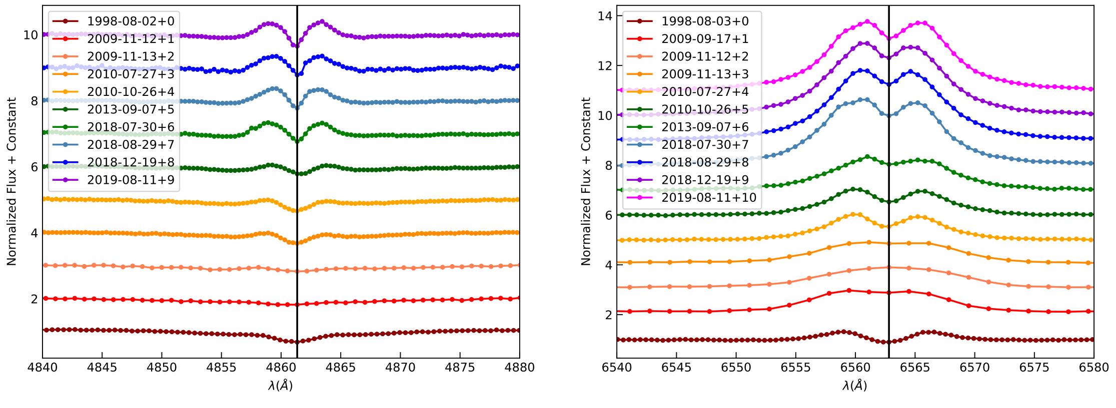

(a)

(b)

FIGURE D.47: A plot showing the normalized Hβ (a) and Hα (b) lines for BD+55 552.

D.48 BD+55 605, HD 14605

Table D.71: The equivalent widths (corrected for absorption) of the Hα and Hβ emission for the star BD+55 605.

Date (MJD) (yr)	EW Hα (Å)	σ(EW Hα) (Å)	EW Hβ (Å)	σ(EW Hβ) (Å)	$v \sin i$ (km s^{-1})	$\sigma(v \sin i)$ (km s^{-1})
51029.64	-9.00	0.08	0.28	0.83	145.17	10.79
55091.75	-10.25	0.18	-	-	-	-
55148.62	-9.41	0.20	-2.79	0.14	230.17	59.77
56537.72	-6.14	0.11	-1.26	0.07	120.3	4.01
58332.06	-0.44	0.07	0.05	0.05	165.16	5.41
58362.93	-0.65	0.09	0.22	0.06	162.84	7.79
58471.24	-3.17	0.07	-1.05	0.16	165.81	11.57

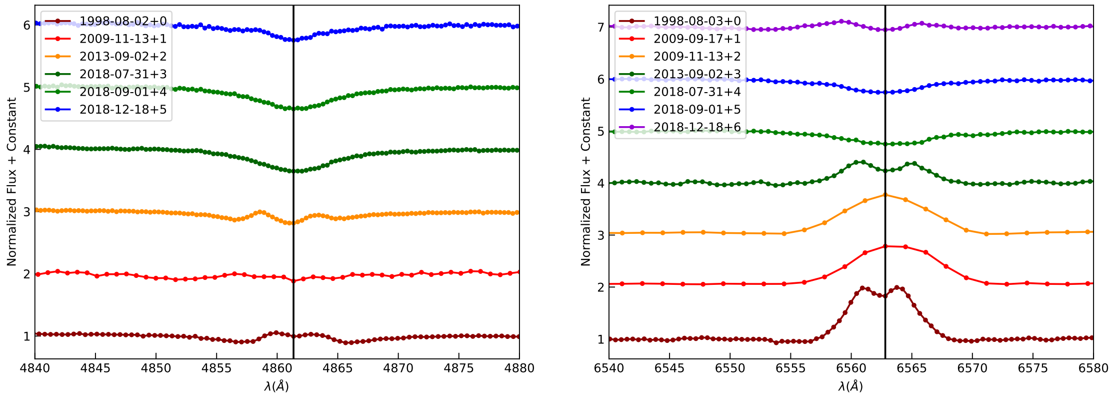

(a)

(b)

Figure D.48: A plot showing the normalized Hβ (a) and Hα (b) lines for BD+55 605.

D.49 BD+55 2411, HD 195554

Table D.72: The equivalent widths (corrected for absorption) of the Hα and Hβ emission for the star BD+55 2411.

Date (MJD) (yr)	EW Hα (Å)	σ(EW Hα) (Å)	EW Hβ (Å)	σ(EW Hβ) (Å)	$v \sin i$ (km s^{-1})	$\sigma(v \sin i)$ (km s^{-1})
51029.64	-6.22	0.04	0.71	0.64	162.05	36.36
55099.75	-10.20	0.12	-	-	-	-
55154.62	-3.75	0.28	-0.37	0.09	199.87	19.26
55396.12	-6.21	0.08	-1.94	0.04	190.18	66.04
55518.86	-6.16	0.09	-1.49	0.06	190.5	21.8
56583.15	-7.35	0.09	-1.16	0.04	200.03	47.98
58204.31	-	-	0.51	0.10	180.16	92.4
58275.62	-5.96	0.08	-0.86	0.05	189.23	70.94
58330.06	-6.62	0.07	-1.53	0.03	197.99	37.0
58360.49	-5.96	0.07	-1.13	0.04	174.32	77.05
58564.55	-6.16	0.06	-1.47	0.06	214.22	172.64
58595.99	-6.85	0.06	-1.54	0.06	248.42	218.18
58626.43	-6.77	0.05	-1.78	0.04	187.26	58.09
58657.86	-5.97	0.06	-1.09	0.03	193.65	40.47
58707.74	-6.06	0.07	-0.40	0.04	186.36	66.76
59034.54	-6.53	0.08	0.21	0.06	211.36	46.07

Table D.73: The $\Delta\lambda$ distance between peaks and V and R peak values for the Hα emission for the star BD+55 2411.

MJD (yr)	$\Delta\lambda_{\mathrm{H}\alpha}$ (Å)	$\sigma(\Delta\lambda_{\mathrm{H}\alpha})$ (Å)	V$_\alpha$	R$_\alpha$
51029.64	2.84	0.98	1.1945	1.1835
55396.12	3.0	1.1	1.2555	1.2405
55518.86	3.0	1.1	1.1648	1.1779
56583.15	2.4	1.1	1.1899	1.2140
59034.54	3.0	1.1	1.1722	1.1789
58707.74	3.0	1.1	1.1589	1.1659
58657.86	3.6	1.1	1.1281	1.1650
58625.99	3.6	1.1	1.1900	1.1565
58595.99	3.0	1.1	1.2075	1.1792
58564.55	3.0	1.1	1.1808	1.1557
58360.49	3.6	1.1	1.1289	1.1476
58330.06	3.0	1.1	1.1746	1.1685
58275.62	3.0	1.1	1.1517	1.1352

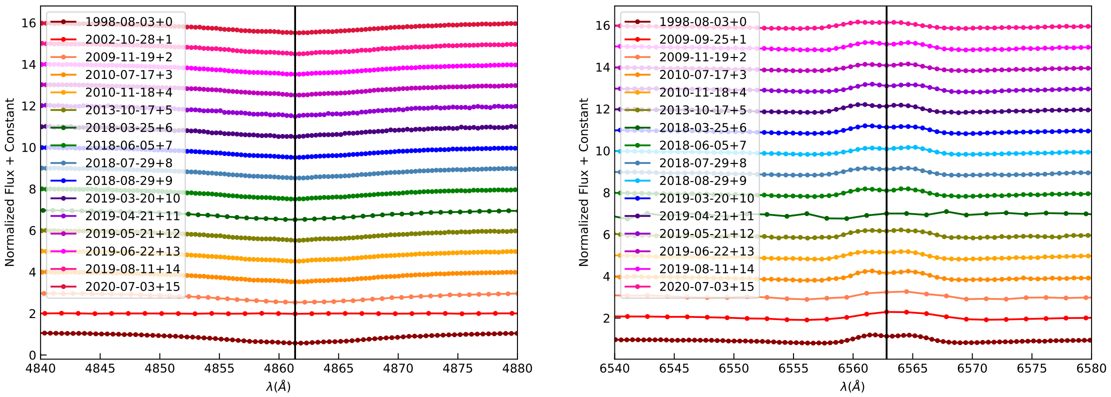

(a) (b)

FIGURE D.49: A plot showing the normalized Hβ (a) and Hα (b) lines for BD+55 2411.

D.50 BD+56 473, V356 Per

TABLE D.74: The equivalent widths (corrected for absorption) of the Hα and Hβ emission for the star BD+56 473, and the rotational velocities calculated from the He I lines.

Date (MJD) (yr)	EW Hα (Å)	σ(EW Hα) (Å)	EW Hβ (Å)	σ(EW Hβ) (Å)	$v \sin i$ (km s^{-1})	$\sigma(v \sin i)$ (km s^{-1})
51029.64	-38.02	0.11	-6.37	0.54	198.13	8.68
55099.75	-22.27	0.23	-	-	-	-
55143.62	-22.73	0.31	-4.70	0.08	171.93	144.02
55410.12	-	-	-4.00	0.05	171.63	37.39
55496.43	-	-	-3.77	0.05	187.6	33.8
56545.72	-17.09	0.14	-3.13	0.05	227.48	8.38
58329.06	-19.22	0.13	-3.82	0.05	226.74	6.48
58360.49	-19.55	0.12	-3.61	0.05	191.66	35.62
58472.24	-	-	-2.72	0.09	284.25	106.71

TABLE D.75: The $\Delta\lambda$ distance between peaks and V and R peak values for the Hα, Hβ and H gamma emission for the star BD+56 473.

MJD (yr)	$\Delta\lambda_{\mathrm{H}\alpha}$ (Å)	$\sigma(\Delta\lambda_{\mathrm{H}\alpha})$ (Å)	V_α	R_α	$\Delta\lambda_{\mathrm{H}\beta}$ (Å)	$\sigma(\Delta\lambda_{\mathrm{H}\beta})$ (Å)	V_β	R_β
51029.64	1.90	0.98	4.1675	4.0359	2.39	0.68	1.4761	1.4091
55410.12	-	-	-	-	3.83	0.49	1.3249	1.3726
55496.43	-	-	-	-	3.49	0.49	1.3218	1.3024
56545.72	3.6	1.1	2.1919	2.1977	3.83	0.49	1.1858	1.1089
58329.06	4.2	1.1	2.5035	2.4496	3.83	0.49	1.1914	1.2015
58360.49	4.2	1.1	2.4623	2.5345	3.48	0.49	1.2012	1.2010
58472.24	-	-	-	-	3.48	0.49	1.0935	1.1779

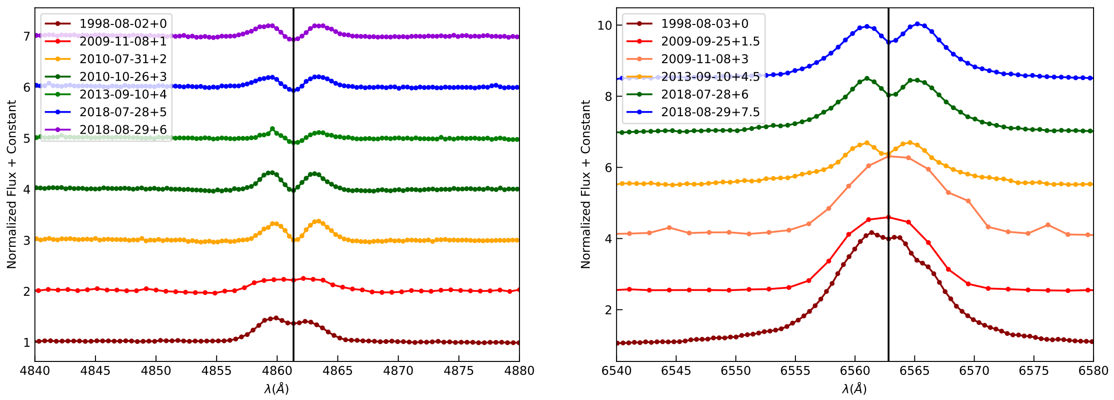

(a) (b)

FIGURE D.50: A plot showing the normalized Hβ (a) and Hα (b) lines for BD+56 473.

D.51 BD+56 478, HD 13890

TABLE D.76: The equivalent widths (corrected for absorption) of the Hα and Hβ emission for the star BD+56 478.

Date (MJD) (yr)	EW Hα (Å)	σ(EW Hα) (Å)	EW Hβ (Å)	σ(EW Hβ) (Å)	$v \sin i$ (km s^{-1})	σ($v \sin i$) (km s^{-1})
51029.64	-11.92	0.08	-3.40	0.53	143.83	3.5
55091.75	-16.34	0.22	-	-	-	-
55143.62	-16.53	0.20	-4.43	0.06	188.27	56.1
55492.43	-21.64	0.14	-4.14	0.04	178.15	23.6
56545.72	-35.87	0.25	-4.30	0.04	156.35	13.43
58332.06	-26.09	0.11	-4.69	0.04	170.2	12.84
58362.49	-25.43	0.10	-4.54	0.03	165.06	6.10
58382.93	-	-	-6.84	0.06	186.84	608.85
58471.24	-40.52	0.17	-6.68	0.04	254.55	87.01
58706.74	-23.85	0.11	-4.84	0.03	171.15	19.68

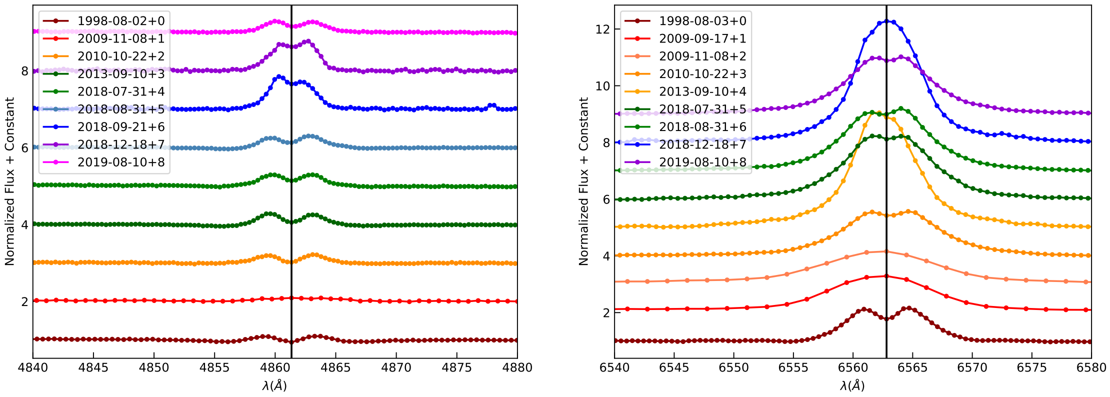

(a)

(b)

FIGURE D.51: A plot showing the normalized Hβ (a) and Hα (b) lines for BD+56 478.

D.52 BD+56 484, V502 Per

TABLE D.77: The equivalent widths (corrected for absorption) of the Hα and Hβ emission for the star BD+56 484, and the rotational velocities calculated from the He I lines.

Date (MJD) (yr)	EW Hα (Å)	σ(EW Hα) (Å)	EW Hβ (Å)	σ(EW Hβ) (Å)	$v \sin i$ (km s^{-1})	$\sigma(v \sin i)$ (km s^{-1})
51029.64	-48.39	0.07	-8.66	0.42	174.12	2.76
55099.75	-47.94	0.21	-	-	-	-
55143.62	-49.95	0.24	-7.48	0.08	228.05	34.9
55404.12	-45.82	0.12	-6.62	0.03	245.87	8.04
55496.43	-39.84	0.10	-6.29	0.06	191.16	33.52
56545.72	-38.98	0.10	-	-	-	-
56555.72	-38.52	0.09	-6.36	0.02	179.11	14.9
58353.49	-38.35	0.09	-6.62	0.04	180.77	6.99
58382.93	-37.38	0.10	-6.38	0.05	186.84	608.85
58471.24	-37.21	0.14	-6.02	0.08	287.73	54.85
59068.98	-39.03	0.09	-	-	-	-

TABLE D.78: The $\Delta\lambda$ distance between peaks and V and R peak values for the Hβ emission for the star BD+56 484.

MJD (yr)	$\Delta\lambda_{\mathrm{H}\beta}$ (Å)	$\sigma(\Delta\lambda_{\mathrm{H}\beta})$ (Å)	V$_\beta$	R$_\beta$
55404.12	1.39	0.49	1.7396	1.9223
56555.72	1.39	0.49	1.9721	1.8213
58353.49	1.74	0.49	1.9105	1.7272
58382.93	1.75	0.49	1.8484	1.7092
58471.24	2.09	0.49	1.6756	1.7590

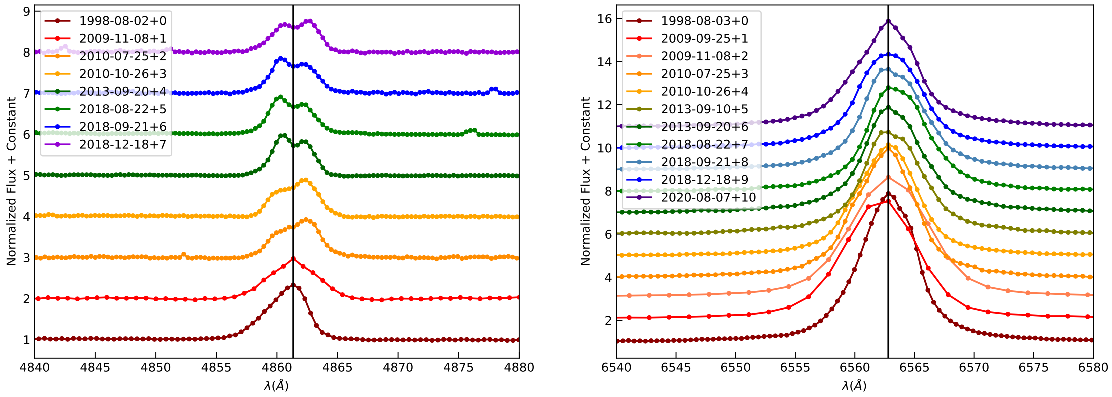

(a) (b)

FIGURE D.52: A plot showing the normalized Hβ (a) and Hα (b) lines for BD+56 484.

D.53 BD+56 493

Table D.79: The equivalent widths (corrected for absorption) of the Hα and Hβ emission for the star BD+56 493.

Date (MJD) (yr)	EW Hα (Å)	σ(EW Hα) (Å)	EW Hβ (Å)	σ(EW Hβ) (Å)	$v \sin i$ (km s^{-1})	$\sigma(v \sin i)$ (km s^{-1})
51029.64	-0.67	0.07	-1.61	0.41	113.66	3.75
55160.62	-0.14	0.33	-1.20	0.13	193.12	32.15
55405.12	-5.02	0.08	-	-	-	-
55496.43	-	-	-7.5	0.13	191.16	33.52
55500.43	-5.42	0.14	-1.85	0.10	251.57	4.88
56537.72	-6.94	0.08	-2.09	0.03	198.76	31.4
58353.49	-2.70	0.05	-1.24	0.06	242.55	16.17
58382.93	-	-	-1.74	0.08	231.56	22.89
58472.24	-0.95	0.09	-0.81	0.17	271.18	98.95
58799.05	-0.04	0.06	-0.95	0.05	241.25	9.73
58830.48	-0.27	0.08	-0.32	0.07	252.05	35.47

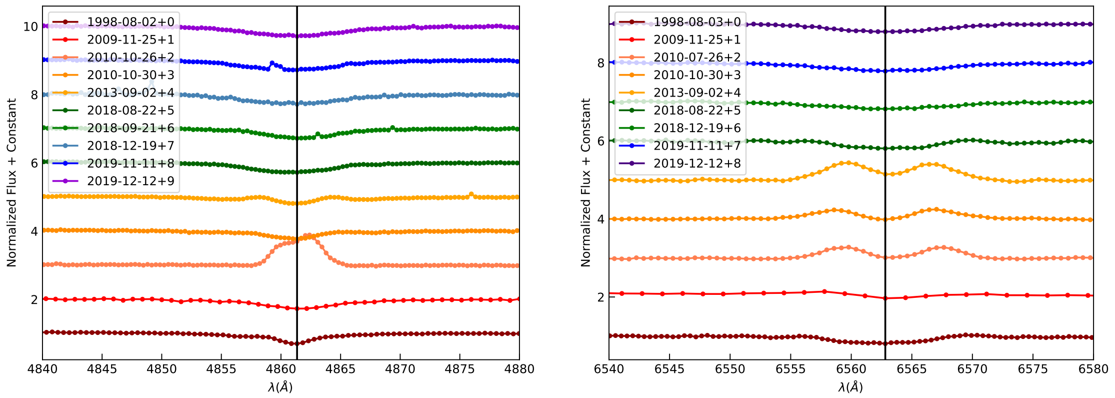

(a)

(b)

Figure D.53: A plot showing the normalized Hβ (a) and Hα (b) lines for BD+56 493.

D.54 BD+56 511

TABLE D.80: The equivalent widths (corrected for absorption) of the Hα and Hβ emission for the star BD+56 511.

Date (MJD) (yr)	EW Hα (Å)	σ(EW Hα) (Å)	EW Hβ (Å)	σ(EW Hβ) (Å)	$v \sin i$ (km s^{-1})	$\sigma(v \sin i)$ (km s^{-1})
51029.64	-7.08	0.12	-1.11	0.41	113.66	3.75
55148.62	-	-	-1.44	0.05	156.49	50.65
55154.62	-7.91	0.33	-1.10	0.09	164.63	4.52
55405.12	-9.72	0.19	-	-	-	-
55496.43	-8.53	0.16	-1.62	0.13	93.7	17.82
56543.72	-7.78	0.17	-1.14	0.03	104.49	1.04
58336.49	-8.94	0.15	-1.34	0.04	89.06	27.14
58474.24	-8.92	0.15	-1.48	0.11	108.4	30.38
58829.48	-8.54	0.15	-0.30	0.15	101.37	16.57
59215.16	-9.38	0.20	-0.96	0.06	104.63	37.77

TABLE D.81: The $\Delta\lambda$ distance between peaks and V and R peak values for the Hα emission of the star BD+56 511.

MJD (yr)	$\Delta\lambda_{\mathrm{H}\alpha}$ (Å)	$\sigma(\Delta\lambda_{\mathrm{H}\alpha})$ (Å)	V_α	R_α
51029.64	4.27	0.98	1.4952	1.3621
55405.12	5.4	1.1	1.6663	1.4529
55526.86	5.4	1.1	1.7146	1.4363
56543.72	4.2	1.1	1.3977	1.5909
58336.49	4.2	1.1	1.5605	1.4721
58474.24	4.8	1.1	1.5096	1.4769
58829.48	4.2	1.1	1.5234	1.5232
59215.16	3.4	1.1	1.4649	1.5424

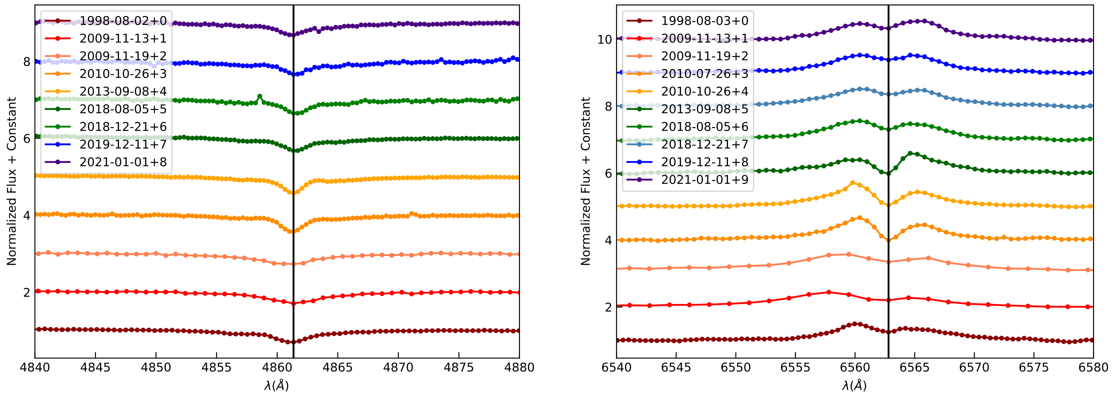

(a) (b)

FIGURE D.54: A plot showing the normalized Hβ (a) and Hα (b) lines for BD+56 511.

D.55 BD+56 573

Table D.82: The equivalent widths (corrected for absorption) of the Hα and Hβ emission for the star BD+56 573.

Date (MJD) (yr)	EW Hα (Å)	σ(EW Hα) (Å)	EW Hβ (Å)	σ(EW Hβ) (Å)	$v \sin i$ (km s^{-1})	$\sigma(v \sin i)$ (km s^{-1})
51029.64	-67.64	0.10	-8.95	0.43	196.16	6.51
55155.62	-75.25	0.25	-8.92	0.25	273.22	200.19
55192.06	-74.98	0.26	-8.56	0.07	233.29	35.14
55494.43	-79.08	0.23	-7.97	0.05	319.05	117.55
56547.72	-78.49	0.15	-9.00	0.02	221.89	12.8
58355.49	-90.07	0.15	-10.13	0.03	211.05	2.5
58385.93	-	-	-10.01	0.14	226.0	38.13
58468.24	-86.81	0.16	-10.91	0.16	338.43	139.03
58498.68	-90.03	0.14	-9.84	0.31	246.84	104.17
58713.74	-	-	-9.05	0.03	230.91	16.5
58829.48	-90.59	0.18	-9.86	0.07	259.3	703.02

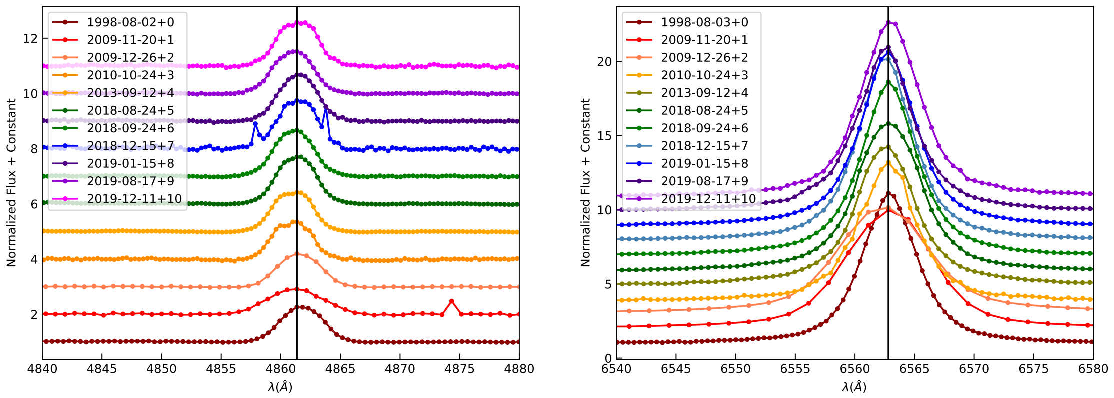

(a)

(b)

Figure D.55: A plot showing the normalized Hβ (a) and Hα (b) lines for BD+56 573.

D.56 BD+57 681, HD 237056

TABLE D.83: The equivalent widths (corrected for absorption) of the Hα and Hβ emission for the star BD+57 681.

Date (MJD) (yr)	EW Hα (Å)	σ(EW Hα) (Å)	EW Hβ (Å)	σ(EW Hβ) (Å)	$v \sin i$ (km s^{-1})	$\sigma(v \sin i)$ (km s^{-1})
51029.64	-2.46	0.07	-0.97	0.52	145.91	4.4
55091.75	-3.73	0.35	-	-	-	-
55143.62	-5.75	0.43	-0.78	0.08	176.39	21.48
55423.55	-2.30	0.07	-0.58	0.06	175.4	30.13
55492.43	-2.62	0.05	-0.66	0.05	151.5	13.33
56554.72	-2.43	0.10	-0.61	0.04	156.45	1.46
58332.06	-30.52	0.13	-5.24	0.05	154.8	13.88
58361.49	-32.28	0.13	-5.84	0.06	167.46	13.72
58470.24	-33.92	0.13	-6.40	0.08	213.91	53.04
58707.74	-33.59	0.11	-5.16	0.07	142.28	14.59
58831.48	-32.05	0.11	-4.38	0.03	133.72	30.94
59212.73	-24.26	0.15	-4.76	0.10	156.38	20.83

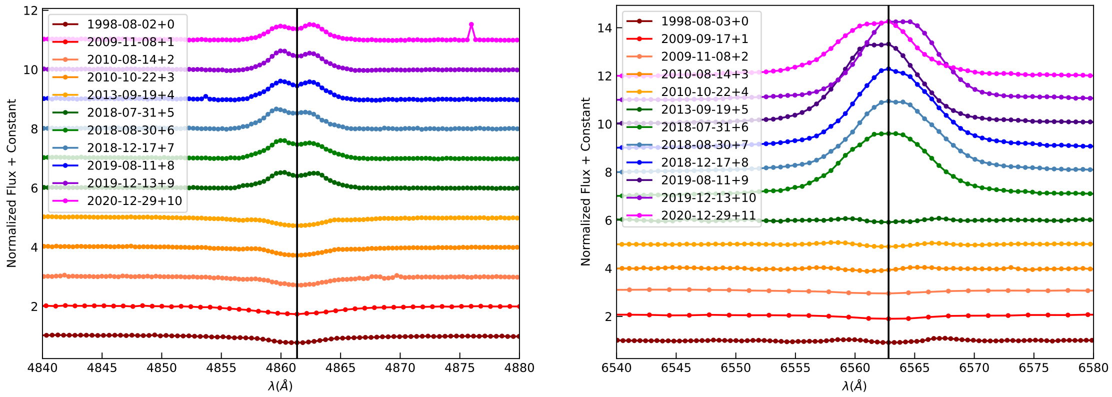

(a)

(b)

FIGURE D.56: A plot showing the normalized Hβ (a) and Hα (b) lines for BD+57 681.

D.57 BD+58 554, HD 237060

TABLE D.84: The equivalent widths (corrected for absorption) of the Hα and Hβ emission for the star BD+58 554.

Date (MJD) (yr)	EW Hα (Å)	σ(EW Hα) (Å)	EW Hβ (Å)	σ(EW Hβ) (Å)	$v \sin i$ (km s^{-1})	$\sigma(v \sin i)$ (km s^{-1})
51028.64	-	-	-1.84	0.63	208.42	6.85
55091.75	-16.40	0.18	-	-	-	-
55146.62	-16.27	0.13	-3.23	0.09	229.71	48.11
55426.55	-16.78	0.11	-3.94	0.06	222.06	24.04
55492.43	-16.46	0.10	-4.34	0.09	211.74	179.78
56556.72	-15.57	0.11	-2.36	0.04	216.64	13.13
58332.49	-15.69	0.08	-2.21	0.06	233.25	22.43
58362.93	-15.71	0.08	-3.52	0.04	198.29	6.2
58468.24	-15.61	0.09	-3.55	0.12	216.75	82.4
58498.68	-15.80	0.08	-3.32	0.12	255.79	149.6
58799.05	-15.47	0.09	-2.64	0.09	224.52	13.5
58830.48	-15.35	0.09	-3.21	0.08	285.24	32.42

TABLE D.85: The $\Delta\lambda$ distance between peaks and V and R peak values for the Hα and Hβ emission for the star BD+58 554.

MJD (yr)	$\Delta\lambda_{\mathrm{H}\alpha}$ (Å)	$\sigma(\Delta\lambda_{\mathrm{H}\alpha})$ (Å)	V_α	R_α	$\Delta\lambda_{\mathrm{H}\beta}$ (Å)	$\sigma(\Delta\lambda_{\mathrm{H}\beta})$ (Å)	V_β	R_β
51028.64	-	-	-	-	3.34	0.49	0.8653	0.8669
55426.55	3.0	1.1	2.3330	2.2746	3.83	0.49	0.8456	0.8410
55492.43	3.0	1.1	2.3390	2.3065	3.48	0.49	0.8260	0.8390
56556.72	2.4	1.1	2.1677	2.1536	2.79	0.49	0.8265	0.8215
58333.06	2.4	1.1	2.2739	2.2024	3.48	0.49	0.8288	0.7980
58362.93	3.0	1.1	2.2740	2.1941	3.48	0.49	0.8269	0.8102
58468.24	3.0	1.1	2.2813	2.1787	2.79	0.49	0.8352	0.8077
58498.68	3.0	1.1	2.2682	2.2129	3.83	0.49	0.8617	0.8363
58799.05	3.0	1.1	2.2310	2.1631	3.83	0.49	0.8359	0.7950
58830.48	3.0	1.1	2.2261	2.2102	3.48	0.68	0.8468	0.8311

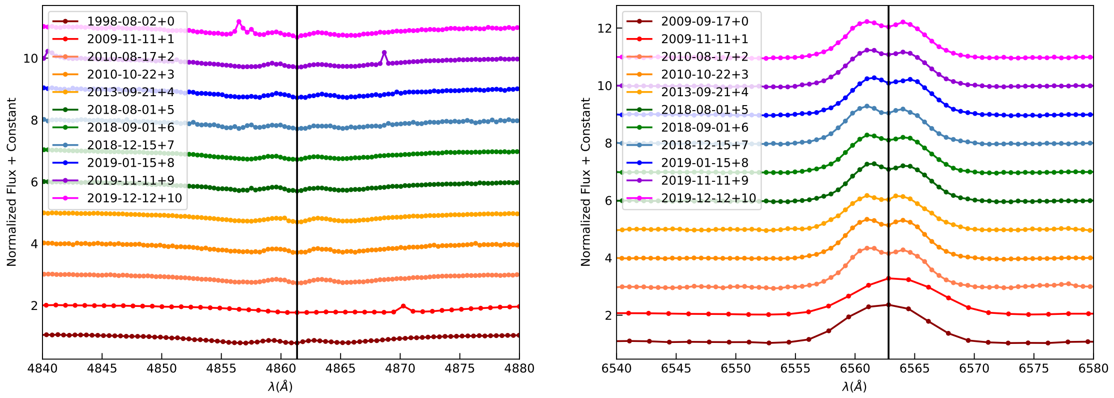

(a) (b)

FIGURE D.57: A plot showing the normalized Hβ (a) and Hα (b) lines for BD+58 554.

D.58 BD+58 2320, HD 239758

TABLE D.86: The equivalent widths (corrected for absorption) of the Hα and Hβ emission for the star BD+58 2320.

Date (MJD) (yr)	EW Hα (Å)	σ(EW Hα) (Å)	EW Hβ (Å)	σ(EW Hβ) (Å)	$v \sin i$ (km s^{-1})	$\sigma(v \sin i)$ (km s^{-1})
51029.64	-7.06	0.08	-1.58	0.6	231.16	4.12
55091.75	-9.15	0.22	-	-	-	-
55146.62	-9.70	0.26	-4.33	0.12	223.78	29.56
55400.12	-10.81	0.14	-2.15	0.06	-	-
55517.86	-10.56	0.13	-1.93	0.05	248.46	3.66
56557.72	-10.45	0.13	-2.04	0.07	239.79	8.79
58329.06	-8.97	0.13	-2.33	0.05	230.9	18.55
58360.49	-8.31	0.10	-3.55	0.14	230.89	14.08
58592.99	-9.31	0.11	-5.12	0.24	293.77	10.41
58653.86	-	-	-	-	438.4	47.9
58712.74	-9.38	0.11	-1.42	0.08	216.79	22.86
59036.54	-12.47	0.11	-2.51	0.05	268.38	20.0

TABLE D.87: The $\Delta\lambda$ distance between peaks and V and R peak values for the Hα and Hβ emission for the star BD+58 2320.

MJD (yr)	$\Delta\lambda_{\mathrm{H}\alpha}$ (Å)	$\sigma(\Delta\lambda_{\mathrm{H}\alpha})$ (Å)	V$_\alpha$	R$_\alpha$	$\Delta\lambda_{\mathrm{H}\beta}$ (Å)	$\sigma(\Delta\lambda_{\mathrm{H}\beta})$ (Å)	V$_\beta$	R$_\beta$
51029.64	7.11	0.98	1.4715	1.4497	5.73	0.68	0.9459	0.9613
55400.12	7.2	1.1	1.5708	1.5486	-	-	-	-
55517.86	6.0	1.1	1.5611	1.6045	5.92	0.49	0.9549	0.9653
56557.72	6.6	1.1	1.5669	1.5629	5.57	0.49	0.9984	0.9543
58329.06	7.2	1.1	1.4545	1.4583	6.27	0.49	0.9227	0.9365
58360.49	6.6	1.1	1.4479	1.4781	6.27	0.49	0.9432	0.9311
58592.99	6.0	1.1	1.5682	1.5682	6.27	0.49	0.9735	0.9879
58653.86	-	-	-	-	5.57	0.49	0.9830	1.0020
58712.74	6.6	1.1	1.5817	1.5451	5.92	0.49	0.9738	0.9194
59036.54	5.4	1.1	1.6784	1.6627	5.92	0.49	0.9969	1.0372

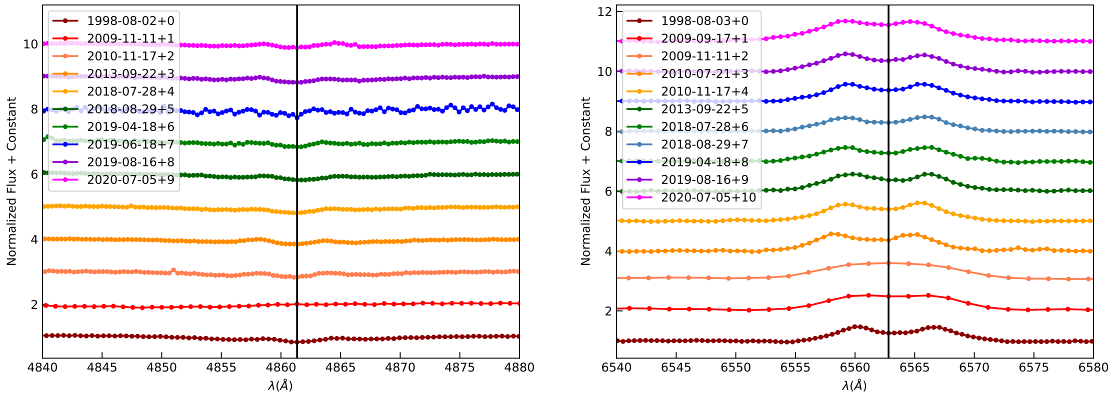

(a) (b)

FIGURE D.58: A plot showing the normalized Hβ (a) and Hα (b) lines for BD+58 2320.

Bibliography

Aerts C., Christensen-Dalsgaard J., Kurtz D. W., 2010, Asteroseismology. Springer Dordrecht

Allen D. A., 1973, Monthly Notices of the Royal Astronomical Society, 161, 145

Allen D. A., Swings J. P., 1976, Astronomy & Astrophysics, 47, 293

Angarita Y., Versteeg M. J. F., Haverkorn M., Rodrigues C. V., Magalhães A. M., Santos-Lima R., Kawabata K. S., 2023, The Astronomical Journal, 166, 34

Angel J. R. P., 1974, in Gehrels T., ed., IAU Colloq. 23: Planets, Stars, and Nebulae: Studied with Photopolarimetry Mechanisms that Produce Linear and Circular Polarization. p. 54

Astropy Collaboration Price-Whelan A. M., Lim P. L., Earl N., Starkman N., Bradley L., Shupe D. L., Patil A. A., Corrales L., Brasseur C. E., Nöthe M., Donath A., Tollerud E., Morris B. M., Ginsburg A., Vaher E., Weaver B. A., Tocknell J., Jamieson W., van Kerkwijk M. H., Robitaille T. P., Merry B., Bachetti M., Günther H. M., Aldcroft T. L., Alvarado-Montes J. A., Astropy Project Contributors 2022, The Astrophysical Journal, 935, 167

Baade D., 1988, in Cayrel de Strobel G., Spite M., eds, The Impact of Very High S/N Spectroscopy on Stellar Physics International Astronomical Union. Symposium no. 132, Nonradial Pulsations and the be Phenomenon. p. 217

Baade D., 1992, in Kondo Y., Sistero R., Polidan R. S., eds, Evolutionary Processes in Interacting Binary Stars Vol. 151, Binary Be-Stars and Be-Binaries. p. 147

Baade D., Labadie-Bartz J., Rivinius T., Carciofi A. C., 2023, Astronomy & Astrophysics, 678, A47

Baade D., Rivinius T., Pigulski A., Carciofi A., Handler G., Kuschnig R., Martayan C., Mehner A., Moffat A. F. J., Pablo H., Popowicz A., Rucinski S. M., Wade G. A., Weiss W. W., Zwintz K., 2017, in Zwintz K., Poretti E., eds, Second BRITE-Constellation

Science Conference: Small Satellites - Big Science Vol. 5, Pulsations and outbursts in Be stars: Small differences - big impacts. pp 196–205

Balmer J. J., 1885, Annalen der Physik, 261, 80

Balona L. A., 2022, Monthly Notices of the Royal Astronomical Society, 516, 3641

Balona L. A., Ozuyar D., 2020, Monthly Notices of the Royal Astronomical Society, 493, 2528

Barnsley R. M., Smith R. J., Steele I. A., 2012, Astronomische Nachrichten, 333, 101

Barnsley R. M., Steele I. A., 2013, Astronomy & Astrophysics, 556, A81

Batten A. H., 1989, Space Science Reviews, 50, 1

Behr A., 1959a, Veroeffentlichungen der Universitaets-Sternwarte zu Goettingen, 7, 199

Behr A., 1959b, Zeitschrift fuer Astrophysik, 47, 54

Berdyugin A., Piirola V., Teerikorpi P., 2014, Astronomy & Astrophysics, 561, A24

Bjorkman J. E., Carciofi A. C., 2005, in Ignace R., Gayley K. G., eds, The Nature and Evolution of Disks Around Hot Stars Vol. 337 of Astronomical Society of the Pacific Conference Series, Modeling the Structure of Hot Star Disks. p. 75

Bjorkman J. E., Cassinelli J. P., 1990, in Willson L. A., Stalio R., eds, Angular Momentum and Mass Loss for Hot Stars Vol. 316 of NATO Advanced Study Institute (ASI) Series C, Constraints on the Thickness of Be-Star Disks Derived from Combined Infrared Excess and Optical Polarimetry Data. p. 185

Bjorkman K. S., Nordsieck K. H., Code A. D., Anderson C. M., Babler B. L., Clayton G. C., Magalhaes A. M., Meade M. R., Nook M. A., Schulte-Ladbeck R. E., Taylor M., Whitney B. A., 1991, The Astrophysical Journal Letters, 383, L67

Blondel P. F. C., Djie H. R. E. T. A., 1994, in The P. S., Perez M. R., van den Heuvel E. P. J., eds, The Nature and Evolutionary Status of Herbig Ae/Be Stars Vol. 62 of Astronomical Society of the Pacific Conference Series, Detection of the accretion disk boundary layer of Herbig Ae/Be stars. p. 211

Bodensteiner J., Shenar T., Sana H., 2020, Astronomy & Astrophysics, 641, A42

Bohr N., 1913, The London, Edinburgh, and Dublin Philosophical Magazine and Journal of Science, 26, 1

Born M., Wolf E., Bhatia A. B., Clemmow P. C., Gabor D., Stokes A. R., Taylor A. M., Wayman P. A., Wilcock W. L., 1999, Principles of Optics: Electromagnetic Theory of Propagation, Interference and Diffraction of Light, 7 edn. Cambridge University Press

Brittain S. D., Kamp I., Meeus G., Oudmaijer R. D., Waters L. B. F. M., 2023, Space Science Reviews, 219, 7

Brown J. C., Cassinelli J. P., Maheswaran M., 2008, The Astrophysical Journal, 688, 1320

Brown J. C., McLean I. S., 1977, Astronomy & Astrophysics, 57, 141

Budding E., Erdem A., Çiçek C., Bulut I., Soydugan F., Soydugan E., Bakiş V., Demircan O., 2004, Astronomy & Astrophysics, 417, 263

Burbidge G. R., Burbidge E. M., 1953, The Astrophysical Journal, 117, 407

Capps R. W., Coyne G. V., Dyck H. M., 1973, The Astrophysical Journal, 184, 173

Carciofi A. C., Bjorkman J. E., 2006, The Astrophysical Journal, 639, 1081

Carciofi A. C., Magalhães A. M., Leister N. V., Bjorkman J. E., Levenhagen R. S., 2007, The Astrophysical Journal Letters, 671, L49

Carciofi A. C., Miroshnichenko A. S., Kusakin A. V., Bjorkman J. E., Bjorkman K. S., Marang F., Kuratov K. S., García-Lario P., Calderón J. V. P., Fabregat J., Magalhães A. M., 2006, The Astrophysical Journal, 652, 1617

Carciofi A. C., Okazaki A. T., Le Bouquin J. B., Štefl S., Rivinius T., Baade D., Bjorkman J. E., Hummel C. A., 2009, Astronomy & Astrophysics, 504, 915

Cardelli J. A., Clayton G. C., Mathis J. S., 1989, The Astrophysical Journal, 345, 245

Cassinelli J. P., Brown J. C., Maheswaran M., Miller N. A., Telfer D. C., 2002, The Astrophysical Journal, 578, 951

Cayrel R., 1988, in Cayrel de Strobel G., Spite M., eds, The Impact of Very High S/N Spectroscopy on Stellar Physics Vol. 132, Data Analysis. p. 345

Chandrasekhar S., 1946, The Astrophysical Journal, 103, 351

Cherchneff I., Sarangi A., 2017, in Miroshnichenko A., Zharikov S., Korčáková D., Wolf M., eds, The B[e] Phenomenon: Forty Years of Studies Vol. 508 of Astronomical Society of the Pacific Conference Series, New Insights on What, Where, and How Dust Forms in Evolved Stars. p. 57

Clark J. S., Steele I. A., 2000, Astronomy and Astrophysics Supplement Series, 141, 65

Clarke D., 1974, in Gehrels T., ed., IAU Colloq. 23: Planets, Stars, and Nebulae: Studied with Photopolarimetry Polarimetric Definitions. p. 45

Clayton G. C., Mathis J. S., 1988, The Astrophysical Journal, 327, 911

Collins George W. I., 1987, in Slettebak A., Snow T. P., eds, IAU Colloq. 92: Physics of Be Stars The Use of Terms and Definitions in the Study of be Stars (review Paper). p. 3

Conti P. S., 1997, in Nota A., Lamers H., eds, Luminous Blue Variables: Massive Stars in Transition Vol. 120 of Astronomical Society of the Pacific Conference Series, B[e] Stars: What Are They and Why Are They At This Workshop?. p. 161

Copeland J. A., Heard J. F., 1963, Publications of the David Dunlap Observatory, 2, 317

Cowley A. P., Marlborough J. M., 1968, Publications of the Astronomical Society of the Pacific, 80, 42

Cox A. N., 2000, Allen's astrophysical quantities. Springer New York

Coyne G. V., 1971, Ricerche Astronomiche, 8, 201

Coyne G. V., 1976, Astronomy & Astrophysics, 49, 89

Coyne G. V., Gehrels T., 1967, The Astronomical Journal, 72, 887

Coyne G. V., Kruszewski A., 1969, The Astronomical Journal, 74, 528

Cranmer S. R., 2005, The Astrophysical Journal, 634, 585

Cranmer S. R., 2009, The Astrophysical Journal, 701, 396

Curtiss R. H., 1916, Publications of Michigan Observatory, 2, 1

Curtiss R. H., 1926, Journal of the RAS of Canada, 20, 19

Davies J. K., Evans A., Bode M. F., Whittet D. C. B., 1990, Monthly Notices of the Royal Astronomical Society, 247, 517

de Jager C., Nieuwenhuijzen H., 1987, Astronomy & Astrophysics, 177, 217

Di Francesco J., Evans Neal J. I., Harvey P. M., Mundy L. G., Guilloteau S., Chandler C. J., 1997, The Astrophysical Journal, 482, 433

Dimitrov D. P., Kjurkchieva D. P., Ivanov E. I., 2018, The Astronomical Journal, 156, 61

Doazan V., Franco M., Rusconi L., Sedmak G., Stalio R., 1983, Astronomy & Astrophysics, 128, 171

Dyson F. W., 1906, Philosophical Transactions of the Royal Society of London Series A, 206, 403

Edlund, E. 1860, Astronomische Nachrichten, 52, 305

Edwards D. L., 1944, Monthly Notices of the Royal Astronomical Society, 104, 283

Eker Z., Bakış V., Bilir S., Soydugan F., Steer I., Soydugan E., Bakış H., Aliçavuş F., Aslan G., Alpsoy M., 2018, Monthly Notices of the Royal Astronomical Society, 479, 5491

Finkenzeller U., 1985, Astronomy & Astrophysics, 151, 340

Fowler E. A., 1922, in Fowler E. A., ed., Proceedings of the 1st General Assembly Vol. 1, Ist General Assembly - Transactions of the IAU Vol. I. p. 100

Frémat Y., Zorec J., Hubert A. M., Floquet M., 2005, Astronomy & Astrophysics, 440, 305

Garrison L. M., Anderson C. M., 1977, The Astrophysical Journal, 218, 438

Gehrels T., 1960, The Astronomical Journal, 65, 470

Gehrels T., 1974, in Gehrels T., ed., IAU Colloq. 23: Planets, Stars, and Nebulae: Studied with Photopolarimetry Introduction and Overview. p. 3

Gehrz R. D., Hackwell J. A., Jones T. W., 1974, The Astrophysical Journal, 191, 675

Gies D. R., Bagnuolo W. G. J., Baines E. K., ten Brummelaar T. A., Farrington C. D., Goldfinger P. J., Grundstrom E. D., Huang W., McAlister H. A., Mérand A., Sturmann J., Sturmann L., Touhami Y., Turner N. H., Wingert D. W., Berger D. H., McSwain M. V., Aufdenberg J. P., Ridgway S. T., Cochran A. L., Lester D. F., Sterling N. C., Bjorkman J. E., Bjorkman K. S., Koubský P., 2007, The Astrophysical Journal, 654, 527

Gontcharov G. A., Mosenkov A. V., 2019, Monthly Notices of the Royal Astronomical Society, 483, 299

Grinin V. P., 1994, in The P. S., Perez M. R., van den Heuvel E. P. J., eds, The Nature and Evolutionary Status of Herbig Ae/Be Stars Vol. 62 of Astronomical Society of the Pacific Conference Series, Polarimetric activity of Herbig Ae/Be stars. p. 63

Grunhut J. H., Wade G. A., Neiner C., Oksala M. E., Petit V., Alecian E., Bohlender D. A., Bouret J. C., Henrichs H. F., Hussain G. A. J., Kochukhov O., MiMeS Collaboration 2017, Monthly Notices of the Royal Astronomical Society, 465, 2432

Hall J. S., 1958, Publications of the U.S. Naval Observatory Second Series, 17, 275

Hanuschik R. W., 1995, Astronomy & Astrophysics, 295, 423

Hanuschik R. W., 1996, Astronomy & Astrophysics, 308, 170

Hanuschik R. W., Hummel W., Dietle O., Sutorius E., 1995, Astronomy & Astrophysics, 300, 163

Hanuschik R. W., Kozok J. R., Kaiser D., 1988, Astronomy & Astrophysics, 189, 147

Hanuschik R. W., Stefl S., Hummel W., Vrancken M., 1995, Be Star Newsletter, 30, 15

Harmanec P., 2002, in Tout C. A., van Hamme W., eds, Exotic Stars as Challenges to Evolution Vol. 279 of Astronomical Society of the Pacific Conference Series, Strange Among the Strange: The B-emission Star γ Cassiopeiæ. p. 221

Harrington M. W., 1884, Sidereal Messenger, 3, 79

Hastings B., Langer N., Wang C., Schootemeijer A., Milone A. P., 2021, Astronomy & Astrophysics, 653, A144

Hastings B., Wang C., Langer N., 2020, Astronomy & Astrophysics, 633, A165

Haucke M., Cidale L. S., Venero R. O. J., Curé M., Kraus M., Kanaan S., Arcos C., 2018, Astronomy & Astrophysics, 614, A91

Hecht E., 2017, Optics. Pearson Education

Heiles C., 2000, The Astronomical Journal, 119, 923

Herbig G. H., 1960, The Astronomical Journal Supplement, 4, 337

Hillenbrand L. A., Strom S. E., Vrba F. J., Keene J., 1992, The Astrophysical Journal, 397, 613

Hiltner W. A., 1947, The Astrophysical Journal, 106, 231

Hiltner W. A., 1949, The Astrophysical Journal, 109, 471

Howells L., Steele I. A., Porter J. M., Etherton J., 2001, Astronomy & Astrophysics, 369, 99

Hubert A. M., 2007, in Okazaki A. T., Owocki S. P., Stefl S., eds, Active OB-Stars: Laboratories for Stellare and Circumstellar Physics Vol. 361 of Astronomical Society of the Pacific Conference Series, Statistical Inference of the Be Star Periodicity. p. 27

Huggins W., 1867, Astronomical register, 5, 34

Hummel W., Vrancken M., 2000, Astronomy & Astrophysics, 359, 1075

Janssen E. M., 1946, The Astrophysical Journal, 103, 380

Jaschek C., Gomez A. E., 1998, Astronomy & Astrophysics, 330, 619

Jaschek M., Egret D., 1982, Proc. IAU Symp., 98, 261

Jaschek M., Slettebak A., Jaschek C., 1981, Be Star Newsletter, 4, 9

Jermak H., Steele I. A., Smith R. J., 2016a, in Evans C. J., Simard L., Takami H., eds, Ground-based and Airborne Instrumentation for Astronomy VI Vol. 9908 of Society of Photo-Optical Instrumentation Engineers (SPIE) Conference Series, MOPTOP: a multi-colour optimised optical polarimeter. p. 99084I

Jermak H., Steele I. A., Smith R. J., 2016b, in Evans C. J., Simard L., Takami H., eds, Ground-based and Airborne Instrumentation for Astronomy VI Vol. 9908 of Society of Photo-Optical Instrumentation Engineers (SPIE) Conference Series, MOPTOP: a multi-colour optimised optical polarimeter. p. 99084I

Jermak H., Steele I. A., Smith R. J., 2018, in Evans C. J., Simard L., Takami H., eds, Ground-based and Airborne Instrumentation for Astronomy VII Vol. 10702 of Society of Photo-Optical Instrumentation Engineers (SPIE) Conference Series, Optical design of the Liverpool Telescope Multicolour OPTimised Optical Polarimeter (MOPTOP). p. 107024Q

Jones C. E., Labadie-Bartz J., Cotton D. V., Nazé Y., Peters G. J., Hillier D. J., Neiner C., Richardson N. D., Hoffman J. L., Carciofi A. C., Wisniewski J. P., Gayley K. G., Suffak M. W., Ignace R., Scowen P. A., 2022, Astrophysics and Space Science, 367, 124

Joy A. H., 1942, Publications of the Astronomical Society of the Pacific, 54, 35

Kaitchuck R. H., Park E. A., 1988, The Astrophysical Journal, 325, 225

Kato S., 1983, Publications of the Astronomical Society of Japan, 35, 249

Kaufer A., Stahl O., Prinja R. K., Witherick D., 2006, Astronomy & Astrophysics, 447, 325

Kaufer A., Stahl O., Wolf B., Gaeng T., Gummersbach C. A., Kovacs J., Mandel H., Szeifert T., 1996, Astronomy & Astrophysics, 305, 887

Klement R., Schaefer G. H., Gies D. R., Wang L., Baade D., Rivinius T., Gallenne A., Carciofi A. C., Monnier J. D., Mérand A., Anugu N., Kraus S., Davies C. L., Lanthermann C., Gardner T., Wysocki P., Ennis J., Labdon A., Setterholm B. R., Le Bouquin J.-B., 2022, The Astrophysical Journal, 926, 213

Kogure T., 1981, Publications of the Astronomical Society of Japan, 33, 399

Kogure T., Suzuki M., 1986, Astrophysics and Space Science, 120, 253

Kramida A. E., 2010, Atomic Data and Nuclear Data Tables, 96, 586

Kraus M., Haucke M., Cidale L. S., Venero R. O. J., Nickeler D. H., Németh P., Niemczura E., Tomić S., Aret A., Kubát J., Kubátová B., Oksala M. E., Curé M., Kamiński K., Dimitrov W., Fagas M., Polińska M., 2015, Astronomy & Astrophysics, 581, A75

Kriz S., Harmanec P., 1975, Bulletin of the Astronomical Institutes of Czechoslovakia, 26, 65

Lagrange C., 1881, Ciel et Terre, 1, 125

Lam M. C., Smith R. J., Arcavi I., Steele I. A., Veitch-Michaelis J., Wyrzykowski L., 2023, The Astronomical Journal, 166, 13

Lamers H. J. G. L. M., Zickgraf F.-J., de Winter D., Houziaux L., Zorec J., 1998, Astronomy & Astrophysics, 340, 117

Lee U., Osaki Y., Saio H., 1991, Monthly Notices of the Royal Astronomical Society, 250, 432

Lequeux J., 2005, The Interstellar Medium. Springer Berlin, Heidelberg

Li A., 2008, arXiv e-prints, p. arXiv:0808.4123

Limber D. N., Marlborough J. M., 1968, The Astrophysical Journal, 152, 181

Lyot B., 1929, PhD thesis, Universite Pierre et Marie Curie (Paris VI), France

Maeder A., 2009, Physics, Formation and Evolution of Rotating Stars. Springer Berlin, Heidelberg

Markova N., Prinja R. K., Markov H., Kolka I., Morrison N., Percy J., Adelman S., 2008, Astronomy & Astrophysics, 487, 211

Marr K. C., Jones C. E., Halonen R. J., 2018, The Astrophysical Journal, 852, 103

Marsh K. A., Van Cleve J. E., Mahoney M. J., Hayward T. L., Houck J. R., 1995, The Astrophysical Journal, 451, 777

Martin P. G., 1972, Monthly Notices of the Royal Astronomical Society, 159, 179

Martínez-Núñez S., Kretschmar P., Bozzo E., Oskinova L. M., Puls J., Sidoli L., Sundqvist J. O., Blay P., Falanga M., Fürst F., Gímenez-García A., Kreykenbohm I., Kühnel M., Sander A., Torrejón J. M., Wilms J., 2017, Space Science Reviews, 212, 59

McLaughlin D. B., 1937, The Astrophysical Journal, 85, 181

McLean I. S., Brown J. C., 1978, Astronomy & Astrophysics, 69, 291

McLean I. S., Clarke D., 1976, in Slettebak A., ed., Be and Shell Stars Vol. 70 of IAU Symposium, Polarization Measurements across the Balmer Lines of be and Shell Stars. p. 261

McSwain M. V., Gies D. R., 2005, The Astronomical Journal Supplement, 161, 118

McSwain M. V., Huang W., Gies D. R., 2009, The Astrophysical Journal, 700, 1216

McSwain M. V., Huang W., Gies D. R., Grundstrom E. D., Townsend R. H. D., 2008, The Astrophysical Journal, 672, 590

Meilland A., Stee P., Zorec J., Kanaan S., 2006, Astronomy & Astrophysics, 455, 953

Mennickent R. E., Sterken C., Vogt N., 1997, Astronomy & Astrophysics, 326, 1167

Mennickent R. E., Vogt N., 1991, Astronomy & Astrophysics, 241, 159

Merrill P. W., Burwell C. G., 1933, The Astrophysical Journal, 78, 87

Merrill P. W., Burwell C. G., 1949, The Astrophysical Journal, 110, 387

Merrill P. W., Humason M. L., Burwell C. G., 1925, Astrophysical Journal, 61, 389

Milne E. A., 1928, Monthly Notices of the Royal Astronomical Society, 89, 3

Miroshnichenko A. S., 2007, The Astrophysical Journal, 667, 497

Miroshnichenko A. S., 2016, in Sigut T. A. A., Jones C. E., eds, Bright Emissaries: Be Stars as Messengers of Star-Disk Physics Vol. 506 of Astronomical Society of the Pacific Conference Series, Binaries Among Be Stars. p. 71

Miroshnichenko A. S., Bjorkman K. S., Krugov V. D., 2002, Publications of the Astronomical Society of the Pacific, 114, 1226

Miroshnichenko A. S., Danford S., Zharikov S. V., Klochkova V. G., Chentsov E. L., Vanbeveren D., Zakhozhay O. V., Manset N., Pogodin M. A., Omarov C. T., Kuratova A. K., Khokhlov S. A., 2020, The Astrophysical Journal, 897, 48

Mitchell S. A., 1947, The Astrophysical Journal, 105, 1

Morales-Rueda L., Carter D., Steele I. A., Charles P. A., Worswick S., 2004, Astronomische Nachrichten, 325, 215

Morgan W. W., Keenan P. C., 1973, Annual Review of Astronomy and Astrophysics, 11, 29

Mourard D., Monnier J. D., Meilland A., Gies D., Millour F., Benisty M., Che X., Grundstrom E. D., Ligi R., Schaefer G., Baron F., Kraus S., Zhao M., Pedretti E., Berio P., Clausse J. M., Nardetto N., Perraut K., Spang A., Stee P., Tallon-Bosc I., McAlister H., ten Brummelaar T., Ridgway S. T., Sturmann J., Sturmann L., Turner N., Farrington C., 2015, Astronomy & Astrophysics, 577, A51

Mundt R., Ray T. P., 1994, in The P. S., Perez M. R., van den Heuvel E. P. J., eds, The Nature and Evolutionary Status of Herbig Ae/Be Stars Vol. 62 of Astronomical Society of the Pacific Conference Series, Optical outflows from Herbig Ae/Be stars and other high luminosity young stellar objects. p. 237

Nickeler D. H., Kraus M., 2024, The Astrophysical Journal, 963, 131

Okazaki A. T., 1991, Publications of the Astronomical Society of Japan, 43, 75

Okazaki A. T., 2007, in Okazaki A. T., Owocki S. P., Stefl S., eds, Active OB-Stars: Laboratories for Stellare and Circumstellar Physics Vol. 361 of Astronomical Society of the Pacific Conference Series, Theory vs. Observation of Circumstellar Disks and Their Formation. p. 230

Okazaki A. T., 2016, in Sigut T. A. A., Jones C. E., eds, Bright Emissaries: Be Stars as Messengers of Star-Disk Physics Vol. 506 of Astronomical Society of the Pacific Conference Series, Current Status of Our Understanding of Be Disk Physics Invited Review. p. 3

Oudmaijer R. D., Miroshnichenko A. S., 2017, in Miroshnichenko A., Zharikov S., Korčáková D., Wolf M., eds, The B[e] Phenomenon: Forty Years of Studies Vol. 508 of Astronomical Society of the Pacific Conference Series, Introduction to the B[e] Phenomenon. p. 3

Oudmaijer R. D., Parr A. M., 2010, Monthly Notices of the Royal Astronomical Society, 405, 2439

Owocki S., 2006, in Kraus M., Miroshnichenko A. S., eds, Stars with the B[e] Phenomenon Vol. 355 of Astronomical Society of the Pacific Conference Series, Formation and Evolution of Disks around Classical Be Stars. p. 219

Owocki S. P., Cranmer S. R., Blondin J. M., 1994, The Astrophysical Journal, 424, 887

Papaloizou J. C., Savonije G. J., Henrichs H. F., 1992, Astronomy & Astrophysics, 265, L45

Pelupessy I., Lamers H. J. G. L. M., Vink J. S., 2000, Astronomy & Astrophysics, 359, 695

Percy J. R., Marinova M. M., BožiĆ H., Harmanec P., 1999, Astronomy & Astrophysics, 348, 553

Perrine C. D., 1902, Lick Observatory Bulletin, 23, 170

Petit V., Owocki S. P., Wade G. A., Cohen D. H., Sundqvist J. O., Gagné M., Maíz Apellániz J., Oksala M. E., Bohlender D. A., Rivinius T., Henrichs H. F., Alecian E., Townsend R. H. D., ud-Doula A., MiMeS Collaboration 2013, Monthly Notices of the Royal Astronomical Society, 429, 398

Piascik A. S., Steele I. A., Bates S. D., Mottram C. J., Smith R. J., Barnsley R. M., Bolton B., 2014, in Ramsay S. K., McLean I. S., Takami H., eds, Ground-based and Airborne Instrumentation for Astronomy V Vol. 9147 of Society of Photo-Optical Instrumentation Engineers (SPIE) Conference Series, SPRAT: Spectrograph for the Rapid Acquisition of Transients. p. 91478H

Pickering E. C., 1887, Harvard College Observatory Papers, 3, K4

Pickering E. C., 1890, Annals of Harvard College Observatory, 27, 1

Pickering E. C., 1908, Annals of Harvard College Observatory, 50, 1

Plavec M., 1970, Publications of the Astronomical Society of the Pacific, 82, 957

Plavec M., Polidan R. S., 1976, in Eggleton P., Mitton S., Whelan J., eds, Structure and Evolution of Close Binary Systems Vol. 73, The ALGOLS, Red Spectra, BE Stars, and Even Neutrinos. p. 289

Poeckert R., Marlborough J. M., 1976, The Astrophysical Journal, 206, 182

Poeckert R., Marlborough J. M., 1978a, The Astrophysical Journal, 220, 940

Poeckert R., Marlborough J. M., 1978b, The Astronomical Journal Supplement, 38, 229

Pols O. R., Cote J., Waters L. B. F. M., Heise J., 1991, Astronomy & Astrophysics, 241, 419

Portegies Zwart S. F., 1995, Astronomy & Astrophysics, 296, 691

Porter J. M., 1996, Monthly Notices of the Royal Astronomical Society, 280, L31

Porter J. M., Rivinius T., 2003, Publications of the Astronomical Society of the Pacific, 115, 1153

Pringle J. E., 1981, Annual Review of Astronomy and Astrophysics, 19, 137

Puls J., Vink J. S., Najarro F., 2008, Astronomy and Astrophysics Reviews, 16, 209

Quirrenbach A., 1994, in Balona L. A., Henrichs H. F., Le Contel J. M., eds, Pulsation; Rotation; and Mass Loss in Early-Type Stars Astronomical Union, Symposium 162, Seven Be stars resolved by optical long-baseline interferometry. p. 450

Quirrenbach A., Bjorkman K. S., Bjorkman J. E., Hummel C. A., Buscher D. F., Armstrong J. T., Mozurkewich D., Elias N. M. I., Babler B. L., 1997, The Astrophysical Journal, 479, 477

Ralchenko Y., 2005, Memorie della Societa Astronomica Italiana Supplementi, 8, 96

Ranyard A. C., 1873, Nature, 7, 201

Ranyard A. C., 1874, Monthly Notices of the Royal Astronomical Society, 34, 489

Rivinius T., Baade D., Stefl S., et al. 1998, in Kaper L., Fullerton A. W., eds, Cyclical Variability in Stellar Winds ESO Astrophysics Symposia, Predicting the Outbursts of the Be Star µ Cen. p. 207

Rivinius T., Baade D., Stefl S., Stahl O., Wolf B., Kaufer A., 1998, Astronomy & Astrophysics, 333, 125

Rivinius T., Carciofi A. C., Martayan C., 2013, Astronomy and Astrophysics Reviews, 21, 69

Roy A. E., 2005, Orbital motion. IOP Publishing Ltd.

Rydberg J., 1890, Recherches sur la constitution des spectres d'émission des éléments chimiques. No. 11 in Kungliga vetenskapsakademiens handlingar, Kungliga Vetenskapsakademien

Salet P., 1936, Journal des Observateurs, 19, 17

Schneider P., 2006, Extragalactic Astronomy and Cosmology. Springer Berlin, Heidelberg

Secchi A., 1866, Astronomische Nachrichten, 68, 63

Secchi, A. 1860, Monthly Notices of the Royal Astronomical Society, 20, 70

Seok J. Y., Li A., 2017, The Astrophysical Journal, 835, 291

Serkowski K., 1968, The Astrophysical Journal, 154, 115

Serkowski K., 1970, The Astrophysical Journal, 160, 1083

Serkowski K., Mathewson D. S., Ford V. L., 1975, The Astrophysical Journal, 196, 261

Shakura N. I., Sunyaev R. A., 1973, Astronomy & Astrophysics, 24, 337

Shrestha M., Steele I. A., Piascik A. S., Jermak H., Smith R. J., Copperwheat C. M., 2020, Monthly Notices of the Royal Astronomical Society, 494, 4676

Sigut T. A. A., Mahjour A. K., Tycner C., 2020, The Astrophysical Journal, 894, 18

Silaj J., Jones C. E., Tycner C., Sigut T. A. A., Smith A. D., 2010, The Astronomical Journal Supplement, 187, 228

Slettebak A., 1949, The Astrophysical Journal, 110, 498

Slettebak A., 1979, Space Science Reviews, 23, 541

Slettebak A., 1982, The Astronomical Journal Supplement, 50, 55

Slettebak A., Collins G., Boyce P., White N. M., Parkinson T., 1975, Astrophysical Journal Supplement Series (Supplement no. 281), vol. 29, May 1975, p. 137-159. Research supported by the Ohio State University, 29, 137

Spitzer L., 1978, Physical processes in the interstellar medium. Wiley

Stee P., 2003, Astronomy & Astrophysics, 403, 1023

Steele I. A., Clark J. S., 2001, Astronomy & Astrophysics, 371, 643

Steele I. A., Negueruela I., Clark J. S., 1999, Astronomy and Astrophysics Supplement Series, 137, 147

Steele I. A., Smith R. J., Rees P. C., Baker I. P., Bates S. D., Bode M. F., Bowman M. K., Carter D., Etherton J., Ford M. J., Fraser S. N., Gomboc A., Lett R. D. J., Mansfield A. G., Marchant J. M., Medrano-Cerda G. A., Mottram C. J., Raback D., Scott A. B., Tomlinson M. D., Zamanov R., 2004, in Oschmann Jacobus M. J., ed., Ground-based Telescopes Vol. 5489 of Society of Photo-Optical Instrumentation Engineers (SPIE) Conference Series, The Liverpool Telescope: performance and first results. pp 679–692

Steele I. A., Wiersema K., McCall C., Newsam A., Shrestha M., 2023, Monthly Notices of the Royal Astronomical Society, 518, 1214

Stokes G. G., 1851, Transactions of the Cambridge Philosophical Society, 9, 399

Struve O., 1931, The Astrophysical Journal, 73, 94

Swings J. P., 1973, Astronomy & Astrophysics, 26, 443

Telting J. H., Heemskerk M. H. M., Henrichs H. F., Savonije G. J., 1994, Astronomy & Astrophysics, 288, 558

Touhami Y., Gies D. R., Schaefer G. H., 2011, The Astrophysical Journal, 729, 17

Townsend R. H. D., 2005, Monthly Notices of the Royal Astronomical Society, 364, 573

Townsend R. H. D., Owocki S. P., Howarth I. D., 2004, Monthly Notices of the Royal Astronomical Society, 350, 189

Trippe S., 2014, Journal of Korean Astronomical Society, 47, 15

ud-Doula A., Owocki S. P., Kee N. D., 2018, Monthly Notices of the Royal Astronomical Society, 478, 3049

Underhill A., Doazan V., 1982, B stars with and without emission lines part I. National Aeronautics and Space Administration

Vakili F., Mourard D., Stee P., Bonneau D., Berio P., Chesneau O., Thureau N., Morand F., Labeyrie A., Tallon-Bosc I., 1998, Astronomy & Astrophysics, 335, 261

van de Hulst H. C., 1950, The Astrophysical Journal, 112, 1

van de Hulst H. C., 1957, Light Scattering by Small Particles. Dover Publications

von Zeipel H., 1924, Monthly Notices of the Royal Astronomical Society, 84, 665

Wade G. A., Petit V., Grunhut J., Neiner C., 2014, arXiv e-prints, p. arXiv:1411.6165

Wade G. A., Petit V., Grunhut J. H., Neiner C., MiMeS Collaboration 2016, in Sigut T. A. A., Jones C. E., eds, Bright Emissaries: Be Stars as Messengers of Star-Disk Physics Vol. 506 of Astronomical Society of the Pacific Conference Series, Magnetic Fields of Be Stars: Preliminary Results from a Hybrid Analysis of the MiMeS Sample. p. 207

Waters L. B. F. M., Waelkens C., 1998, Annual Review of Astronomy and Astrophysics, 36, 233

Wisniewski J. P., Draper Z. H., Bjorkman K. S., Meade M. R., Bjorkman J. E., Kowalski A. F., 2010, The Astrophysical Journal, 709, 1306

Wood K., Bjorkman K. S., Bjorkman J. E., 1997, The Astrophysical Journal, 477, 926

Wood R., 1922, The London, Edinburgh, and Dublin Philosophical Magazine and Journal of Science, 44, 538

Woolf N. J., Stein W. A., Strittmatter P. A., 1970, Astronomy & Astrophysics, 9, 252

Wyse A. B., 1934, Lick Observatory Bulletin, 464, 37

Yudin R. V., 2001, Astronomy & Astrophysics, 368, 912

Zamanov R. K., Stoyanov K. A., Stefanov S. Y., Bode M. F., Minev M. S., 2023, Astronomische Nachrichten, 344, e20230022

Zellner B. H., Serkowski K., 1972, Publications of the Astronomical Society of the Pacific, 84, 619

Zorec J., Frémat Y., Domiciano de Souza A., Royer F., Cidale L., Hubert A. M., Semaan T., Martayan C., Cochetti Y. R., Arias M. L., Aidelman Y., Stee P., 2016, Astronomy & Astrophysics, 595, A132

Zwintz K., Pigulski A., Kuschnig R., Wade G. A., Doherty G., Earl M., Lovekin C., Müllner M., Piché-Perrier S., Steindl T., Beck P. G., Bicz K., Bowman D. M., Handler G., Pablo B., Popowicz A., Różański T., Mikołajczyk P., Baade D., Koudelka O., Moffat A. F. J., Neiner C., Orleański P., Smolec R., Louis N. S., Weiss W. W., Wenger M., Zocłońska E., 2024, Astronomy & Astrophysics, 683, A49